Processing, Forming and Modifying Cellulose to Produce Sustainable Materials and Composites

Coombs O'Brien, James

Award date:
2018

Awarding institution:
University of Bath

Processing, Forming and Modifying Cellulose to Produce Sustainable Materials and Composites

submitted by

James Coombs OBrien

for the degree of Doctor of Philosophy

of the

University of Bath

Department of Chemistry

May 2018

"If you trust in yourself and believe in your dreams and follow your star, you'll still get beaten by people who spent their time working hard and learning things and weren't so lazy."
Terry Pratchett, *The Wee Free Men*, 2003

Abstract

The recent rise in public and governmental awareness of the negative effects of plastic waste has made sustainable biodegradable materials all the more sought after. This is evident in the recent ban on synthetic microbeads for use in personal care products in the UK, providing an even greater push in academia and industry for the production of non-persistent materials which can be manufactured at scale.

This thesis details a multidisciplinary approach to the continuous manufacturing of cellulose microbeads as a sustainable alternative to plastic microparticles. It consists of an Introduction (Chapter 1) describing the context and motivation for the project, a Literature Review (Chapter 2) detailing and interpreting the relevant research from the wider scientific and engineering community, Experimental Procedures (Chapter 3) describing the materials, experimentation and analysis conducted, Research Chapters (Chapter 4 - 6) documenting the underpinning theory and research conducted for this thesis (described in greater detail below), Overall Conclusion (Chapter 7) providing an overview of the findings of this thesis as well as potential future considerations and an Appendix containing information that supports the research chapters.

The dissolution of cellulose in an organic electrolyte solution (OES, based on an ionic liquid coupled with a co-solvent) is a widely applied method for this polymer's sustainable processing. This thesis details the use of such a route for the production of cellulose microbeads via coagulation, using an anti-solvent, from emulsions of cellulose-OES in sunflower oil (SFO)-Span 80. Membrane emulsification is utilised to generate these emulsions and, as far as the author is aware, is the first example of the generation of cellulose microbeads utilising membrane technology and was formally reported in a paper published from the

work detailed in this thesis.

In Chapter 4, the use of ionic liquids, in conjunction with a co-solvent, is explored for the sustainable processing of cellulose. The solutions are characterised according to key parameters used for processing biphasic systems: rheology, interfacial tension and contact angle, when emulsified in a sunflower oil continuous phase using a membrane. With the aid of experimental design, it was concluded that a solvent system of [EMIm][OAc]:DMSO (30:70, w/w) was optimal for dissolution of cellulose with the formed solution showing Newtonian flow profiles and interfacial stability in a sunflower oil-Span 80 continuous phase.

These findings were used to design and construct a membrane emulsification rig suitable for continuous production of cellulose microbeads. In Chapter 5, a systematic analysis of process parameters is described. The dimensionless force ratios - capillary number (Ca) and Weber number (We) - were mapped and it was determined that, as with many examples in the literature, a low Weber number provided the optimal removal of droplets from the membrane surface producing cellulose beads in a controllable reproducible manner, after the addition of an anti-solvent. The cellulose-OES solutions were also applied to the production of larger cellulose beads via a scaled up dropping process. A techno-economic analysis highlighted the feasibility of this production process in terms of materials cost, aided by efficient recycling and separation streams.

Chapter 6 details the post processing of the formed cellulose beads to produce a range of materials of differing mechanical strength and surface functionality. Cross-linked cellulose beads with enhanced mechanical strength were prepared for potential use in abrasive applications. This was coupled with topographical alterations, via enzyme and acid etching, producing significantly rougher surfaces, useful for use as supports in extraction applications. Surface functionalisation to impart a hydrophobic surface functionality as well as coating with another biopolymer, chitosan, expanded the potential use of these materials further.

Finally, in Chapter 7 the overall findings of this thesis are detailed and potential extensions of this work, both with regards to production processes and materials, are discussed

Acknowledgements

The research detailed in this thesis could not have been conducted without the help and support of my supervisors, Professor Janet L. Scott, Professor Davide Mattia, Dr Laura Torrente Murciano and Dr Paul Murray, who have provided me with sound guidance and inspiration throughout my project. My sincerest thanks go to the Centre for Sustainable Chemical Technologies (CSCT), with specific mention to cohort 2013 who have represented the diversity and passion of the CSCT. I would also like to thank a number of PhD and Post-Doctoral researchers across a range of departments and disciplines who've helped me on a day to day basis over the past 3 years, including: Dr Marcus Johns, Jamie Courtenay, Dr Simon Bishopp, Dr Victoria Garcia Rocha, Dr Alavro Cruz-Izquierdo, Dr Saravana Chandrasekaran, Dr Nicholas Taylor, Dr Ella Gale, Dr Paul McKeown, Dr Julian Schmitt, Dr Martin Depardieu and Dr Ekanem Ekanem. I would also like to specifically mention James Close and Davide Califano who helped collect data which contributed to this thesis.

My thanks also go out to the technical staff of the Departments of Chemical Engineering, Chemistry and Pharmacy and Pharmacology at the University of Bath as well as those of the Microscope and Analysis Suite (MAS) and Chemical Characterisation and Analysis Facility (CCAF), who have shared their knowledge and advice on a consistent basis. I would like to acknowledge the University of Bath and the Engineering and Physical Sciences Research Council for funding

(DTC in Sustainable Chemical Technologies grant number: EP/G03768X/1) alongside the Worshipful Company of Armourers and Brasiers for travel funding. Finally, I'd like to thank my family and friends for putting up with this crazy pursuit of knowledge.

Contents

[1]Some experimental data in this section was collected in conjunction with Davide Califano, a full list of which can be found in the Appendix.

[2]Some experimental data in this section was collected in conjunction with James Close during an MEng project, a full list of which can be found in the Appendix.

Abbreviations

AMA Acryloyl malic acid

APP Ammonium polyphosphate

[**BMIm**][**Cl**] 1-Butyl-3-methylimidazolium chloride

BP Boiling point

CA Contact angle

DMDHEU Dimethylol dihydroxy ethylene urea

DoE Design of experiments

DP Degree of polymerisation

EDX Energy dispersive X-ray spectroscopy

[**EMIm**][**OAc**] 1-Ethyl-3-methylimidazolium acetate

HLB Hydrophilic-lipophilic balance

ID Inner diameter

IFT Interfacial tension

IL Ionic liquid

ISO International Organisation for Standardisation

MCC Microcrystalline cellulose

NMR Nuclear Magnetic Resonance

OD Outer diameter

OECD Organisation for Economic Co-operation and Development

OES Organic electrolyte solution

OVAT One variable at a time

PE Polyethylene

PS Polystyrene

RTIL Room temperature ionic liquid

SEM Scanning electron microscopy

SFO Sunflower oil

SPG Shirasu porous glass

TMS Trimethylchlorosilane

TOS Trichloro(octadecyl)silane

Nomenclature

$Dv(10)$ Maximum particle diameter below which 10% of the sample volume exists

$Dv(50)$ Maximum particle diameter below which 50% of the sample volume exists (median particle size by volume)

$Dv(90)$ Maximum particle diameter below which 90% of the sample volume exists

Re Reynolds number

D_{mem} Inner diameter of the tubular membrane

σ Shear stress

$\dot{\gamma}$ Shear rate

F_D Drag force

F_{In} Inertial force

F_γ Interfacial tension force

F_B Buoyancy force

J_d Flux of the disperse phase

K Membrane permeability

A Surface area of a membrane

θ Contact angle (three way) between the membrane surface disperse phase droplet and continuous phase

Ca Capillary number

$D[3,2]$ Sauter mean particle diameter

d_d Droplet diameter

ΔP Pressure drop

ρ_{cp} Density of the continuous phase

ρ_{dp} Density of the disperse phase

d_p Diameter of pore

$D_{peakmax}$ Diameter at which the largest volume % presides

ε Porosity of a membrane

f Friction factor

$fwhm$ Full width half maximum

γ Interfacial tension

k_x Wall correction factor

L Thickness of membrane

n Number of membrane pores

P_c Critical pressure

$P_{(c,in)}$ Pressure of the continuous phase at the membrane inlet

$P_{(c,out)}$ Pressure of the continuous phase at the membrane outlet

P_d Pressure imparted on the disperse phase

P_{tm} Transmembrane pressure

q Flow rate through a single pore

Q_{cp} Continuous phase flow rate

Q_{dp} Total disperse phase flow rate through the membrane

r_d Radius of droplet

r_p Radius of pore

μ_{cp} Viscosity of the continuous phase

μ_{dp} Viscosity of the disperse phase

v_{cp} Velocity of the continuous phase

v_d Velocity of the disperse phase in the pore

τ_w Wall shear force

We Weber number

List of Figures

List of Tables

Research Dissemination

In keeping with the spirit of the Centre for Sustainable Technology (CSCT), I have had the opportunity to discuss my research with a wide range of people during public engagement events including the Green Man Festival, Research Objects (AgeUK) and I'm a Scientist Get Me Out of Here! I have also given oral and poster presentations at symposia organised through the CSCT including: The Summer Showcase (2014, 2015, 2016 and 2017), Symposia on "Renewable Feedstocks: Fantasy or Reality" (2015) and "Enabling Healthcare Technologies: Synthesis, Biomaterials and Sensing" (2015). Externally, I have attended and presented posters at New Horizons for Nanocellulose (The Royal Society) and COIL-6 (Congress On Ionic Liquids) with the aid of travel and expenses grants from the Worshipful Company of Armourers and Brasiers and the CSCT.

Publications

Research documented in the three research chapters in this thesis has contributed to the attached open access publication, provided here:

ACS Sustainable Chemistry & Engineering

Research Article

pubs.acs.org/journal/ascecg

Continuous Production of Cellulose Microbeads via Membrane Emulsification

James Coombs OBrien,[†,‡] Laura Torrente-Murciano,[§,∥] Davide Mattia,*[,§,∥] and Janet L. Scott*[,†,∥]

[†]Department of Chemistry, [‡]EPSRC Doctoral Training Centre in Sustainable Chemical Technologies, [§]Department of Chemical Engineering, and [∥]Centre for Sustainable Chemical Technologies, University of Bath, Claverton Down, Bath BA2 7AY, United Kingdom

Supporting Information

ABSTRACT: We report on the continuous manufacturing of cellulose microbeads as a sustainable alternative to plastic microparticles, currently used in a wide range of consumer products from toothpaste to paints. Plastic microbeads are not retained by, or degraded in, wastewater treatment plants (due to their size and composition), accumulating in the environment in general and aquatic life in particular, eventually finding their way into the human food supply chain. Here, it is demonstrated, for the first time, that a cross-flow membrane emulsification−phase inversion process can be used to generate stabilized microdroplets of cellulose dissolved in an organic electrolyte solution (1-ethyl-3-methylimidazolium acetate:DMSO) in a sunflower oil-Span 80 continuous phase. The emulsion is subsequently coagulated with an antisolvent, resulting in the formation of solid, spherical, and biodegradable cellulose microbeads. A systematic analysis of process parameters (continuous and disperse phase flow rate, viscosity, and applied pressure) allowed the determination of a regime within which microspheres can be predictably produced using a 10 μm pore-sized porous glass membrane. Cross-linking of the cellulose beads with glyoxal led to a 3-fold increase in compressive strength of the beads, broadening the potential range of applications where these biodegradable particles could replace current environmentally persistent materials.

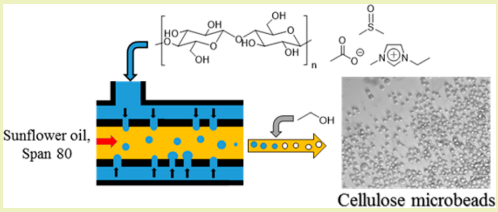

KEYWORDS: *Cellulose, Microbeads, Ionic liquid, Organic electrolyte solution (OES), Membrane emulsification, Cross-linking, Continuous manufacturing*

INTRODUCTION

Plastic microbeads are produced at scale for use in a wide range of consumer products from personal care products to abrasives and paints.[1,2] Such microparticles are typically composed of environmentally persistent polymers, including polyethylene, polystyrene, or polypropylene, and are applied in products such as facial scrubs, hand-cleansers, soaps, shaving foams, and toothpastes,[3] products that are, by their very nature, single use and designed to "wash away" into the wastewater disposal system. The small size of the microparticles used (in the range of sub-100 μm to ca. 500 μm for these personal care product applications) allows them to elude removal in wastewater treatment plants.[4,5] The synthetic polymers employed do not biodegrade, and there is strong evidence of their persistence in aquatic environments and of ingestion by marine organisms leading to potential dietary exposure for shellfish consumers.[6−9] It was estimated that in the USA as many as 8 trillion microbeads are transferred into aquatic habitats daily.[10] This evidence, combined with increased public awareness of the issue,[11,12] has led to the passing of legislation banning microbeads, notably in the USA[13] with the UK expected to follow suit by October 2017.[14,15] While many producers of personal care products have responded by phasing out plastic microparticles in their products, replacements do not always offer the same performance characteristics as plastic microbeads; thus, there is a need for more environmentally sustainable alternatives that can be manufactured at scale and provide the performance expected in use, yet break down into innocuous products at end-of-life. In addition to the personal care product applications highlighted, plastic microbeads are used in significant quantities as abrasives, paint additives, and polymeric fillers—all of which have the potential to result in significant release to the environment.

Cellulose is the most abundant biopolymer on the planet (an estimated 1.5×10^{12} tons is produced in the biosphere annually[16]), and there is a plethora of research documenting its use in a wide range of applications.[17,18] Cellulose in bead form has been prepared for use in applications from chromatography to drug delivery.[19,20] The microbeads to be banned appear in personal care products, and efforts have been made to replace these, for example, with cellulose agglomerates,[21] or flocculated microcrystalline cellulose.[22] In addition to being prepared from a renewable resource, cellulose particles/beads have the added

Received: March 2, 2017
Revised: May 26, 2017
Published: May 31, 2017

DOI: 10.1021/acssuschemeng.7b00662
ACS Sustainable Chem. Eng. 2017, 5, 5931−5939

benefit of being degraded by current wastewater treatment plants, so avoiding accumulation in aquatic ecosystems.[23]

Cellulose beads may be formed from droplets by batch extrusion or emulsification procedures[20] and more precise, but difficult to scale, processes include microfluidics[24] or single channel extrusion (needle).[25] Many processes rely on the formation of soluble cellulose derivatives to yield a dispersible phase appropriate for emulsion formation; for example, cellulose acetate solutions may be dispersed as droplets and then regenerated by treatment with a base.[26] More recently, the application of ionic liquid (IL) solvents for cellulose dissolution[27,28] has enabled the formation of beads from nonderivatizing cellulose solutions.[29] All rely upon batch processes, which are energetically inefficient resulting in an increase in the cost of the final product. There remains a need for a scalable (preferably continuous), energy efficient, low waste process that allows fine control over cellulose bead shape and size.

Membrane emulsification is an ideal candidate for continuous cellulose microbead formation as it is an efficient, low energy, and scalable emulsion production process.[30] An emulsion is obtained by inducing permeation of one liquid (the disperse phase) through the pores of a membrane into another liquid (the continuous phase) flowing perpendicular to the membrane.[31] The mobile continuous phase creates a wall shear which cleaves the growing droplet from the membrane surface, forming an emulsion in a consistent and reproducible manner. This controlled droplet formation process is referred to as a "dripping regime".[32] An imbalance in forces governing emulsion formation can lead to the disperse phase "jetting" out of the membrane pores in string-like formations, which later destabilize forming emulsion droplets of varying size. This "jetting regime" is a result of too high a disperse phase flux or excessive continuous phase flow rate.[31] As such, to generate emulsion droplets with narrow size distribution, a dripping regime should be used.[33] Cross-flow membrane emulsification processes require less energy compared with rotary droplet formation techniques, due to smaller shear forces, and allow for greater control over the size of the droplets formed.[34]

While membrane emulsification has been utilized to form solid spherical particles, such as agarose beads,[31,35,36] this continuous, scalable, low-energy technique has yet to be applied to the production of cellulose beads, largely because simple dissolution/precipitation or solidification processes are not readily applied to intractable cellulose. Combining knowledge of membrane technology and cellulose processing, we demonstrate, for the first time, the continuous production of cellulose microbeads from a cross-flow membrane emulsification–phase inversion process by using a continuous phase as a carrier. The process is scalable, and the spherical cellulose microbeads are produced in a range of tunable particle sizes. Further, hardness can be modulated by cross-linking, suggesting applications in a range of products in place of nonbiodegradable microbeads.

EXPERIMENTAL SECTION

Materials. Microcrystalline cellulose (MC, Sigma-Aldrich, powder, 20 μm particle size) was azeotropically dried from *n*-butanol (Fisher Scientific, > 99% purity) on a rotary evaporator before use. Dimethyl sulfoxide (Alfa Aesar, > 99% purity) and toluene (Sigma-Aldrich, anhydrous, 99.8% purity) were dried and stored over molecular sieves (3 Å). 1-Ethyl-3-methylimidazolium acetate ([EMIm][OAc], > 95% purity, BASF, Basionics, 0.5% moisture content), sulfuric acid (VWR, 95% purity), and sunflower oil (Tesco) were used as received. Ethanol (absolute, ≥ 99.8% purity), trichloro(octadecyl)silane (≥90% purity), Span 80, sodium hydroxide (pellets), rose bengal (95% dye content), glyoxal (40 wt % in H_2O), and glycolic acid (99% purity) were all used as received from Sigma-Aldrich.

Preparation of Cellulose Solutions. Microcrystalline cellulose (MC) was dispersed in DMSO using an overhead stirrer (900 rpm) with a PTFE stirrer head for 5 min at room temperature. The required amount of 1-ethyl-3-methylimidazolium acetate (30:70 w/w, [EMIm]-[OAc]:DMSO in all cases) was added via a glass pipet to the dispersion and allowed to mix for 1 h at room temperature resulting in either 4 or 8 wt % cellulose (in a cellulose:solvent−cosolvent mixture) solution. Prior to membrane emulsification, a small amount of rose bengal (~10 mg) was added to the disperse phase to aid in visualization of droplets.

Membrane Silylation. Tubular Shirasu porous glass membranes (SPG, Shirasu Porous Glass Technology Co., Ltd., 10 μm pore size, length 12.5 cm, diameter 1.0(5) cm, thickness 7.00(3) mm) were calcined (air, 2 h, 500 °C) and hydrophobized by heating under reflux in a solution of 5 vol % trichloro(octadecyl)silane in toluene (48 g) for 3 h. Hydrophobization of the surfaces of the SPG membranes was required in order to minimize wettability by the polar cellulose disperse phase.[31] The hydrophobized membranes were rinsed in fresh toluene, dried using compressed air, and stored suspended in sunflower oil (membranes were degassed under vacuum prior to use).

Membrane Emulsification. Using pressure from an air cylinder, cellulose solutions (4 or 8 wt % MC dissolved in 30:70 w/w, [EMIm][OAc]:DMSO) dyed with rose bengal (for ease of visualization) were driven through an SPG membrane (10 μm pore), using a transmembrane pressure (P_{tm}) (eq 1) higher than the critical pressure (P_c) (eq 2), into a circulating continuous phase (2 wt % Span 80 in sunflower oil) flowing parallel to the internal membrane surface (Figure 1).

$$P_{tm} = P_d - \frac{(P_{c,in} + P_{c,out})}{2} \quad (1)$$

$$P_c = \frac{4\gamma \cos\theta}{d_p} \quad (2)$$

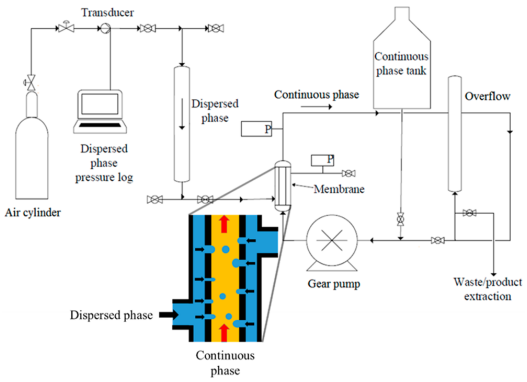

Figure 1. Process flow diagram for the cross-flow membrane emulsification apparatus used. The inset shows a schematic of the membrane module and the droplet formation process.

The P_{tm} (eq 1) is calculated from the pressure imparted on the disperse phase (P_d) and the pressure of the continuous phase at the membrane inlet/outlet ($P_{c,in}/P_{c,out}$). The P_c (eq 2) can be calculated from the interfacial tension (γ), contact angle between the growing emulsion droplet, membrane surface and continuous phase (θ), and the pore diameter (d_p).

DOI: 10.1021/acssuschemeng.7b00662
ACS Sustainable Chem. Eng. 2017, 5, 5931−5939

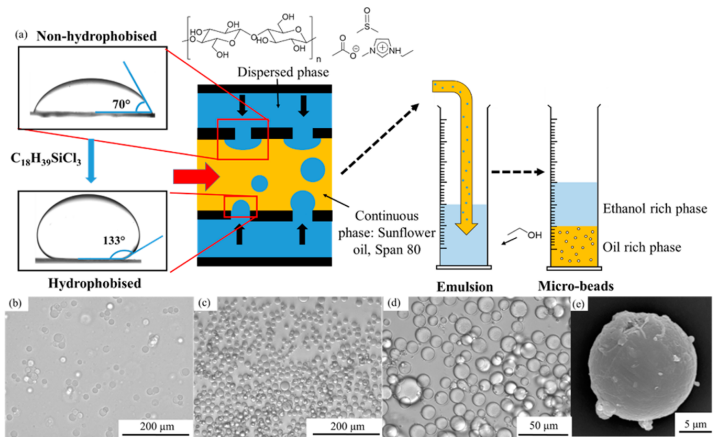

Figure 2. (a) Schematic of the continuous membrane emulsification−phase inversion process for the generation of cellulose microbeads along with the contact angles of the disperse phase before and after hydrophobization of the SPG membranes (all membranes were hydrophobized prior to use). (b) Optical micrograph of emulsion droplets of 8 wt % MC (dissolved in 30:70, w/w, [EMIm][OAc]:DMSO) dispersed in sunflower oil−2 wt % Span 80 mixture. (c, d) Cellulose microbeads formed by phase inversion with ethanol. (e) SEM image of a single cellulose bead. (Widefield micrograph images, showing the range of bead sizes for further samples, are provided in Figure S3.)

The formed emulsion stabilized in the continuous phase (~300 mL) was extracted directly into a measuring cylinder containing ethanol (300 mL), resulting in the formation of solid cellulose microbeads by antisolvent precipitation or phase inversion. The coagulated beads where extracted by suction filtration (0.2 μm, nylon-66 filter paper), washed (three 20 mL aliquots of ethanol), and redispersed in deionized water (30 mL) with brief sonication (37 Hz, 20 s pulse, 80% power, Fisherbrand ultrasonic cleaner). A detailed process flow diagram and procedure for using the described apparatus can be found in the Supporting Information (Figure S1, Section S1).

As in all continuous processes, material produced during start-up must be removed and discarded; thus, the laboratory scale rig developed (Figure 1) was designed to enable the removal of the "start-up" emulsion into a collection vessel, without cessation of operation. The first few minutes of production (starting from when a positive P_{tm} was applied above the P_c) were not indicative of the bulk emulsion formed across the whole process (Figure S2) with a clear narrowing in the polydispersity of beads measured as the experiment progressed toward steady state, after which consistent size distributions were measured. In all cases, this start-up emulsion was extracted and retained before producing the final emulsion.

Preparation of mm-Diameter Cellulose Beads. To test modulation of material properties upon cross-linking, larger beads were required to mimic the microbeads. Cellulose solutions as prepared for emulsification were continuously extruded (syringe pump) at a flow rate of 50 μL/min as droplets via a stainless steel needle (21 gauge, length = 12 cm) into ethanol (500 mL). The viscosity of the dropping solution had to be high enough to withstand impact on the surface of the antisolvent. Optimal conditions were found to be a distance of 7 cm between the needle tip and meniscus of ethanol using an 8 wt % cellulose dropping solution. Decreasing the concentration of cellulose to a 4 wt % solution resulted in disc-shaped particles due to the reduction in viscosity. The average diameter of the formed beads was determined using a J500 extreme USB microscope (1 mm graticule, ImageJ software—3 measurements per bead, 10 beads per image, 3 images). Residual [EMIm][OAc]:DMSO was removed by Soxhlet extraction with ethanol overnight.

Cross-Linking of Cellulose Beads. Cellulose beads were suspended in aqueous solutions of 6 or 12 wt % glyoxal (molar ratio of 70:1 and 136:1 glyoxal:anhydroglucose units, respectively) and stirred for 3 h (25 °C). The beads were briefly blotted with filter paper to remove excess cross-linking solution and cross-linking effected at 160 °C (Buchi glass oven, B-580) for 1 h. The extent of cross-linking was determined by HPLC analysis following a method adapted from Schramm et al.[37] Cross-linked cellulose bead samples (<0.2 g) were exposed to 4 M NaOH (90 °C, 30 min) to expel the cross-linker agent as glycolic acid from the cellulose matrix. The extraction solution and washes (10 mL deionized water) were combined and filtered through a PTFE syringe filter (0.2 μm). Concentration of glycolic acid in each solution was determined by HPLC analysis: Aminex organic acid analysis column (HPX-87H, 300 mm × 7.8 mm, 50 °C), mobile phase 0.01 M H_2SO_4 (0.6 L/min), and UV detector λ = 210 nm. Concentration was determined by comparison to the average of triplicate analyses to an appropriate calibration curve.

Mechanical characterization of the cross-linked samples was conducted using an Instron 3369 at a compressive extension of 0.1 mm/min using a 100 N load cell for noncross-linked samples and a 1 kN load cellulose for all cross-linked samples.

Characterization. Viscosity values for the continuous phase (sunflower oil, 2 wt % Span 80) and disperse phases (4 or 8 wt % MC in 30:70, w/w, [EMIm][OAc]:DMSO) were determined using a Brookfield DV-III-HA ULTRA programmable rheometer attached to a Brookfield TC-650 temperature controller (30 °C). Each sample was exposed to an ascending and descending shear rate sweep of 30 readings between 0.08−200 s^{-1} (60 in total) and average viscosity in the Newtonian range taken.

Density values of the cellulose solutions were measured using a standard pycnometry procedure: 10 mL pycnometer, triplicate measurements, temperature fluctuations less than 2% in all cases.

Contact angle measurements were taken using an OCA 15EC video-based measuring system. A droplet (5 μL) of disperse phase was placed on a hydrophobized glass microscope slide (hydrophobized as per the SPG membranes) suspended in the continuous phase (sunflower oil, 2 wt % Span 80). An average of 10 readings at different locations and on each side of the glass were taken per sample (errors $\leq \pm 2°$ in all cases). Interfacial tension measurements were conducted on the same instrument using a pendant drop method with the camera rotated by 90°. A droplet (1.6 or 1.8 μL for 4 or 8 wt % MC, respectively) of disperse phase was suspended from a needle (18 gauge, length = 1.5 in.) into a transparent cuvette containing the continuous phase. An average of 10 droplets were used per sample with an error between repeats of less than 3%.

Optical micrographs were taken using an EVOS AMG (AMF 4300) optical microscope.

Scanning electron micrographs were obtained on a JEOL SEM648OLV scanning electron microscope. Prior to imaging, samples

DOI: 10.1021/acssuschemeng.7b00662
ACS Sustainable Chem. Eng. 2017, 5, 5931−5939

Table 1. Disperse Phase Composition, Process Parameters, Calculated Values for *We* and *Ca*, and Parameters Describing Microbead Size and Distribution for the Range of Samples Represented in Figure 3

sample	cellulose wt %	Q_{cp} (L/min)	P_{tm} (bar)	v_0 (m/s)	Q_{dp} (L/min)	*We*	*Ca*	$D_{peak\ max}$[a] (μm)	*fwhm*[b] (μm)
1	8	1.4	0.02[c]	5.19×10^{-5}	6.1×10^{-3}	2.0×10^{-8}	7.4	65	86(3)
2	4	1.4	0.03[d]	8.22×10^{-4}	9.6×10^{-2}	4.5×10^{-6}	6.8	42	144(10)
3	8	1.4	0.25	9.22×10^{-4}	1.1×10^{-1}	6.1×10^{-6}	7.4	135	318(19)
4	8	1.9	0.03	8.98×10^{-5}	1.1×10^{-2}	5.8×10^{-8}	10.0	19	21(1)
5	4	2.4	0.05	1.53×10^{-3}	1.8×10^{-1}	1.5×10^{-5}	11.7	135	281(16)
6	8	2.4	0.06	2.03×10^{-4}	2.4×10^{-2}	3.0×10^{-7}	12.6	25	51(1)
7	8	2.4	0.01	1.41×10^{-5}	1.6×10^{-3}	1.4×10^{-9}	12.6	17	14(1)

[a]Mode, diameter at peak maximum for the dominant peak. [b]*fwhm*, full width at half-maximum. [c]P_c = 0.004 bar; applicable to all 8 wt % cellulose samples. [d]P_c = 0.005 bar, applicable to all 4 wt % cellulose samples.

were dried from *n*-butanol (80 °C, vacuum) and flash frozen in liquid nitrogen. The frozen samples were ruptured in a pestle and mortar to generate cleaved samples for cross-section images. Samples were gold coated (Edwards sputter coater, S150B, 4 min) prior to imaging.

Volume-weighted particle size distributions were obtained for cellulose microbead samples using a Malvern Mastersizer X (300 mm lens, 1.2−600 μm detection range, dispersion unit controller, 1800 rpm, Mastersizer X software v 2.19). Triplicate measurements were conducted on discrete samples, where each measurement was derived from five repeats of 2000 sweeps. Multimodal particle size distributions were deconvoluted by fitting of Gaussian distributions to the separate populations and volume %, diameters, and distributions of the dominant microbead population compared using the values of the mode or $D_{peak\ max}$ (the diameter at peak maximum for the dominant peak, comparable to D(v, 0.5) for the fitted distribution) and full width at half-maximum (fwhm) of the data as collected.

RESULTS AND DISCUSSION

Cellulose microbeads were produced from solutions of microcrystalline cellulose (MC) dissolved in an organic electrolyte solution (OES) dispersed as droplets via a continuous cross-flow membrane emulsification process followed by phase inversion in ethanol (Figure 2). An OES comprised of 30:70 w/w [EMIm][OAc]:DMSO was selected as a cellulose solvent because (a) this mixture is known to be particularly efficient for dissolution of cellulose,[28,38] (b) use of a mixture of DMSO with IL instead of pure IL is less costly, and (c) the solvent mixture provides solutions of 4 and 8 wt % cellulose with viscosities appropriate for extrusion through the porous membrane in the emulsification process (0.13 and 1.18 Pa.s, respectively).[39,40]

As shown schematically in Figure 2a, the disperse phase of cellulose dissolved in an OES is extruded through the pores of a tubular porous membrane (held in a cylindrical stainless steel housing) into the lumen through which a continuous carrier phase of sunflower oil containing 2 wt % Span 80 flows. Droplets form at the pore outlets, as the disperse phase does not wet the hydrophobized glass membrane surface (Figure 2a), and are swept from the surface once these reach a size determined by the balance of forces discussed below. Recirculation of the formed emulsion (Figure 2b) through the interior of the tubular membrane enabled an increase in concentration prior to phase inversion, which was conducted following the process described by Rogers and co-workers in 2002, leading to the formation of solid cellulose microbeads (Figures 2c, d, and e).[27] Ethanol was used in preference to water as it is partially miscible (*ca.* 12−13 vol %) in the sunflower oil continuous phase allowing the simple "setting" of the beads. Cellulose beads can then be leached of residual IL and DMSO by repeated immersion in ethanol (from which both OES components and pure ethanol can be recovered for reuse).

In addition to providing a continuous scalable manufacturing process, the use of membrane emulsification allows exquisite control over droplet (and thus bead) size, potentially producing materials with narrow bead diameter distribution. (As droplet size is primarily a function of membrane pore size, selection of membranes with larger, or smaller, pores provides a means for gross changes in bead size, but here, we focus on the finer control required to control size and size range in a single membrane.) Various process parameters including the pressure applied to the disperse phase and continuous phase flow rate can be varied to allow tuning of the process conditions and, consequently, the size of the beads produced. In addition, variation of the disperse phase composition and thus viscosity also provides a means of controlling droplet production.

To achieve such control, it is critical to ensure that droplets are produced in a "dripping" mode, where individual droplets are sheared from the membrane surface, rather than a "jetting" mode, where droplet size is controlled by jet breakup due to Rayleigh−Taylor instability.[41] (The terms "dripping" and "jetting" are used following Pathak,[32] but the term "continuous outflow regime" may be preferred by some to describe the regime in which disperse phase is extruded as a semicontinuous stream.)

Pathak[32] highlighted a clear transition between dripping and jetting droplet production regimes expressed in terms of dimensionless capillary (*Ca*) and Weber (*We*) numbers, represented in eqs 3 and 4:

$$Ca = \frac{\mu_{cp} v_{cp}}{\gamma} \tag{3}$$

$$We = \frac{\rho_{dp} v_0^2 D_0}{\gamma} \tag{4}$$

where μ_{cp} is the viscosity of the continuous phase, v_{cp} is the velocity of continuous phase at the inlet to membrane, γ is the interfacial tension between disperse and continuous phases, ρ_{dp} is the density of the disperse phase, v_0 is the velocity of disperse phase at a pore entrance, and D_0 is the average pore diameter of the membrane. *Ca* and *We* represent the ratio of viscous and inertial to interfacial tension forces in the emulsion formation process. The effect of disperse phase composition (MC wt %), transmembrane pressure (P_{tm}, selected based on the critical pressure, P_c), disperse phase velocity at one pore, v_0, and total flow rate, Q_{dp}, along with the continuous phase flow rate, Q_{cp}, on *Ca* and *We* for the range of conditions and samples studied herein are presented in Table 1.

DOI: 10.1021/acssuschemeng.7b00662
ACS Sustainable Chem. Eng. 2017, 5, 5931−5939

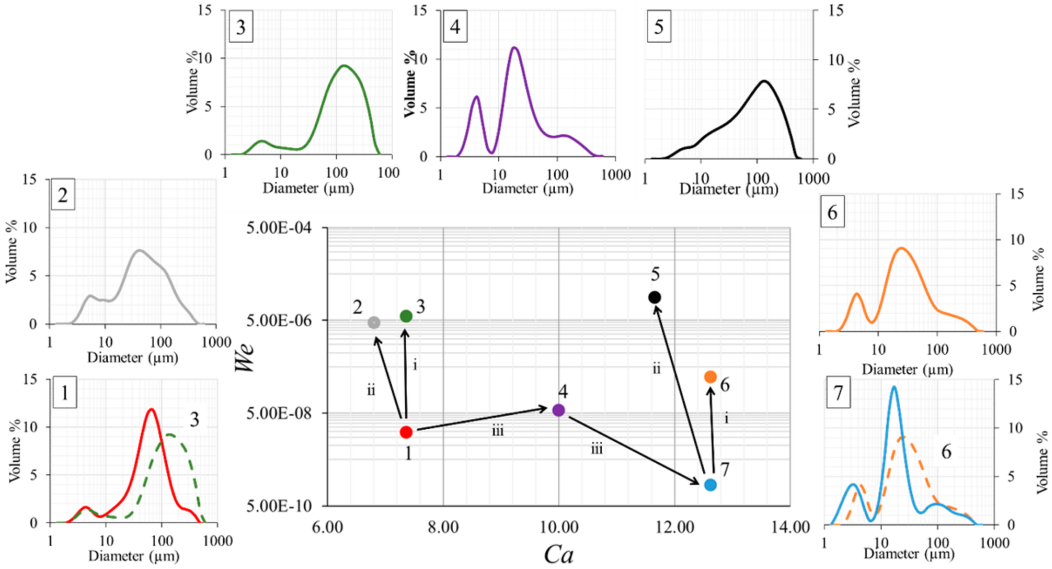

Figure 3. Particle size distributions for a range of cellulose microbead dispersions as a function of the *Ca* and *We* values used to produce their corresponding emulsions (Table 1). For samples 1 and 7, the higher P_{tm} jetting counterparts (samples 3 and 6, respectively) are also shown by dashed lines. The central chart depicts the changing values of *Ca* and *We* for all sets of conditions, and arrows represent (i) increase in transmembrane pressure (P_{tm}) and therefore the disperse phase velocity (v_0), (ii) reduction of the concentration of cellulose in the disperse phase (from 8 to 4 wt %), and (iii) increase in the continuous phase flow rate (Q_{cp}) and therefore the continuous phase velocity (v_{cp}) from 1.4 to 1.9 to 2.4 L/min for samples 1, 4, and 7 respectively.

The concentration of cellulose (8 and 4 wt %), flow rate of the continuous phase (Q_{cp}), and transmembrane pressure (P_{tm}) were systematically varied (Table 1) to produce a range of emulsions which were converted to microbead dispersions for particle size measurements (Figure 3).

All samples produced exhibited multimodal particle size profiles, and in particular, the appearance of a population of beads with diameters significantly below that of the membrane pore nominal size of 10 μm (Figure 3) was noted. In these experiments, the emulsions produced were recirculated using a gear pump. To test the hypothesis that this could lead to breakup of droplets in the pump due to shear forces,[31] a time-resolved experiment was conducted with all process parameters held constant and samples extracted at 15 min intervals. The volume percent of the population of microbeads with diameter <10 μm remained constant (Figure S4a), as did the Sauter mean diameter for each sample (Figure S4b), suggesting that breakup was not the main source of these small beads but that these arose from a constant factor in the experiment. A very small number of larger beads (invisible in number based distributions) also appeared, and close examination of the inner surfaces of SPG membranes revealed occasional "pits" on the membrane surfaces (Figure S5). We return to the likely consequence of these larger "pores" below. The population of small particles was discounted to allow comparison of the effect of process parameters on the main population (by volume).

Since the membrane pore size and composition of the continuous oil phase were kept constant and changes in interfacial tension (γ) showed little variation between 4 or 8 wt % cellulose in the OES (Table S1), *Ca* was solely influenced by the value of the velocity of the continuous phase (v_{cp}). Similarly, *We* was mainly influenced by the velocity of the disperse phase at the pore entrance (v_0) as there was little variation in the density of the disperse phase (ρ_{dp}) within the range of composition studied (Table S1).

Applying a $P_{tm} \leq 7.5 \times P_c$ to an 8 wt % cellulose disperse phase formed dispersions of cellulose microbeads with a narrower size distribution (for the main population of beads). This was achieved for continuous phase flow rates of 1.4, 1.9, and 2.4 L/min (Figure 3, samples 1, 4, and 7), representing the three lowest values of disperse phase velocity (v_0) and therefore *We* values (Table 1). On increasing v_0 (indicated by arrow i, Figure 3), a transition occurred from a dripping regime to a jetting regime in emulsion droplet production, reflected in the broadened particle size distribution (Figure 3, dashed lines in samples 1 and 7 graphs). A similar increase in polydispersity was also observed upon reduction of the concentration of cellulose in the disperse phase (Figure 3, arrow (ii). This arises from the inverse relationship between the total flow rate of the disperse phase (Q_{dp}) and the viscosity of the disperse phase (μ_{dp}) defined in eq 5 (derived in Section S2).

$$Q_{dp} = \frac{A\varepsilon r^2 \Delta P}{8\mu_{dp} L} \tag{5}$$

where A is the membrane surface area, ε is the membrane porosity (57% for the SPG membranes used here[42]), r is the radius of the pore, ΔP is the pressure drop, and L is the thickness of the membrane wall. The less viscous 4 wt % solution was therefore extruded from the membrane pores at a much higher rate than its 8 wt % counterpart due to its lower viscosity: 0.13 versus 1.18 Pa.s (Table S1).

The mobility of the continuous phase is responsible for cleavage of the growing emulsion droplets from the surface of

DOI: 10.1021/acssuschemeng.7b00662
ACS Sustainable Chem. Eng. 2017, 5, 5931−5939

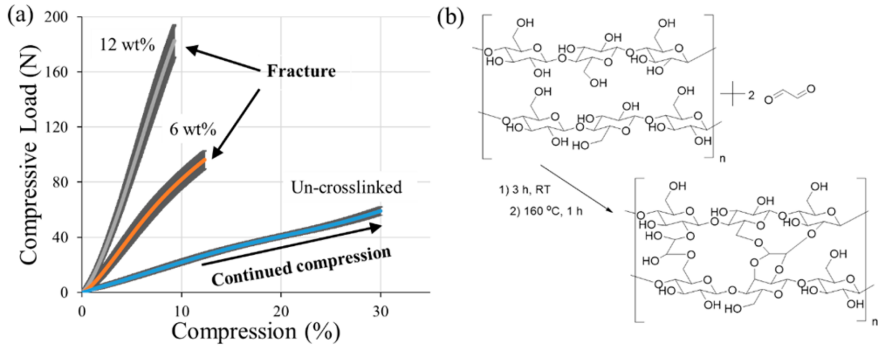

Figure 4. (a) Effect of applied compressive force on the compression % of a cellulose bead cross-linked using two concentrations of glyoxal cross-linking solution. (b) Cellulose cross-linking via acetal and hemiacetal linkages.[47]

the membrane via the generation of a wall shear force (τ), which can be calculated from the friction factor and Reynolds number (Re).[43] Here, continuous phase flow rates of 1.4, 1.9, and 2.4 L/min imparted a wall shear on a growing emulsion droplet of 9, 13, and 16 Pa, respectively. This increase in shear force reduced the droplet growth period before cleavage from the membrane surface, giving smaller droplets (arrow iii, Figure 3). This was reflected in the particle size data (Figure 3) for samples 1, 4, and 7 where an increased flow rate led to a significant reduction in the average bead diameter, $D_{peak\ max}$, from 65 to 19 and 17 μm, respectively (with concomitant narrowing of distribution from 86 to 21 and 14 μm), in agreement with previously published data on membrane emulsification.[44,45]

In the range investigated, Ca did not have a significant impact in promoting jetting behavior in the emulsion formation process. Comparison of samples 1 and 4 (Figure 3) reveals an increase in the volume % of small particles (< ~5 μm) in sample 4, although the peak reflecting the largest population of particles remained narrow. We hypothesize that sample 4 represented a situation in which a small proportion of larger membrane pores was producing droplets in a jetting manner bought about by a higher P_{tm} compared with samples 1 and 7 (Table 1), while the majority of pores produced droplets in a dripping regime (while pore size ranges in SPG membranes are narrow, these are not without some larger outlet pores arising from the tortuous paths resulting from the spinodal decomposition mechanism used to produce the membranes, Figure S5).[46]

Thus, careful consideration of the effect of controllable factors on We and Ca allow one to discern appropriate conditions for the generation of microbeads with defined size and narrow polydispersity. Here, parameters must be selected to yield a low We (i.e., interfacial tension forces dominating), which can be achieved by the combined effect of a higher viscosity disperse phase and a lower applied transmembrane pressure (P_{tm}) resulting in a low v_0.

In this system, use of a disperse phase with higher viscosity provided a clear benefit for production of microbeads with narrow polydispersity, though it also resulted in a reduction of Q_{dp} which, in turn, reduced the quantity of product generated per unit time and membrane area. From the calculated Q_{dp} (Table 1), the productivity of cellulose microbead generation in the systems used to prepare samples 1 and 7 was determined to be 11 and 3 $kg.h^{-1}.m^{-2}$, assuming no membrane fouling or product loss. Clearly, an increase in productivity could be achieved with a higher P_{tm}, such as that used to generate sample 3, with a productivity of 197 $kg.h^{-1}.m^{-2}$, but at the cost of a greater droplet (and hence bead) polydispersity, resulting from disperse phase jetting and, possibly, subsequent breakup into droplets of variable diameter. Alternatively, productivity can be easily enhanced by numbering up of membranes or increasing the membrane area by use of longer tubular membranes.

With the ability to continuously produce cellulose microbeads of well-defined diameter with reduced polydispersity in hand, we turned our attention to the tribological properties that might be required to make such beads applicable to a range of products. For example, production of hard cellulose microbeads of high mechanical strength may be required for abrasive applications. To modulate bead hardness, cross-linking was employed.

A dropping-phase inversion process was used to generate larger cellulose beads, with diameters in the millimeter range, from 8 wt % cellulose solutions (MC:[EMIm][OAc]:DMSO), for testing of their mechanical properties. The commercially available, REACH-registered dialdehyde, glyoxal, was used to form acetal/hemiacetal linkages between the cellulose chains within the bead (Figure 4b).[47] Following phase inversion and OES leaching (with a final ethanol Soxhlet step), beads were soaked in either an aqueous 6 or 12 wt % glyoxal cross-linking solution, and reaction was initiated by heating. Analysis of the resultant materials indicated a cross-linker:anhydroglucose unit (AGU) molar ratio in the cross-linked samples of 1.4 or 2.1, respectively (determined by HPLC, Table S2). In the latter case, a molar ratio of cross-linked:AGU of greater than 1.5 suggested some dimerization of the cross-linker since each AGU has three hydroxyl groups available to react with glyoxal. Cross-linking of the cellulose matrix had three effects (Table 2): (a) reduction of shrinkage of the cellulose beads upon heating and drying, (b) an increase in mechanical strength of

Table 2. Effects of Cross-Linking on Bead Size, Hardness, and Brittleness

cross-linking degree (glyoxal:AGU)	shrinkage on drying (change in diameter)	force required for compression up to 30% (N)	compression at fracture
0	56%	59	no fracture
1.4	49%	98	12%
2.1	43%	186	9%

DOI: 10.1021/acssuschemeng.7b00662
ACS Sustainable Chem. Eng. 2017, 5, 5931−5939

the beads (Figure 4a), and (c) an increase in brittleness reflected in a decrease in compressibility prior to fracture.

Cross-linking also influenced the internal and external structure of the cellulose beads. Drying of noncross-linked beads led to shrinkage and development of a rough surface topography and a dense inner structure (Figure 5a and Figure S6a). This roughening of the surface, suggested to arise from the shrinkage of beads with a dense "skin" layer developed during phase inversion, was reduced in bead samples reacted with 6 wt % glyoxal (Figure 5b and Figure S6b). In this case, after cross-linking, the surface appeared generally smooth with some locations showing signs of pitting, presumably arising during heating and drying (Figure 5c). At the same time, the internal structure appeared less dense than that of its noncross-linked counterparts (Figure S6c) as expected from the lower shrinkage. Increasing the concentration of glyoxal in the cross-linking solution to 12 wt % created a consistently dimpled surface topography (Figure 5d), and the presence of some craters was also noted (Figure S6d). The internal structure appeared very similar to samples with lower degrees of cross-linking, showing some granularity or porosity.

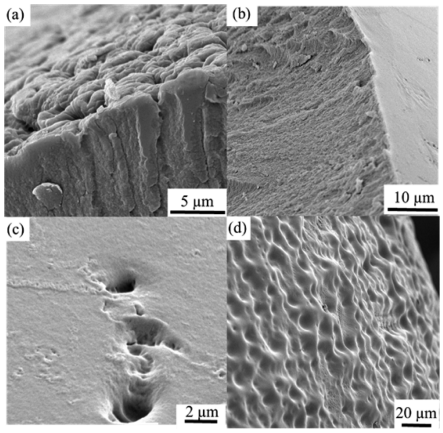

Figure 5. SEM micrographs of cellulose beads: (a) no cross-linking, (b) reacted with a 6 wt % glyoxal solution, (c) cratered surface of a bead cross-linked with 6 wt % glyoxal, and (d) surface of a bead cross-linked with 12 wt % glyoxal. More SEM images can be found in Figure S6.

Biodegradability of cellulose is well documented, but standard tests, in accordance with recognized guidelines (e.g., OECD Guidelines for the Testing of Chemicals), would be required to provide assurance that glyoxal cross-linked materials are not persistent. Preliminary results obtained in our laboratories, as part of a larger study on the effect of cellulose modification on degradability, suggest that glyoxal cross-linking, at the levels used here, slightly reduces initial rates of enzyme mediated saccharification but does not significantly compromise degradability.

CONCLUSIONS

Cross-flow membrane emulsification technology, although widely used for other applications, is here applied, for the first time, to the formation of consistently sized cellulose microbeads, which could be suitable replacements for persistent plastic microbeads in, for example, personal care products. This process for preparation of cellulose microbeads by a continuous, scalable membrane emulsification process coupled with phase inversion allows for close control of the sizes of the spherical beads produced, making it a viable method for the production of alternatives to environmentally persistent plastic microbeads, which are, or will be, banned for use in numerous applications in many countries. Examination of the effect of controllable process parameters on capillary and Weber numbers, *Ca* and *We*, allows mapping of the "process space" that would lead to production of microbeads of defined particle size with narrow polydispersity by defining where dripping to jetting regime changes would occur: Within the range investigated, a low *We* is required to prevent jetting of disperse phase from the pores; increasing *Ca*, by increasing the flow rate of the continuous phase, leads to a decrease in the size of the microbeads produced. Wet bead diameters in the range from 17 to 65 μm are reliably accessible using the 10 μm pore size SPG membranes applied here, but variation of membrane pore size could be applied to broaden this range if larger or smaller particles were required.

Finally, cellulose beads may be cross-linked by changing the final washing and drying steps to soaking in aqueous glyoxal solutions, heating, and drying, which are operations that can easily be incorporated into the process. Bead hardness scales with the degree of cross-linking, providing access to a range of materials that could replace plastic microbeads in a range of applications from personal care products to abrasives.

ASSOCIATED CONTENT

Supporting Information

The Supporting Information is available free of charge on the ACS Publications website at DOI: 10.1021/acssuschemeng.7b00662.

Full details of the membrane emulsification rig design and operation, further experimental details, derivation of some equations, and additional particle and materials characterization data. (PDF)

AUTHOR INFORMATION

Corresponding Authors

*E-mail: D.Mattia@bath.ac.uk (D. Mattia).
*E-mail: J.L.Scott@bath.ac.uk (J. L. Scott).

ORCID

Laura Torrente-Murciano: 0000-0002-7938-2587
Davide Mattia: 0000-0002-7679-4105
Janet L. Scott: 0000-0001-8021-2860

Present Address

Laura Torrente-Murciano: Department of Chemical Engineering and Biotechnology, University of Cambridge, Cambridge, CB3 0AS, United Kingdom.

Notes

The authors declare no competing financial interest.
All data supporting this paper are openly available from the University of Bath data archive at https://doi.org/10.15125/BATH-00379.

ACKNOWLEDGMENTS

We thank the UK Engineering and Physical Sciences Research Council (EPSRC) for a Ph.D. studentship funding for J.C.O via

the EPSRC Doctoral Training Centre in Sustainable Chemical Technologies, University of Bath, (EP/G03768X/1).

ABBREVIATIONS

AGU = anhydroglucose unit; [EMIm][OAc] = 1-ethyl-3-methylimidazolium acetate; IL = ionic liquid; MC = microcrystalline cellulose; OES = organic electrolyte solution; SFO = sunflower oil

REFERENCES

(1) Song, Y. K.; Hong, S. H.; Jang, M.; Kang, J. H.; Kwon, O. Y.; Han, G. M.; Shim, W. J. Large Accumulation of Micro-Sized Synthetic Polymer Particles in the Sea Surface Microlayer. *Environ. Sci. Technol.* **2014**, *48* (16), 9014−9021.
(2) Leslie, H. A.*Plastic in Cosmetics*; United Nationals Environmental Programme, 2015; pp 1−38.
(3) Napper, I. E.; Bakir, A.; Rowland, S. J.; Thompson, R. C. Characterisation, Quantity and Sorptive Properties of Microplastics Extracted from Cosmetics. *Mar. Pollut. Bull.* **2015**, *99* (1−2), 178−185.
(4) Murphy, F.; Ewins, C.; Carbonnier, F.; Quinn, B. Wastewater Treatment Works (WwTW) as a Source of Microplastics in the Aquatic Environment. *Environ. Sci. Technol.* **2016**, *50* (11), 5800−5808.
(5) Fendall, L. S.; Sewell, M. A. Contributing to Marine Pollution by Washing Your Face: Microplastics in Facial Cleansers. *Mar. Pollut. Bull.* **2009**, *58* (8), 1225−1228.
(6) Van Cauwenberghe, L.; Janssen, C. R. Microplastics in Bivalves Cultured for Human Consumption. *Environ. Pollut.* **2014**, *193*, 65−70.
(7) Mazurais, D.; Ernande, B.; Quazuguel, P.; Severe, A.; Huelvan, C.; Madec, L.; Mouchel, O.; Soudant, P.; Robbens, J.; Huvet, A.; Zambonino-Infante, J. Evaluation of the Impact of Polyethylene Microbeads Ingestion in European Sea Bass (Dicentrarchus Labrax) Larvae. *Mar. Environ. Res.* **2015**, *112*, 78−85.
(8) Van Cauwenberghe, L.; Claessens, M.; Vandegehuchte, M. B.; Janssen, C. R. Microplastics Are Taken up by Mussels (Mytilus Edulis) and Lugworms (Arenicola Marina) Living in Natural Habitats. *Environ. Pollut.* **2015**, *199*, 10−17.
(9) Gregory, M. R. Plastic Scrubbers' in Hand Cleansers: A Further (and Minor) Source for Marine Pollution Identified. *Mar. Pollut. Bull.* **1996**, *32* (12), 867−871.
(10) Rochman, C. M.; Kross, S. M.; Armstrong, J. B.; Bogan, M. T.; Darling, E. S.; Green, S. J.; Smyth, A. R.; Veríssimo, D. Scientific Evidence Supports a Ban on Microbeads. *Environ. Sci. Technol.* **2015**, *49* (18), 10759−10761.
(11) BBC. Plastic microbeads to be banned by 2017, UK government pledges. http://www.bbc.co.uk/news/uk-37263087 (accessed November 28, 2016).
(12) The Guardian. UK government to ban microbeads from cosmetics by end of 2017. https://www.theguardian.com/environment/2016/sep/02/uk-government-to-ban-microbeads-from-cosmetics-by-end-of-2017 (accessed December 5, 2016).
(13) U.S. Congress. *Microbead-Free Waters Act of 2015*; 2015; Public Law, pp 3129−3130.
(14) Hirst, D.; Bennet, O. Microbeads and Microplastics in Cosmetic and Personal Care Products. *House Commons Libr.* **2017**, No. No. 7510, 1−16.
(15) Leadsom, A. Department of Environmetal, Food & Rural Affairs. Government sets out next steps to ban microbeads. https://www.gov.uk/government/news/government-sets-out-next-steps-to-ban-microbeads (accessed February 17, 2017).
(16) Klemm, D.; Heublein, B.; Fink, H.-P.; Bohn, A. Cellulose: Fascinating Biopolymer and Sustainable Raw Material. *Angew. Chem., Int. Ed.* **2005**, *44* (22), 3358−3393.
(17) Crawford, R. J.; Edler, K. J.; Lindhoud, S.; Scott, J. L.; Unali, G. Formation of Shear Thinning Gels from Partially Oxidised Cellulose Nanofibrils. *Green Chem.* **2012**, *14* (2), 300−303.
(18) Chang, C.; Zhang, L. Cellulose-Based Hydrogels: Present Status and Application Prospects. *Carbohydr. Polym.* **2011**, *84* (1), 40−53.
(19) Zhang, Q.-L.; Shi, F.; Wang, P.; Lin, D.-Q.; Yao, S.-J. Preparation of Cellulose Adsorbents with Ionic Liquid and Pore Expansion for Chromatographic Applications. *J. Appl. Polym. Sci.* **2014**, *131* (7), 1−8.
(20) Gericke, M.; Trygg, J.; Fardim, P. Functional Cellulose Beads: Preparation, Characterization, and Applications. *Chem. Rev.* **2013**, *113*, 4812−4836.
(21) Schweikert, K.; Egorova, M.; Juch, R.-D.; Lefevre, F.; Westenfelder, H. Exfoliating Cellulose Beads and Cosmetic Uses Thereof. European Patent EP2907498, 2015.
(22) Gerard, L. M. Beads and Methods of Preparation. U.S. Patent US20040131690, 2003.
(23) Pérez, J.; Muñoz-Dorado, J.; De La Rubia, T.; Martínez, J. Biodegradation and Biological Treatments of Cellulose, Hemicellulose and Lignin: An Overview. *Int. Microbiol.* **2002**, *5* (2), 53−63.
(24) Carrick, C.; Larsson, P. a.; Brismar, H.; Aidun, C.; Wågberg, L. Native and Functionalized Micrometre-Sized Cellulose Capsules Prepared by Microfluidic Flow Focusing. *RSC Adv.* **2014**, *4* (37), 19061−19067.
(25) Voon, L. K.; Pang, S. C.; Chin, S. F. Highly Porous Cellulose Beads of Controllable Sizes Derived from Regenerated Cellulose of Printed Paper Wastes. *Mater. Lett.* **2016**, *164*, 264−266.
(26) Fischer, S.; Thümmler, K.; Volkert, B.; Hettrich, K.; Schmidt, I.; Fischer, K. Properties and Applications of Cellulose Acetate. *Macromol. Symp.* **2008**, *262* (1), 89−96.
(27) Swatloski, R. P.; Spear, S. K.; Holbrey, J. D.; Rogers, R. D. Dissolution of Cellulose with Ionic Liquids. *J. Am. Chem. Soc.* **2002**, *124* (18), 4974−4975.
(28) Rinaldi, R. Instantaneous Dissolution of Cellulose in Organic Electrolyte Solutions. *Chem. Commun.* **2011**, *47* (1), 511−513.
(29) Zhang, Q. L.; Shi, F.; Wang, P.; Lin, D. Q.; Yao, S. J. Preparation of Cellulose Adsorbents with Ionic Liquid and Pore Expansion for Chromatographic Applications. *J. Appl. Polym. Sci.* **2014**, *131* (7), 1−8.
(30) Williams, R. A.; Peng, S. J.; Wheeler, D. A.; Morley, N. C.; Taylor, D.; Whalley, M.; Houldsworth, D. W. Controlled Production of Emulsions Using a Crossflow Membrane. Part II: Industrial Scale Manufacture. *Inst. Chem. Eng.* **1998**, *76* (8), 902−910.
(31) Vladisavljevic, G. T. Structured Microparticles with Tailored Properties Produced by Membrane Emulsification. *Adv. Colloid Interface Sci.* **2015**, *225*, 53−87.
(32) Pathak, M. Numerical Simulation of Membrane Emulsification: Effect of Flow Properties in the Transition from Dripping to Jetting. *J. Membr. Sci.* **2011**, *382*, 166−176.
(33) Spyropoulos, F.; Lloyd, D. M.; Hancocks, R. D.; Pawlik, A. K. Advances in Membrane Emulsification. Part B: Recent Developments in Modelling and Scale-up Approaches. *J. Sci. Food Agric.* **2014**, *94* (4), 628−638.
(34) Spyropoulos, F.; Lloyd, D. M.; Hancocks, R. D.; Pawlik, A. K. Advances in Membrane Emulsification. Part A: Recent Developments in Processing Aspects and Microstructural Design Approaches. *J. Sci. Food Agric.* **2014**, *94* (4), 613−627.
(35) Li, X. Q.; Li, Q.; Gong, F. L.; Lei, J. D.; Zhao, X.; Ma, G. H.; Su, Z. G. Preparation of Large-Sized Highly Uniform Agarose Beads by Novel Rotating Membrane Emulsification. *J. Membr. Sci.* **2015**, *476*, 30−39.
(36) Vladisavljevic, G. T.; Williams, R. A. Recent Developments in Manufacturing Emulsions and Particulate Products Using Membranes. *Adv. Colloid Interface Sci.* **2005**, *113* (1), 1−20.
(37) Schramm, C.; Rinderer, B. Determination of Cotton-Bound Glyoxal via an Internal Cannizzaro Reaction by Means of High-Performance Liquid Chromatography. *Anal. Chem.* **2000**, *72* (23), 5829−5833.
(38) Gale, E.; Wirawan, R. H.; Silveira, R. L.; Pereira, C. S.; Johns, M. A.; Skaf, M. S.; Scott, J. L. Directed Discovery of Greener Cosolvents: New Cosolvents for Use in Ionic Liquid Based Organic Electrolyte Solutions for Cellulose Dissolution. *ACS Sustainable Chem. Eng.* **2016**, *4* (11), 6200−6207.

DOI: 10.1021/acssuschemeng.7b00662
ACS Sustainable Chem. Eng. 2017, 5, 5931−5939

(39) Gericke, M.; Schlufter, K.; Liebert, T.; Heinze, T.; Budtova, T. Rheological Properties of Cellulose/Ionic Liquid Solutions: From Dilute to Concentrated States. *Biomacromolecules* **2009**, *10*, 1188−1194.
(40) Lv, Y.; Wu, J.; Zhang, J.; Niu, Y.; Liu, C. Y.; He, J.; Zhang, J. Rheological Properties of Cellulose/ionic Liquid/dimethylsulfoxide (DMSO) Solutions. *Polymer* **2012**, *53* (12), 2524−2531.
(41) de Gennes, P.-G.; Brochard-Wyart, F.; Quere, D. *Capillarity and Wetting Phenomena: Drops, Bubbles, Pearls Waves*; Springer-Verlag: New York, 2004.
(42) Vladisavljević, G. T.; Shimizu, M.; Nakashima, T. Permeability of Hydrophilic and Hydrophobic Shirasu-Porous-Glass (SPG) Membranes to Pure Liquids and Its Microstructure. *J. Membr. Sci.* **2005**, *250* (1−2), 69−77.
(43) Peng, S. J.; Williams, R. A. Controlled Production of Emulsions Using a Crossflow Membrane. Part I: Droplet Formation from a Single Pore. *Inst. Chem. Eng.* **1998**, *76*, 894−901.
(44) Joscelyne, S. M.; Trägårdh, G. Membrane Emulsification - A Literature Review. *J. Membr. Sci.* **2000**, *169* (1), 107−117.
(45) Vladisavljević, G. T.; Schubert, H. Influence of Process Parameters on Droplet Size Distribution in SPG Membrane Emulsification and Stability of Prepared Emulsion Droplets. *J. Membr. Sci.* **2003**, *225* (1−2), 15−23.
(46) Vladisavljevic, G.; Shimizu, M.; Nakashima, T. Permeability of Hydrophilic and Hydrophobic Shirasu-Porous-Glass (SPG) Membranes to Pure Liquids and Its Microstructure. *J. Membr. Sci.* **2005**, *250* (1−2), 69−77.
(47) Quero, F.; Nogi, M.; Lee, K.; Poel, G. V.; Bismarck, A.; Mantalaris, A.; Yano, H.; Eichhorn, S. J. *ACS Appl. Mater. Interfaces* **2011**, *3* (2), 490−499.

DOI: 10.1021/acssuschemeng.7b00662
ACS Sustainable Chem. Eng. 2017, 5, 5931−5939

Supporting Information

Continuous Production of Cellulose Microbeads via Membrane Emulsification

James Coombs OBrien,[†,‡] *Laura Torrente-Murciano,*[‖,⊥] *Davide Mattia,*[*‖,⊥] *and Janet L. Scott*[*†,⊥]

[†] Department of Chemistry, [‡] EPSRC Doctoral Training Centre in Sustainable Chemical Technologies, [‖] Department of Chemical Engineering and [⊥] Centre for Sustainable Chemical Technologies, University of Bath, Claverton Down, Bath, BA2 7AY, United Kingdom.

Pages 8, Figures 6, Tables 2.

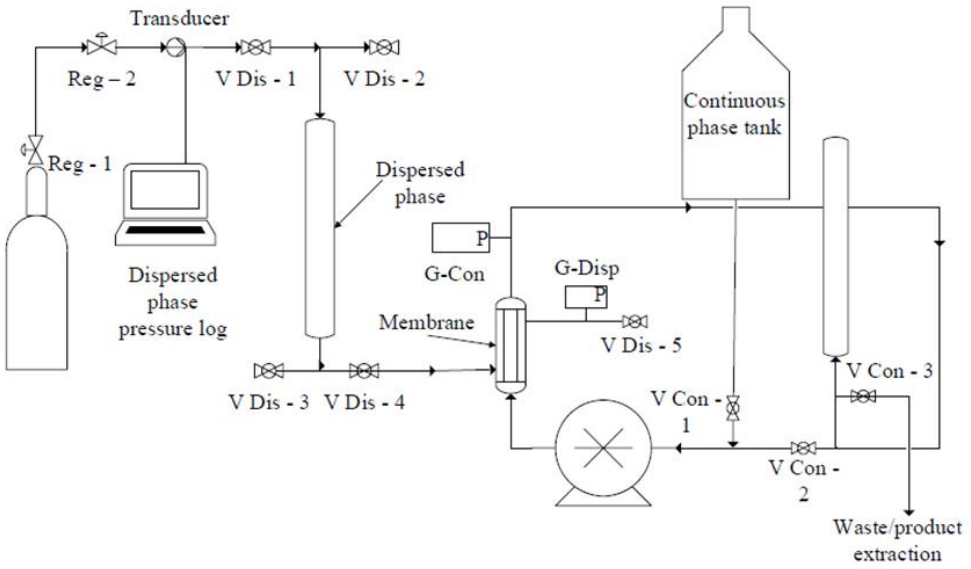

Figure S1. Schematic for the membrane emulsification apparatus developed.

Section S1

Membrane Emulsification: Start Up. A hydrophobised SPG membrane (10 μm pore size) was loaded into the membrane module followed by addition of the disperse phase (4 or 8 wt% MC dissolved in, 30:70 w/w, [EMIm][OAc]:DMSO) through disperse phase valve 3 (V-Dis 3) ensuring valve 1 and 4 (V-Dis 1/4) were close and valve 2 open (V-Dis 2). Once the required volume of disperse phase had been loaded V-Dis 3/2 was closed. The continuous phase (sunflower oil – 2 wt% Span 80) was loaded into its tank (V-Con 1 closed). V-Dis 5 was opened and the disperse phase allowed to fill the membrane module using a low pressure from the air cylinder (set by Reg – 2, Reg – 1 set at 1.5 bar) by opening V-Dis 1 and controlling the flow rate of liquid with V-Dis 4 until the disperse phase was seen to briefly expel from V-Dis 5. V-Dis 4 was then closed, closely followed by V-Dis 5 and 1. V-Con 1 was then opened (V-Con 2 and 3

remained closed) enabling the continuous phase to fill the rest of the apparatus. The waste/product pipe was then placed in a waste container of appropriate size and the pump turned on to a low flow rate (V-Con 3 opened to waste). The pump was turned off and V-Con 1 closed once all air was seen to have been removed from the tubing. V-Con 2 was opened, V-Con 3 closed, and the pump turned on to a low flow rate.

Membrane Emulsification: Formation of Emulsion. The appropriate disperse phase pressure was set at Reg-2 (measured by the transducer) and V-Dis 1 opened (V-Dis 4 remained closed). Concurrently, the pump flow rate was increased and V-Dis 4 opened (V-Dis 5 remained closed) at a rate in which the pressure of the continuous and disperse phases (measured at G-Con, G-Disp) remained the same. If need be, the pressure was adjusted at Reg-2 to prevent permeation of the disperse phase or back flow of the continuous phase through the membrane. Once the required continuous phase flow rate was met (1.4, 1.9 or 2.4 L/min) the disperse phase pressure was increased (measured at G-Disp and controlled at Reg-2) to a transmembrane pressure (P_{tm}) above the critical pressure (P_c). The level of permeation of the of dyed disperse phase through the membrane was observed via the reduction in its volume visible through the disperse phase tubing (between V-Dis 4 and 1) and the increase in turbidity of the circulating continuous phase due to the formation of an emulsion.

Membrane Emulsification: Removal of Emulsion/Coagulation of Cellulose. Once the required volume of disperse phase had permeated the membrane, the product tube (connected to V-Con 3) was placed below the meniscus of ethanol (300 mL) contained in a measuring cylinder (1 L). V-Con 3 was then opened followed by V-Con 1 which increased the volume of continuous phase in the system, driving the emulsion up into the collection vessel and out into the measuring cylinder. Once the emulsion was seen to have been removed (300 mL of emulsion containing

continuous phase) V-Con 1 was closed followed by V-Con 3. The coagulated cellulose beads contained in the measuring cylinder where then extracted by suction filtration (0.2 μm, nylon 66 filter paper) and washed (3 aliquots of 20 mL ethanol once microbeads were separated from continuous phase) then re-dispersed in deionised water (30 mL) with brief sonication (37 Hz, 20 secs pulse, 80% power, Fisherbrand Ultrasonic cleaner).

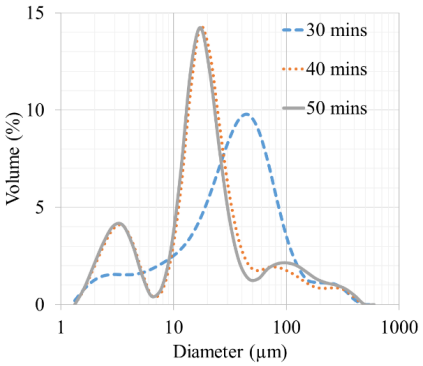

Figure S2. The change in particle size distribution of cellulose microbeads throughout the emulsification process for sample 6 (Figure 3).

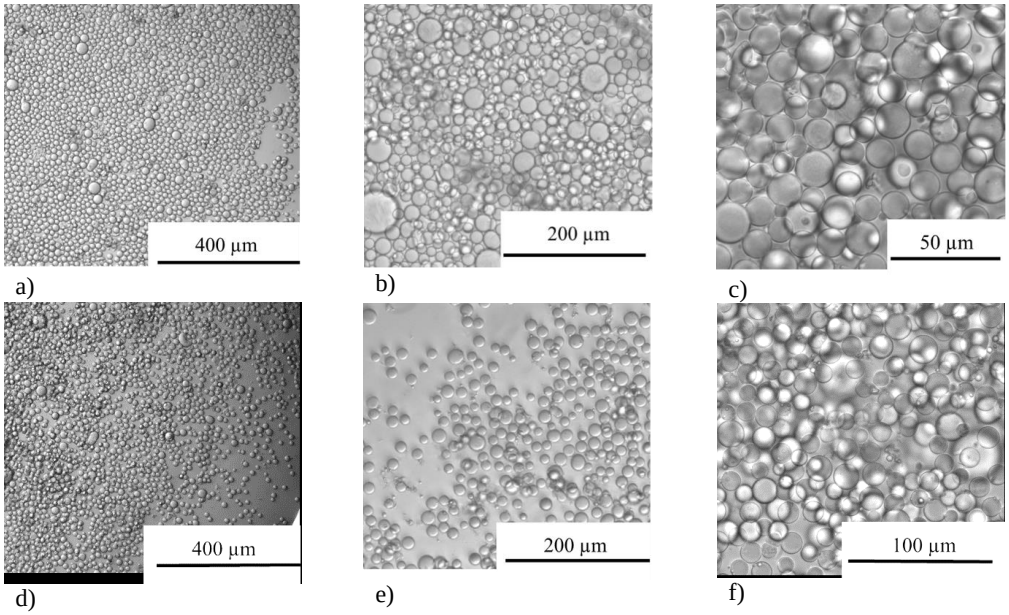

Figure S3. Optical micrographs of microbeads, obtained post phase inversion and leaching, suspended in liquid. Sample 4 (a-c) and sample 7 (d-f) at a range of magnifications. It is clear that, while most beads fall into a narrow particle size range, some larger (small in number, but comprising a large volume percent) and smaller beads do occur.

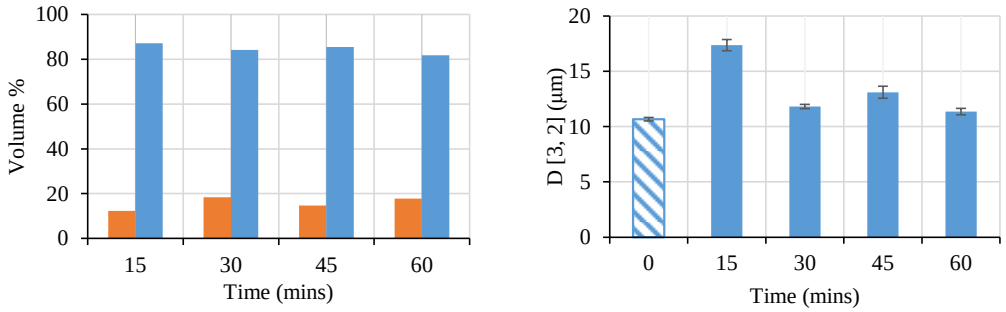

a) b)

Figure S4. Comparison of time resolved data a) the relative quantity of beads, expressed as volume percent, of the population with diameter <10 µm (orange bars), with that of the main population (blue bars) and b) the Sauter mean diameter, D[3,2] of the samples collected at various time intervals (the striped bar denotes the value for sample 4, collected immediately after extrusion was halted, while filled bars are from a separate experiment with samples collected over an extended period of time). Notably, samples represented in Table1 and Figure 3 were collected at t <20 mins. Neither measured points suggested significant breakup arising during recirculation and the population of sub 10 µm particles detected in all samples arises from some constant factor in the experiments, not droplet break-up.

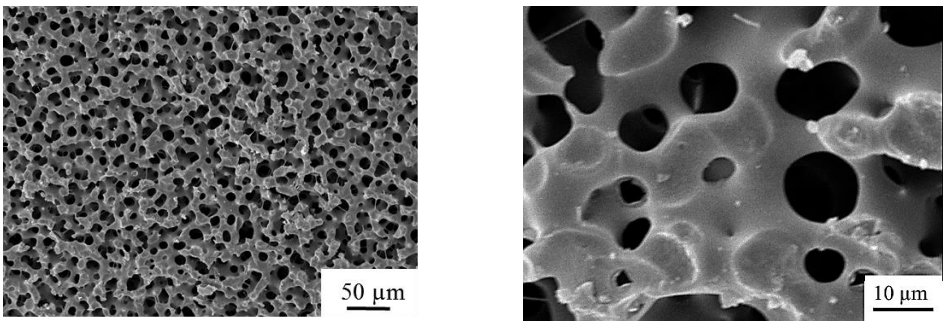

a) b)

Figure S5. SEM micrographs of the inner surface of the SPG membrane employed. a) Showing a large part of the surface and b) at higher magnification. While the majority of pores reflect the 10 µm pore size described, it is clear, in the closeup view, that variable size pores do exist and that some pores combine to form surface "pits" (not larger pores), which could result in

coagulation of forming droplets (although larger beads are few and undetectable in number based distributions).

Table S1. Physical values for the disperse phase solutions each utilising a 30:70 w/w [EMIm][OAc]:DMSO solvent system.

Cellulose concentration (wt.%)	Viscosity (Pa.s) [a]	Density (g/mL)	Interfacial tension (mN/m) [b]	Contact angle (°) [c]
8	1.18 (± 0.01)	1.13 (± 0.0004)	1.57 (± 0.02)	133 (± 2)
4	0.13 (± 0.01)	1.12 (± 0.001)	1.70 (± 0.04)	136 (± 2)

[a] average across Newtonian range; [b] with sunflower oil-2 wt% Span 80; [c] on hydrophobised glass

Section S2. Flow rate of disperse phase through membrane

The flow rate of the disperse phase through the membrane (Q_m) can be related to the flow rate through one pore (q) multiplied by the number of pores (n) (Equation 1).

$$Q_m = q.n \quad (1)$$

The flow rate from a single pore can be calculated from the Hagen-Poiseuille (Equation 2) using the pressure drop (ΔP) radius of the pore (r), viscosity of the disperse phase (μ_{dp}) and thickness of the membrane (L).

$$q = \frac{\Delta P \pi r^4}{8 \mu_{dp} L} \quad (2)$$

Knowing the porosity of the membrane (taken from Vladisavljevic *et al.*[1]) the number of pores in the membrane can be calculated from the surface area of the membrane (A) (Equation 3).

$$\varepsilon = \sum_{i=1}^{n} \frac{\pi r^2}{A} \approx \frac{n \pi r^2}{A} \rightarrow n = \frac{A \varepsilon}{\pi r^2} \quad (3)$$

The flow rate of the disperse phase through the membrane can therefore be defined as (Equation 4):

$$Q_m = \frac{\Delta P \pi r^4}{\varepsilon 8 \mu_{dp} L} \times \frac{A\varepsilon}{\pi r^2} \rightarrow \frac{A\varepsilon r^2 \Delta P}{8 \mu_{dp} L} \quad (4)$$

Table S2. High Performance Liquid Chromatography data for the detection of glycolic acid – extent of glyoxal cross-linking

Glyoxal/AGU in cross-linking solution (mol.)	Cross-linking solution (wt.%)	Moles of glycolic acid removed from sample (mM)	Mass of glyoxal (mg)	Cross-linked glyoxal/AGU molar ratio
70.0	6.0	0.89 (± 0.06)	51.8 (± 3.3)	1.41 (± 0.08)
136.4	11.9	1.37 (± 0.21)	79.5 (± 11.9)	2.08 (± 0.04)

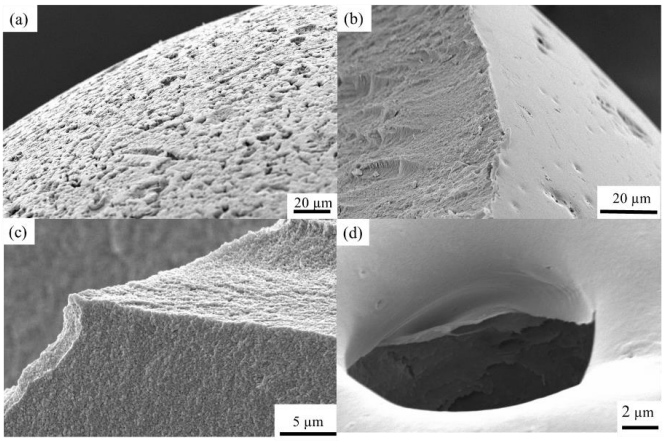

Figure S6. SEM images of cellulose beads (a) un-cross-linked surface, (b) cross section reacted with a 6 wt.% cross-linking solution (c) internal structure reacted with a 6 wt.% solution, (d) crater observed in samples reacted with a 12 wt.% solution.

References

(1) Vladisavljevic, G.; Shimizu, M.; Nakashima, T. Permeability of Hydrophilic and Hydrophobic Shirasu-Porous-Glass (SPG) Membranes to Pure Liquids and Its

Microstructure. *J. Memb. Sci.* **2005**, *250* (1–2), 69–77, DOI: 10.1016/j.memsci.2004.10.017.

Chapter 1

Introduction

Approximately 6300 million tonnes of plastic waste was generated in the period 1950-2015, since the onset of large scale production.[1] Of that, 9% has been recycled, 12% incinerated and 79% accumulated in landfill, or more worryingly, the natural environment. Plastics are inherently designed to resist natural degradation pathways, which is beneficial during use, but problematic at end of life, especially for single use applications, for example in some packaging. Therefore, the design and manufacture of biodegradable materials, where appropriate, is an attractive option to prevent further build-up of plastic waste to help achieve the European Union's aim to recycle or reused all plastics by 2030.[2,3]

Microbeads are a source of plastic waste that could be problematic for achieving this target. Microbeads are small (< 5 mm) spherical particles usually formed of polystyrene (PS) or polyethylene (PE) and present in some cosmetics and personal care products to generate abrasive and tribological enhancements to the formulation.[4,5] The reduced size enables microbeads to pass through waste water treatment plants directly into natural waterways where they can be ingested by lower trophic organisms (Figure 1).[6,7] The market in microbeads is significant, reaching \$2.3 billion globally in 2014 and expected to reach \$3.5 billion by 2020.[8] The effect of plastic waste on the marine environment has gained much public visibility, attributed to the efforts of non-government organisations and the widely publicised "Blue Planet Effect".[9]

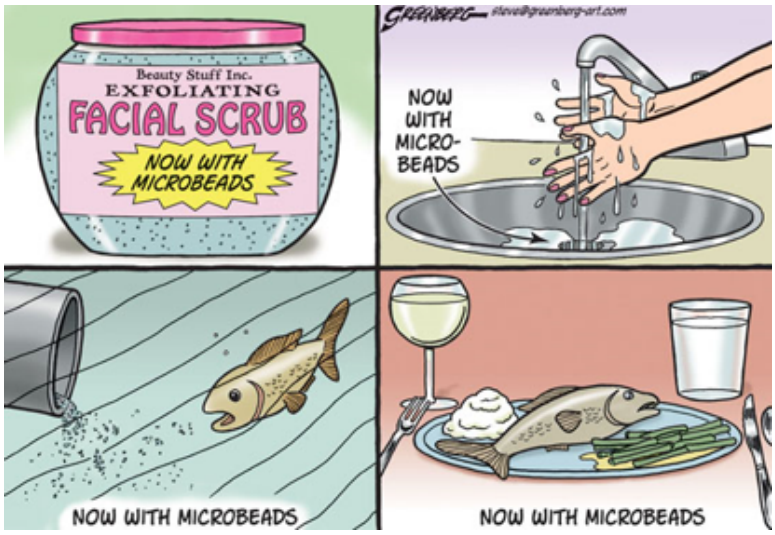

Figure 1: A general portrayal of the end of life culmination of microbeads. Reproduced with permission from Steve Greenberg.[7]

The potential issue of microbeads made of persistent plastics as a source of aquatic waste was first raised in the 1990s.[4,10] Over the past decade a plethora of scientific evidence for their presence in many food and beverage products, such as bottled water,[11] sea salt,[12] molluscs and fish,[13] has led to bans on the use of microbeads in consumer products across the globe including in the UK, USA and Canada.[14–17] The cumulative effects of microbeads on the marine environment remain unknown, however there is a substantial drive to replace persistent plastic microbeads with (bio)degradable alternatives and, with the amount of plastic in the oceans expected to treble in the next decade (2015 - 2025), there is still more that can be done.[5,18–20]

A biodegradable polymer that could potentially be used in place of PE/PS based microbeads is cellulose, the most abundant biopolymer on the planet.[21] Cellulose is, however, notoriously difficult to sustainably process, with many procedures in the literature used for the generation of cellulose beads not applicable in large scale manufacturing.[22]

The research documented in this PhD thesis assesses the potential use of cross-flow membrane emulsification for the continuous production of cellulose microbeads. The use of a non-derivatising ionic liquid co-solvent (Organic Electrolyte solution, OES) to dissolve cellulose, followed by subsequent

emulsification and coagulation in an anti-solvent, was shown to be a progressive route to the formation of biodegradable cellulose microbeads. This was supported by investigations into the solvent system and post processing of the formed beads to impart specific mechanical, topographical and functional properties to the materials. In addition, a scaled-up apparatus based on a dropping process is presented as an efficient route to the formation of larger cellulose beads (1-3 mm in diameter) not readily obtainable by emulsification. These materials also have potential applications outside of personal care products, including as supports for extraction processes in waste water treatment or in chromatography[22–25] and in the controlled release of active compounds for agricultural and healthcare applications.[22,26]

Chapter 2

Literature Review

2.1 Cellulose

The abundance of the biopolymer cellulose in the troposphere is unrivalled by any other polymer, with an estimated 1.5×10^{12} tons generated annually.[21] Although this estimation changes depending on the literature source, it is generally agreed that the number is at least in the 10's of billions of tons.[21,27] Unsurprisingly, cellulose is seen by many, and has been for decades, as an almost inexhaustible source of material.[21] This is reflected in the tonnage of cellulose that is already processed yearly, which stands at around 200 million tons. Even this large quantity is but a fraction of what is readily available.[27] Thus, it is reasonable to assert that cellulose is an underutilised resource.

Cellulose is highly functionalisable, mechanically rigid and is non-digestible by humans, therefore use of cellulose as a feedstock should have no impedance on food production, indeed agricultural waste can even be a good source of cellulose.[22,28] Apart from its abundance and natural degradation pathways, the desirable structure of cellulose is a significant reason why many are interested in using this biopolymer as a material.

2.1.1 Structure

Cellulose exists naturally as a composite with another polysaccharide, hemicellulose, and the aromatic biopolymer lignin.[29] It is comprised of repeating monomeric glucopyranose units linked in straight, rigid chains via 1,4-β glycosidic bonds. The terminal ends are composed of a C4 hydroxy group (non-reducing end) and a C1 hydroxy group in equilibrium with an aldehyde moiety (reducing end) (Figure 2).[21]

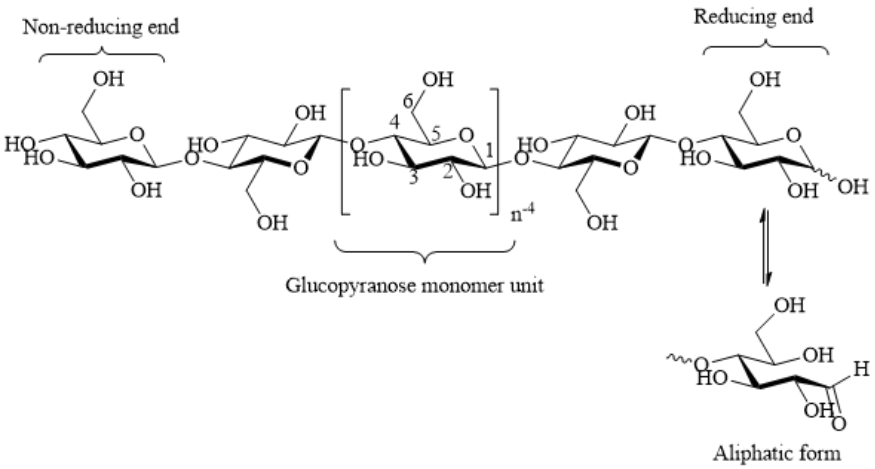

Figure 2: The structure of cellulose highlighting the two terminal groups; reducing and non-reducing.

The degree of polymerisation (DP) of cellulose typically ranges between 150-10,000 units, depending on the source.[21] Bacterial sources give the highest DP and microcrystalline cellulose (MCC) some of the lowest, due to post extraction processing in which the cellulose undergoes chain scission via acid hydrolysis in the amorphous region. The linearity of the β-glycosidic bonds enables a high degree of intra- and inter-chain hydrogen bonding generating a supramolecular sheet structure and subsequent macroscopic arrangement into fibrils.[29]

Crystalline cellulose exists in several different polymorphs of which cellulose *I* (Figure 3A), as the natural crystalline form, is the most common.[28] Solid-state carbon-13 nuclear magnetic resonance (NMR) experiments conducted by Atalla *et al.* highlighted that the native cellulose *I* form existed as multiple crystal forms, namely $I\alpha$ and $I\beta$, the structures of which were elucidated by Nishiyama

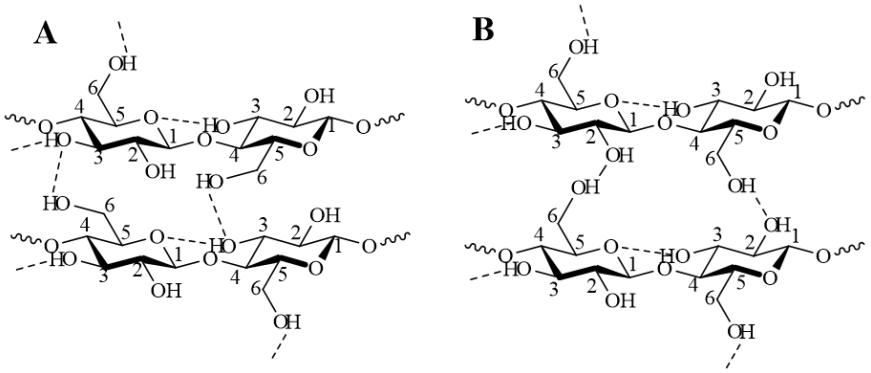

Figure 3: The difference in intermolecular hydrogen bonding in cellulose *I* (**A**—parallel stacking) and *II* (**B**—anti-parallel stacking) polymorphs.[28]

et al. using X-ray and neutron data.[30–32]

The cellulose *I* crystal structure is thermodynamically metastable, so can be converted, via dissolution and subsequent regeneration, to the more stable polymorph - cellulose *II* (Figure 3B)- or via ammonium treatment to a cellulose *III* form.[33,34] Differences in the crystal structure between cellulose *I* and *II* are present in the inter-chain, but not intra-chain bonding, which is itself dominated by hydrogen bonding between the O3 hydroxy group and O5 position in the ring in both polymorphs (Figure 3).[21] Accompanying this, the cellulose *I* structure also exhibits interactions between the O6 and O3 positions, which promotes the parallel packing of the polymer (Figure 3A). On the other hand, the more thermodynamically stable cellulose *II* intermolecularly bonds via the O6 and O2 hydroxy groups promoting an anti-parallel ordering of chains (Figure 3B).[28]

As referred to previously, cellulose exists naturally as a composite with hemicellulose and lignin. The low MW hemicellulose polymer binds non-covalently to the surface of cellulose fibrils and is subsequently entangled and covalently bound to lignin via a ferulic acid sub unit (Figure 4).[29] The relative quantities of each component will differ depending on the source of biomass (softwood, hardwood, grasses etc) with cellulose accounting for 35-50 % of the mass.[29]

The isolation of the components of the lignocellulosic composite requires a versatile method applicable to various types of seasonal lignocellulosic biomass

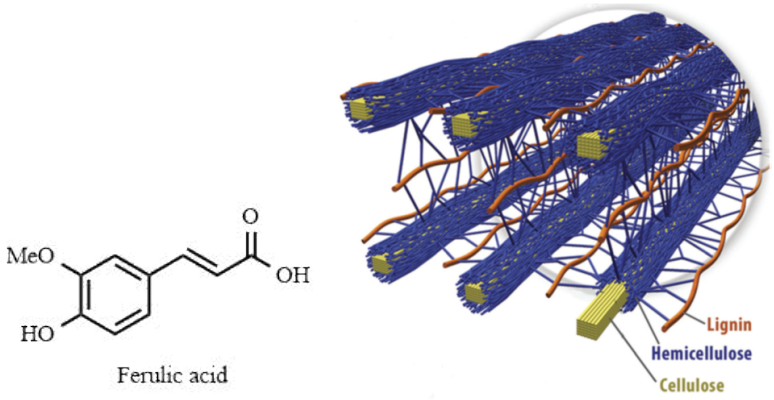

Figure 4: The structure of ferulic acid responsible for covalently binding lignin and hemicellulose together and the arrangement of the lignocellulose composite in the plant cellulose wall, reproduced with permission from Brandt *et al.*[29]

(varying ratios of each biopolymer).[29] Historically the Kraft process has been used, utilising NaOH and Na_2S to remove the lignin and hemicellulose parts of the composite, creating cellulose-rich pulps for the generation of fibres or paper.[29] A good proportion of the current research into cellulose dissolution is focused on the lignocellulose-to-bioethanol route, which aims to maximise sugar output via a dissolution and depolymerisation process.[29] This differs for that of materials production which must be optimised for high cellulose yields, i.e. little/no reduction in DP or unwanted functionalisation of cellulose, during dissolution and reshaping into the required form.[35] Generally, cellulose processing takes place via three stages, dissolution, shaping and coagulation,[36] each of which will be discussed in the subsequent sections.

2.2 Cellulose Solubilisation

Polymer processing generally takes place in a liquid phase. This is typically achieved by heating the polymer above its melting point – so called "melt processing" – or by dissolving it in an appropriate solvent system. The extensive hydrogen bonding network of cellulose counteracts the biopolymer's processability by preventing the formation of a liquid state via heating. Cellulose is not thermoplastic, i.e., it does not exhibit a solid to liquid phase transition (melt) and undergoes thermal decomposition before a liquid state can be achieved. This

extensive hydrogen bonding network also renders it insoluble in many common solvents. The cellulose monomer, glucose, is soluble in water, but with repeat units becomes insoluble once the chain length reaches *ca.* 6 anhydroglucose units (AGU) (cellohexaose) and above.[28]

2.2.1 Derivatising Solvents

To achieve full dissolution of cellulose, the secondary bonding between chains must be disrupted. One method to achieve this is to functionalise the hydroxy groups responsible for chain binding in order to reduce chain interaction, thus rendering the polymer soluble. Cellulose is recovered from solutions of derivatised cellulose by removal of the imparted functionality, leading to the reformation of the cellulose bulk structure.[21]

The Viscose process dominates the global production of reformed cellulose materials. It involves the transformation of the polymer into fibres and films via functionalisation with carbon disulfide resulting in cellulose xanthogenate (Figure 5), which is soluble in sodium hydroxide.[37] This "Viscose" mix is then shaped into the desired product – e.g. fibres or films - followed by cleavage of the xanthate moiety using a mineral acid, forming the final cellulose product.[21]

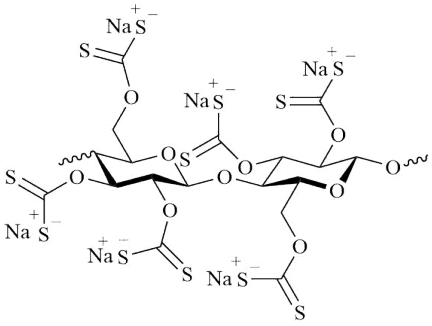

Figure 5: Cellulose xanthogenate formed during the Viscose process via the reaction of cellulose with CS_2 and solubilisation in NaOH.

Although the Viscose process is by far the most widely utilised cellulose processing technology, it has several environmental issues which have prompted the search for other methods. The main drawbacks can be summed up as: Use of toxic CS_2 and high volumes of fresh water. The toxicity of CS_2 is a

major drawback. Efforts to recycle it have been hindered by the volumes of fresh water required to do so, leading to increased complexity and cost. Along with this, the sheer amount of auxiliaries required – CS_2, NaOH, H_2SO_4 – are more than twice that of the processed cellulose produced.[27,37] It is preferable to solubilise cellulose in non-derivatising solvents avoiding extra chemical steps, in which functionality must be added and then removed, incurring chemical waste and risking potential chain scission of the polymer backbone. This has fuelled research into non-derivatising cellulose solvent systems, such as those forming the basis of the Lyocell process.

2.2.2 Non-Derivatising Solvents

The fundamental basis for designing an effective non-derivatising solvent system for cellulose is linked to the ability of the solvent to preferentially form hydrogen bonds with the polymer. If the affinity of this hydrogen bond formation is high enough then the polymer will interact with the solvent in preference to itself, resulting in dissolution. The Lyocell process was the first commercialised non-derivatising cellulose processing route with solutions of up to 23 wt% cellulose in water and *N*-methylmorpholine-*N*-oxide (NMMO)(Figure 6) at temperatures above 74 °C being obtained.[21]

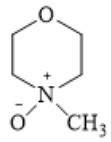

Figure 6: *N*-Methylmorpholine-*N*-oxide (NMMO), the non-derivatising solvent for cellulose used in the Lyocell process.

The strong N-O dipole present in NMMO enables the solvent to overcome the hydrogen bonding network in cellulose, rendering it soluble, after which the solution is shaped and the cellulose reformed using a water anti-solvent bath.[21] Potential issues have been raised about NMMO thermal instability.[21] However, the substantial cost, mainly of safety technology, has been the chief source of opposition to the wide scale use of this process and has hindered its competition with the extensively used Viscose process (Figure 7). The Viscose

process therefore still accounts for approximately 95% of all processed cellulose production volumes.[27,38]

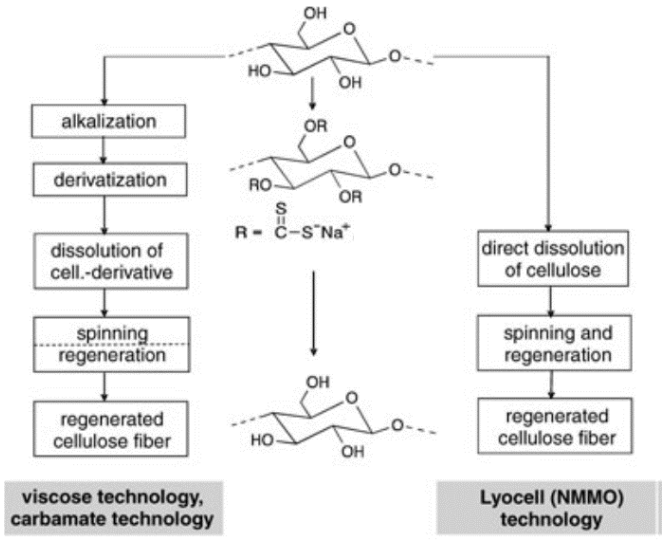

Figure 7: A flow diagram comparing the Viscose and Lyocell processes. Reproduced with permission from Klemm *et al.*[21]

Other cellulose non-derivatising solvent systems also exist such as dimethylacetamide/LiCl,[39] and those based on phosphoric acid.[40] The absence of a scalable, environmentally friendly route for processing cellulose is a major hindrance to the wide scale use of this truly sustainable polymer. For just over a decade however, ionic liquids (IL) have been shown to fill this gap for the non-derivatising dissolution of cellulose.[38]

2.2.3 Ionic Liquids

ILs are unique compounds which consist solely of ions. They differ from other ionic materials by having a low lattice energy, a result of bulky often asymmetrical organic cations, rendering them liquid at reasonable temperatures (<100°C), with a subsection specified as room temperature ionic liquids (RTIL).[41,42] ILs typically exhibit negligible vapour pressures, enabling efficient recycling streams, but can be distilled under very high vacuum and temperatures.[43] The broad descriptions that qualify a compound as an IL have led to a plethora of possible compounds that can be qualified as such (estimated

>1,000,000) and is why they have been designated "designer solvents".[41] ILs have use in numerous research and industrial areas including in electrochemistry,[44] as polymeric materials,[45] as surfactants,[46] for mercury removal from gas streams,[47] and most interestingly, in terms of this report, biomass processing.[29,38,48–50]

Ionic Liquid Polysaccharide Processing

ILs can be utilised during both the deconstruction of biomass and dissolution of the resulting biopolymers. Two approaches exist for deconstructing lignocellulose using ILs: either complete composite dissolution, or one in which the cellulose portion remains largely untouched. The former process tends to be exploited for biofuel production while the latter is more useful for cellulose recovery.[29] In both, cases ILs have been shown to accomplish full/partial dissolution of the biomass from a variety of lignocellulosic sources.[29,48,51,52]

The versatility of ionic liquids for biomass processing is clear, not only due to the extent of different types of woody biomass that can be dissolved, but also due to applicability to non-wood-based systems, such as chitinous sources. Rogers *et al.* have shown that raw crustacean shells can be dissolved using the IL 1-ethyl-3-methyl-imidazolium acetate ([EMIm][AcO]) (Figure 9) which can be used to produce pure chitin powder.[50] Chitin, the second most abundant biopolymer after cellulose, suffers from similar processing issues, but is of particular interest in the biomedical field.[53] It differs from the structure of cellulose at the C2 position in which an acetamido group is present in place of the hydroxy (Figure 9). Chitin is, in fact, a co-polymer with its deacetylated form, chitosan.[54]

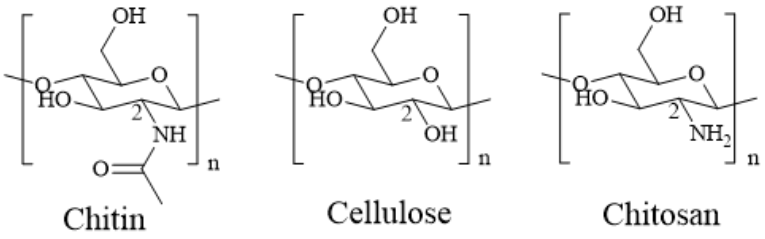

Figure 8: The structure of the polysaccharides cellulose, chitin and chitosan

However, most of the literature on IL biopolymer processing is concentrated

on cellulose. Work by Rogers *et al.* in 2002 is often attributed as the seminal work in the field of cellulose processing using ILs, but was not the first example of IL mediated cellulose dissolution, which should be attributed to Graenacher (1934), although the process took place at >100 °C.[49,55] Since 2002, the extent of research and understanding of cellulose solubility in ILs has grown exponentially along with the list of ILs, of varying properties, able to dissolve cellulose.[38] Some common traits of ILs that are effective cellulose solvents can be extracted from the literature. As with most non-derivatising cellulose solvents, a strong hydrogen bonding acceptance ability is needed, usually attributed to the anion of the IL.[38] Those with high hydrogen basicity/acceptor ability (chlorides, acetates etc.) have been shown to have a greater dissolution power towards cellulose with a clear trend existing between hydrogen bond basicity and maximum cellulose solubility.[29,56] The cation also has an important role to play, although this is less clear than that of the anion. The most widely studied cations are aromatic and bear a delocalised positive charge, a property hypothesised to lead to a reduction in the interaction between the ions in the IL, allowing the anion a greater opportunity to interact with cellulose.[38] Some have suggested that the cation can increase cellulose solubility by forming hydrogen bonds with hydroxy oxygen atoms and the oxygen atom of the pyranose ring, or decrease the solubility by competing with the anion or through steric hindrance.[57] The dissolving power of the IL is also inversely proportional to the cationic alkyl chain length, an increase in which increases the MW of the cation effectively decreasing the concentration of the anion.[38] An increase in alkyl chain length has also been linked with increased toxicity to various aquatic organisms due to greater lipid solubility.[58,59] Out of the extensive list of IL utilised for cellulose dissolution [EMIm][OAc] (Figure 9) is the most intensely researched due to it being a RTIL, able to dissolve large quantities of cellulose and being relatively environmentally benign, which will be discussed in greater detail in due course.[60] This is reflected in the average number of papers published on its use per year, currently standing at 108 (average per year between 2011-2016).[61] [EMIm][OAc] has also been shown to be a good solvent for other biopolymer such as lignin and chitin.[8,50,62]

There are common issues, however, throughout the field of ILs that could hinder wide-scale industrial use of this solvent:

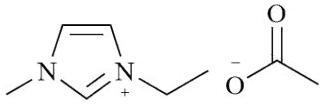

Figure 9: The structure of the ionic liquid 1-ethyl-3-methyl-imidazolium acetate([EMIm][OAc])

Cost: ILs are generally expensive. A techno-economic analysis of IL use for bioethanol production has found that the IL would be, by far, the greatest expense to a biorefinery, as ILs are typically 5 - 20 times more expensive than molecular solvents.[37,63] This issue can be somewhat overcome with efficient recycling streams, enabled by the negligible vapour pressure of ILs, or the use of new "low-cost ionic liquids". Work by Hallett *et al.* presented the development of sulfuric acid and basic amine ILs which showed similar properties to [EMIm][OAc] at a fraction of the price.[60] The fraction of IL use for cellulose dissolution can also be decreased by the addition of a co-solvent, which is covered in greater detail in section 2.2.4.[56]

Hydrophilicity: Another potential issue is the inherent hydrophilicity of many of ILs. Significant water absorption from the atmosphere and/or the inherently wet biomass can reduce the dissolution capability of the IL, hypothesised to be because of competitive hydrogen bonding between the IL and water, and has a significant impact on the viscosity of the ionic liquid.[29,64,65] Ohno *et al.* have shown that this can be overcome by utilising a tetrabutylphosphonium hydroxide IL. Cellulose solutions containing up to 40 wt% water were shown to dissolve up to 20 wt% cellulose at room temperature.[66] The same group also used similar reasoning to design ILs that were both hydrophobic and polar, yet evidence for a cellulose dissolution capability has yet to be published.[67]

Thermal decomposition/side reactions: IL are often quoted as being thermally stable, but this is dependent on the IL used.[29,68,69] When nucleophilic ions are also present, the possibility of side reactions is increased, especially at higher temperatures. Work published by Clough *et al.*,[70] building on previous research by Ebner *et al.*,[71] has shown extensive reactions between monomers and oligomers of cellulose (Figure 10) with commonly used dialkylammonium ILs, including [EMIm][OAc], not only limited to the reactive terminal positions

of the biopolymer. Although these experiments were carried out at 120 °C for 48 hours when many of these solvents dissolve cellulose rapidly (< 1 h) at lower temperatures (room temperature), it still highlights the possibility of side reactions of common ILs.

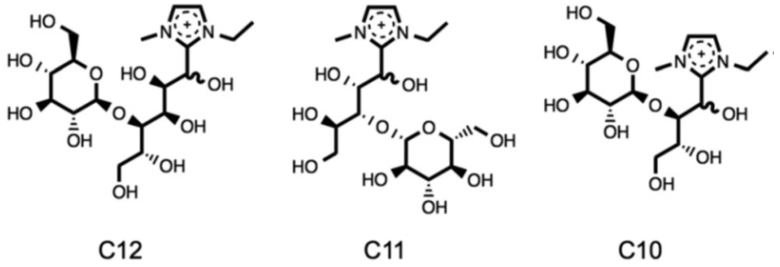

Figure 10: The products of the reaction of [EMIm][OAc] and cellobiose (10 wt%, 120 °C, 0.25 h) determined by mass spectrometry and HPLC. Reproduced with permission from Clough *et al.*[70]

Although increasing the temperature has been shown to increase the dissolution ability of the solvent, this is not a thermodynamic effect. Recently, Gomes *et al.* determined an exothermic heat of dissolution of -132±8 Jg^{-1} for the dissolution of cellulose by [EMIm][OAc].[72] This suggested that heating did not favour the dissolution process in terms of its thermodynamics but that apparent enhanced dissolution rates are due to greater mass transport via a reduction in the viscosity of the solvent.

Toxicity and Biodegradation: to be considered truly sustainable, the question of toxicity and what happens to an IL at the end of life, must be answered. Due to negligible vapour pressure, the likelihood of release to the atmosphere is low, however significant solubility in water provides a readily accessible pathway to environmental pollution.[73] It is difficult to draw general conclusions about IL toxicity and biodegradability due to the plethora of ILs available, however, some general comments can be made. It is generally considered that the cation is responsible for any toxicity imparted by an IL, the effect of which has been mapped by Amde *et al.*: toxicity clearly increased with chain length due to a greater interaction with the cellular membrane.[73] Some ILs have also been shown to be toxic to a range of enzymes, algae and fish.[61,73] The effect of the anion can be investigated when the cation is fairly non-toxic, showing a clear increase in toxicity with increasing lipophilicity and instability

of the anion, especially when fluorinated.[61] The current toxicological data on [EMIm][OAc], the IL utilised in this thesis, remains limited in the literature and from suppliers.[61] At the time of writing (early 2018), it is currently preregistered by the Registration, Evaluation, Authorization, and Restriction of Chemicals (REACH) database (list number: 604-344-8) as a skin (H315) and eye (H319) irritant.[74] The acetate anion appears to be benign, as is the IL as a whole, however the toxicological data on this remains sparse. In small quantities, [EMIm][OAc] does appear to be mostly non-toxic and environmentally non-damaging.[61] Many imidazolium-based IL have been shown to not be readily biodegradable under International Organisation for Standardisation (ISO) or Organisation for Economic Co-operation and Development (OECD) test conditions.[75] Ultimately, prevention of IL loss in the environment is critical and will be enabled by efficient processes and water treatment in industrial areas. The high economic cost of IL may actually be a benefit from an environmental stand point, due to the greater economic need to recover and reuse as much as possible.

Pilot Scale Ionic Liquid Cellulose Dissolution

ILs have generated much interest industrially with the likes of BASF launching a pilot scale plant based on the dissolution and wet spinning of cellulose-[EMIm][OAc] solutions.[27] The Joint BioEnergy Institute (JBEI) presented an initial technoeconomic analysis, which highlighted the feasibility of [EMIm][OAc] pretreatment of lignocellulosic biomass for the production of biofuels.[61] A pilot scale process based on dissolution and reforming IL cellulose solutions as films and/or fibres, known as KH-NILCELL^{TM} and jointly developed by ICCAS and Shandong Henglian New Materials Co. Ltd, is claimed to have an economic benefit over the widely used Viscose process, attributed to the efficient recycling of the IL.[76] It appears that the first small steps towards the greater industrial use of IL for cellulose processing have been taken.

2.2.4 Organic Electrolyte Solutions

As implied already, the dissolution of cellulose can be made more rapid, whilst minimising the volume of IL used, by the use of a co-solvent. In fact, the addition of DMSO to [EMIm][OAc] resulted in an almost instantaneous dissolution of cellulose (10 wt%).[56] Considering that an IL must consist solely of ions, these solutions have been named "Organic Electrolyte Solutions" (OES). This has significant implications for the processability of cellulose solutions as it reduces the amount of IL required to fully dissolve the biopolymer, reduces the dissolution time and enables the reduction and control of the viscosity of the solution without adjustment of temperature, avoiding potential side reactions and reducing operating costs.[77] Several co-solvents have been investigated to enhance the dissolution capability of the IL for cellulose by Rinaldi.[56] Gale *et al.* extended this work and sought greener co-solvents.[78] Using the Kamlet-Taft parameters (α: hydrogen bond donor/acidity, β: hydrogen bond acceptor/basicity and π^*: polarisability) Rinaldi concluded that the co-solvent should have a high β value and a zero α value to aid in the dissolution of cellulose. Gale *et al.* showed that the need for zero α was not as prevalent at low IL mole fractions and highlighted a similarity between the solvation mechanism of cellulose with DMSO and the acetate anion from [EMIm][OAc] (with preferential solvation by the latter). The hydrogen donor and acceptor ability of [EMIm][OAc] was hypothesised to lead to enhanced dissolution of cellulose.[78] Although IL based dissolution processes for cellulose have been noted in the literature, there have been no documented attempts to scale up OES based dissolution processes.

The use of ILs in the dissolution of cellulose has opened a new route for potential cellulose utilisation. Research into the shaping of these IL – cellulose solutions into usable products has been widely reported with forms including films,[79,80] fibres,[49] composites,[81] aerogels,[37] and beads.[22] The last example is of specific interest in this thesis due its numerous applicable areas ranging from cosmetics and personal care products, to supports in extraction processes, as shown in the literature.[8,22,24,82–84]

2.3 Cellulose Beads

Spherical cellulose materials (cellulose beads) can be formed from dissolved cellulose solutions via shaping into droplets and subsequent regeneration of the cellulose hydrogen bonding network by the addition of a protic anti-solvent, in which the cellulose polymer is insoluble, forming solid, spherical beads of cellulose. The anti-solvent, typically hydrogen bond donating solvents (water, alcohols etc.),[85] preferentially bind with the anion of the IL in place of the hydroxy groups on cellulose allowing the reformation of the cellulose hydrogen-bonding network and coagulation of the polymeric material from the solvent (Figure 11). Co-solvents, used alongside ILs, can also have an anti-solvent effect on cellulose at high concentrations as they compete in a similar manner to associate with the IL.

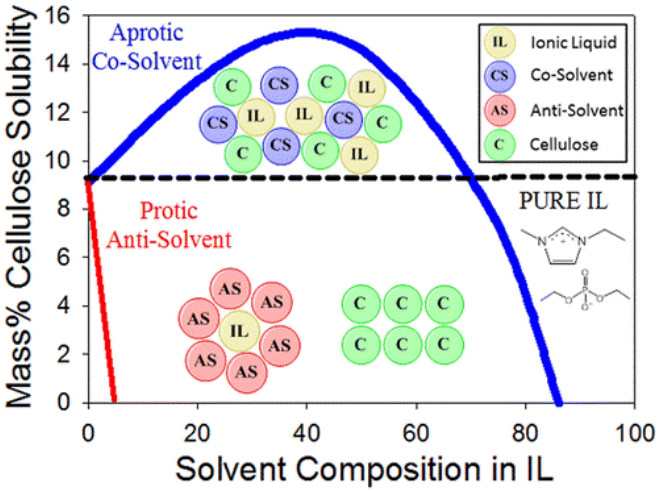

Figure 11: A graphical representation of the effect of a co-solvent and anti-solvent on cellulose dissolved in 1-ethyl-3-methylimidazolium diethyl phosphate. Reproduced with permission from Minnick *et al.*.[85]

Cellulose beads have applications in extraction technologies[24] and as fillers,[84] tribological modifiers[86] and abrasives,[82] as well as delivery systems.[22] In many cases, spherical beads are less likely to aggregate and provide superior flow profiles when placed in a packed bed.[8,23,87]

2.3.1 Formation

In general, the formation of cellulose beads occurs via one of two techniques:

1. Dropping techniques, and,
2. Dispersion/Emulsion techniques

Dropping Techniques

In 1951, the first route to the formation of cellulose beads was patented (*US 2543928 A*) and documented the utilisation of a dropping technique and a Viscose cellulose solvent system.[88] Although this was performed by hand, the principles of the dropping process remain the same to this day. Typically producing larger beads (0.5 - 3 mm), dropping techniques involve passing a cellulose solution through a small aperture producing a drop, into an anti-solvent bath (Figure 12 A).[22] Other techniques also exist that can be automated and produce beads at a higher throughput (Figure 12 B-D).

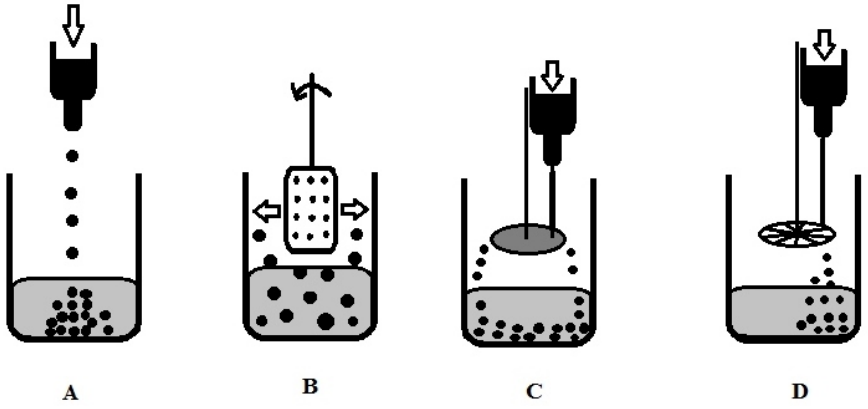

Figure 12: Different dropping techniques used in the formation of cellulose beads: A: dropping, B: spinning in a porous housing, C: spinning disc and D: jet cutting.[22] In each case the cellulose solution is dropped into an anti-solvent bath. Redrawn from Gericke *et al.*.[22]

Droplet distortion into teardrop, or disc, shapes is a potential issue with dropping techniques, although some regard disc shaped structures as sought after materials.[22,89] Tear shaped particles are formed if too shallow a dropping height

is used, preventing the full stabilisation of the droplets shape, via the interfacial tension which drives the formation of a lower energy sphere (compared with a tear drop) (Figure 13). A disc can be formed if the surface tension of the anti-solvent is too high compared to that of the droplet, or if the droplet falls from too high a height, which may cause mishaping of the droplet when the two come into contact (Figure 13).[22]

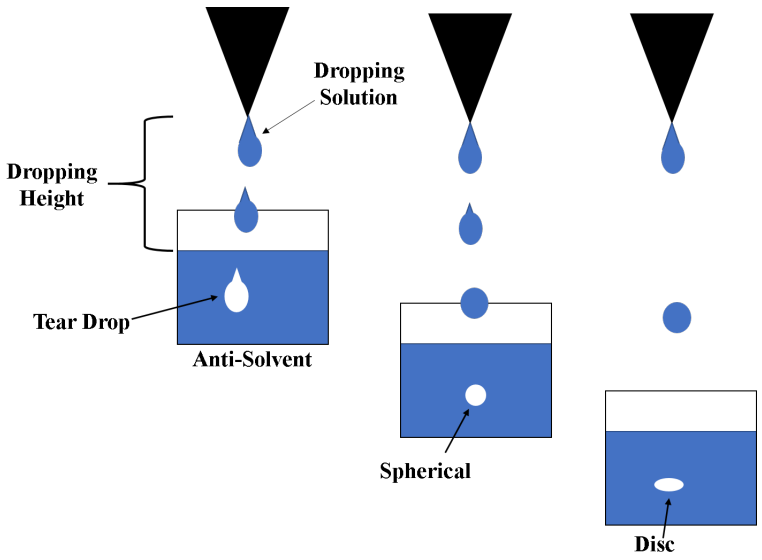

Figure 13: The effect of dropping height on the shape of particle produced during a dropping process. Too shallow a dropping height results in teardrop shaped particles where as too excessive a height produces discs.[22]

The temperature of the anti-solvent bath has also been shown to influence the rate of cellulose coagulation, with high temperatures rapidly forming less dense materials generally of larger size than those formed at lower temperatures.[36] Examples of the formation of cellulose beads using this process are prolific in the literature due the ease of formation and use of widely available apparatus. Some have highlighted the use of IL based media as the dropping solutions[90] including with other polymers, such as chitin and chitosan.[36,91–94] Dropping processes are relatively low throughput due to the use of a single needle-syringe or pipette, and if large quantities of smaller diameters beads are required, dispersion techniques are often used.

Dispersion Techniques

Dispersion techniques, unlike dropping techniques, rely on the formation of an emulsion before the biopolymer is coagulated from solution. The disperse phase is disrupted in a continuous phase, in which it is not miscible, resulting in the formation of droplets that can be stabilised by the presence of a surface active agent forming an emulsion. The addition of an anti-solvent follows this causing the coagulation of the polymer from solution to solid spherical beads. Typical particle sizes for this process range between 10-100s μm in diameter, 10 times smaller than those from dropping techniques, due to increased shear forces.[95] There is a strong relationship between stirring speed and bead size, an increase in the former leading to a decrease in the latter.[22] Rotary processes do suffer from variation in the shear rate applied throughout the dispersing vessel, with high shear in close proximity to the rotor head and the presence of "dead zones" with lower shear, which can lead to polydisperse emulsions.[96] The simplicity of this process has resulted in several routes being commercialised for cellulose bead production.[22] Again, there are many examples of the use of dispersion techniques for the production of cellulose,[22,23,83,97] cellulose-composite[57,87] and other biopolymer beads.[8] IL have also been shown to be applicable to cellulose bead formation via this process, typically dispersed in an oil.[83,95,98] Many of the methods reviewed use the IL reported in Rogers *et al.*'s 2002 landmark paper on cellulose dissolution, [BMIm][Cl], admittedly in some cases with different co-solvents.[49,99] The use of surfactants in the process is a necessity. Suzuki *et al.* found that high MW stabilisers – Silaplane FM-3321 (a polysiloxane with amino terminal groups) - were preferred over those of lower MW – Span80 or 85 - to prevent coalescence of the cellulose-[BMIm][Cl] droplets.[97] It is interesting to note however, that the non-ionic surfactant, Span 80, has been widely used throughout the literature for the stabilisation of IL and other emulsions with no mention of coalescence.[100–102] In the case of Suzuki's research this lack of stability may have been brought about by the low concentration of surfactant in the oil phase (0.25 wt%).[100]

There are no examples in the literature, however, of a continuous emulsification based process for the production of cellulose beads. Each of the examples described in this section have relied on batch processes which have

limitations when applied to full scale manufacturing. The lack of a continuous process for the formation of cellulose beads limits the wide scale use of these sustainable materials, a hurdle that could be overcome with the use of a continuous emulsification process.

Anti-Solvent Effect

The anti-solvent used to regenerate the cellulose matrix has been shown to influence the crystallinity and morphology of the cellulose bead produced, and ultimately its digestibility.[36,62] Geng *et al.* showed that, when water was used as an anti-solvent, the particle clusters formed differed from the spongy material resulting from phase inversion in ethanol or isopropanol (anti-solvent poured into a cellulose-IL mix with agitation producing flocs of cellulose).[62] The Kamlet-Taft parameters were used to map the anti-solvents and compare them with the β value of [EMIm][OAc] (0.95). Water strongly interacted with the IL due to its high α value (1.17), readily displacing the ions from the cellulose polymer, resulting in rapid coagulation. Compared with the lower values of α for the alcohols (ethanol: 0.86, isopropanol: 0.76), coagulation was hypothesised to occur less rapidly and progress via gel formation prior to full cellulose coagulation. Interestingly, it was also shown that coagulation in water promoted the formation of the cellulose II crystal structure, whereas coagulation in either of the alcohols lead to an amorphous structure (Figure 14 A).[62] These latter materials showed a much more rapid degradation in enzymatic solutions (cellulase) due to the reduction in crystallinity (Figure 14 B).

Aqueous solutions of nitric acid have been shown to form different cellulose particle morphologies, which could be altered with the concentration of acid.[36] The physical properties of the beads can also be altered using post processing drying methods. Drying from a solvent under vacuum produces dense beads whereas freeze drying procedures provide a high surface area, porous structure.[97] Beads made from high concentration cellulose solutions have also been shown to produce denser structures.[22] Zhang *et al.* showed that the porosity of a bead can also be controlled by blending starch with cellulose and coagulating the two polymers into a composite bead, which when exposed to an amylase enzyme,

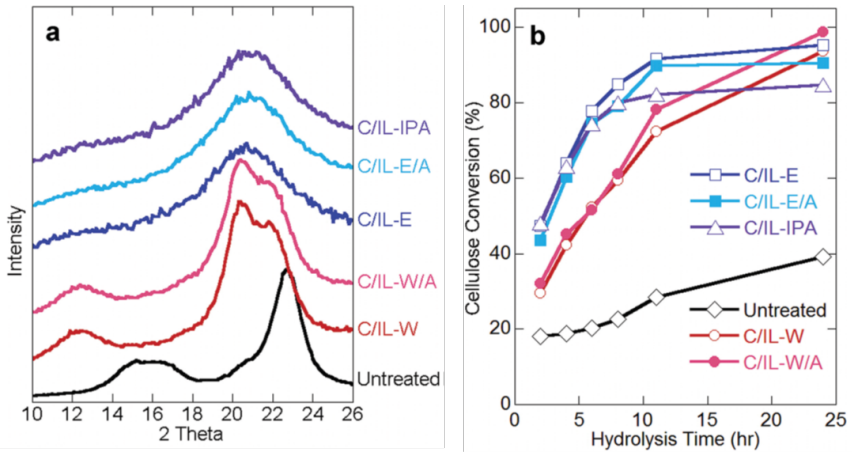

Figure 14: The effect of coagulating cellulose from a solution of MCC (5 wt%) dissolved in [EMIm][OAc] using water (W), water-acetone (W/A, 1/1, v/v), ethanol (E), isopropyl alcohol (IPA) and ethanol-acetone (E/A, 1/1, v/v) on the A: X-Ray diffraction patterns and B: enzymatic degradation (cellulase) of the coagulated polymer. Reproduced with permission from Geng *et al.*.[62]

produced porous beads.[95] Encapsulation of active compounds in the cellulose matrix was also demonstrated to be possible using a solvent release method in which beads were swelled in a solution containing the active compound, then dried locking-in the active contained inside the bead. The active was shown to be released over time.[99]

2.4 Cellulose Functionalisation

Cellulose can be functionalised via a vast array of reactions typical for conversion of hydroxy functionalities. Gericke *et al.* have tabulated a list of 60 functionalisation reactions with specific applications.[22] Each of the reactions listed were conducted as a heterogeneous modification of (predominantly) the surface of the cellulose bead, although some degree of internal functionalisation will occur. Homogenous reactions with cellulose in solution would run the risk of the hydrogen bonding network being permanently disrupted giving the material product sub-optimal mechanical strength, if it can be reformed at all. These functionalisations enable an array of specific applications for cellulose beads, especially in the field of chromatography and water purification in which specific

adsorption of targeted species, such as proteins[95] or metal compounds,[100] can be achieved.[22,25]

2.4.1 Cross-Linking

It is possible to improve the mechanical strength, reduce the swelling (depending on the size of the cross-linker) and shrinkage of the beads caused by solvent addition/removal, and prevent dissolution of cellulose by utilising cross-linking reactions with (at least) di-functional molecules.[22,83] Cross-linking of cellulose is conducted industrially as an anti-wrinkle treatment for cotton, usually via reaction with the dialdehyde glyoxal, or more traditionally, dimethylol dihydroxy ethylene urea (DMDHEU) (Figure 15). Over time DMDHEU has been shown to break down and release the carcinogen formaldehyde. Since the 1990s, researchers have endeavoured to investigate more benign "formaldehyde free" cellulose cross-linkers.[103] Glyoxal has been widely applied in the cotton industry and for other cellulose based materials in a research environment, due to its biodegradability and potentially renewable synthesis.[104,105] The dialdehyde has been shown to efficiently cross-link a wide range of cellulose films,[105] fabrics,[104] fibres[106] and beads.[107] The formed hemi-acetal/acetal cross-links cause an increase in the dry and wet strength of cellulose based materials.[104] Quero *et al.* showed that glyoxal cross-linking of bacterial cellulose produced no measurable change in the polymer crystalline structure, which suggested the reaction favourably took place in the amorphous regions.[105] This reduced swelling and increased embrittlement of the material. Other cross-linkers for cellulose, including acryloyl malic acid (AMA) and citric acid, have also been applied (Figure 15).[103,107]

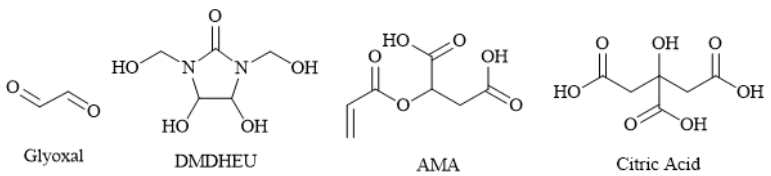

Figure 15: The structure of literature cellulose cross-linkers; glyoxal, dimethylol dihydroxy ethylene urea (DMDHEU), acryloyl malic acid (AMA) and citric acid.

2.5 Membrane Emulsification

Although there is an abundance of research into the formation, functionalisation and utilisation of cellulose beads from ILs, most of the emulsion forming techniques utilise bulk processes. The transition to a continuous system could be achieved with the use of membrane technology which provides the potential for a large scale, and importantly, controllable processes. Using a membrane to disperse one phase into another has numerous benefits including uniform droplet size, low spatial variation providing uniform shear stresses, low energy input, mild operational conditions, applicability at various scales and technological versatility that can be applied to a variety of systems and compositions, including oil-in-water (O/W), water-in-oil (W/O) and double emulsions (W/O/W, O/W/O).[108–110] Since its invention in 1988, membrane emulsification has grown in popularity industrially and academically reflected in the growth in the number of patents filed between 2003-2014 accounting for 66% of the total ever filed.[111]

It is possible to form an emulsion by directly injecting the disperse phase through a porous membrane into a stationary continuous phase, causing the formation of droplets of wide polydispersity, unless the disperse phase is a premixed emulsion, purely by interfacial forces.[96] However, it is more conventional to generate a wall shear force on the surface on the membrane to form more consistent droplet sizes. This shear can be formed by either moving the continuous phase or the membrane.[110] Examples include rotary systems, in which the membrane or the continuous phase is rotated, vibration systems or cross-flow membrane emulsification in which the shear force is generated by flowing the continuous phase perpendicular to the membrane surface (Figure 16).[96]

Cross-flow membrane emulsification remains the simplest and least laborious to operate. Shirasu Porous Glass (SPG) membranes are typically used since they are simple to functionalise to hydrophilic/phobic surfaces and have a low pore size distribution, however ceramic, polymeric and metal membranes have also been used in the literature.[112,113]

There are examples in the literature of the application of membrane

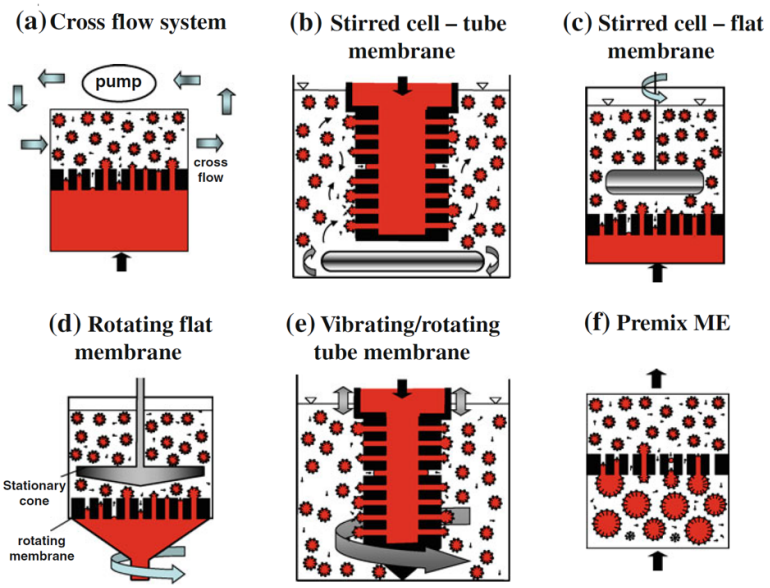

Figure 16: Reproduced diagrams of membrane emulsification techniques utilising different methods to generated shear on the membrane surface. Reproduced with permission from Vladisavljevic *et al.*[96]

emulsifications industrially including in the production of milk and margarine with many considering the technology to be in its exploratory and development phase.[111]

2.5.1 Particles from Membrane Emulsification

The use of membranes to produce emulsion droplets and particles is widely documented in the literature.[111,114,115] However, membranes have yet to be applied to the generation of cellulose beads, most likely due to the high viscosity of many cellulose solutions, although examples do exist for the generation of polysaccharide beads based on agarose.[116] There are a plethora of examples, however, for other particulates formed utilising membrane emulsification. It has been shown that silica microparticles can be formed from a disperse phase of acidified sodium silicate solution emulsified in a continuous phase of toluene stabilised by a PE-64 surfactant.[114] Polymeric microspheres have also been formed utilising membrane technology via a process called suspension polymerisation. This involved dispersing solutions containing a monomer,

initiator, and in some cases other additives such as cross-linkers or solvent, into a continuous phase containing a surfactant and an inhibitor preventing secondary nucleation of polymer particles in the continuous phase. The polymerisation was initiated by heating this suspension, leading to the formation of polymer microbeads.[117] Stirred cell-flat membrane (SCFM) emulsification has been shown to be an efficient process for the formation of polymer microbeads (Figure 17).[117] Utilising a ring style nickel membrane (10 μm) with wall shear generated by an impeller, solutions of methyl methacrylate (with the initiator lauryl peroxide) were emulsified into an aqueous continuous phase containing polyvinylalcohol as a stabiliser (Figure 17 A). The formed emulsion was passed into a reactor (75 °C) to initiator polymerisation (Figure 17 B).[117] There are many examples in the literature of the use of this and similar processes for the formation of polymer microbeads, the reader's attention is drawn to a review by Vladisavljevic containing an extensive list of examples.[114]

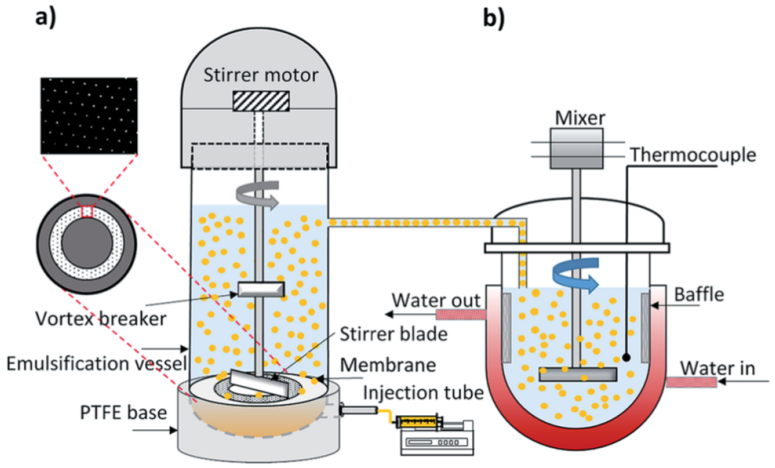

Figure 17: Reproduced diagram of A: a stirred membrane emulsification vessel utilising a nickel membrane, attached to a B: suspension polymerisation reactor. Reproduced with permission from Alroaithi *et al.*.[117]

Moving on from synthetic particles, there are also examples of the generation of chitosan,[115] agarose[118] and alginate microbeads.[110] The latter were form from aqueous Na-alginate solutions into an oil-Span 80 continuous phase. The droplets were cross-linked upon addition of $CaCl_2$ forming solid cross-linked alginate beads.[114] There are no examples in the literature however of the bridging of cellulose dissolution technology and membrane emulsification.

2.6 PhD Aims and Objectives

Aim

To investigate the processability of cellulose, solubilised in an ionic liquid solvent system, towards the production of sustainable cellulose bead-based materials utilising membrane emulsification and dropping processes.

Objectives

The main aim was split into specific objectives:

1. Investigate the applicability of cellulose-OES as a processing route for cellulose, specifically towards the formation of cellulose beads.
   (a) Probe the physical characteristics of the cellulose-OES solutions (rheology, interfacial tension, contact angle etc.) relevant to membrane emulsification.
   (b) Determine a suitable solvent system for the processing of cellulose.
2. Develop a suitably controllable process using membrane emulsification for the formation of cellulose microbeads in a robust, scalable and reproducible manner.
   (a) Design and build a system able to form cellulose microbeads using membrane emulsification.
   (b) Map the achievable range of cellulose microbead sizes and size distributions through adjustments to the processing parameters and emulsion phase compositions.
3. Adjust the mechanical strength and chemical functionality of the cellulose bead materials for specific application.
   (a) Adjust the mechanical strength of beads via differing levels of cross-linking in the cellulose matrix.

(b) Impart chemical and physical alterations to the bead chemistry and topography.

Chapter 3

Experimental Procedures

Experimental protocols for the three research chapters are detailed in this chapter. The accompanying theory for each research chapter is detailed at the start of each chapter.

3.1 Materials

Microcrystalline cellulose (MCC, Sigma-Aldrich, powder, 20 μm particle size) was azeotropically dried from *n*-butanol (Fisher Scientific, >99 % purity) on a rotary evaporator (50 °C) before use. Dimethylsulfoxide (Alfa Aesar, >99 % purity) and toluene (Sigma-Aldrich, anhydrous, 99.8 % purity) were dried using activated molecular sieves (3 Å). 1-Ethyl-3-methylimidazolium acetate ([EMIm][OAc], >95 % purity, BASF, Basionics, 0.5 % moisture content), sulfuric acid (95 % purity, VWR), ammonium polyphosphate (APP, MW = 97, Chemox Pound) and sunflower oil (SFO, Tesco) were used as received. Ethanol (absolute, >99.8 % purity), trichloro(octadecyl)silane (TOS, >90 % purity), trimethylchlorosilane (TMS, >99.0 %), sodium hydroxide (pellets, ground before use), acetic acid ($\geq$ 99%), citric acid monohydrate ($\geq$ 99%), cellulase (*Trichoderma reesei*, aqueous solution), glyoxal (40 wt.% in H_2O), glycolic acid (99 % purity), chitosan (low MW, MW = 26 kDa, degree of acetylation = 23 % - determined by Marcus Johns[119]), Rose Bengal (Dye-content

95 %), hydrochloric acid (37 %) and Span 80 were all used as received from Sigma-Aldrich.

3.2 Cellulose Dissolution

Two processes were exploited for the dissolution of cellulose (microcrystalline and α variants) in an [EMIm][OAc] and DMSO organic electrolyte solution (OES). Cellulose concentrations were presented as a wt% of the whole system (including solvents). From Chapter 5, section 5.3.2 onwards, prior to membrane emulsification cellulose-OES solutions (300 mL) were dyed with Rose Bengal ($\sim$ 10 mg) and mixed until homogeneously stained to aid in detection during emulsification.

Standard Dissolution Procedure: The required quantity of DMSO was added to dried cellulose and dispersed using an overhead stirrer (Heidolph RZR 2051, 900 rpm), with a PTFE stirrer head, for five minutes at room temperature. The required amount of [EMIm][OAc] was then added via a glass pipette during mixing, after which the vessel was covered with parafilm (making sure not to come in contact with the stirrer head) and allowed to mix for 1 h at room temperature. This resulted in full dissolution of the polymer giving a yellow/orange transparent solution. The stirrer head was removed, and the vessel sealed with a lid.

Extended Dissolution Procedure: DMSO was added, using a syringe via a septum, into a two necked round bottom flask containing a stirrer bar and the required amount of dried cellulose under an argon atmosphere (Schlenk line). The suspension was degassed (3 $\times$ exhaustion and Ar refilling cycles) and allowed to mix under argon for 5 minutes after which the appropriate amount of [EMIm][OAc] was added via a syringe and septum. The dispersion was placed in a silicon oil bath at 60 °C for 24 h with stirring.

3.3 Glass Hydrophobisation

Microscope slides were used to mimic a glass membrane and functionalised using either a literature process[113] or a refined process.

Literature Process:[113] The microscope slides were heated in hydrochloric acid (2 M, 70 °C, 2 h) and washed with distilled water. The slides were dried under vacuum (70 °C), placed in a Schlenk flask and covered with dry toluene (∼30 mL) followed by 3 × exhaustion and Ar filling cycles on a Schlenk line. Trichloro(octadecyl)silane (TOS) was added via a syringe and septum to form a 5 vol% solution. The flask was then sealed under Ar, placed in an oil bath and heated under reflux for 7 h, rendering the slides hydrophobic. The slides were washed in fresh toluene and dried under vacuum before being placed in a solution of trimethylchlorosilane (TMS, 1 vol%) for 2 h at room temperature. The hydrophobic slides were rinsed with toluene followed by the continuous phase and stored until required in excess of continuous phase.

Refined Process: The microscope slides were heated in hydrochloric acid (2 M, 70 °C, 2 h), washed with distilled water and dried under vacuum (80 °C) . They were then placed in a Schlenk flask and covered with dry toluene (30 mL), degassed and placed under Ar on a Schlenk line (3 × exhaustion and Ar filling cycles). TOS was added via a syringe and septum to form a 5 vol% solution. The flask was then sealed under Ar, placed in an oil bath and heated under reflux for 3 h. The slides were washed in fresh toluene, dried under vacuum and stored in excess of continuous phase.

Functionalisation Robustness Testing: The functionalised microscope slides where placed in an round bottom flask containing an excess of DMSO:[EMIm][OAc] (OES, 70:30, w/w) and heated with stirring to 80 °C for 42 h. The water contact angle was determined before and after addition to the OES.

3.4 Cellulose Bead Production

3.4.1 Membrane Emulsification

Two cross-flow membrane emulsification rigs were developed as part of this research. The Shirasu Porous Glass (SPG) membranes used in both were subject to the same hydrophobisation reaction as per the refined processes described in Chapter 3, section 3.3.

Membrane treatment

Tubular hydrophilic Shirasu Porous Glass membranes (SPG, 1 or 10 μm average pore diameter, length 12.5 cm, diameter 1.0 $\pm$5 cm, thickness 7.00 $\pm$3 mm) were purchased from SPG Technology Co., Ltd. The membranes were calcined at 500 °C (oxidative atmosphere, 5 °C min^{-1}) for 2 h followed by heating in hydrochloric acid (2 M, 70 °C, 2 h), washed with distilled water and dried under vacuum (80 °C). The membranes were then hydrophobised as per the refined process described in Chapter 3 section 3.3 and stored in the continuous phase until required.

First Generation Rig Operation

Start Up: A hydrophobised SPG membrane was placed into the membrane module which was sealed at both ends. The disperse phase was introduced via a 50 mL syringe through disperse phase valve 3 (V-Dis 3) ensuring valve 1 and 4 (V-Dis 1 and 4) were close and valve 2 open (V-Dis 2). Once the required volume of disperse phase had been loaded V,-Dis 3 and 2 were closed. The continuous phase was placed into the collection vessel (2 L crystallising dish). V-Dis 4 and 5 were opened and the disperse phase allowed to fill the membrane module using a low pressure from the air cylinder (set by Reg – 2, Reg – 1 set at 1.5 bar) by opening V-Dis 1 and controlling the flow rate of liquid with V-Dis 4 until the disperse phase was seen to briefly expel from V-Dis 5. V-Dis 4 was then closed, followed by V-Dis 5 and V-Dis 1. The pump was turned on to a low flow rate

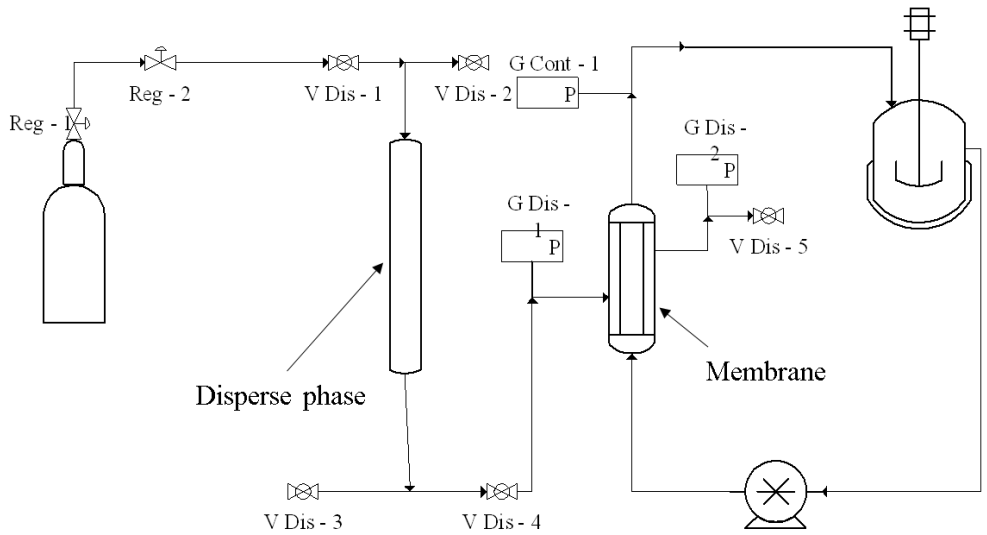

Figure 18: Schematic for the first generation cross-flow membrane emulsification apparatus developed. *V*: valve, *G*: Gauge and *Reg*: Regulator for the *Disp*: Disperse or *Cont*: Continuous phase

filling the rig with the continuous phase. The pump was turned off once the system was seen to be filled (with no air bubbles).

Formation of Emulsion: The appropriate disperse phase pressure was set at Reg-2 and V-Dis 1 opened (V-Dis 2, 3, 4 and 5 remained closed). Concurrently, the pump flow rate was increased and V-Dis 4 opened (V-Dis 5 remained closed) at a rate in which the pressure of the continuous and disperse phases (measured at G-Cont - 1, G-Disp) remained the same. If need be, the pressure was adjusted at Reg-2 to prevent permeation of the disperse phase, or back flow of the continuous phase, through the membrane. Once the required continuous phase flow rate was met (0.4, 1.4, 1.9 or 2.4 Lmin^{-1}) the disperse phase pressure was increased (measured at G-Disp-2 and controlled at Reg-2) to the required operational transmembrane pressure (P_{tm}). The level of permeation of the cellulose-OES disperse phase through the membrane was observed via the reduction in its volume, visible through the disperse phase tubing (between V-Dis 4 and 1), and the increase in turbidity of the circulating continuous phase due to the formation of an emulsion.

Removal of Emulsion/Coagulation of Cellulose: Once the required volume of disperse phase had permeated the membrane, V-Dis 4 was closed and

the flow rate of the pump reduced until off. V-Dis 5 was briefly opened to removed residual pressure. The tube exiting the collection vessel, flowing towards the pump, was placed in beaker of fresh continuous phase (1 L) and the flow rate of the pump increased slightly to remove any emulsion contained within the system into the collection vessel. Ethanol (300 mL) was then poured into the collection vessel, coagulating the cellulose from the emulsion droplets. The coagulated cellulose beads were then extracted by suction filtration (0.2 μm, nylon 66 filter paper) and washed (3 aliquots of 20 mL ethanol once microbeads were separated from continuous phase). The extracted beads were then placed in a Soxhlet thimble and extracted using ethanol (>12 h).

Second Generation Rig Operation

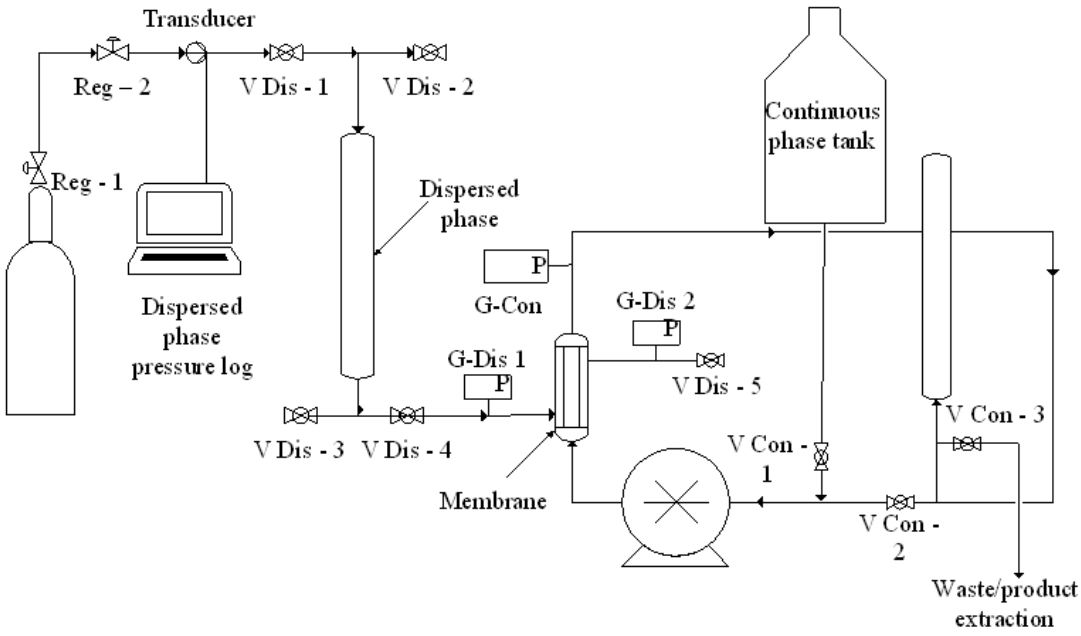

Figure 19: Schematic for the second generation cross-flow membrane emulsification apparatus developed.

Start Up: A hydrophobised SPG membrane was loaded into the membrane module followed by addition of the disperse phase through disperse phase valve 3 (V-Dis 3) ensuring valve 1 and 4 (V-Dis 1 and 4) were closed and valve 2 open (V-Dis 2). Once the required volume of disperse phase had been loaded V-Dis

3 and 2 was closed. The continuous phase was loaded into its tank (V-Con 1 closed). V-Dis 4 and 5 were opened and the disperse phase allowed to fill the membrane module using a low pressure from the air cylinder (set by Reg – 2, Reg – 1 set at 1.5 bar) by opening V-Dis 1 and controlling the flow rate of liquid with V-Dis 4 until the disperse phase was seen to briefly expel from V-Dis 5. V-Dis 4 was then closed, followed by V-Dis 5 and 1. V-Con 1 was then opened (V-Con 2 and 3 remained closed) enabling the continuous phase to fill the rest of the apparatus. The waste/product pipe was then placed in a waste container of appropriate size and the pump turned on to a low flow rate (V-Con 3 opened to waste). The pump was turned off and V-Con 1 closed once all air was seen to have been removed from the tubing. V-Con 2 was opened, V-Con 3 closed, and the pump turned on to a low flow rate.

Formation of Emulsion: The appropriate disperse phase pressure was set at Reg-2 (measured by the transducer) and V-Dis 1 opened (V-Dis 4 remained closed). Concurrently, the pump flow rate was increased and V-Dis 4 opened (V-Dis 5 remained closed) at a rate in which the pressure of the continuous and disperse phases (measured at G-Con, G-Disp) remained the same. If need be, the pressure was adjusted at Reg-2 to prevent permeation of the disperse phase or back flow of the continuous phase through the membrane. Once the required continuous phase flow rate was met (0.4, 1.4, 1.9 or 2.4 Lmin^{-1}) the disperse phase pressure was increased (measured at G-Disp and controlled at Reg-2) to a transmembrane pressure (P_{tm}) above the critical pressure (P_c). The level of permeation of the dyed disperse phase through the membrane was observed via the reduction in its volume visible through the disperse phase tubing (between V-Dis 4 and 1) and the increase in turbidity of the circulating continuous phase due to the formation of an emulsion.

Removal of Emulsion/Coagulation of Cellulose: Once the required volume of disperse phase had permeated the membrane, the product tube (connected to V-Con 3) was placed below the meniscus of ethanol (300 mL) contained in a measuring cylinder (1 L). V-Con 3 was then opened followed by V-Con 1 which increased the volume of continuous phase in the system, driving the emulsion up into the collection vessel and out into the measuring cylinder. Once the emulsion was seen to have been removed (300 mL of emulsion containing

continuous phase) V-Con 1 was closed followed by V-Con 3. The coagulated cellulose beads contained in the measuring cylinder where then extracted by suction filtration (0.2 μm, nylon 66 filter paper) and washed (3 aliquots of 20 mL ethanol once microbeads were separated from continuous phase). The extracted beads were then placed in a Soxhlet thimble and extracted using ethanol (>12 h).

If required, the beads were dried on a rotary evaporator (50 °C) after being dispersed with minimal ethanol in an round bottom flask.

Emulsion Recirculation Experiment: To test if emulsion breakup was occurring during production, a emulsion was formed, as per the "start-up" and "formation of emulsion" procedures listed above, using a continuous phase flow rate of 1.9 Lmin^{-1}, transmembrane pressure of 0.01 bar, disperse phase of 8 wt% MCC-OES into a continuous phase of sunflower oil with 2 wt% Span 80. In all cases, start-up was removed prior to forming the emulsion. The disperse phase was allowed to permeate the membrane over a 20 minute period, after which the transmembrane pressure was reduced to zero and the emulsion allowed to circulate for 10, 30, 45 mins or 1 h. After that period, the emulsion was extracted as per the emulsion removal step.

3.4.2 Dropping Process

Millimetre-sized cellulose beads were formed from two different scale dropping processes.

Single Head

Cellulose-OES (4 or 8 wt% MCC), as prepared for emulsification, were continuously extruded (syringe pump), from a 50 mL syringe at a flow rate of 50 μLmin^{-1}, as droplets via a stainless steel needle (21 gauge, length = 12 cm) into an ethanol bath (500 mL) (7 cm between the needle tip and meniscus of ethanol) with mild stirring. Residual OES was removed by Soxhlet extraction with ethanol overnight (>12 h). The average diameter of the formed beads was determined

using a J500 extreme USB microscope (1 mm graticule, ImageJ software – 3 measurements per bead, 10 beads per image, 3 images).

Mutilhead

The dropping process was scaled up using a peristaltic pump (dosing 1 mL every 9.9 secs) used to push a solution of cellulose-OES (8 wt% MCC, 1.8 L) through 9 × 8-channel manifolds (BRAND, Sigma Aldrich) placed between 7-12 cm from the surface of a 2.5 L tank of ethanol on a rocker. The pump was initially primed with the dropping phase before setting it to dose sufficiently to promote droplet formation from the tips, over jetting. The formed beads were removed from the solvent bath and placed in a Soxhlet (1 L) and extracted using ethanol (24 h).

3.5 Cellulose Bead Post-Formation Treatment

3.5.1 Glyoxal Cross-linking

Cellulose beads, swollen in water, were suspended in aqueous solutions of glyoxal (up to 40 wt%) with agitation (stirring or rocking) for 3 h (25 °C). The beads were briefly blotted with filter paper or washed with deionised water to remove excess cross-linking solution. The cross-linking was effected at 160 °C (Buchi glass oven - B-580 or a Vacutherm oven for larger quantities) for 1 h.

High-Performance Liquid Chromatography Cross-linker Quantification

The extent of cross-linking was determined by HPLC analysis following a method adapted from Schramm *et al.*[104] Cross-linked cellulose bead samples (<0.2 g) were exposed to 4 M NaOH (40 mL, 90 °C, 30 mins) to expel the cross-linker agent as glycolate (Figure 78) via an internal Cannizarro reaction (Figure 20) with a yellow solution resulting (Figure S7). The extraction solution and washes (10 mL deionised water) were combined and filtered through a

PTFE syringe filter (0.2 μm). The concentration of glycolic acid, formed by acidification of glycolate in the mobile phase (0.01 M H_2SO_4, 50 °C), in each solution was determined by HPLC analysis: Aminex Organic Acid Analysis Column (HPX-87H, 300 mm × 7.8 mm, 50 °C), mobile phase 0.01 M H_2SO_4 (0.6 $mLmin^{-1}$) and UV detector $\lambda = 210$ nm, by comparison of triplicates to an appropriate calibration curve of glycolic acid at concentrations of 20, 50, 120, 480, 990, 5020, 10085 and 30100 mg/L (Figure S9).

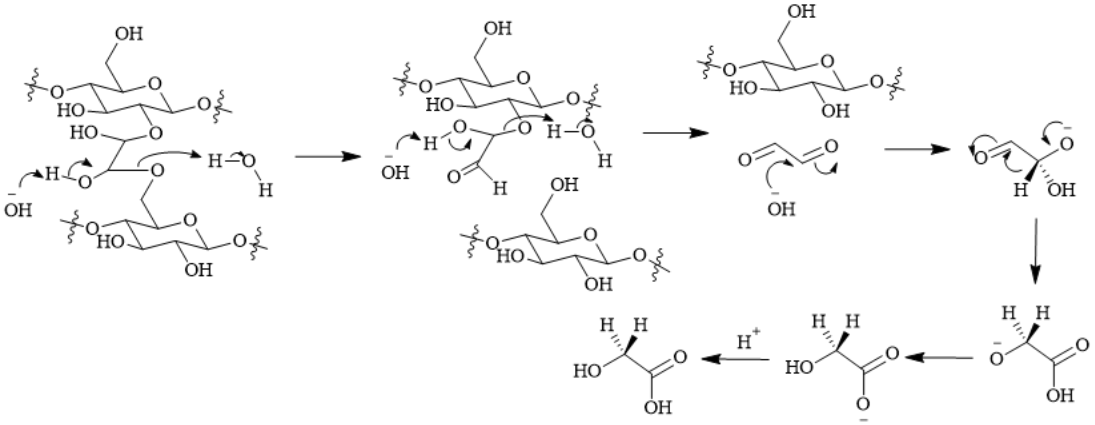

Figure 20: The mechanism for glycolic acid formation from cellulose cross-linked via reaction with glyoxal. The expelled glyoxal reacts with base via an internal Cannizzaro reaction forming a glycolate anion that is protonated in excess 0.01 M H_2SO_4 mobile phase during HPLC analysis.[104]

3.5.2 Reaction with Trichloro(octadecyl)silane

Dried cellulose beads (0.2059 g), formed from the small scale dropping process described earlier in the chapter (section 3.4.2), were stirred in dried toluene (20 mL) under nitrogen. Trichloro(octadecyl)silane (TOS, 1.18 g) was added by a syringe via a septum and the dispersion stirrer at room temperature for 1 h. The beads were washed in fresh toluene followed by ethanol and dried under vacuum (80 °C). The silicon content of the beads was determined by heating under air to 900 °C (10 °C/min) producing SiO_2.

3.5.3 Enzymatic Treatment

Stock 0.05 M citric acid buffer solution was formed from citric acid monohydrate (210 g) and NaOH (pellets ground with a pestle and mortar to a fine powder 50 - 60 g, to gain pH 4.3) made up to 1000 mL with distilled water. Dried cellulose beads (5 g, cross-linked and/or non-cross-linked variants) formed from the small scale dropping process described in Chapter 5 section 3.4.2, were placed in a 30 mL vial along with citrate buffer (9.5 mL, 0.05 M) and cellulase enzyme solution (aqueous, 0.5 mL) and heated in a water bath at 50 °C for 1 h. The beads were removed from the solution, briefly washed with deionised water and dried under vacuum (80 °C).

3.5.4 Acid Treatment

Cross-linked cellulose beads (20 mg) were added to aqueous solutions of 1, 2.5 and 4 M HCl and H_2SO_4 (5 mL) and placed in a 65 °C oil bath for 10, 35 or 60 mins with stirring. The beads were removed from the aqueous acid and placed in fresh deionised water (2 × 7 mL) and dried under vacuum (80 °C).

3.6 Chitosan Coated Beads

Low MW chitosan (2 wt%, 54.94 g, MW = 26 kDa) was dispersed in water (2626.78 g) followed by addition of acetic acid (67.01 g, 0.43 M in final solution). Dissolution took place at room temperature using an overhead stirrer (800 rpm) overnight. The resulting viscous solution was diluted with deionised water resulting in 0.24 M acetic acid and 1.2 wt% chitosan. This solution was used in place of ethanol in an anti-solvent bath for the formation of cellulose beads using the multihead dropping process described earlier in section 3.4.2. The formed beads were filtered through a sintered funnel (pore 3), washed with deionised water to remove excess acid from the surface, and extracted via Soxhlet (ethanol, overnight). The formed beads were cross-linked using glyoxal via the process described in section 3.5.1.

3.7 Cellulose - Ammonium Polyphosphate Composite Beads

Ammonium polyphosphate (APP) was dispersed in DMSO alongside MCC and subject to the general dissolution procedure described in Chapter 3 section 3.2 at an overhead stirrer speed of 1200 rpm. The concentration of APP in the disperse phase was calculated as 5, 10 or 15 wt% of the filler in the final bead samples (after removal of the solvent system) and were labelled low, mid and high concentration. To test the removal of larger APP particles from the dispersion, an aliquot of the most concentrated dispersion was centrifuged (Eppendorf Centrifuge Model 5702) at 3000 rpm for 3 mins. The four formed dispersions (low, mid, high and centrifuged) were subject to the Single Head dropping process described previously in section 3.4.2. The centrifuged sample was also subject to membrane emulsification according to the Second Generation Procedure documented in section 3.4.1 under the following conditions: continuous phase flow rate = 1.4 $Lmin^{-1}$, transmembrane pressure = 0.03 bar, continuous phase composition = 2 wt% Span 80 in SFO.

3.8 Material Analysis

3.8.1 Karl Fischer Titration

The water content of materials was determined using Coulometric Karl Fischer titration (Equation 1 and 2) (Mettler DL37 KF Coulometer, HYDRANAL Coulomat AG and CG - methanol based, Sigma Aldrich) from an average of five runs per sample. Water contents were determined as a parts-per-million value and converted to a wt% of the tested sample.

$$CH_3OH + SO_2 + RN \rightleftharpoons [RNH]SO_3CH_3 \quad (1)$$

$$[\mathrm{RNH}]\mathrm{SO_3CH_3} + \mathrm{I_2} + \mathrm{H_2O} + 2\,\mathrm{RN} \rightleftharpoons [\mathrm{RNH}]\mathrm{SO_4CH_3} + 2\,[\mathrm{RNH}]\mathrm{I} \qquad (2)$$

3.8.2 Pycnometry

Density values of the cellulose-OES disperse and SFO-continuous phases were measured using a standard pycnometry procedure using 10 mL pycnometer bottles with triplicate measurements (temperature fluctuations <2 % in all cases).

3.8.3 Rheometry

Two cone and plate rheometers were used to evaluate the viscosity of solutions. The first (Bohlin High Resolution C-VOR Torque Rebalance connected to a Haake GH-D8 Fusion temperature controller, CP4 ° 40 mm cone, 150 µm gap) was used to collect the data in Chapter 4, section 4.3 using an ascending shear rate sweep of 30 points between 0.07-200 s^{-1}. An average viscosity in the Newtonian range was taken.

The second rheometer (Brookfield DV-III-HA ULTRA Programmable Rheometer, using a CP-52 spindle and a Brookfield TC-650 temperature controller) was used to assess the viscosity of the three cellulose solutions of varying MCC concentration (4, 6 and 8 wt%) dissolved in a 70:30 DMSO:[EMIm][OAc] OES documented in Chapter 4, section 4.3.3, Figure 33 and in the same section the viscosity of sunflower oil-Span 80 continuous phases (0, 0.25, 1.13 and 2.00 wt% Span 80)(Figure 34). Each sample was analysed at 30, 45 and 60 °C and exposed to an ascending and descending shear rate sweep of 30 readings between 0.08 - 200 s^{-1} (60 in total). An average viscosity in the Newtonian range was taken.

3.8.4 Determination of Interfacial Tension

Interfacial tension measurements were conducted on an OCA 15EC video-based measuring system using a pendant drop method with the camera rotated by 90°. A stable droplet of cellulose-OES (as large as possible) was suspended from a needle (18 gauge, length = 1.5 inch,) into a transparent cuvette containing the continuous phase. An average value was determined from 10 droplets per sample with an error between repeats of <3 %.

3.8.5 Contact Angle Measurements

Contact angle measurements were taken using an OCA 15EC video-based measuring system. A droplet (5 µL) of cellulose-OES (with varying concentrations of cellulose) was placed on a hydrophobised glass microscope slide (hydrophobised as per the refined process, section 3.3) suspended in the continuous phase (sunflower oil – with varying concentrations of Span 80). An average value was determined from 10 readings at different locations and on each side of the glass (errors <3 ° in all cases).

3.8.6 Particle Size Determination

Two different laser scattering instruments were utilised to measure particle size histograms of the formed cellulose microbeads.

Mastersizer X

Volume weighted distributions of the cellulose beads suspended in deionised water were obtained using a Malvern Mastersizer X (Mastersizer X software v 2.19) with a 300 mm lens capable of detecting particles in the range of 1.2-600 μm. A Small Volume Dispersion Unit (1800 rpm, Dispersion Unit Controller, water) was used to cycle the bead system. Each sample was exposed to 2000 sweeps for each experiment with a total of 5 experiments for each run and a total

of 3 runs per sample, replacing the sample after each run. All data collected in Chapter 5, excluding Section 5.3.3, was done using this process.

Matersizer 3000

The particle size distributions obtained in Section 5.3.3 were gained using a Malvern Mastersizer 3000 (He-Ne laser, 0.01-3500 μm detection range, small volume dispersion unit, 2000 rpm in water). The particle size distributions were presented as a average of 3 analysis runs of fresh sample (5 experiments per run).

Extend Period size analysis: A Mastersizer 3000 was automated to measure a particle size distribution every 80 secs for 117 mins followed by every hour for 62 h. Cellulose microbeads were prepared (membrane emulsification - 10 μm pore, continuous phase flow rate: 2.4 $Lmin^{-1}$, transmembrane pressure, continuous phase: 2 wt% Span-80 in SFO) from a disperse phase of 8 wt% cellulose OES, extracted using a Soxhlet (ethanol) and dried (rotary evaporator, 50 °C, from ethanol) before being dispersed in water through the Mastersizer 3000 using the dispersion unit. Measurements were taken at set intervals whilst the sample was continuously circulated through the instrument (2000 rpm).

3.8.7 Microscopy

Optical Microscopy

An EVOS AMG (AMF 4300) optical microscope was used to image each bead system at ×4, ×10, ×20, ×40 and ×60 magnifications. The solutions were first agitated within the sample bottle and then, using a pipette, an aliquot removed and spread thinly on a microscope slide for viewing. Colour images were taken using the same process using a Brunel Microscope (Ltd).

Scanning Electron Microscopy

Scanning electron micrographs were obtained on a JEOL SEM648OLV Scanning Electron Microscope. Prior to imaging, samples were dried (80 °C, vacuum) and if a cross section was required, flash frozen in liquid nitrogen and ruptured in a pestle and mortar to generate cleaved samples. Samples were gold coated (Edwards Sputter Coater - S150B, 4 mins) prior to imaging.

Energy Dispersive X-Ray Spectroscopy

Energy Dispersive X-Ray Analysis (EDX, Oxford, INCA X-Act SDD X-ray detector) was used to determine elemental composition of samples using a line scan along a cross section of sample and quantification mapping to determine elemental build up in the sample.

3.8.8 Nuclear Magnetic Resonance

All ^{1}H Nuclear Magnetic Resonance (NMR, 400 MHz, Bruker Avance III, 298 K) were run under the same conditions using $CDCl_3$ as a solvent.

3.8.9 Compression Analysis

Mechanical characterisation of the cross-linked samples was conducted using an Instron 3369 at a compressive extension of 0.1 mm/min using a 100 N load cell for non-cross-linked and composite samples and a 1 kN load cell for all cross-linked samples.

3.8.10 Thermogravimetric Analysis

Thermogravimetric analysis (TGA, Setaram Setsys Evolution) was conducted on samples up to a maximum temperature of 400, 800 or 900 °C (held at max temperature for 1 h) at a ramp rate of either 5 or 10 °C/min under

air or argon (20 mLmin^{-1}) (specific experimental conditions are presented in the text with the relevant data). Unless otherwise stated, all samples underwent a drying process within the instrument (heating to 100 °C, held for 1 h) prior to cooling and further analysis.

3.9 Data Analysis

3.9.1 Deconvolution of Particle size data

Multimodal particle size distributions were deconvoluted by fitting of Gaussian distributions to the separate populations using the following equation:

$$y = A \times exp\left(-0.5\left(\frac{\frac{x}{\mu}}{\sigma}\right)^2 \right) \tag{3}$$

In which A = amplitude of the distribution, μ = the mean diameter of the distribution and σ = the width of the peak (standard deviation). Each of these values were varied to best represent the original data (Figure 21 A, B).

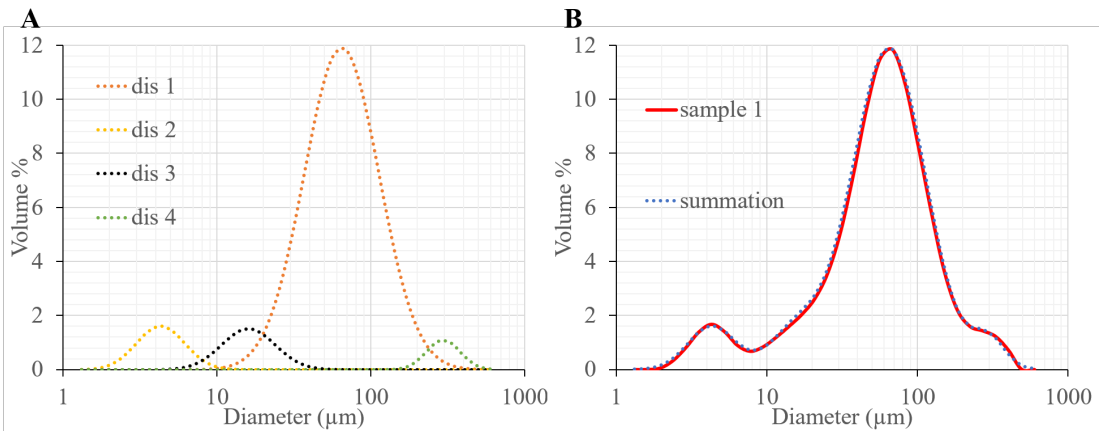

Figure 21: A: Deconvoluted particle size distributions and B: an overlay of the summed deconvoluted data (dotted distribution) and original measured distribution (solid distribution).

Each deconvoluted distribution contained three to four distributions in the final summation. Diameters and distributions of the dominant microbead population (Figure 21 A Dis 1) were compared using the values of the mode, or $D_{peakmax}$ (the diameter at peak maximum for the dominant peak, comparable to D(v, 0.5) for the fitted distribution) and full width at half maximum ($fwhm$) of the data as collected.

3.9.2 Techno-Economic Analysis

The material cost of producing cellulose beads via the multihead dropping process detailed in section 3.4.2, was assessed. The following prices were used to determine overall materials cost per gram of product produced (Table 1):

Table 1: The price and supplier of the raw materials used to determine costs for the formation of cellulose beads from a multihead dropping process.

Materials	Bulk Cost (GBP)	Quantity	Price per gram (GBP)	Supplier
MCC	108.00	1 kg	0.11	Sigma Aldrich
DMSO	59.40	2.5 L	0.02	VWR
[EMIm][OAc]	2963.10	10 kg	0.30	Iolitec
Ethanol	180.61	2.5 L	0.09	VWR

Material cost calculations were based on processing 2 kg of cellulose-OES solution consisting of 8 wt% MCC dissolved in a solvent system of 70:30 (w/w) DMSO:[EMIm][OAc] into a 2.5 L ethanol anti-solvent bath. The formed beads were extracted via Soxhlet using 2 L of ethanol. It was assumed that no transfer loss had occurred before the recycling process was conducted (Figure 76). After the first distillation step, it was assumed that 0.5 % of the total mass of [EMIm][OAc] was lost due to transfer loss and 0.5 % of the mass of DMSO distilled alongside ethanol. During the second distillation is was again assumed that 0.5 % of mass of [EMIm][OAc] was lost, which is in agreement with other IL based recycling processes.[42,76] Quantification of each component before and after separation was calculated from NMR data detailed in the appendix (Figure S4 - S6).

Chapter 4

The Physical Properties of Cellulose Solutions

4.1 Introduction

The IL [EMIm][OAc] was selected as a solvent for cellulose coupled with DMSO as a co-solvent. This widely applied pairing has been well researched and used as a robust dissolution medium for cellulose.[56,76,78,120] Rinaldi appropriately described these and similar solvent pairings as organic electrolyte solutions (OES), this terminology will also be applied here.[56] Use of an OES system based on [EMIm][OAc] and DMSO enables the formation of reasonably high concentration cellulose solutions under mild conditions, whilst minimising the concentration of expensive [EMIm][OAc] by coupling it with a co-solvent.

Preliminary experiments were used to define and build a design of experiments (DoE) for each section and used to develop the experimental processes described in subsequent sections. The DoEs developed were used to investigate the following physical properties:

- The rheology of cellulose-[EMIm][OAc]-DMSO solutions (OES).
- The interfacial tension between a cellulose-OES droplet and a sunflower oil based continuous phase (applicable to emulsion processes).

- The three way contact angle between cellulose-OES solution, a sunflower oil continuous phase and the membrane surface (specifically geared towards membrane emulsification processes).

The fundamental findings arising from the DoEs were used as a foundation upon which to develop emulsification and dropping based production routes for the formation of cellulose beads (Chapter 5). The following chapter describes how the physical properties of the disperse phases changed when varying the composition of cellulose-[EMIm][OAc]-DMSO solutions and, specific to membrane emulsification, how the interaction of cellulose solutions with a membrane surface and the continuous phase alter.

4.2 Underpinning Theory and Concepts

4.2.1 Experimental Design

Experimental design was applied throughout this research as an efficient use of experimentation to maximise output. This statistical approach to experimentation enabled a wider coverage of the experimental space, compared with a traditional one variable at a time (OVAT) approach (Figure 22 A), and in fewer experiments.

One Variable at a Time vs Design of Experiments

For a two factor OVAT experiment, one factor would be varied until a local maximum was found, followed by the second factor to arrive at a "maximum" for that space (Figure 22 A). Unless a vast number of experiments are conducted, this approach will lead to a limited coverage of the experimental space, often missing the true maximum and misunderstanding the system. Experimental Design/Design of experiments (DoE) enables the investigation of numerous factors in a limited number of experiments, covering a wider "design space" (Figure 22 B). This method also probes interactions between factors. In the case

of this thesis, MODDE (Umetrics, software version 11) was utilised to generate designs and fit models to the obtained data.

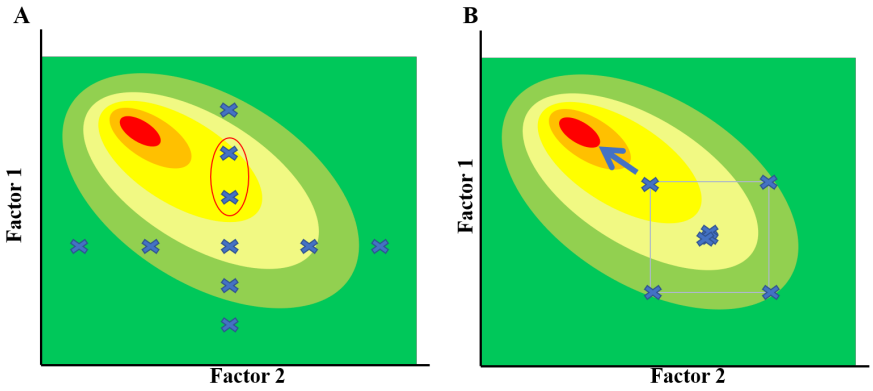

Figure 22: Graphs representing the difference between A: One Variable at a Time (OVAT) and B: Design of Experiments (DoE) approach to experimentation.

Screening

Screening experiments are often used to initially map the design space determining which factors are influencing the measured output and whether the ranges chosen are relevant. Each factor is assigned a high and low value as well as three mid point replicate experiments to determine the experimental reproducibility/error. Using a full factorial design, the number of experiments can be calculated from the number of factors (n) chosen plus the three replicate mid points (Equation 4):

$$no.of experiments = 2^n + 3 \tag{4}$$

A typical two level (high and low) design using two factors would therefore appear as (Table 2):

Table 2: Example of the experiments needed for a two factor, level 2, full factorial experimental design.

Experiment number	Factor 1	Factor 2
1	high	high
2	low	low
3	high	low
4	low	high
5	mid	mid
6	mid	mid
7	mid	mid

Fractional Factorial Designs

When a greater number of factors are to be investigated, a full factorial design may not be the most efficient approach, due to the large number of experiments required. A useful tool for screening lots of factors is a fractional factorial design in which some experiments are omitted (Figure 23 B, Equation 5) whilst, in most cases, still producing a valid model, albeit of lower resolution (depending on the number of omitted experiments).[121]

$$no.of experiments = 2^{n-1} + 3 \tag{5}$$

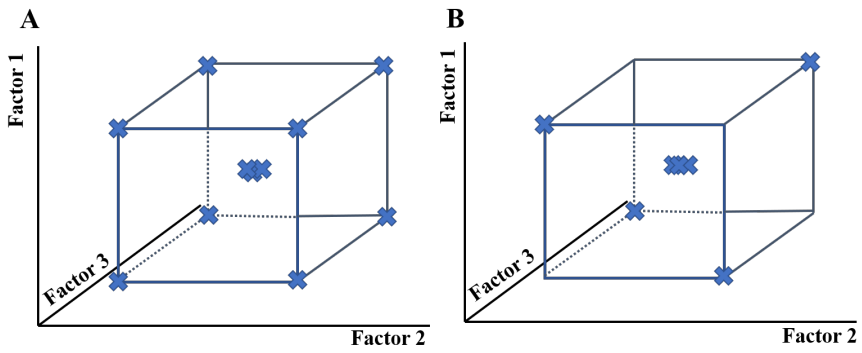

Figure 23: Graphs representing the difference between A: a full factorial and B: fractional factorial design of experiments.

Fitting a Model

Modelling of the measured data via regression analysis is employed to determine a response (y) via the summation of the input variables (x^i) multiplied by the relevant linear dependence factor (b^i) plus the error in experimentation (e) and midpoint response (b^0). For example, for a three factor system (Equation 6):

$$y = b^0 + b^1x^1 + b^2x^2 + b^3x^3 + e \tag{6}$$

Interaction terms can also be input if the resolution of the model is high enough (resolution IV or higher) - $b^{1,2}x^{1,2}$, which represents an interaction between factor 1 and 2.

Model refinement is conducted by observing the regression analysis terms to determine whether the removal of a factor is required. Four parameters can be used to judge this:[122]

- R^2 - the "goodness of fit", which measures how well the regression model can fit the raw data (<1);
- Q^2 - the "goodness of prediction", which represents how well the model predicts new experiments (>0.5 is a good model and should not differ from R^2 by more than 0.3);
- Model Validity - expresses how relevant the chosen model is for the data obtained (<0.25 requires change to the model); and
- Reproducibility - represents the variation in replicates (mid points) compared to overall variability.

In some cases, the model validity can be displayed as a negative value when a high Q^2 and/or limited variation between replicates is obtained. This is a function of the software and is openly noted in the program (MODDE). Model refinement takes place by viewing the regression coefficients plot and removing factors and

interaction terms from the model that have confidence intervals passing through 0, meaning they have no discernible impact on the system. As an example, Figure 24 shows the refinement of the model used to investigate the average diameter of cellulose beads document in Chapter 5 Section 5.3.1.

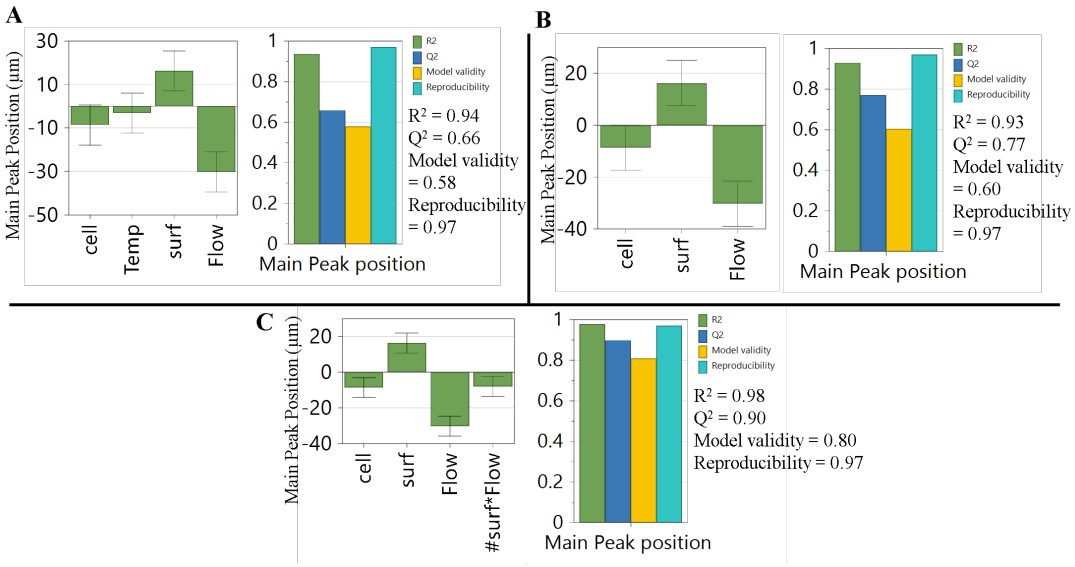

Figure 24: Graphs representing the refinement of a fractional factorial resolution IV design (Chapter 5, section 5.3.1). A: the model with no refinement, B: the effect of removing temperature as a factor and C: introducing the interaction term between surfactant concentration and continuous phase flow rate - surf*Flow). Note the increase in R^2 and Q^2 during refinement.

With no refinement, the separation between R^2 and Q^2 was quite high (0.28) and the confidence interval for temperature (Temp) passed through 0, meaning it is not significant (Figure 24 A). Removing temperature as a factor reduced the difference between R^2 and Q^2 (0.16) producing a more relevant model. The model produced by this stage of the refinement was adequate for further analysis, but, upon investigating potential interaction terms, an interaction between surfactant concentration and continuous phase flow rate (surf*Flow) was found (Figure 24 C). Inclusion of this factor increased the model validity and Q^2 producing an even more relevant model, which better described the measured data.

4.2.2 Interfacial Tension

Tension at an interface is formed due to a difference in energy between molecules located at an interface compared with those of the bulk.[123] In the case of this thesis, the interfacial tension between a deformed cellulose-OES droplet in a SFO-based continuous phase was determined using a pendant drop method. A pendant droplet abides by the Young-Laplace equation (Equation 7) which relates the pressure across an interface with the interfacial tension and the curvature at the interface in balance with the gravitational pull.[123,124]

$$\gamma\left(\frac{1}{R_1}+\frac{1}{R_2}\right)=\Delta P+\rho g z \tag{7}$$

Where R_1 and R_2 are the radii of curvature, γ the interfacial tension, ρ the difference in density between the droplet and continuous phase, g the gravitational constant, z the vertical distance between the droplet and a reference point and ΔP the difference in pressure between the droplet and its surroundings ($P_{in} - P_{out}$). Image analysis of the pendant drop can provide values for R_1, R_2 and z from which γ can be established if the density of each phase is known.[124,125] The theory pertaining to emulsification, which is related to this section, will be discussed in Chapter 5 section 5.2.

4.2.3 Rheology

Rheology can be defined as "the study of the deformation of matter resulting from the application of force".[126] It was applied in this research to investigate how solutions flowed, the understanding of which was vital to processing of cellulose-OES.

When a tangential stress (shear stress σ), defined as the force divided by the area over which it is applied (Equation 8), is applied to a material, that material deforms by a certain distance, defined as the shear strain (Equation 9, γ) or deformation per unit length (Figure 25).[126]

$$\sigma = \frac{F}{A} \tag{8}$$

$$\gamma = \frac{\Delta x}{h} \tag{9}$$

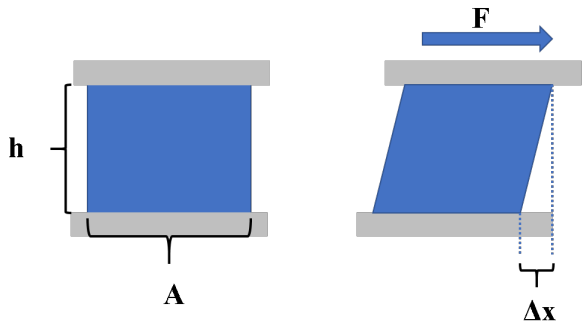

Figure 25: The definition of shear stress and shear strain calculated from the height (h) and area (A) of the material, the tangential force applied (F) and deformation distance (Δ x).

In terms of rheology, it is more conventional to use shear rate/strain rate ($\dot{\gamma}$), which is constant with time, instead of strain, which varies as the experiment progresses.[124] If the σ of a liquid scales linearly with strain, said liquid can be considered Newtonian, with the proportionality constant between the two being defined as the viscosity (μ) (Equation 10).

$$\sigma = \mu\dot{\gamma} \tag{10}$$

A Newtonian liquid could also be described as one in which μ remains constant with increasing shear rate ($\dot{\gamma}$). If the viscosity increases with increasing $\dot{\gamma}$, then it is deemed as a shear thickening fluid, if it decreases, a shear thinning fluid.

Rheology of Polymer Solutions

The rheology of solubilised polymer systems is inherently linked with the properties of the polymer. The degree of polymerisation (DP), the level of branching and interactions between chains defines how polymers arrange in solution and therefore how the bulk solution reacts to, and resists, shear. Generally, the viscosity of a solution will increase as the number and size of solute molecules increase. Polymeric solutions are typically shear thinning, decreasing in viscosity with increased shear, as secondary bonding between chains begins to break, untangling the polymers, reducing the overall viscosity of the solution.[86] A plateau in the viscosity is reached once chains are untangled at which point the viscosity no longer drops with increased shear. The level of entanglement scales with DP and concentration, with four concentration regimes typically specified in the literature (Figure 26).

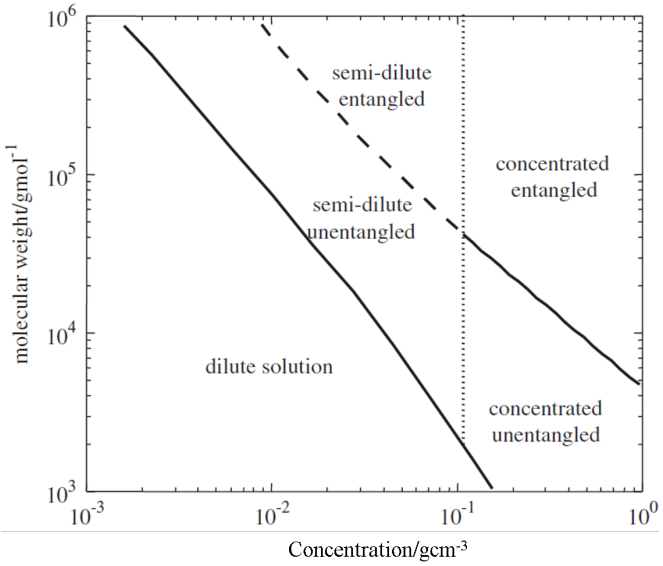

Figure 26: An example of the relationship between molecular weight and concentration of a polymer in solution with the different concentration regions for polybutadiene, each producing different rheological responses. Reproduced from *Rheology for Chemists: An Introduction*.[126]

In reality, the transition between concentration regimes will not be as sharp as represented in Figure 26, however, this serves as an adequate representation. This concentration-viscosity dependence can be split into four

concentration regimes (for uncharged polymers) described as: i) dilute - the concentration at which it is assumed chains do not come into contact or interact, ii) unentangled semi-dilute - chains are in contact but have not entangled, iii) entangled semi-dilute - chains have begun interpenetrating and entangling potentially reducing the volume and iv) concentrated - chains are entangled to the greatest proportion. Two critical concentrations can also be defined: the critical chain overlap concentration (c*) – concentration at which chains begin to overlap and the critical entanglement concentration (ce) – the concentration at which chain entanglement begins to occur.[86,120] Above c*, the viscosity-concentration dependence transfers from a linear dependence to a power dependence, with the viscosity of the solution rapidly increasing with increasing polymer concentration.[127] Viscosity also increases with the level of branching and cross-linking between chains as the polymer becomes more rigid and therefore the overall solution more viscous.[126]

Results and Discussion

4.3 Rheometry of Cellulose Solutions

Rheology defines how a material reacts to shear and therefore plays a vital role in processing of polymer solutions.[128] This was investigated in this section utilising DoE. However, before conducting a DoE investigation into the rheology of cellulose-OES it was important to define the experimental ranges and investigate factors that may influence the viscosity that may not be directly varied within the DoE. Initially experiments were designed to test the effect of water content and cellulose DP on the viscosity of these solutions.

4.3.1 Water Content

Due to the hygroscopic nature of the components used (DMSO, [EMIm][OAc] and cellulose) it was of vital importance to determine the effect of water content on the viscosity of the solutions and then make an informed

decision on the need to control water content and, if required, then to what extent.

Measurements of water concentration, determined from Karl Fischer titrations, showed that undried microcystalline cellulose (MCC) contained the highest quantity of water (4 wt%) of each component. An azeotropic drying process, using *n*-butanol as a solvent, was employed to reduce the water concentration to 0.5 wt%. Beneficially, the extracted solvent mixture (water and *n*-butanol) forms a binary azeotrope (BP) (92.4 °C) with the distillate forming a biphasic system consisting of an upper water rich layer (*ca.* 79.9 %) and a lower *n*-butanol rich layer.[129] This provides for interesting recycling pathways in which the two layers can be separated and the lower *n*-butanol rich layer reused for further drying. Both [EMIm][OAc] and DMSO, as received, had lower water content of < 0.5 wt% and displayed no significant reduction after attempts to dry (vacuum heating) (DMSO - 0.14 to 0.12 wt %, [EMIm][OAc] - 0.50 to 0.46 wt % water). Clearly, harsher, extended drying processes would be required to reduce the water concentration further, which can be problematic due to the potential for degradation of the both the IL and co-solvent and the chance of thermal runaway upon heating of DMSO.[130,131] Due to the low initial water content of DMSO and [EMIm][OAc], the decision was made to only dry the MCC component prior to dissolution due to the polymer containing the majority of the moisture, and the effectiveness of the drying process.

The rate of water absorption from the atmosphere by the cellulose-OES solution was also investigated to gauge the requirements for storage and handling of these polymeric solutions. Solutions of 4 wt% MCC dissolved in 70:30 (w/w) DMSO:[EMIm][OAc] were equilibrated with the atmosphere over 5 days, during which aliquots were analysed for water content and viscosity. Despite initial concerns, water absorption was not as rapid as expected with no detectable change up to 6 h of atmospheric equilibration (*ca.* 0.2 wt% water) and a steady increase between 12 h and 5 days reaching a final concentration of 1.9 wt% (Figure 27). This rate of water uptake would clearly change with humidity and temperature.

Comparing the viscosity of aliquots of "dried" (0.2 wt% water) and "wet"

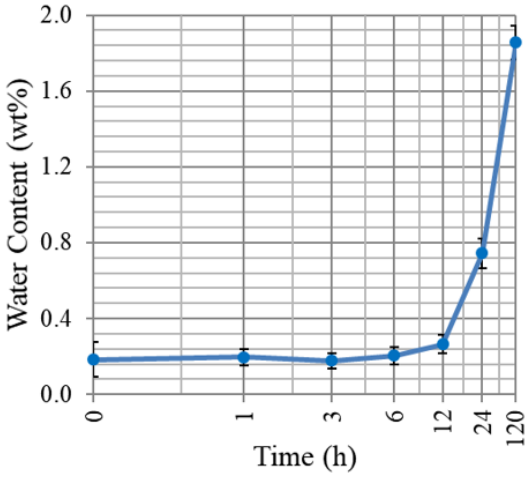

Figure 27: The rate of water absorption from the atmosphere by a 4 wt % MCC solution dissolved in 70:30 w/w DMSO:[EMIm][OAc] over a five day period.

cellulose solutions (1.9 wt% water) after 5 days of atmospheric equilibration highlighted no significant change in the average viscosity measured in the Newtonian region (Figure 28).

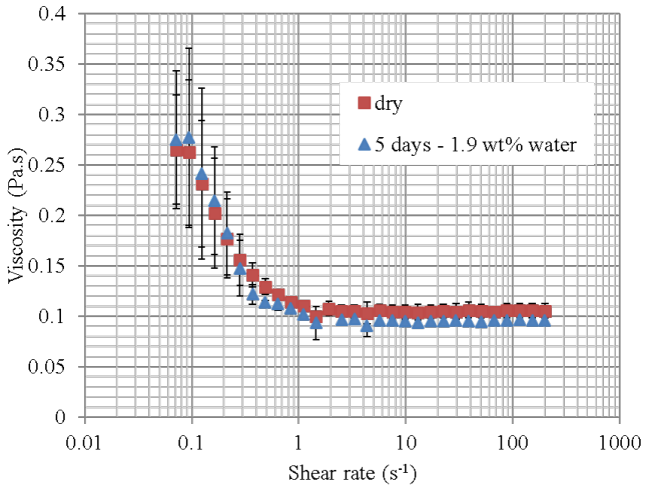

Figure 28: The flow curves for solutions of 4 wt% MCC dissolved in 70:30 (w/w) DMSO:[EMIm][OAc] containing 0.2 wt% water and, after 5 days of atmospheric equilibration, containing 1.9 wt% water.

Contrary to this, reports in the scientific literature document a significant decrease in the viscosity of IL-cellulose solutions with increased water content.[64,65] However, most reported examples describe systems with much higher water

concentration than those used here, usually up to 20 wt%.[65] Some have, however, shown the large effect water can have on cellulose-[EMIm][OAc] solutions even at low concentration (0.25 wt %).[128] It was clear that the presence of a co-solvent, DMSO, greatly reduced the impact of water concentration on the viscosity of the solution, as a solution containing DMSO had a much lower viscosity than many previously described in the literature, and therefore the addition of water had a less significant effect on the viscosity. These results suggested that containment in a dry atmosphere was not required during storage or dissolution, although precautions were made to reduce moisture uptake to levels < 1 % for the sake of consistency between samples. It was concluded that [EMIm][OAc] and DMSO did not require drying before use and that the emulsification process could be carried out in air. MCC was azeotropically dried from n-butanol before use.

4.3.2 The Effect of Polymer Chain Length

As previously discussed in the underpinning theory section (4.2), the degree of polymerisation (DP) of cellulose has a substantial influence on the rheology of cellulose solutions. MCC and α-cellulose have substantially different DPs. MCC is formed from the hydrolysis of higher DP cellulose using dilute acid solutions resulting in polymer with DP values between 150-300, while for α-cellulose this rises to between 800-1,000.[21,64,132–134] Comparing the flow profiles of the two polymeric solutions highlighted the profound effect DP had on the viscosity and flow curves of the solutions (Figure 29).

Two significant differences were noted in the rheology of the two systems. First, the α-cellulose solution showed an order of magnitude higher viscosity compared with that of the MCC and second, no Newtonian region was observed for the α-cellulose sample in the shear rate range investigated (Figure 29 A, B). Both samples exhibited shear thinning, typical of polymeric solutions, with the MCC sample exhibiting a Newtonian plateau above 1 s^{-1} (Figure 29 B) due to a reduction in chain entanglement at higher shear rates enabled by shorter chains, a characteristic that was not seen for the higher DP sample (Figure 29 A).[65,86] Other researchers have reported the existence of a Newtonian plateau for high DP cellulose solutions in comparable shear rate ranges, which was evidently not the

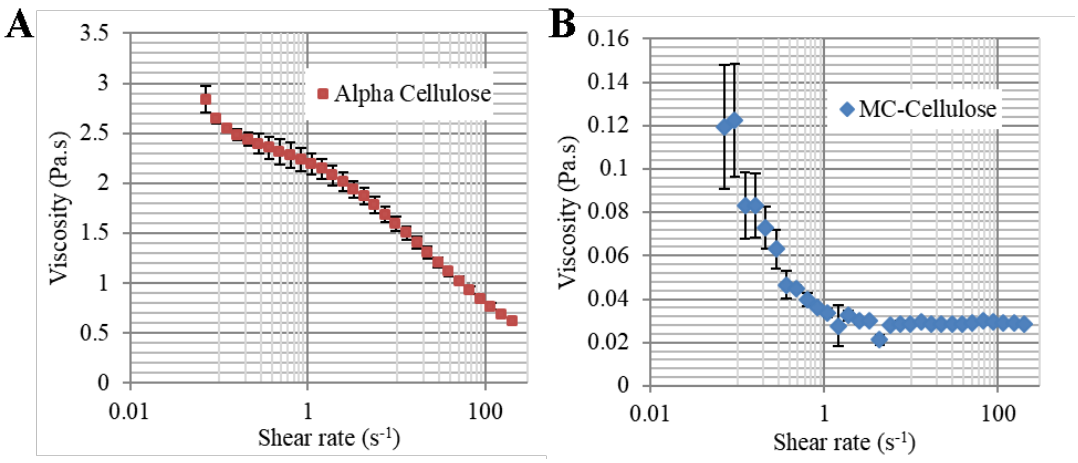

Figure 29: Comparison between the flow profiles of A: α and B: microcrystalline cellulose (MCC) under an increasing shear rate sweep of 0.1-200 s^{-1} (30 points), averaged over three runs. Both solutions consisted of 2 wt% cellulose (α or MCC) and a solvent system of 30 wt% DMSO and 70 wt% [EMIm][OAc] combined at room temperature using an overhead stirrer for 1 h. Data were collected at 80 °C.

case in this system.[127] This led to two hypotheses: either the α-cellulose sample was not fully dissolved under the mild dissolution conditions (room temperature, 1 h stirring) used, or the harsh dissolution conditions typically reported in the literature – high temperatures for an extended time – could be inducing side reactions and degradation of the polymer chain, reducing DP and resulting in Newtonian flow curves.[70,135]

This hypothesis was tested by subjecting the α-cellulose sample to harsher dissolution conditions, at an elevated temperature (60 °C) for a longer period of time (24 h) and assessing any change in the rheological profiles of the formed solution. The temperature chosen (60 °C) was selected as one that would not be expected to induce significant chain scission.[135,136] The OES mix was also adjusted by increasing the concentration of DMSO (to 85 %, 15 wt% [EMIm][OAc]) again with the goal of reducing the likelihood of chain scission, a process which can be driven by reaction with the IL.[70] (It is appropriate to highlight that there are numerous examples in the literature of extended high temperature IL-based dissolution conditions, which could be reducing the DP of the polymers, although this is often ignored).[127,137]

Increasing the temperature (RT to 60 °C) and heating time (1 to 24 h)

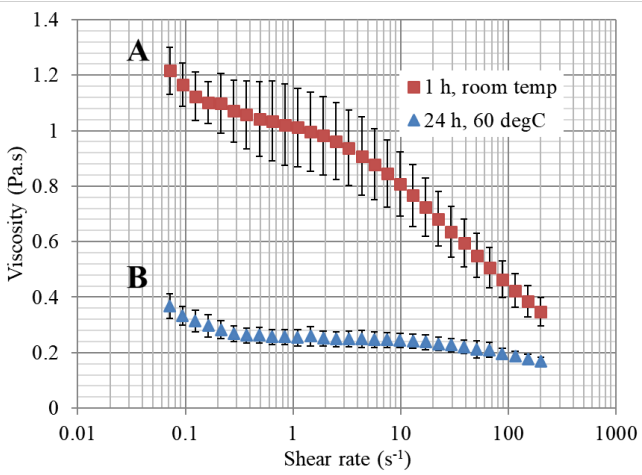

Figure 30: Comparison between the flow curves of α-cellulose solutions subject to different dissolution processes, A: 1 h room temperature using an overhead stirrer (top red squares) and B: 24 h at 60 °C. Both solutions had the same composition, consisting of 2 wt% α-cellulose dissolved in 85:15 DMSO:[EMIm][OAc] w/w. Data were collected at 40 °C with an increasing shear rate sweep from 0.1-200 s^{-1} (30 points) and the results are averages of the three runs.

had a significant effect on the rheology of the α-cellulose solutions, reducing the overall viscosity and producing a Newtonian region (Figure 30). Interestingly, subjecting a shorter chain length MCC sample (3 wt% MC, 58:42, w/w, DMSO:[EMIm][OAc]) to the same experimental dissolution conditions provided no significant change in the rheology profiles (Figure 31). This suggested that harsher dissolution conditions led to a greater extent of dissolution of α-celluloses rather than degradation of the polymer. If degradation was occurring, then one would have expected to see a drop in the viscosity of the shorter chain MCC samples when exposed to the same harsh dissolution conditions, which was not observed (Figure 31).[135]

Due to the relatively lengthy time required to fully solubilise α-cellulose in the DMSO:[EMIm][OAc] solvent system and the high viscosity of the resultant solutions, it was decided that MCC would be utilised moving forward. The favourable formation of low viscosity MCC solutions at high cellulose concentration would enable a greater amount of polymer to be processed per volume of solution, along with less complex flow dynamics due to its Newtonian fluid behaviour. Full dissolution could also be achieved under milder conditions

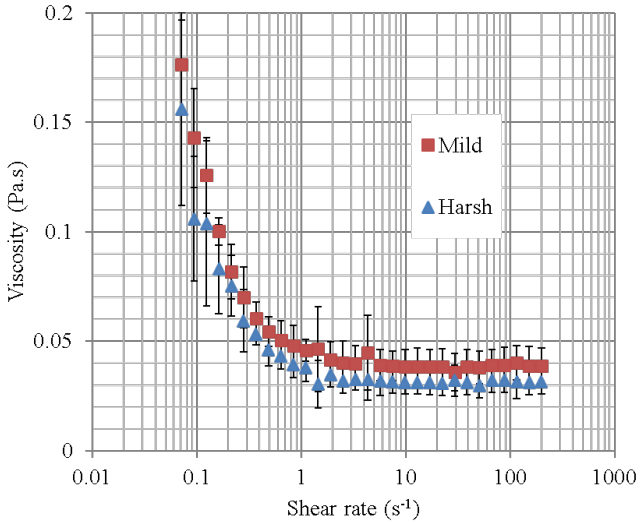

Figure 31: The flow curves for solutions of 3 wt% MCC dissolved in 57.5:42.5 (w/w) DMSO:[EMIm][OAc] having been dissolved under mild (1 h overhead stirrer) or harsh (60 °C, 24 h) dissolution processes.

by mixing for $<$ 1 h at room temperature, making the overall process more efficient, less energy intensive and more sustainable. Some have noted that the lower DP cellulose has a negative impact on the tensile strength of cellulose fibres compared with higher DP samples.[136] In a beaded form however, cellulose would not typically be subject to these forms of stress, i.e. elongation, but could be exposed to compressive forces.

4.3.3 Experimental Design - The Effect of Temperature and Solution Composition on Viscosity

DoE was exploited for the development of an appropriate cellulose solution that could be used to generate a wide range of cellulose materials. The effect of solution composition and temperature on the viscosity of the final solution was investigated. Table 3 denotes all of the factors that would influence the rheology of the cellulose solution, both inherently and during the dissolution process, along with the factors that were selected for investigation.

All the factors concerning the dissolution process (dissolution time,

Table 3: Factors that influence cellulose dissolution and the final solution viscosity

Chosen Variables	MCC concentration (2-4 wt%) DMSO concentration (30-85 wt%) Temperature (40-80°C)
Controlled Parameters	Ionic Liquid Type Co-solvent type Dissolution time Dissolution shear force Dissolution method Water content Vessel type Purity of components Cellulose DP Order of addition (of components during dissolution)
Disregarded Parameters	Humidity (water content <1 %)

temperature, shear force, method, order of addition) could be fixed by using a consistent dissolution method for each sample; one which achieved full dissolution of the polymer. The type of IL and co-solvent used were also fixed since it is widely documented that a [EMIm][OAc] and DMSO solvent system is optimal for cellulose dissolution.[78] The weight ratio of DMSO to [EMIm][OAc] is quoted separately to the concentration of cellulose, which is quoted with respect to the entire system e.g. 8 wt% cellulose dissolved in an OES of 70:30 DMSO:[EMIm][OAc] (w/w). The decision was made to disregard humidity as a factor due to the relatively slow uptake and low impact of water on the viscosity of the solutions, discussed previously in section 4.3.

A two level full factorial resolution V interaction design was developed to investigate the three factors. Using the ranges noted in Table 3, the design consisted of eight experiments plus three repeats (Table 4). For each of the solutions, an average value derived from the Newtonian region (1-200 s^{-1}) was used as the response for viscosity.

Table 4: Experiments conducted for the viscosity experimental design (Figure 32).

Run order	Cellulose concentration (wt%)	DMSO:[EMIm][OAc] ratio (w/w)	Temperature (°C)	Newtonian Viscosity (Pa.s)	Error (Pa.s)
1	3	57.5 : 42.5	60	0.0459	±0.0039
2	2	85 : 15	80	0.0084	±0.0020
3	4	85 : 15	80	0.0220	±0.0039
4	2	30 : 70	80	0.0289	±0.0023
5	4	30 : 70	40	0.3207	±0.0022
6	2	30 : 70	40	0.0745	±0.0026
7	2	85 : 15	40	0.0152	±0.0022
8	3	57.5 : 42.5	60	0.0361	±0.0027
9	4	30 : 70	80	0.1072	±0.0034
10	4	85 : 15	40	0.0494	±0.0019
11	3	57.5 : 42.5	60	0.0376	±0.0030

An interaction model was successfully generated for the obtained data (R^2 = 0.98, Q^2 =0.95) with each factor selected shown to have a significant effect on the measured Newtonian viscosity (Figure 32 B). No interaction terms were found. Increasing the DMSO concentration or temperature reduced the viscosity of the solution, whilst increasing the cellulose concentration had the opposite effect, leading to an increase in the viscosity of the solution (Figure 32 B). The DMSO concentration was found to have the largest effect on the viscosity under the ranges investigated (30-80 wt% DMSO). The results were to be expected, however, it was important to know the extent to which each factor influenced the viscosity of the cellulose-OES. A 4-D contour plot of these factors highlighted a non-linear rapid increase in viscosity of the solutions with increased cellulose concentration at lower temperatures (40 °C) and DMSO concentrations (30 wt%) (Figure 32 D). Similar results have been reported in the literature and the authors state that this is due to a change in the concentration regime, from dilute to one above c^*, which can be observed in the viscosity by a linear to power dependency change.[127]

The viscosity study was expanded further by investigating the effect of temperature (30, 45 and 60 °C) and a higher cellulose concentration (4, 6 and 8

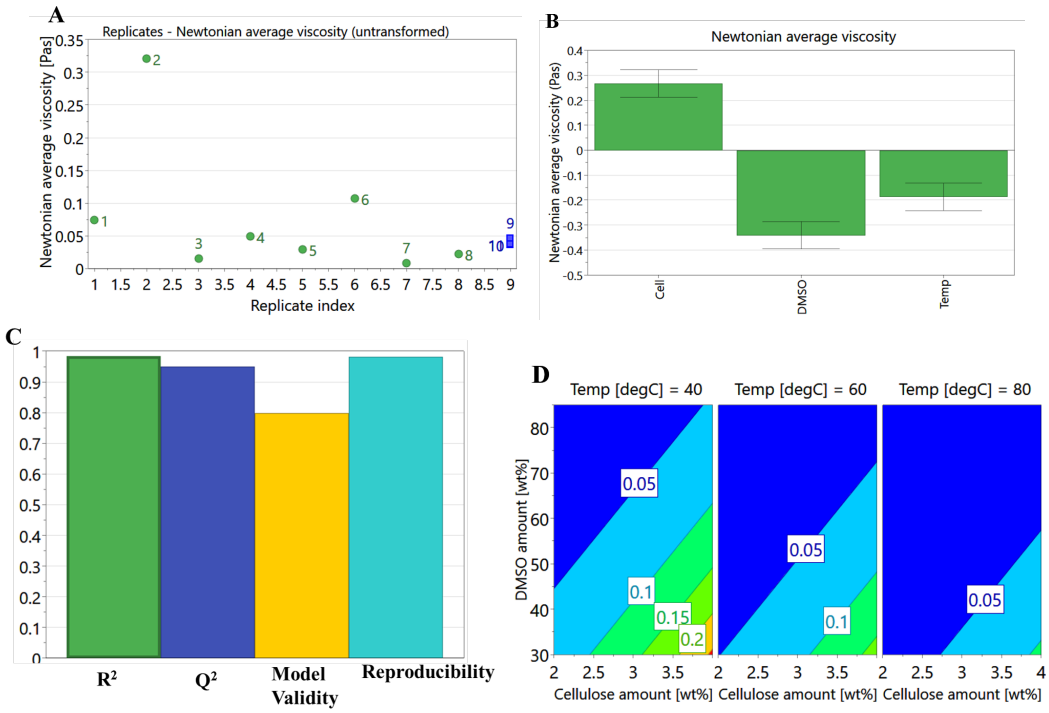

Figure 32: Overview of the two level full factorial resolution V interaction design used to determine the effect on viscosity showing A: each experiment and the measured Newtonian viscosity (Pa.s), B: the level of effect of factor on the viscosity, C: an overview of the model (from left to right - R^2, Q^2, model validity and reproducibility) and D: a 4-D contour plot of the results of the design.

wt%), whilst fixing the OES weight ratio to 70:30 DMSO:[EMIm][OAc] (Figure 33). Again, at lower temperatures (30 °C), increasing cellulose concentration had a profound effect on the viscosity of the solutions, which suggested that these were in a concentration regime above c^*, inferred from the extent of increase in viscosity with increasing cellulose concentration (Figure 33, Table 5). At higher temperatures, there was a lower degree of chain entanglement and therefore an increase in cellulose concentration had less of an effect on viscosity, which has also been reported for similar systems.[127,132] This was also true for lower concentration solutions, in which the temperature had less of an effect due to lower levels of chain entanglement. Values of c^* have been quoted as around 2 wt% for MCC dissolved in pure [EMIm][OAc].[132]

The viscosity of cellulose-OES solutions could be altered significantly with temperature, cellulose and co-solvent concentration. When selecting a cellulose

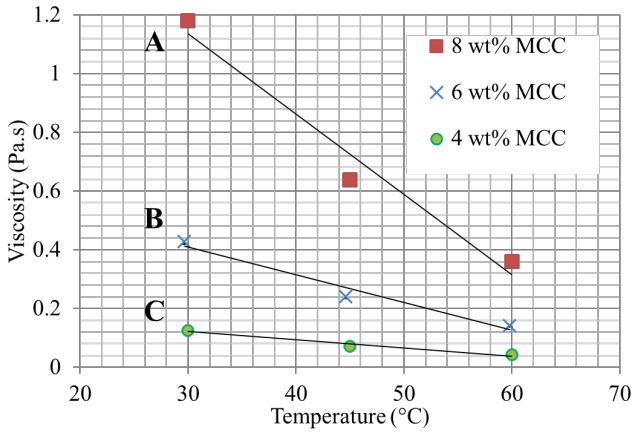

Figure 33: Temperature and cellulose concentration dependence of A: 8 , B: 6 and C: 4 wt% MCC dissolved in DMSO:[EMIm][OAc] (70:30, w/w). Equations for linear trend lines are given in Table 5.

Table 5: Linear trend line equations for Figure 33.

Line	Cellulose concentration (wt%)	Trend line equation	R^2
A	8	y = -0.0273x + 1.9544	0.9661
B	6	y = -0.0095x + 0.6927	0.9662
C	4	y = -0.0028x + 0.2055	0.9713

solution composition to generate cellulose beads using a membrane emulsification or dropping process, it was desirable to select one with a low IL concentration able to dissolve a high concentration of cellulose, producing a solution of relatively low viscosity. In the case of membrane emulsification, this would enable simpler handling of the solution and higher flux at lower pressures (desirable for processing of solutions) as well as reducing costs of the overall process, due to a lower concentration of costly IL. However, a compromise had to be made between these three requirements since reducing the IL concentration reduced the achievable maximum dissolvable cellulose concentration at room temperature and increasing the biopolymer concentration produced a more viscous solution, which was more challenging to process. From these findings, a solvent ratio of 70:30 DMSO:[EMIm][OAc] (w/w) was selected for use throughout material production and only the concentration of cellulose was changed. This solvent weight ratio was able to dissolve reasonable quantities of cellulose (>15 wt%) under mild dissolution conditions.[78]

Looking towards the continuous phase, the viscosity of sunflower oil (SFO, continuous phase) influences the cleavage of droplets from the membrane surface. This was also measured at different temperatures and surfactant loading (Figure 34). A small increase in the viscosity was observed when Span 80 was added to SFO, but remained constant with increasing surfactant concentration (Figure 34). Increasing temperature was shown to reduce the viscosity of the solution.

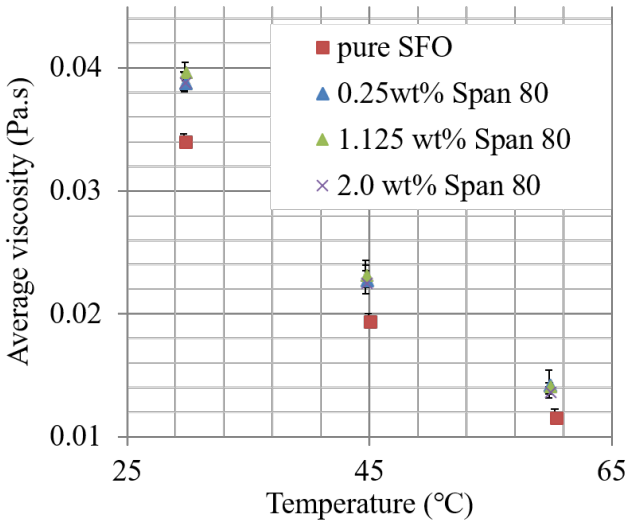

Figure 34: The average viscosity of sunflower oil and sunflower oil with 0.25, 1.13 and 2 wt% Span 80 at 30, 45 and 60 °C. Data was averaged from an up and down shear rate sweep from 7-200 s^{-1} (60 points).

4.4 Interfacial Tension

The interfacial tension between an emulsion droplet and the continuous phase is related to the Gibbs free energy of formation of the emulsion via Equation 11, discussed in Chapter 5. In membrane emulsification, a higher interfacial tension leads to an extended droplet growth stage as detachment becomes less favourable. Formed droplets are also more likely to coalesce to minimise surface energy, via a reduction in the surface to volume ratio, resulting in larger droplets. At lower interfacial tensions, droplet detachment becomes a more favourable process and coalescence becomes less likely, resulting in smaller droplets.[109,138] Emulsion generation/stabilisation can also be aided by the

addition of an appropriately chosen surfactant, which will migrate to the interface between the two phases reducing the tension between the two. Research within the group and by others has highlighted the non-ionic surfactant Span 80 as a suitable surfactant for similar systems.[100] Span 80 has a hydrophilic-lipophilic balance (HLB) of 4.3, meaning that it was readily soluble in the non-polar continuous phase (SFO).[139]

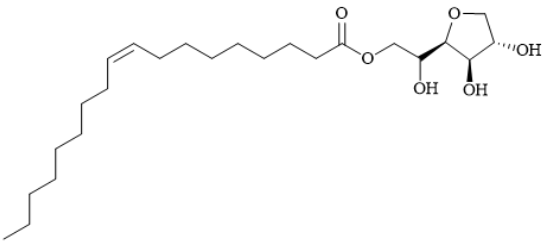

Figure 35: The structure of the surfactant Span 80, which was dissolved in sunflower oil and used to stabilise cellulose-OES emulsion droplets.

To investigate interfacial tension, a droplet of cellulose-OES was suspended from a tip of a needle immersed in sunflower oil-Span 80. The concentration of Span 80 (0.25 – 2.00 wt%) and concentration of cellulose in the disperse phase droplet (4 – 8 wt%) were investigated for their impact on interfacial tension using a full factorial resolution V interaction experimental design (4 experiments, 3 repeats)(Table 6). The OES was kept constant at a 70:30 (w/w) ratio of DMSO:[EMIm][OAc]. Sunflower oil (SFO) was selected as a continuous media for emulsion generation due to its wide availability and low cost along with its renewability and proven ability (within the group) to enable emulsification of the cellulose-OES. The obtained data (10 repeats of each experiment) was fitted to a valid model (Figure 36), which required no further refinement.

Each selected factor was found to have a significant effect on the interfacial tension when varied and the obtained model was deemed significant ($R^2 = 0.99$, $Q^2 = 0.99$, model validity was negative due to little variation between mid point replicates and high Q^2). Increasing the concentration of surfactant is often used to reduce the interfacial tension and therefore increase the stability of the emulsion, which could also be applied here (Figure 36 B). The surfactant was by far the most significant factor in controlling the interfacial tension in the ranges selected and showed that Span 80 acted as an adequate surfactant for stabilisation of this

Table 6: The experiments conducted for the interfacial tension experimental design (averaged from 10 repeat experiments).

Run Order	Cellulose Concentration (wt%)	Surfactant Concentration (wt%)	Average Interfacial Tension (mNm^{-1})	Error (mNm^{-1})
1	6	1.13	2.20	±0.03
2	4	2	1.70	±0.04
3	4	0.25	2.78	±0.39
4	6	1.13	2.22	±0.04
5	8	0.25	2.85	±0.01
6	8	2	1.57	±0.02
7	6	1.13	2.22	±0.04

p

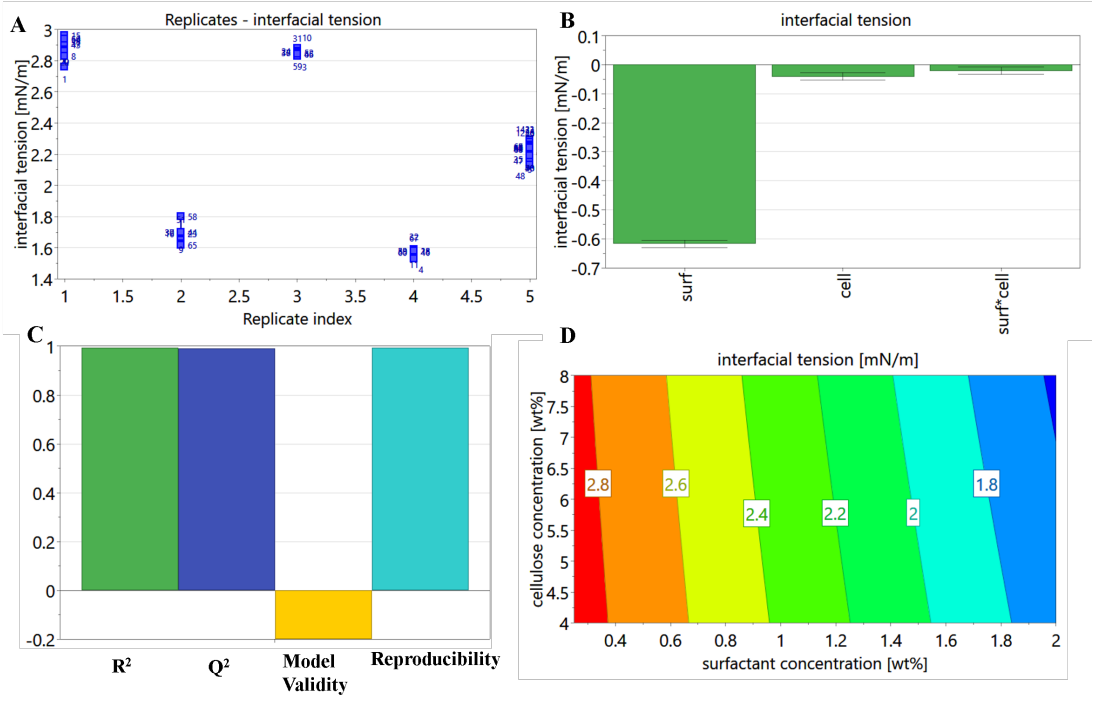

Figure 36: Overview of the experiments and model generated from the interfacial tension experimental design showing A: each experiment and the measured interfacial tension (mN/m), B: the extent of the effect of each factor on the interfacial tension, C: an overview of the model (from left to right - R^2, Q^2, model validity and reproducibility) and D: a 3-D contour plot of the results of the DoE.

emulsion. The concentration of cellulose did also have a small effect, with an increase in cellulose concentration leading to a decrease in the interfacial tension, suggesting a small stabilisation effect imparted by the cellulose polymer at the interface. Others have also noted the decrease in surface tension of solutions of cellulose-[EMIm][OAc] with increased polymer concentration.[140] Further evidence for this was the occurrence of an interaction response between the concentration of cellulose and surfactant concentration, suggesting a synergistic effect between the two factors in reducing the interfacial tension, when the concentrations of both were increased (Figure 37). The model (interaction model resolution V) allowed for the detection of two-way interactions between factors, therefore, even though this was a mild effect, it can still be considered significant.

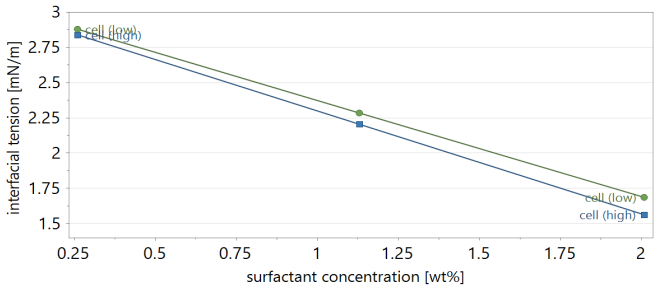

Figure 37: A plot of surfactant concentration (wt%) versus interfacial tension (mN/m) at high (8 wt%) and low (4 wt%) cellulose concentration. This highlighted a mild, but still significant, interaction effect between cellulose concentration and surfactant concentration.

For a membrane emulsification process, the interaction between the membrane surface and growing emulsion droplet will also define the size of the final droplet. This can be described using the contact angle between the three phases: the disperse phase, continuous phase and membrane surface (here glass).

4.5 Contact Angle

The wettability of a membrane by the disperse phase should be minimised to the greatest possible extent, to prevent coalescence between droplets emerging from pores on the surface of the membrane. In the case of the membrane apparatus developed, the Shirasu Porous Glass (SPG) membranes used were

hydrophilic and required functionalisation to render these hydrophobic, as the cellulose-OES solutions were hydrophilic. A method commonly applied utilised two silanes: trichloro(octadecyl)silane (TOS) and trimethylchlorosilane (TMS) (Figure 38).[108,109,113]

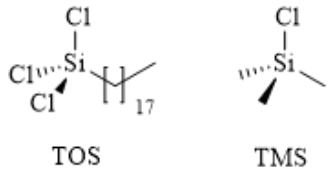

Figure 38: The structure of trichloro(octadecyl)silane (TOS) (left) and trimethylchlorosilane (TMS) (right).

The functionalisation process required extended heating under reflux (8 h) and two silylation reactions to render the membrane hydrophobic.[113] An investigation into whether reaction times and silane use could be reduced was conducted. Glass microscope slides were used to mimic the surface of the SPG membrane material and the effectiveness of hydrophobisation tested by contact angle measurements with water (Table 7). The robustness of the surface functionality was also tested by exposing the silanized glass to heated [EMIm][OAc]-DMSO followed by observation of any change in the water contact angle. The microscope slides used were SiO_2-B_2O_3 glass and the SPG membranes were fabricated from SiO_2-Al_2O_3 glass, so was considered to be a reasonable proxy system.[141]

The inclusion of the hydrophobic surface functionality resulted in a clear increase in the water contact angle of the glass by >60 ° (Table 7) placing the material definitively in the hydrophobic regime (water contact angle increased to 105-109 °>90 °). No significant change in the wettability of the glass resulted with decreased reaction time or removal of the TMS silylation step. It appeared that the second silylation was not required and that the reaction time could be reduced, greatly speeding membrane hydrophobisation and reducing silane use.

To test the robustness of the coating to the [EMIm][OAc]-DMSO solvent system, functionalised glass slides, treated using the extended process, described in the literature, and refined process, were exposed to the solvent system at 80 °C for an extended period of time (>20 h). The hydrophobic coating was found

Table 7: The effect of different silylation reactions with glass on the resulting water contact angle (averaged from 10 repeat experiments) including the effect of heated DMSO:[EMIm][OAc] exposure.

Hydrophobisation conditions	Water contact angle (θ °)
Unfunctionalised	39 ±11
7 h reflux TOS, overnight TMS (literature)[113]	107 ±4
7 h reflux TOS	105 ±4
3 h reflux TOS	109 ±4
Robustness tests	
7 h reflux TOS, overnight TMS exposed to 80 °C 70:30 DMSO:[EMIm][OAc] for 21 h.	106 ±2
3 h reflux TOS exposed to 80 °C 70:30 DMSO:[EMIm][OAc] for 42 h.	106 ±2

to be robust under these conditions with no significant reduction in the water contact angle observed (Table 7). Therefore, all membranes were hydrophobised using these refined conditions (3 h, TOS, reflux).

These experiments were extended further by investigating the effect of the membrane functionalisation on the contact angle with a cellulose-OES solution. A droplet of cellulose-OES solution was placed on the functionalised glass submerged in the continuous phase (SFO-2 wt% Span 80) and the three phase contact angle measured (Figure 39). The initial experiments highlighted the substantial increase in contact angle once the glass surface had been reacted with TOS (Figure 40). A small drop in the angle was observed when Span 80 (2 wt%) was introduced into the oil phase, as the presence of surfactant aids wetting of a surface, but the contact angle remained sufficiently high (136 ±2 °).

Having refined the hydrophobisation process compared with that described in the literature[113] and showing that the membrane chemical modification was robust, it was important to investigate how changes in the composition of both the disperse and continuous phases would influence the contact angle with the membrane. The three phase contact angle between the membrane surface, growing emulsion droplet and continuous phase will define the growth rate and detachment size of the droplet.[109] A full factorial resolution V interaction model

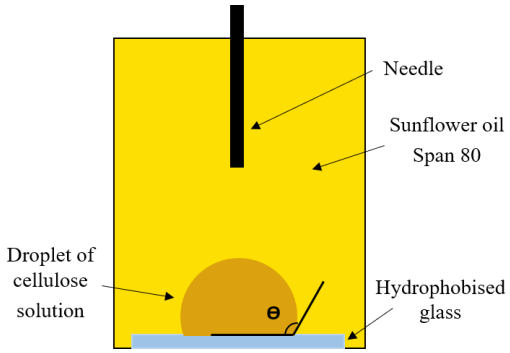

Figure 39: Diagram representing the three phase contact angle measurements between a droplet of dissolved cellulose on hydrophobised glass, simulating a membrane surface, in a sunflower oil - Span 80 continuous phase

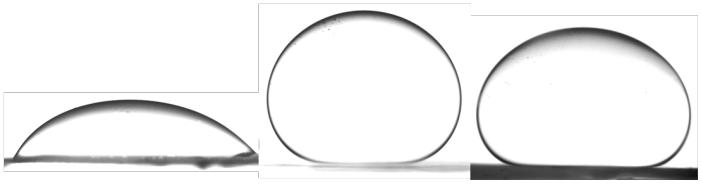

	A	B	C
Hydrophobised glass	×	✓	✓
Surfactant (2 wt% Span 80)	✓	×	✓

Figure 40: Droplets of 4 wt% microcrystalline cellulose dissolved in DMSO:[EMIm][OAc] (70:30, w/w) on A: unfunctionalised glass immersed in sunflower oil - 2 wt% Span 80, B: glass hydrophobised with octadecyltrichlorosilane (3 h reflux) immersed in pure sunflower oil and C: hydrophobised glass immersed in sunflower oil - 2 wt% Span 80

was again utilised to generate a set of experiments to investigate the effect of surfactant concentration (0.25 - 2 wt% Span 80), in the continuous phase, and cellulose concentration (4 - 8 wt%), in the disperse phase, on the final three phase contact angle. Full experimental conditions and results are listed in Table 8.

The variation in the measured contact angles, between experiments, lay just outside of experimental error enabling the formation of a valid model (R^2 = 0.59, Q^2 = 0.57). Unsurprisingly both the surfactant and cellulose concentration had the same general effect on the contact angle as on the interfacial tension: an increase in either led to a decrease in the contact angle. Interestingly, increasing

Table 8: List of Contact Angle Experimental Design Experiments and the measured contact angles (averaged from 10 repeat experiments)

Run Order	Cellulose Concentration (wt%)	Surfactant Concentration (wt%)	Average Contact Angle (°)	Error (°)
1	6	1.13	138	±3
2	4	0.25	142	±2
3	4	2	136	±2
4	6	1.13	137	±2
5	8	2	133	±3
6	8	0.25	139	±2
7	6	1.13	140	±2

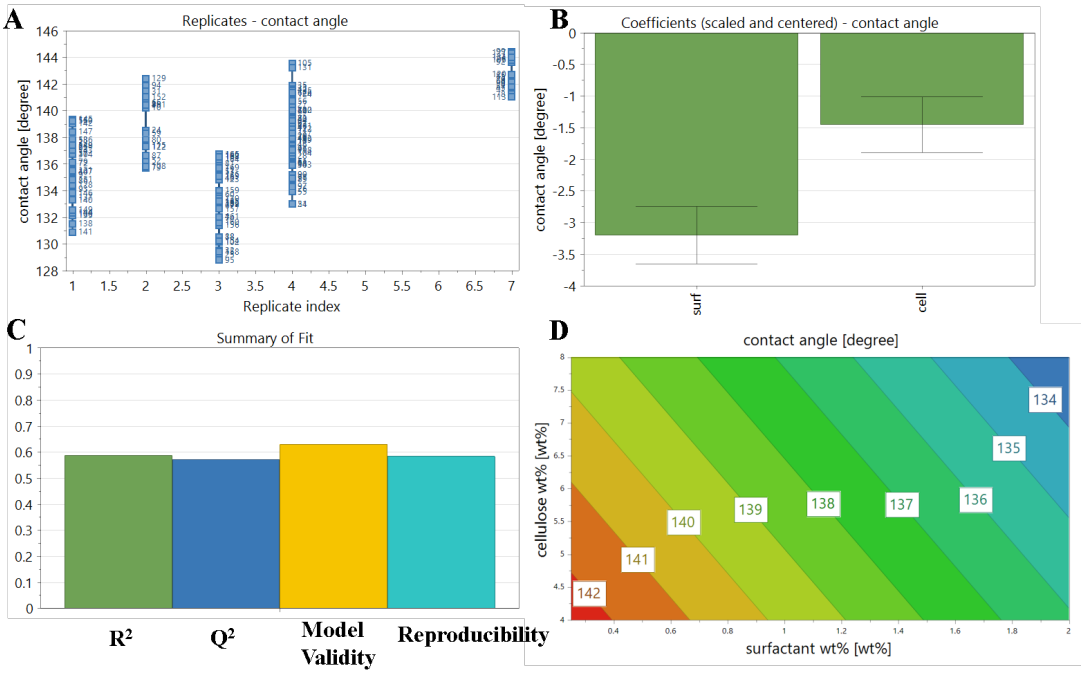

Figure 41: Overview of the experiments and model generated from the contact angle experimental design showing A: each experiment and the measured contact angle (°), B: the response of each factor on the contact angle, C: an overview of the model (from left to right - R^2, Q^2, model validity and reproducibility) and D: a 3-D contour plot of the results of the design.

the cellulose concentration had a greater impact on reducing the contact angle than it did the interfacial tension (Figure 41). With the ranges investigated, the density of the cellulose-OES increased at a much higher rate when the concentration of cellulose was increased (Figure 42 A) compared with that of the continuous phase when the surfactant concentration was increased (Figure 42 B). This led to a greater spreading of the denser droplets on the glass surface, giving a smaller contact angle. The density values for cellulose-OES solutions were comparable with those found in the literature.[140]

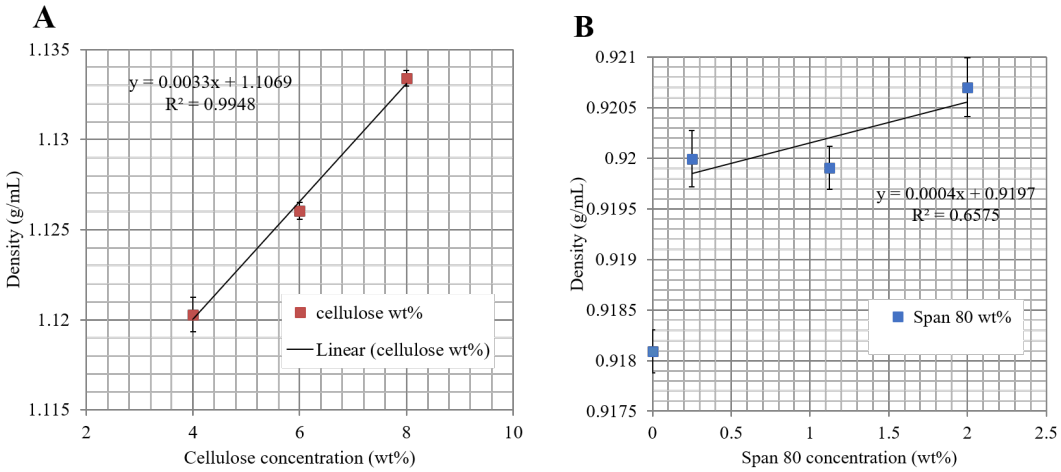

Figure 42: Pycnometry measurements for A: cellulose-[EMIm][OAc]-DMSO solutions (4, 6 and 8 wt% microcrystalline cellulose) at 20.2 °C (±0.2 °C) and B: sunflower oil-Span 80 solutions (0.25, 1.13 and 2 wt% Span 80) at 18.1 °C (±0.3 °C)

Measurements of contact angles remained high with a low level of interaction between the emulsion droplet and glass surface, leading to the conclusion that little droplet spreading would occur across the membrane surface in a membrane emulsification process.

4.6 Chapter 4 Conclusions

The physical properties of a solution define the limits within which it can be processed. The results from this chapter were used to develop and enable the selection of an appropriate range of cellulose solutions for use in the generation of cellulose beads via membrane emulsification and dropping processes. The

viscosity of the cellulose solution was shown to be greatly impacted by the solution composition - the concentration of DMSO and cellulose - and the temperature of the solutions. The findings of a rheological investigation led to the conclusion that a cellulose solvent ratio of 70:30 DMSO:[EMIm][OAc] was ideal to produce a solution of low viscosity with enough "space" to alter the cellulose concentration without locking out some processing routes. This composition was suited to both membrane emulsification and dropping bead formation processes. Water concentration was shown to have little impact on the rheology of the solutions, contrary to some reports pertaining to pure IL solvents. This was ascribed to the high concentrations of the co-solvent DMSO.

Investigations into the contact angle and interfacial tension showed that emulsions of cellulose-OES could be generated in a SFO-Span 80 continuous phase with suitably low interfacial tension. The wettability of the glass membrane surface by these solutions was also shown to be minimised via chemical modification of the membrane. This modification process was refined through examination of reaction parameters, resulting in a reduction in reaction time and removal of the requirement for a second reaction with TMS. This was coupled with stability testing, which showed that the hydrophobic coating was stable to heated OES for extended periods of time (48 h). Both the interfacial tension and contact angle were shown to be influenced by the concentration of surfactant in the oil phase and concentration of cellulose in the disperse phase. The latter factor had a much greater impact on the contact angle due to the effect of density when the cellulose concentration of the droplet was increased.

Determining the limits of the processability of these cellulose solutions informed the processing routes taken in subsequent chapters.

Chapter 5

The Continuous Production of Cellulose Beads

5.1 Introduction

Cellulose based materials are a clear alternative to many persistent plastics, especially when using OES processing routes (Chapter 4 using a 70:30 w/w DMSO:[EMIm][OAc]). This section details the generation, testing and optimisation of two processes used to form cellulose beads, of varying diameter, using an OES:

- Membrane emulsification, diameter: 5 - 500 μm
- Dropping procedure, diameter: 1 - 3 mm

Both groups of materials have application in a wide range of industries where their biodegradability and sustainability are sought after attributes. Both can be applied as supports in extraction processes,[22] but cellulose microbeads also have application in the cosmetic and personal care product industry for use as abrasives and tribological modifiers.[82,142] To the best of our knowledge, this is the first example of the use of membrane emulsification to produce cellulose microbeads.

5.2 Underpinning Theory and Concepts

5.2.1 Emulsification

Emulsions are dispersions of a liquid (disperse phase) in another liquid in which it is immiscible (continuous phase). The most common examples are those of oil droplets dispersed in water (oil in water emulsion - O/W) or aqueous droplets dispersed in an oil (water in oil emulsion (W/O). Energy is often required to form an emulsion via the dispersion of one phase in the other, due to the increased the interfacial area between the two phases and therefore the free energy of the system.[143] Binary emulsions are therefore typically thermodynamically unstable, without the addition of a surface active agent, due to a positive free energy (Equation 11). For an emulsion to be considered thermodynamically stable, ΔG must be negative, which in general can be brought about by a sufficiently low interfacial tension (γ), often only seen for microemulsions (fractions of $\mathrm{mNm^{-1}}$).[124,144]

$$\Delta G = \gamma \Delta A - T\Delta S \tag{11}$$

Where ΔG is the change in Gibbs free energy upon dispersion, γ the interfacial tension, ΔA the change in interfacial area with dispersion, T the temperature and ΔS the change in entropy with dispersion.[144] It can be seen from Equation 11 that a reduction in the total area of the droplet is energetically favourable, due to the decrease in Laplace pressure (Δp) with increasing droplet size (radius of droplet curvature = a).[124] The equation for the Laplace pressure (Equation 12) highlights the pressure difference found across a curved liquid-liquid interface which is larger for smaller droplets.

$$\Delta p = \frac{2\gamma}{a} \tag{12}$$

Emulsion Instability

The decrease in Gibbs free energy with increasing droplet size is the driving force behind droplet coalescence, ripening and ultimate emulsion instability.[124] Emulsions with a diameter >100 nm are thermodynamically unstable and require steps to be kinetically stabilised to prevent de-emulsification via addition of an appropriate surfactant to reduce the γ.[143] The hydrophilic–lipophilic balance can be used to determine an appropriate surfactant to stabilise O/W or W/O emulsions, with a value nearing 0 representing a surfactant that is more soluble in oil and therefore benefiting stabilisation of W/O emulsions and up to 20 favouring O/W emulsions.[145] Generally, the continuous phase can be defined as the phase in which the surfactant is more soluble.[86]

De-emulsification, or the collapse of an emulsion, can occur via two main routes, both driven by the production of larger droplets with a lower free energy. Coalescence is the process by which adjacent droplets fuse into a larger lower energy one to minimise total surface area (Figure 43 A). It is driven by the rupturing of the thin films of continuous phase, of thickness h (Figure 43 A) between droplets, caused by the Van der Waals attraction between adjacent droplets.[145] The thin continuous phase film is pushed away from the two droplets allowing for droplet coalescence. The rate of this can be reduced via the addition of a surfactant (Figure 43 B) which acts as a repulsive barrier between adjacent droplets. Coalescence can still occur when a surfactant is present due to short-lived openings in the surfactant coating presenting areas of attraction between droplets. This can be minimised by promoting greater surface coverage by using a high concentration of surfactant.[86,124]

Another emulsion instability mechanism is Ostwald Ripening which can be recognised by an increase in the average droplet size and monodispersity of an emulsion with time, a process which is again driven by the pressure difference across a curved interface (Equation 12). Disperse phase molecules located in small droplets will migrate through the continuous phase into larger droplets leading to a reduction in the overall free energy of the emulsion due to a drop in ΔA.[124] If an emulsion is monodispersed however, this ripening mechanism is less likely to occur due to the lack of pressure difference between droplets.

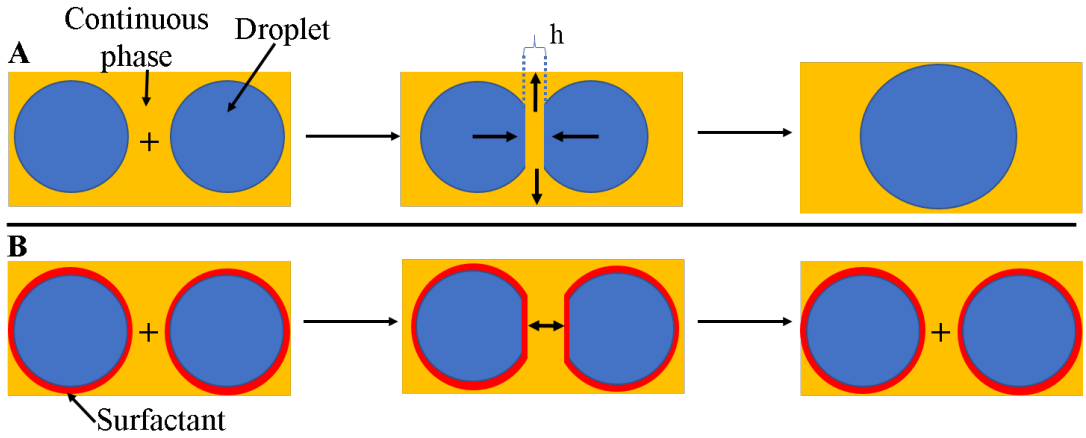

Figure 43: Schematics showing A: the Coalescence of unstable emulsion droplets and B: the stabilisation of emulsion droplets with a surfactant.

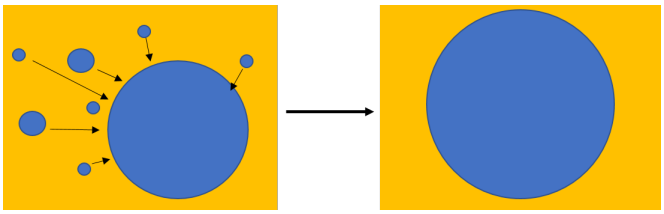

Figure 44: Schematic representing Ostwald ripening, a process by which an unstable emulsion will reduce the total free energy of the system by molecules in smaller droplets diffusing to larger ones.

5.2.2 Membrane Emulsification

Membrane emulsification involves injecting one phase through multiple pores (membrane) into a continuous phase in such a way that promotes droplet formation and detachment at the exit of the pore. Pressure applied to the disperse phase must be greater than that imparted by the continuous phase to promote permeation through the membrane. This is defined by the transmembrane pressure (P_{tm})(Equation 13), which must be positive for permeation to occur:

$$P_{tm} = P_d - \frac{(P_{c,in} + P_{c,out})}{2} \tag{13}$$

The P_{tm} can be calculated from the pressure imparted on the disperse phase (P_d) and the pressure of the continuous phase at the membrane inlet/outlet to the membrane ($P_{(c,in)}$/ $P_{(c,out)}$). The P_{tm} required to drive the disperse phase through a pore is known as the critical pressure (P_c) and can be calculated from the interfacial tension(γ), three way contact angle between the disperse phase, membrane surface and continuous phase (θ) and the average pore size (d_p) (Equation 14):[146]

$$P_c = \frac{4\gamma cos\theta}{d_p} \tag{14}$$

The calculation for P_c assumes the pores to be ideal cylinders, which is not the case with SPG membranes which are highly tortuous, and does not account for wetting of the membrane by the continuous phase. Due to this, it is often found experimentally that the required P_{tm} will be higher than the value calculated.[108] The average droplet diameter d_d of the produced emulsion is linearly related to d_p multiplied by a constant (c)(Equation 15):

$$d_d = cd_p \tag{15}$$

Based on literature sources, the value of c typically varies between 2.5-10 and represents factors other than the pore diameter which influence droplet size, such as continuous phase flow rate (Q_{cp}) and interfacial tension (γ).[102,146] This linear relationship means that the average droplet size scales with the average size of the pore from which they were produced.

To ensure consistent production of droplets it is important to understand how process parameters influence droplet formation. Figure 45 shows a membrane module containing a tubular membrane during droplet production. Potential droplet formation pathways are presented and will be discussed. Droplet production involves two main stages: droplet growth and droplet detachment.[146]

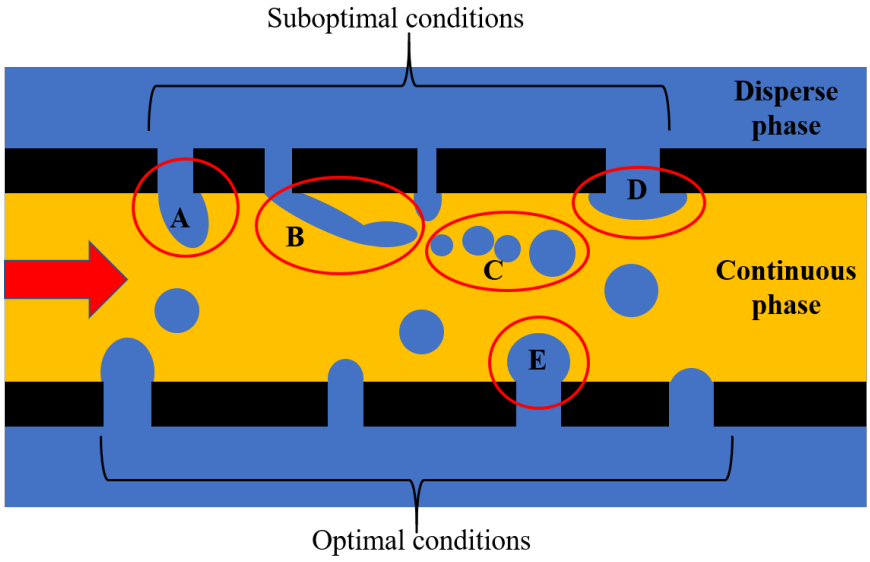

Figure 45: A schematic of the membrane module during operation highlighting the different droplet production processes. A: a high continuous phase flow rate compared with the interfacial tension, B: jetting production and the C: droplets produced, D: membrane wetted by the disperse phase and E: dripping formation process. Red arrow = direction of flow.

Figure 45 A shows the result of a high continuous phase flow rate compared with the interfacial tension. This is not necessarily an issue unless there are nearby pores and/or the disperse phase wets the membrane surface (Figure 45 E) which can lead to coalescence between growing emulsion droplets.[110] This can be avoided by reducing the wettability of the disperse phase on the membrane surface, as discussed in Chapter 4 section 4.5.[146] In the case of

cross-flow membrane emulsification, the disperse phase droplets protruding from the membrane pores are cleaved off by flowing the continuous phase parallel to the membrane surface generating a wall shear stress (τ_w)(Equation 16). The τ_w will impact on the growth period on the surface of the membrane and is therefore a major contributor to determining droplet size.

$$f = \frac{2\tau_w}{v_{cp}^2 \rho_{cp}} = \frac{16}{Re} \tag{16}$$

The τ_w can be calculated from the cross-flow velocity of the continuous phase (v_{cp}), the density of the continuous phase (ρ_{cp}), the friction factor (f) and the Reynolds number (Re), which is the ratio of inertial to viscous forces.[147] Re can be calculated from ρ_{cp}, v_{cp}, the inner diameter of the tubular membrane (D_{mem}) and the viscosity of the continuous phase (μ_{cp}).

$$Re = \frac{\rho_{cp} v_{cp} D_{mem}}{\mu_{cp}} \tag{17}$$

Generally, the average droplet size reduces as τ_w increases (Figure 46), due to a reduction in the period of droplet growth on the membrane surface.[102] This effect is more prevalent at a lower wall shear stress and tails off as τ_w increases as a minimum droplet size at which detachment can occur is reached.

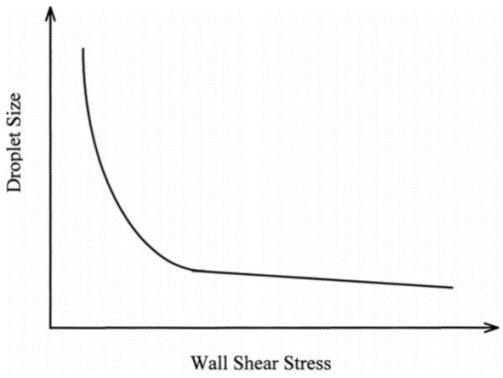

Figure 46: A schematic showing the relationship between average droplet size and wall shear force (τ_w). Reproduced with permission from Joscelyne *et al.*[102]

Droplet production can occur via two regimes, *dripping* or *jetting*. Dripping is the ideal process for droplet production, in which droplets are produced in a consistent manner, in terms of both size and rate, forming emulsions as close to monodispersed as possible, depending on the pore size distribution of the membrane (Figure 45 E). Jetting is the production of strand like structures which break up forming droplets (Figure 45 B, C) of varying diameter further down from the original channel. This process removes the system's control of the droplet size. Whether droplets are produced in a jetting or dripping manner is defined by a balance between the forces responsible for droplet growth and detachment.

Force Balances

The forces which dictate droplet growth on, and detachment from, the membrane surface are:

- F_D - the drag force imposed on the droplet via the flow of the continuous phase: f is the friction factor, k_x wall correction factor (1.7),[146] ρ_{cp} the density of the continuous phase, υ_{cp} the velocity of the continuous phase, r_d the radius of the droplet and τ_w the wall shear force (Equation 18).[146] During emulsion generation, r_d will increase leading to an increase in F_D.

$$F_D = 3\pi f k_x \rho_{cp} {\upsilon_{cp}}^2 {r_d}^2 = 10.205\pi {r_d}^2 \tau_w \tag{18}$$

- F_{In} - the inertial force which promotes permeation of the disperse phase into the continuous phase: ρ_{dp} is the density of the disperse phase, r_p the radius of the pore and v_d the velocity of the disperse phase (Equation 19).[147]

$$F_{In} = \frac{\rho_{dp}\pi {r_p}^2 {\upsilon_d}^2}{4} \tag{19}$$

- F_γ - the interfacial tension force represents the tension generated at the interface between the two phases, generating the droplet's spherical shape, and initially working against droplet detachment: γ is the interfacial tension (Equation 20).

$$F_\gamma = 2\pi\gamma r_p \tag{20}$$

- F_B - the buoyancy force which will have an influence when the disperse phase in less dense than the continuous phase, which is not the case for cellulose-OES emulsion droplets in SFO, therefore this force has no contribution in this system (Equation 21).

$$F_b = \frac{4}{3}\pi {r_d}^3(\rho_{cp} - \rho_{dp})g \tag{21}$$

As the droplet grows on the surface of the pore, F_D is not large enough to overcome the effects of F_γ acting against its detachment, leading to droplet growth via the disperse phase pressure and F_{In} (Figure 47 A). As the droplet grows into the continuous phase, the F_γ begins to work to minimise the surface energy and try to form a lower energy shape i.e. a sphere/droplet (Figure 47 B). Now the combined efforts of F_D and F_γ overcome F_{In} and the droplet will detach.

An increase in F_{In}, via a higher disperse phase pressure, can cause jetting due to F_D and F_γ being too low to cause detachment. This leads to growth of the disperse phase into the continuous phase in strands rather than a droplet. This is a very high energy structure but the driving force of the disperse phase causes its growth until F_γ has increased to the point that it prevails over F_{In} and the jet breaks down into numerous secondary droplets of varying sizes away from the pore.[147] Jetting can be overcome with a larger F_D by increasing the continuous phase flow rate promoting droplet detachment before the formation of strands, or by lowering F_{In} via a reduction in the disperse phase pressure (or P_{tm}). The F_{In} has been shown to have negligible effect during a dripping regime which is mainly controlled by F_D and F_γ.[147]

The balance of forces during droplet growth can be described by two different balances, depending on the shape of the droplet. Equation 22 if the droplet is assumed to be spherical and Equation 23 if deformed towards the membrane surface. In most cases the droplet will fall into range given by the two

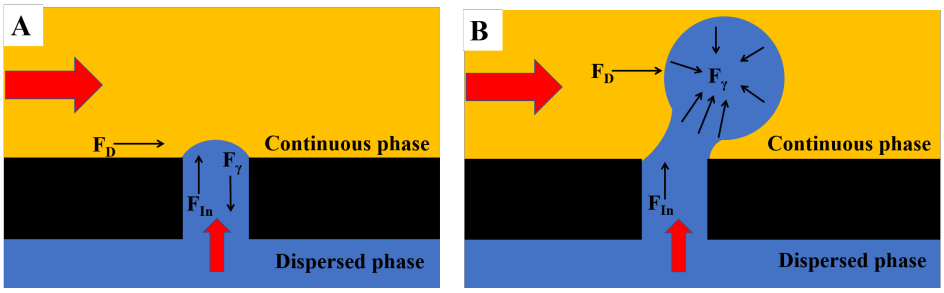

Figure 47: A graphical representation of the forces in effect during A: droplet growth and B: droplet detachment. The red arrow parallel to the membrane surface represents the flow of the continuous phase and the one perpendicular to it, the flow of the disperse phase (P_{tm}).

equations.[146]

$$(F_D + F_B)r_d = F_\gamma r_p \tag{22}$$

$$F_D + F_B = F_\gamma \tag{23}$$

Capillary and Weber Numbers

The balance of the forces dictating droplet growth can also be expressed as the dimensionless quantities the capillary number (Ca), which expresses the ratio of viscous to interfacial forces (Equation 24), and the Weber number (We), the ratio of inertial to interfacial tension forces (Equation 25), coupled with the Re already discussed.

$$Ca = \frac{\mu_{cp} v_{cp}}{\gamma} \tag{24}$$

$$We = \frac{\rho_{dp} {v_d}^2 d_p}{\gamma} \tag{25}$$

Pathak has shown through simulations the existence of a critical We from which dripping and jetting zones can be mapped when plotting Ca vs We (Figure 48).[147]

Jetting is seen at high We where the F_{In} is dominant over F_γ, usually

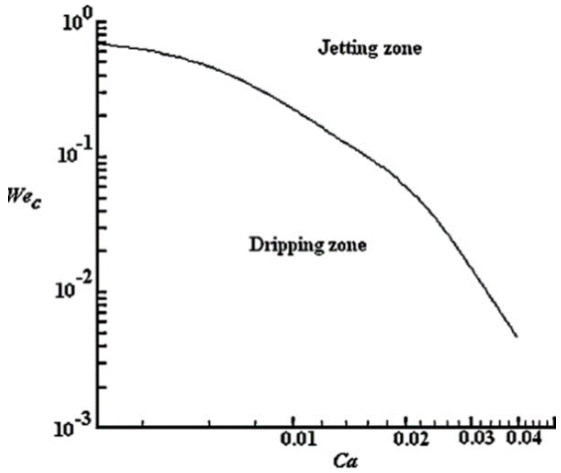

Figure 48: Reproduced graph of the Weber (We) and capillary numbers (Ca) highlighting the shift from a dripping to jetting regime. Reproduced with permission from Pathak.[147]

achieved when an excessive P_{tm} is applied. A high Ca, caused by a large F_D compared with F_γ, can in some cases lead to jetting when We is sufficiently high.[147]

Other Relevant Calculations

The flux of the disperse phase (J_d) represents the rate of product production and can be calculated from the membrane permeability (K), P_{tm}, μ_{dp} and the membrane thickness (L) via Darcy's law (Equation 26):

$$J_d = \frac{K\Delta P_{tm}}{\mu_{dp} L} \tag{26}$$

A higher P_{tm} leads to a greater amount of the disperse phase entering the continuous phase. This coupled with a high K will produce a high J_d and generally a larger average particle size.[108] Smaller pores, a more viscous disperse phase or a thicker membrane wall will have the inverse effect. The K of a membrane and can be defined as (Equation 27):

$$K = \frac{n{r_p}^2}{8\pi} \tag{27}$$

In which n is the number of uniform cylindrical pores of radius r_p. The K of a membrane, and therefore the flux of the disperse phase, is directly related to the number and size of the pores in the membrane. It is important to note that if number of pores is increased, without increase the size of the membrane, there is an greater chance of coalescence on the surface of the membrane between adjacent growing droplets.

The total flow rate of the disperse phase through the membrane (Q_{dp}) can be related to the flow rate through one pore (q) multiplied by the number of pores per area (n) (Equation 28).

$$Q_{dp} = q.n \tag{28}$$

The flow rate from a single pore can be calculated from the Hagen-Poiseuille (Equation 29) using the pressure drop (ΔP), radius of the pore (r_p), viscosity of the disperse phase (μ_{dp}) and thickness of the membrane (L).

$$q = \frac{\Delta P \pi {r_p}^4}{8\mu_{dp}L} \tag{29}$$

Knowing the porosity of the membrane (ε)(55 %, taken from Vladisavljevic *et al.*[141]) the number of pores in the membrane can be calculated from the surface area of the active membrane (A) (Equation 30) .

$$\varepsilon = \sum_{i=1}^{n} \frac{\pi {r_p}^2}{A} \approx \frac{n\pi {r_p}^2}{A} \rightarrow n = \frac{A\varepsilon}{\pi {r_p}^2} \tag{30}$$

The total flow rate of the disperse phase through the membrane can therefore be defined as (Equation 31):

$$Q_{dp} = \frac{\Delta P \pi {r_p}^4}{8\mu_{dp}L} \times \frac{A\varepsilon}{\pi {r_p}^2} \rightarrow \frac{A\varepsilon {r_p}^2 \Delta P}{8\mu_{dp}L} \tag{31}$$

5.2.3 Laser Scattering

The size of a particle can be determined from the angle and intensity of light that it scatters. Smaller particles scatter light to a larger angle from the incident beam compared with larger particles (Figure 49).[148] The intensity of light scattered from smaller samples is also lower that from large particles.[149]

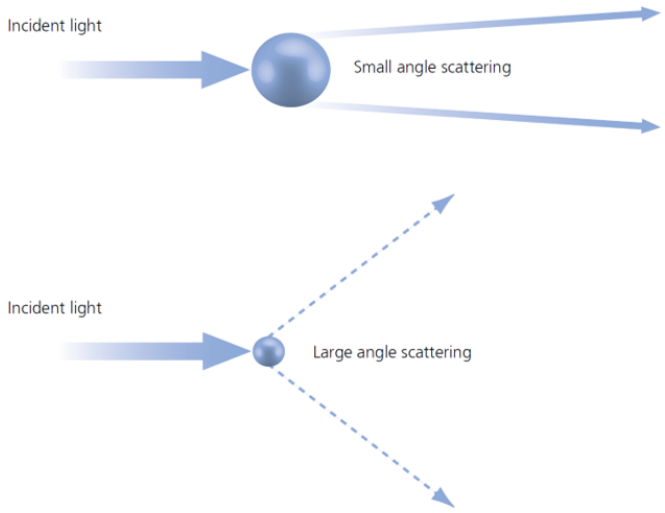

Figure 49: A schematic representing the scattering angle and intensity of light scattered by a small and large particle. Reproduced from *A Basic Guide to Particle Charaterization*.[148]

Mie Theory is used to determine expected diffraction patterns calculated from the refractive index of the particles and continuous phase as well as the particle size. Assuming particles to be perfect spheres, it is possible to back calculate to determine a particle's size from its scattering pattern.[124] If not spherical, the sample is assumed to be a sphere of equivalent volume to the particle volume measured.[149]

Particle size data is typically expressed as a volume weighted distribution in which the contribution of each particle relates to its volume, and expressed as a volume % of the total sample. Particle size data is sorted into bins with diameter ranges producing a final histogram. The data obtained can be expressed as percentiles; for example $Dv(50)$ (or median) is the volume at which 50% of the samples volume is above and below that value (similarly, $Dv(10)$ - 10 % of the sample is below this size, $Dv(90)$ - 90% of the sample is below this size).

The Sauter mean ($D[3,2]$ or surface area mean) is also a commonly quoted when comparing particle size and is calculated from the sum of the geometric mean (D) of each bin (Equation 32).[149]

$$D[3,2] = \frac{\sum_1^n D^3{}_i v_i}{\sum_1^n D^2{}_i v_i} \tag{32}$$

5.2.4 Scanning Electron Microscopy and Energy Dispersive X-Ray Spectroscopy

Using electrons to image materials enables a much higher resolution at high magnifications when compared with optical microscopy, primarily due to the shorter wavelength compared with visible light.[124] An electron beam can produce numerous signals from a sample, however for scanning electron microscopy (SEM) secondary electron and back-scattered electron signals are used. Secondary electrons are generated inelastically when hit by the incident beam. The electrons that are detected originate from a maximum depth of 10 nm in the sample, as being of lower energy those generated at a lower depth will reabsorb into the sample. Secondary electrons therefore provide topographical information about a material. Back-scattered electrons on the other had are generated elastically and have an energy similar to the incident beam so can be formed deeper within the sample. These provide compositional information about the material.[124] X-rays produced alongside electrons can also be detected to determine elemental compositions and mapping of a material (EDX).[124]

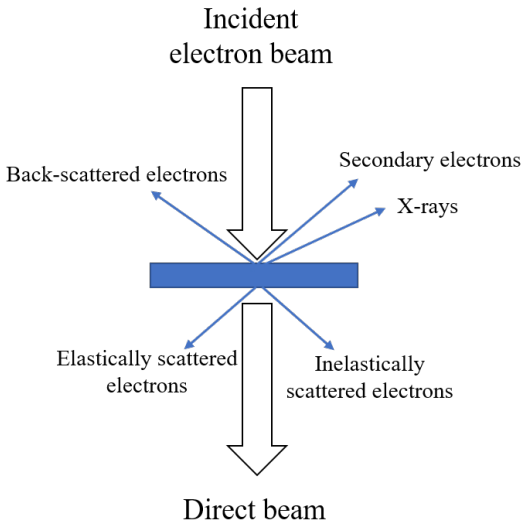

Figure 50: Signals that can be produced by an electron beam. Redrawn from *Colloid Science: Principles, Methods and Applications*.[124]

Results and Discussion

5.3 Membrane Emulsification

In this section, the design, building and improvement of a membrane emulsification rig used to form cellulose microbeads from emulsification of a cellulose-OES disperse phase in a sunflower oil (SFO)-Span 80 continuous phase will be outlined. Process parameters, as well as the composition of each emulsion phase, were investigated for their impact on the average bead size and particle size distribution. It has already been demonstrated in Chapter 4 that the viscosity of cellulose-OES solutions can be manipulated (section 4.3), which enabled processing via membrane emulsification. Treatment of a membrane has also been shown to result in an increase in the three phase contact angle between the disperse phase solution, membrane surface and continuous phase, promoting droplet detachment and lowering the risk of cross-pore droplet coalescence.

5.3.1 Design and Development of a Cross-Flow Membrane Emulsification Apparatus

A range of tubular membrane materials are available for use in cross-flow membrane emulsification.[150] SPG membranes were selected due to the adjustable contact angle between the disperse phase and the membrane surface via a known silinisation reaction, the relative ease of cleaning (calcination) and the range of dimensions (thickness, length) and pore sizes (of narrow pore size distribution) available, which provided potential avenues to scale up. SPG membranes are known to suffer from some drawbacks, including highly tortuous pores (i.e. not ideal cylinders), leading to the need for a greater P_{tm} pressures compared with the calculated P_c,[141] high economic cost and cornering of the market by a single supplier (SPG Technology Co, Ltd) which could lead to potential supply issues. The selected tubular SPG membrane was housed in a membrane module (Figure 51), the location of which can be seen in Figure 52 A, in which the continuous phase was flowed through the lumen of the membrane with the pressurised disperse phase allowed to permeate from the exterior to the interior of the membrane.

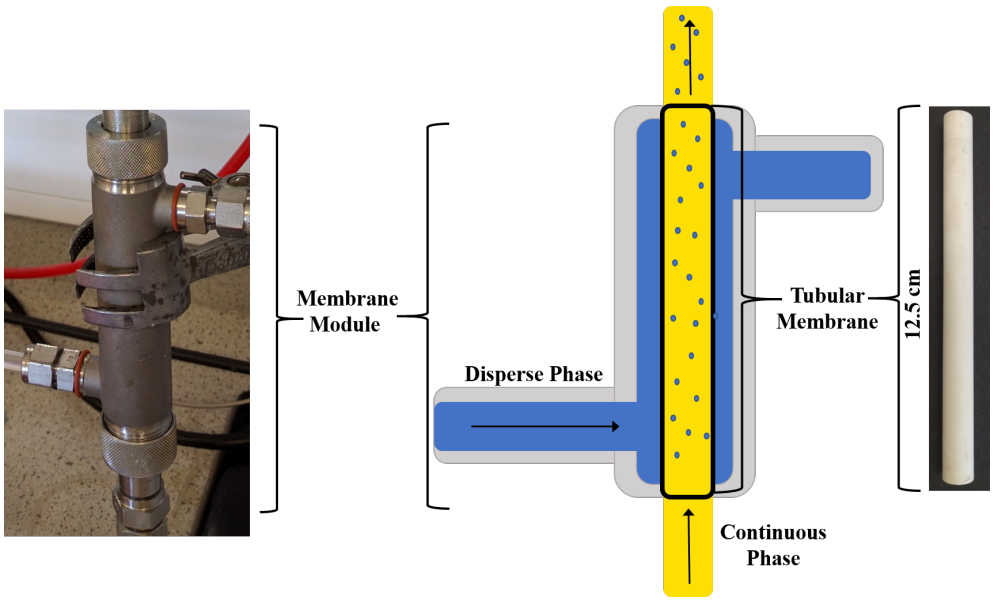

Figure 51: An image and schematic showing the membrane module used to house a Shirasu Porous Glass (SPG) tubular membrane. The modules location in the rig can be see in Figure 52 A.

A gear pump was selected to flow the continuous phase (Figure 52 B) as a constant high flow rate was required for long periods of operation to generate enough wall shear force to cleave off the viscous cellulose-OES solution droplets from the membrane surface.[112,150] Previously, the potential for breakup of the formed emulsion droplets in the gears of the pump has been noted.[151] This was less likely in the system applied here due to the high viscosity of the disperse phase. Nevertheless, this was thoroughly investigated and will be presented in due course. Air pressure (Figure 52 C) was used to drive the disperse phase through the membrane and the formed emulsion was recirculated though the system to generate a more concentrated emulsion. A "once through" approach, in which the emulsion was passed through the membrane once, would have required a large volume of continuous phase and would result in a very low volume fraction of disperse phase droplets, due to the flow rates required to generate a great enough wall shear force to promote droplet detachment and relatively low flux of the disperse phase through the membrane.[152] The continuous phase flowed in a loop via an open air stirred vessel which allowed for sampling and removal of the emulsion as well as heating of the continuous phase (Figure 52 D).

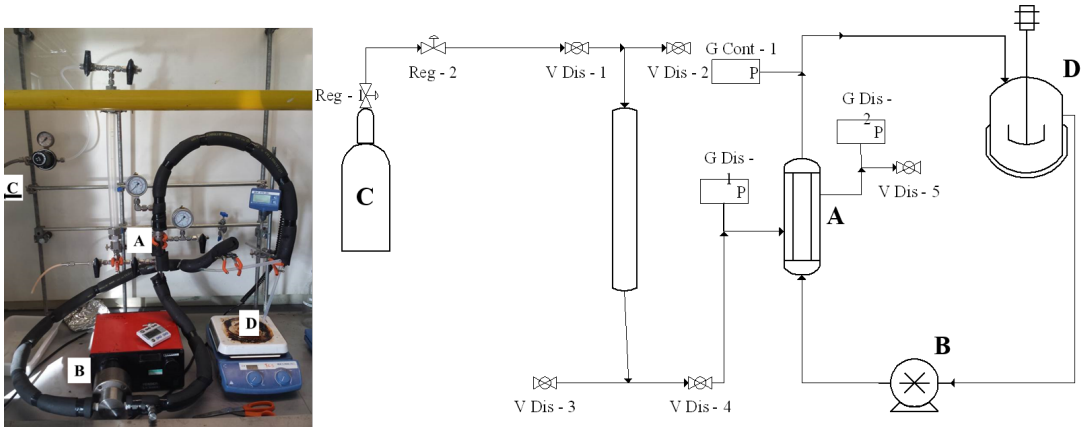

Figure 52: Picture and diagram of the initially developed cross-flow membrane emulsification rig developed. The A: membrane module, B: gear pump, C: gas cylinder use to pressurise the disperse phase vessel and D: stirred collection vessel are labelled.

Once the emulsion was formed, coagulation of the cellulose polymer from the cellulose-OES droplets was achieved by bringing the emulsion into contact with ethanol, which is partially soluble in the continuous phase (previous unpublished

results have shown SFO can tolerate between 12-13 wt% ethanol before a biphasic system results). Ethanol was also used for extraction of the cellulose solvent system (EMIMAc-DMSO) via repeat immersion of the cellulose materials in the anti-solvent, which could then be recycled via distillation.

Experimental Design - Controlling Cellulose Bead Particle size

The ability to control cellulose bead particle size using this first generation rig was assessed using a fraction factorial resolution IV experimental design varying four factors: 1) MCC concentration in the disperse phase (4 - 8 wt%), 2) continuous phase temperature (30 - 60 °C), 3) surfactant concentration in the continuous phase (0.25- 2.00 wt%) and 4) continuous phase flow rate (Q_{cp}) (0.4 - 2.4 $Lmin^{-1}$). A hydrophobised 10 µm pore size SPG membrane was used to disperse the emulsion under the experimental conditions listed in Table 9. In each experiment, the transmembrane pressure (P_{tm}) was kept below 0.1 bar (the lowest disperse phase pressure that could be accurately applied using the apparatus available).

Table 9: The experimental design to determine the effect of the cellulose concentration, continuous phase flow rate, continuous phase temperature and Span 80 concentration on the size of cellulose beads.

Experiment Number	Cellulose Concentration in Disperse phase (wt%)	Continuous Phase Flow Rate (Q_{cp}) ($Lmin^{-1}$)	Continuous Phase Temperature (°C)	Span 80 Concentration in Continuous phase (wt%)
1	4	0.4	30	0.25
2	8	2.4	30	0.25
3	4	2.4	60	0.25
4	8	0.4	60	0.25
5	4	2.4	30	2.00
6	8	0.4	30	2.00
7	4	0.4	60	2.00
8	8	2.4	60	2.00
9, 10 ,11	6	1.4	45	1.13

To ensure that variation in average bead size was occurring under the ranges chosen, experiments 1, 8 and 9 (experiments consisting of all low, high and mid values for each factor) were conducted first. Significant variation in the

particle size distribution of the cellulose beads generated (Figure 53) suggested that variation of the factors selected were influencing the sizes of beads produced.

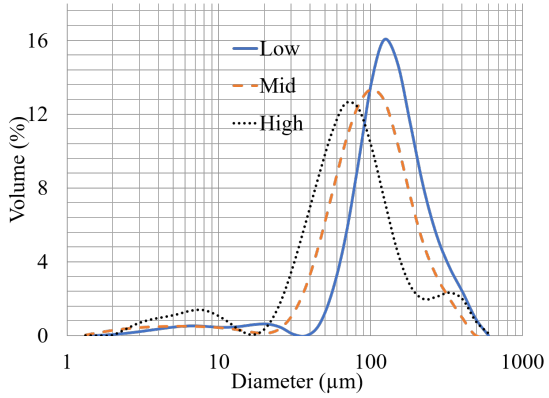

Figure 53: Particle size distributions for cellulose beads generated using the experimental conditions for Exp 1 (low), 9 (mid) and 8 (high) listed in Table 9.

Following the completion of the full set of the experiments (Figure S1), a model was successfully generated from the particle size data obtained for each cellulose microbead dispersion (Figure 54)($R^2 = 0.98$,$Q^2 = 0.90$). The average diameter ($Dv(50)$) of the dominant (by volume) peak was used to represent the average size of the beads.

Increasing Q_{cp} was shown to reduce the average size of the particles generated (Figure 54 B, D) via an increase in τ_w and F_D which imparted a short droplet growth period from the pore. This was the dominant factor in controlling average particle size (Figure 54 B). Increasing the MCC concentration in the disperse phase was shown to decrease the average diameter of the product suspension (Figure 54 B, D). Typically, increasing the disperse phase viscosity leads to an increase in droplet diameter, which suggested that the effect of cellulose concentration was not only a viscosity effect. It was shown in Chapter 4, Section 4.4 that a higher cellulose concentration led to slightly lower interfacial tension and therefore a more stable droplet, increasing the likelihood of smaller droplets. However, increasing the surfactant concentration, which reduced the interfacial tension, elevated the average particle diameter, which could be accounted for by the increased stabilisation of larger droplets typically produced when operating in a jetting regime (Figure 54 B) (Section 5.2). These larger droplets were shown to settle and form a disperse phase film on the base of

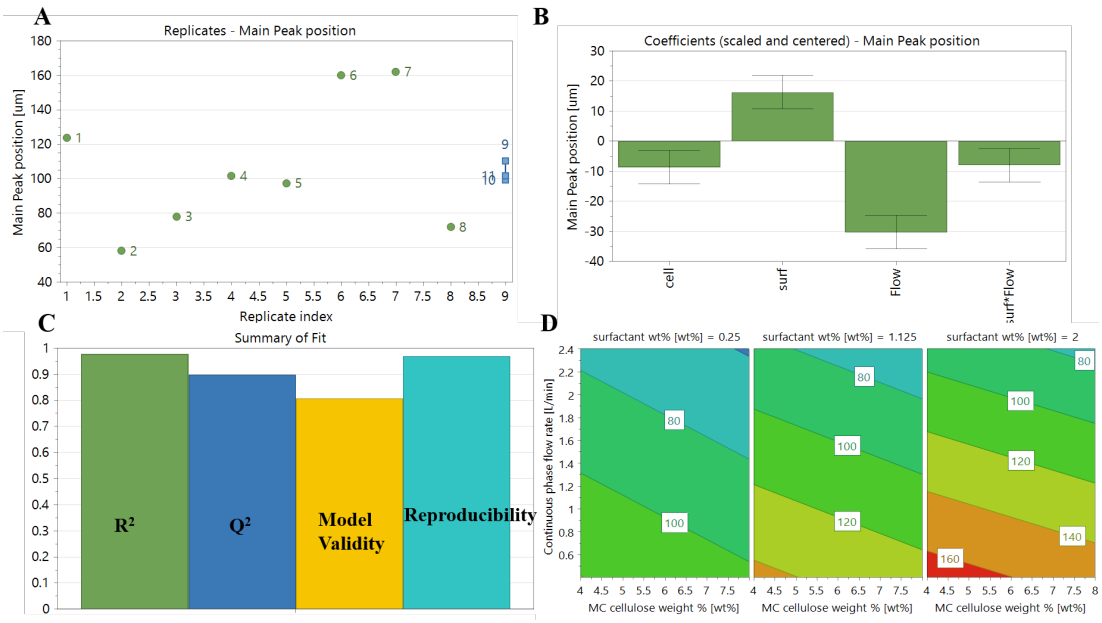

Figure 54: Overview of the experiments and model generated from the average diameter of the main particle size distribution of cellulose beads formed from the experimental conditions listed in Table 9. A: each experiment and the measured average peak position (μm), B: the effect of each factor on average peak position (cell = cellulose concentration, surf = surfactant concentration, Flow = continuous phase flow rate (Q_{cp}) and surf*Flow = an interaction term between the surfactant concentration and Q_{cp}), C: an overview of the model and D: a 3-D contour plot of the results of the model.

the collection vessel at lower surfactant concentrations (Figure 57 A) leading to the observed decrease in average bead size as the larger droplets were no longer dispersed, and therefore, not collected as beads. Stabilisation of these droplets with increased surfactant concentration would therefore appear as an increase in the average droplet diameter. A significant interaction was shown to exist between the surfactant concentration and flow rate of the continuous phase (Figure 54 B surf*Flow), increasing both factors concurrently led to smaller than expected droplets due to a shorter droplet growth period on the exit of the pore at higher Q_{cp} and surfactant concentrations (Figure 55).

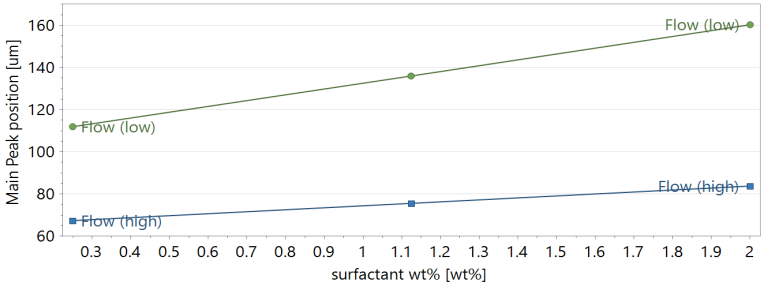

Figure 55: The interaction between continuous phase flow rate (Flow) and surfactant concentration.

As described previously (5.2.2), the detachment of an emulsion droplet is driven by the force balance between the wall shear force and interfacial tension, so it was not a surprise to find this interaction term. It was interesting to find that the temperature of the continuous phase had no significant effect on the size of the product beads, and so could be omitted from the model, as it has been shown to influence the viscosity of the disperse and continuous phases (discussed later, section 5.3.2) and therefore the drag force (Chapter 4, Section 33). Potentially the effect of temperature was subtle and dwarfed by the other factors.

Each set of beads also exhibited a small distinctly separate, population of particles with average diameters of < 10 µm. This was a consistent feature of almost every product and was confirmed by optical microscopy to be cellulose microbeads. Multi particle size regimes could potentially be useful for some applications, in which high packing of material is required, as suspensions containing a range of particle sizes promote much greater packing.[86] In any case, this consistent feature will be investigated further later in the chapter.

There was however, a potential issue with a lack of reproducibility between repeat experiments in the particle size distributions. Comparing the size distributions obtained for beads produced from the three mid point experiments (9, 10, 11), highlighted a significant difference between one of the experiments (Figure 56 A, Exp 9).

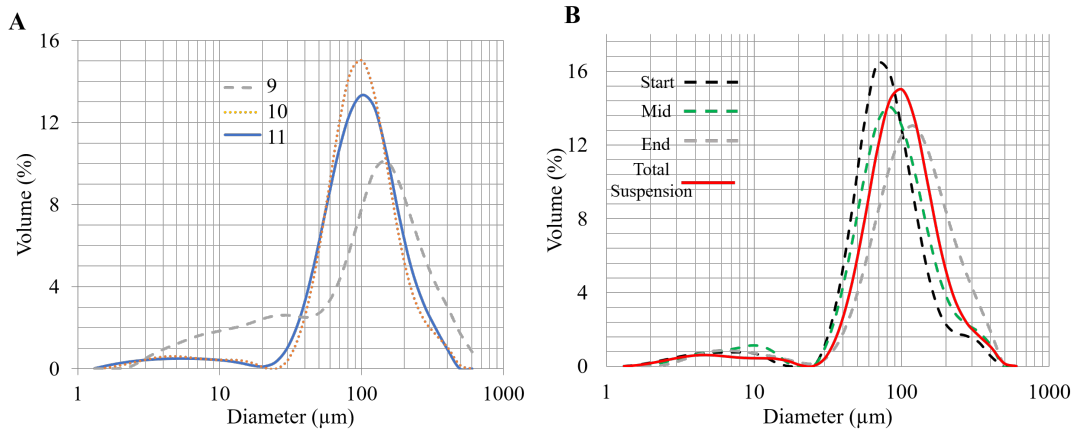

Figure 56: Particle size distributions for A: cellulose beads generated using the mid point experimental conditions (Exp 9, 10 and 11) listed in Table 9 and B: Exp 9 (mid) which were collected at the start of emulsion generation, at the mid point and end of emulsion generation. The particle size distribution for the final extracted suspension is also shown.

The same 10 μm membrane was used for each experiment and therefore the reasoning must lie in the operation of the system or an attribute of the emulsion formed, potentially coalescence or Ostwald ripening. To test whether this was the case, a mid point experiment was again conducted and allowed to cycle through the system. Three aliquots were removed from the bulk emulsion at different time intervals (Figure 56 B).

The first sample taken, which had not been cycled back through the system, showed the narrowest size distribution which broadened with operation time/number of cycles, with the final sample having the widest distribution of sizes (Figure 56 B). This suggested that coalescence or Ostwald ripening was occurring. It was found that the collection vessel (Figure 52 D) contained a film of disperse phase on the bottom after each run, which became more prevalent when the vessel was heated. In the case of the room temperature experiments, it was found that the film formed due to the close proximity of the tube outlet and

vessel bottom, meaning that when the emulsion exited the tube it was forced into the base of the vessel, forming a film (Figure 57 A). However, cellulose droplets and therefore beads were successfully produced even with this film formation, albeit with significant loss of product.

Rig and Process Development

During operation of the initially developed rig (Figure 52) it became clear that improvements could be made to the apparatus and procedure. To overcome the formation of a disperse phase film, the collection vessel was replaced with an overflow chamber, effectively closing the flowing route for the continuous phase which overcame the coalescence/ripening issue (Figure 57 B). This ensured that the emulsion was continuously suspended and the majority of the emulsion was passed directly into the anti-solvent during product extraction. As continuous phase temperature was shown to not have an observable effect on the produced cellulose microbead size (section 5.3.1) and led to partial destruction of the emulsion (film formation), all subsequent experiments were run at ambient temperature (no heating).

Coalescence of the emulsion droplets could also potentially occur upon addition of the emulsion to the anti-solvent, ethanol. This could have occurred via the dissolution of the surfactant (Span 80) from the interface of the emulsion droplet, by the anti-solvent, prior to full coagulation and hardening, and therefore stabilisation, of cellulose contained within the droplet. This may have increased the potential of coalescence or, in major cases, complete destruction of emulsion and formation of a disperse phase film on the base of the collection vessel. This offered a potential explanation to why an increase in surfactant concentration was leading to larger beads (Section 5.3.1, Figure 54) as at lower surfactant loadings, one would expect a greater amount of film formation primarily generated from larger droplets, whilst smaller droplets remained suspended. Increasing the surfactant amount would stabilise these larger droplets making it appear as there were more in the final system.

The formation of a film could be overcome by increasing the coagulation of cellulose when extracted from the system. This was achieved by increasing

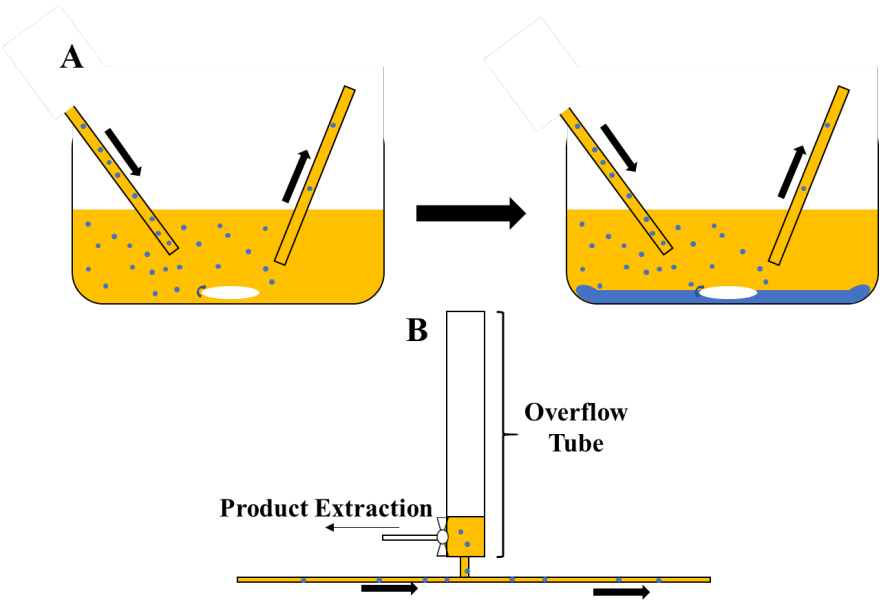

Figure 57: Diagram showing A: the generation of a disperse phase film in in the collection vessel (Figure 52 D) throughout operation of the rig described in Figure 52 and B: how this was rectified with the addition of an overflow chamber and product extraction tube (Figure 60).

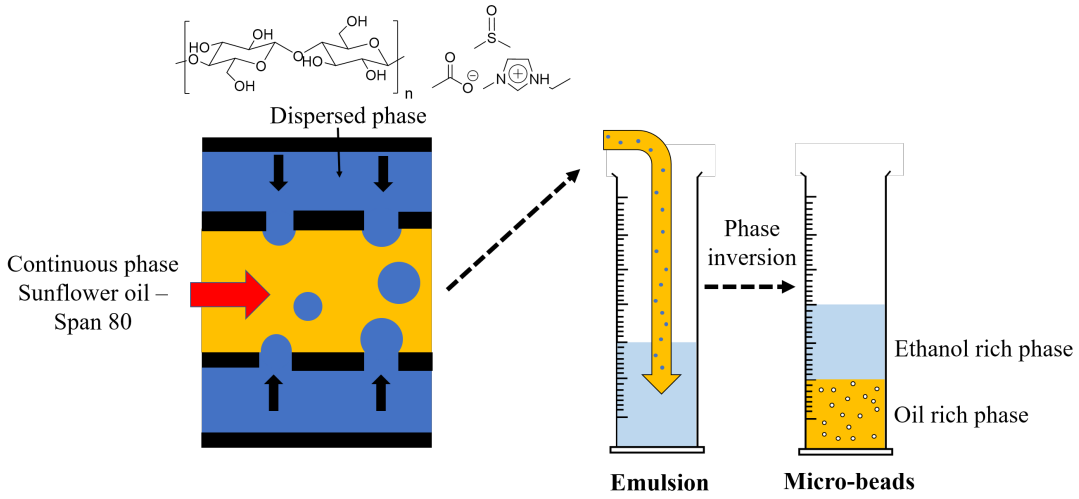

Figure 58: A graphical representation of the membrane emulsification - phase inversion process used to synthesise cellulose microbeads.[142]

emulsion contact with the upper ethanol rich phase by passing the emulsion into a column of anti-solvent and keeping the exit of the tube in contact with the ethanol concentrated layer (upper) (Figure 58). This ensured that the outer shell

of the droplets had been hardened sufficiently to prevent coalescence and allowed enough distance between the tube and vessel base to prevent film formation by increasing the time the droplets were exposed to the ethanol rich layer (Figure 58). This improved product extraction process also helped reduce the number of "tailed" beads witnessed in the final cellulose bead dispersion (Figure 59), a result of the beads being exposed to a shear force before being fully hardened. Tailing could potentially be a problem when the beads are used in a final application, as the "tails" represent areas of mechanical weakness and therefore increase the likelihood of material breakdown.

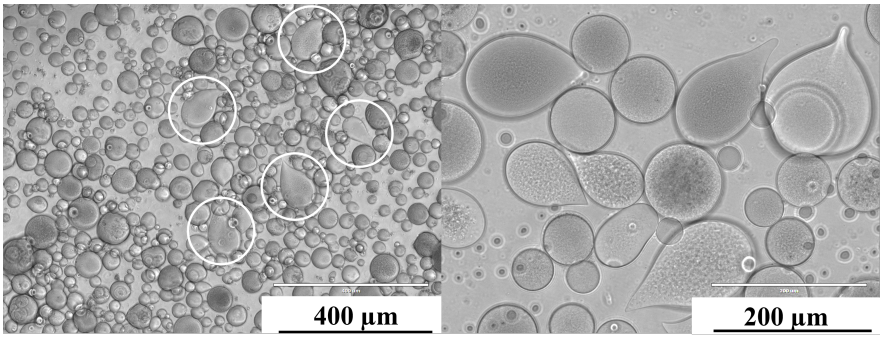

Figure 59: Optical micrographs of "tailing" witnessed in the majority of samples produced from the first cross-flow apparatus developed.

The pressure applied to the disperse phase is a leading factor in controlling droplet size distribution (dripping vs jetting regimes, Section 5.2.2) and therefore needed to be precisely monitored and accurately controlled. The addition of a transducer (Figure 60 A), able to measure the pressure applied to the disperse phase digitally, gave a more precise measure, and therefore application of pressure.

Further, to aid in detection of droplets once permeated through the membrane, the cellulose-OES was dyed with Rose Bengal (Figure 61). This enabled more accurate visual determination of the emulsion once it had been formed by imparting a colour change to the emulsion droplets in the continuous phase in addition to the increase in turbidity. Extended periods of storage of the dyed cellulose-OES solution was found to lead to discolouration (Figure S2), so the disperse phase was dyed just before emulsification.

The addition of a continuous phase tank next to the inlet of the pump (Figure 60 B) enabled removal of the formed emulsion without having to cease

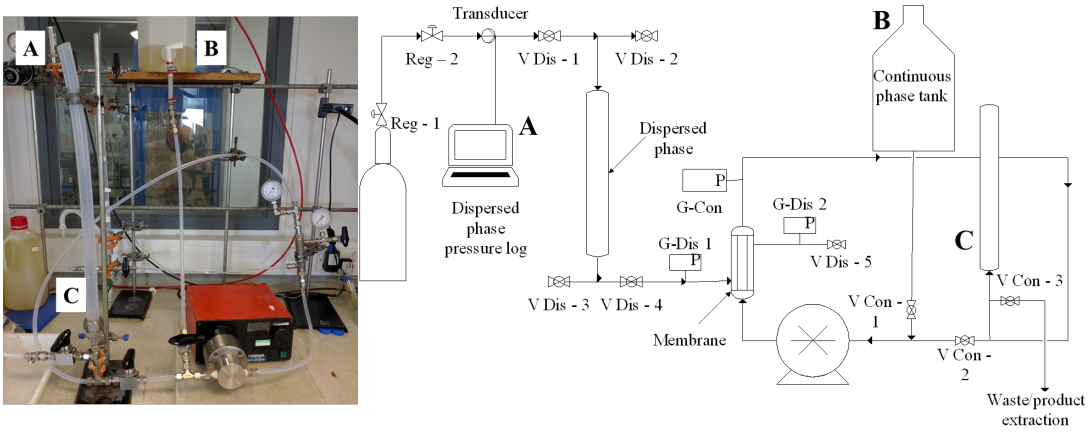

Figure 60: Picture and diagram of the second iteration of a cross-flow membrane emulsification rig with the addition of a disperse phase pressure transducer (A), continuous phase tank (B) and overflow/product extraction/sampling tube (C).

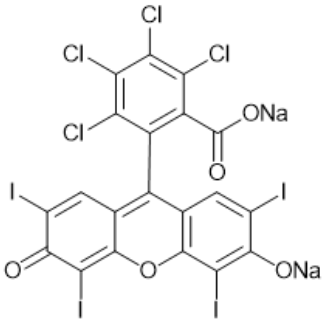

Figure 61: The structure of the dye Rose Bengal, used to stain the disperse phase to aid in emulsion detection.

emulsion production. Opening the valve to the continuous phase tank pulled fresh continuous phase into the system, driving the emulsion into the overflow tubing, which could then be removed from the system directly into the anti-solvent via the product extraction tube (Figure 57 B). This could be accomplished whilst maintaining disperse phase permeation through the membrane, enabling continuous emulsion production.

The redeveloped cross-flow membrane emulsification rig (Figure 60) and process for bead formation overcame many of the problems associated with the previous design (Figure 52). One potential issue that remained from the initial rig design was the need to discard/remove material produce during "start-up". When starting production, the first droplets formed showed particle size distributions

different to those of subsequent samples (Figure 62). All subsequent runs remained consistent as long as the disperse phase was continuously permeating the membrane. The removal of one run was minimal in terms of product loss.

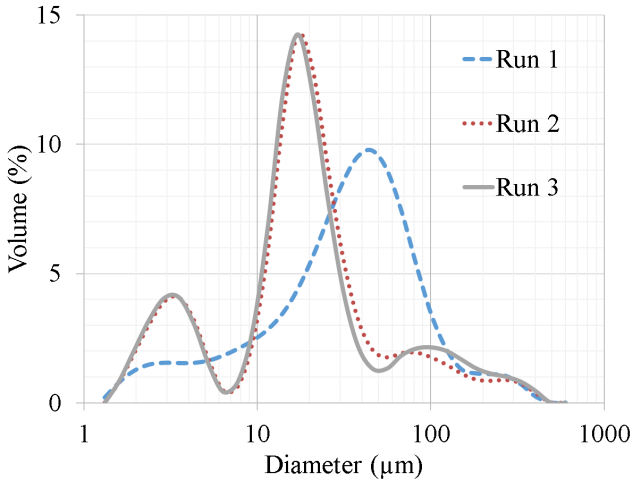

Figure 62: Beads produced using the second generation membrane emulsification rig showing the change in particle size distribution of cellulose microbeads between subsequent runs collected at 30, 40 and 50 mins of operation. The parameters used were as follows: a 10 μm membrane using a 8 wt% microcrystalline cellulose solution dissolved in [EMIm][OAc]:DMSO (30:70, w/w) with a transmembrane pressure of 0.02 bar and a continuous phase of 2 wt% Span 80-sunflower oil at a flow rate of 2.4 $Lmin^{-1}$.[142]

5.3.2 Controlling Particle Size

As with the first generation rig, all cellulose microbead samples produced using the improved system exhibited multimodal particle size profiles and, in particular, the appearance of a population of beads with diameter significantly below that of the membrane pore nominal size of 10 μm (Figure 70). With this improved cross-flow system, the effect of recirculating the emulsion through the gear pump was reassessed to test the hypothesis that this could lead to breakup of droplets.[114] A time resolved experiment was conducted in which an emulsion was produced and allowed to circulate through the continuous phase system with samples extracted at 15 minute intervals.

The volume percent of the population of microbeads with diameter <10

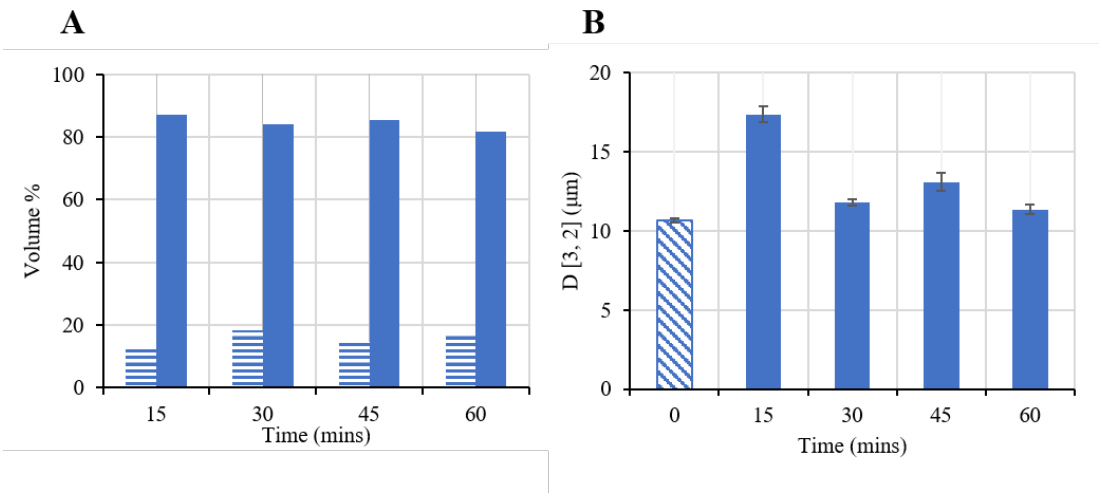

Figure 63: Comparison of time resolved data A: the relative quantity of beads, expressed as volume percent, of the population with diameter <10 μm (stripped bars), with that of the main population (solid bars) and B: the Sauter mean diameter, $D[3,2]$, of the samples collected at various time intervals (the striped bar denotes the value collected from a repeated experiment immediately after extrusion was halted).[142]

μm remained constant (Figure 63 A), and the Sauter mean diameter for each sample did not reduce (Figure 63 B), suggesting that breakup in the pump was not the main source of these small beads, but that these arose from a constant factor in the experiment. Along with this, a very small number of larger beads (invisible in number based distributions) were also observed in the particle size distributions. Upon close examination of the inner surfaces of SPG membranes, occasional "pits" on the membrane surfaces into which pores extruded (Figure 65), were observed (Figure 64). It was postulated that these could be promoting droplet coalescence on the surface of the membrane (Figure 65).

Some other researchers have also raised the hypothesis that the undulating nature of the membrane surface could lead to "shielding" of the wall shear force imparted by the continuous phase.[150] A droplet growing in a "trough" on the membrane surface would be expected to be subject to a lower wall shear force compared to growth on a "hill". Optical micrographs confirmed that the artefacts responsible for the <10 μm distribution were beads (Figure 66). These factors inherent to the membrane could have been leading to the polydispersed distributions measured. Due to these small beads being a consistent artefact

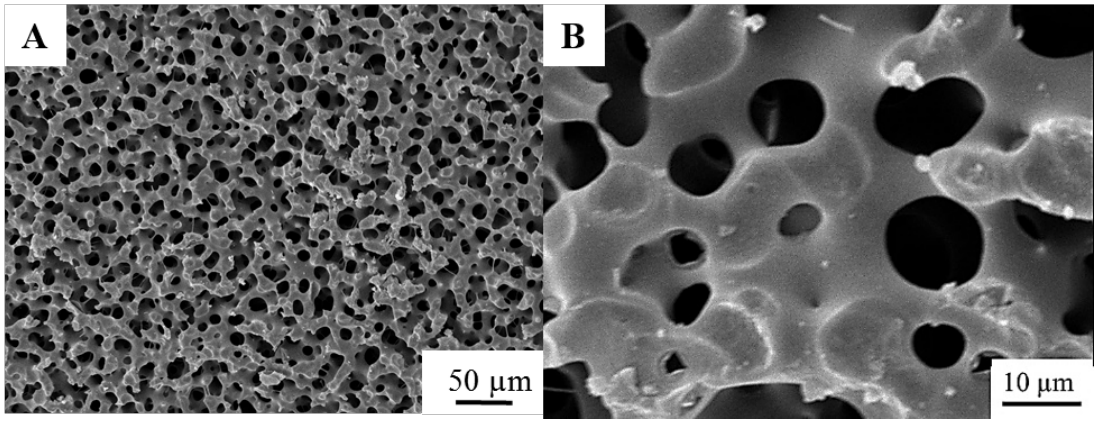

Figure 64: SEM micrographs of the inner surface of the SPG membrane employed. A: Showing a large part of the surface and B: at higher magnification. While the majority of pores reflect the 10 μm pore size described, it is clear, in the closeup view, that variable size pores did exist and that some pores combine to form surface "pits" (not larger pores), which could result in coagulation of forming droplets (Figure 65).[142]

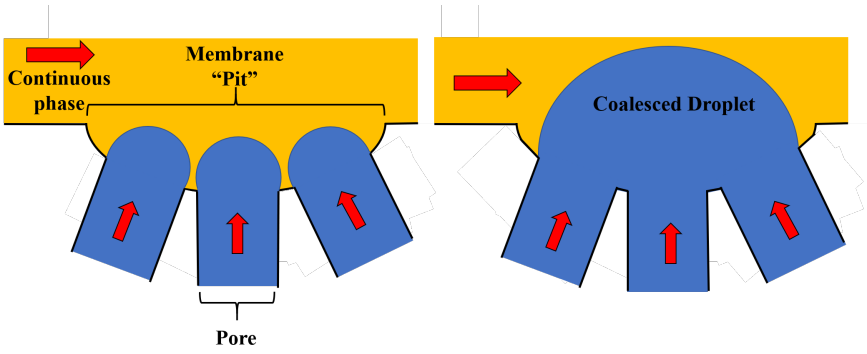

Figure 65: Graphical representation of the potential effect of pores exiting into a larger pit on the surface of the membrane.

in all experiments, the dominant peaks (by volume) for each experiment were compared in subsequent experiments.

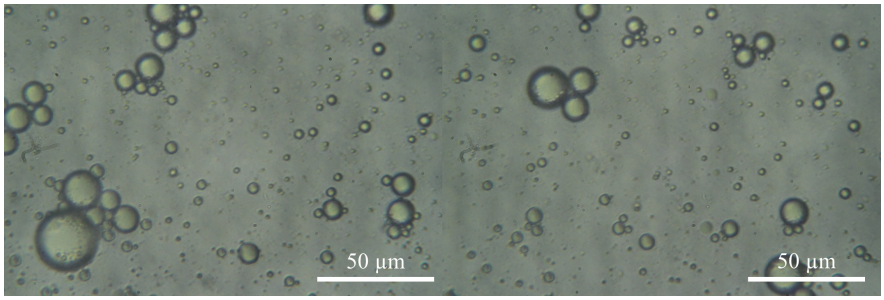

Figure 66: Optical micrographs highlighting the presence of microbeads of $<\sim 10$ μm in diameter, a feature which was consistent between all samples.

An investigation into the effect of surfactant concentration on average microbead size was conducted in an attempt to determine an optimal continuous phase composition (surfactant concentration).

Surfactant concentration[1]

In a previous chapter (Chapter 4: Sections 4.4 and 4.5), it was found that the surfactant concentration was the foremost factor in controlling the interfacial tension (γ)(Figure 36) of the cellulose-OES emulsion droplet as well as the contact angle of said droplet on the membrane surface (Figure 41). Increasing the surfactant concentration decreased the γ and contact angle (represented in Figure 67). One would therefore expect that altering the surfactant concentration would influence the final microbead size due to its impact on the force balance which defines droplet growth and detachment from the membrane surface.

To test the effect of interfacial tension on bead size and indeed the size distribution, three continuous phase compositions with varying concentrations of Span 80 (0.25, 1.13 and 2.00 wt% in SFO) were used for emulsion generation. Both the disperse phase composition (8 wt% MCC in 70:30 DMSO:[EMIm][OAc] (w/w)) and Q_{cp} were kept constant to highlight the surfactant effect. A low Q_{cp}

[1]Some experimental data in this section was collected in conjunction with James Close during an MEng project, a full list of which can be found in the appendix.

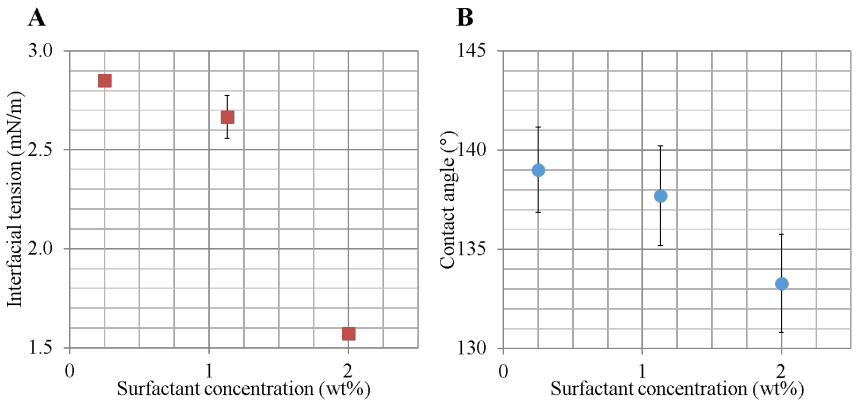

Figure 67: The effect of changing surfactant concentration (0.25, 1.13, 2 wt% Span 80 in sunflower oil) on A: the interfacial tension (mN/m) and B: the contact angle (°) of a droplet of 8 wt% MCC dissolved in 70:30 DMSO:[EMIm][OAc] (w/w). Values are listed in Table 10.

was used (0.4 Lmin^{-1}, wall shear force = 3 Pa) as the interfacial tension has been shown to have a greater effect on droplet size at lower flow rates.[147]

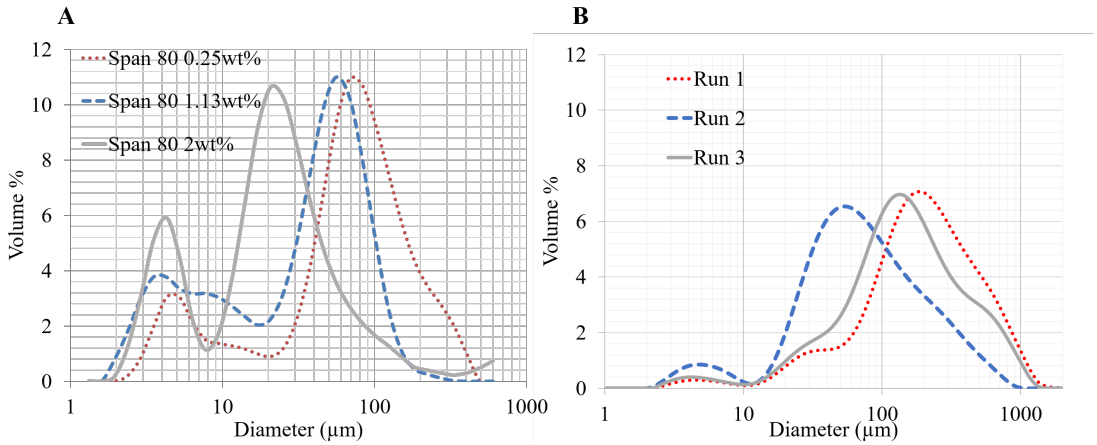

Figure 68: Particle size distributions comparing microbeads produced from a solution of 8 wt% cellulose dissolved in 70:30 (w/w) DMSO:[EMIm][OAc] using a 10 μm pore membrane (d_p) and a continuous phase flow rate of of 0.4 Lmin^{-1}(Q_{cp}) using A: varying concentration of Span 80 dissolved in SFO and B: pure sunflower oil after the "start-up" material had been discarded. Experimental conditions for A are documented in Table 10.

An increase in surfactant concentration led to a decrease in interfacial tension (Figure 67) and therefore a reduction in the period of growth of the droplet on the surface of the membrane, producing beads of progressively smaller

Table 10: List of experimental conditions used to produce cellulose microbeads using a 10 μm pore membrane (d_p) and a continuous phase flow rate of 0.4 Lmin^{-1}(Q_{cp}). The disperse phase consisted of 8 wt% cellulose dissolved in 70:30 (w/w) DMSO:[EMIm][OAc]. The interfacial tension (IFT) and contact angle (CA) values are also recorded. The distributions are presented in Figure 68 A.

Distribution	Span 80 (wt%)	P_{tm} (bar)	P_c (bar)	IFT (mN/m)	CA (°)	$D_{peak\ max}$ (μm)	$fwhm$ (μm)	Ca	We
A	0.25	0.03	0.009	2.85 (±0.01)	139 (±2)	76	113	1.1	5.0×10^{-10}
B	1.13	0.02	0.008	2.67 (±0.11)	138 (±3)	57	66	1.2	2.44×10^{-10}
C	2.00	0.04	0.004	1.57 (±0.02)	133 (±2)	22	31	2.1	1.7×10^{-9}

average diameter (Figure 68 A), a relationship which has also be found in the literature.[147] This can be seen in the reduction of $D_{peakmax}$ with increasing surfactant concentration (Figure 68 A, Table 10). Increasing the surfactant concentration also produced narrower particle size distributions with respect to the main peak ($fwhm$ 113 to 31 μm). It appeared that the increased stability imparted by a higher surfactant concentration gave a narrower spread of particle sizes, potentially due to increased interface coverage by the surfactant reducing the likelihood of coalescence (Section 5.2.2).

Using a continuous phase without a surfactant (pure SFO) lead to broad particle size distributions as well as an increase in the average particle size (Figure 68 B). Optical micrographs also highlighted the presence of non-bead material in the dispersion when no surfactant was used (Figure 69 A), which appeared to be due to beads being set mid coalescence (Figure 69 B). This suggested instability of the droplets before coagulation of cellulose from the droplets when in the anti-solvent, as did the inconsistency between the particle size distributions between subsequent runs (Figure 68 B Run 1-3).

Clearly, Span 80 had a stabilising effect on the droplets and a great impact on producing beads of consistent shape and size. Due to this, the subsequent experiments utilised 2 wt% Span 80 in the continuous phase to fully stabilise the emulsion droplets.

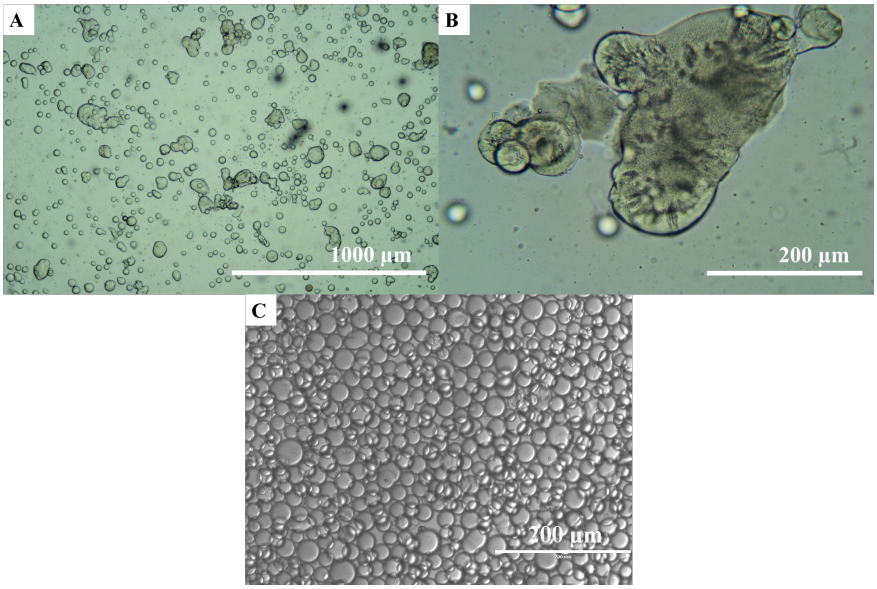

Figure 69: Optical micrographs of A, B: non-spherical particles resulting from the lack of a surfactant in the continuous phase (particle size distribution - Figure 68 B) and C: beads produced when using a continuous phase containing 2 wt% Span 80 (particle size distribution - Figure 68 A). Beads had been set by phase inversion in ethanol, filtered and redispersed in water.

Capillary and Weber Numbers

Pathak[147] highlighted a clear transition between dripping and jetting droplet production regimes expressed in terms of dimensionless (Ca) and Weber (We) numbers, represented in Equations 24 and 25. The effect of the disperse phase composition (MC wt%), transmembrane pressure (P_{tm}, selected based on the critical pressure, P_c), disperse phase velocity at one pore, v_d, and total disperse phase flow rate, Q_{dp}, along with the continuous phase flow rate, Q_{cp}, on Ca and We for the range of conditions and samples studied herein are presented in Table 11. Ca and We were calculated from measured values of interfacial tension (γ), density of the disperse phase (ρ_{dp}) as well as the viscosity of the continuous phase (μ_{cp}) determined in Chapter 4.

The membrane pore size and composition of the continuous oil phase were kept constant in these sets of experiments and will be investigated in subsequent sections. As discussed in Chapter 4, the interfacial tension (γ) showed little variation with changing cellulose concentration in the disperse phase (4 or 8 wt%

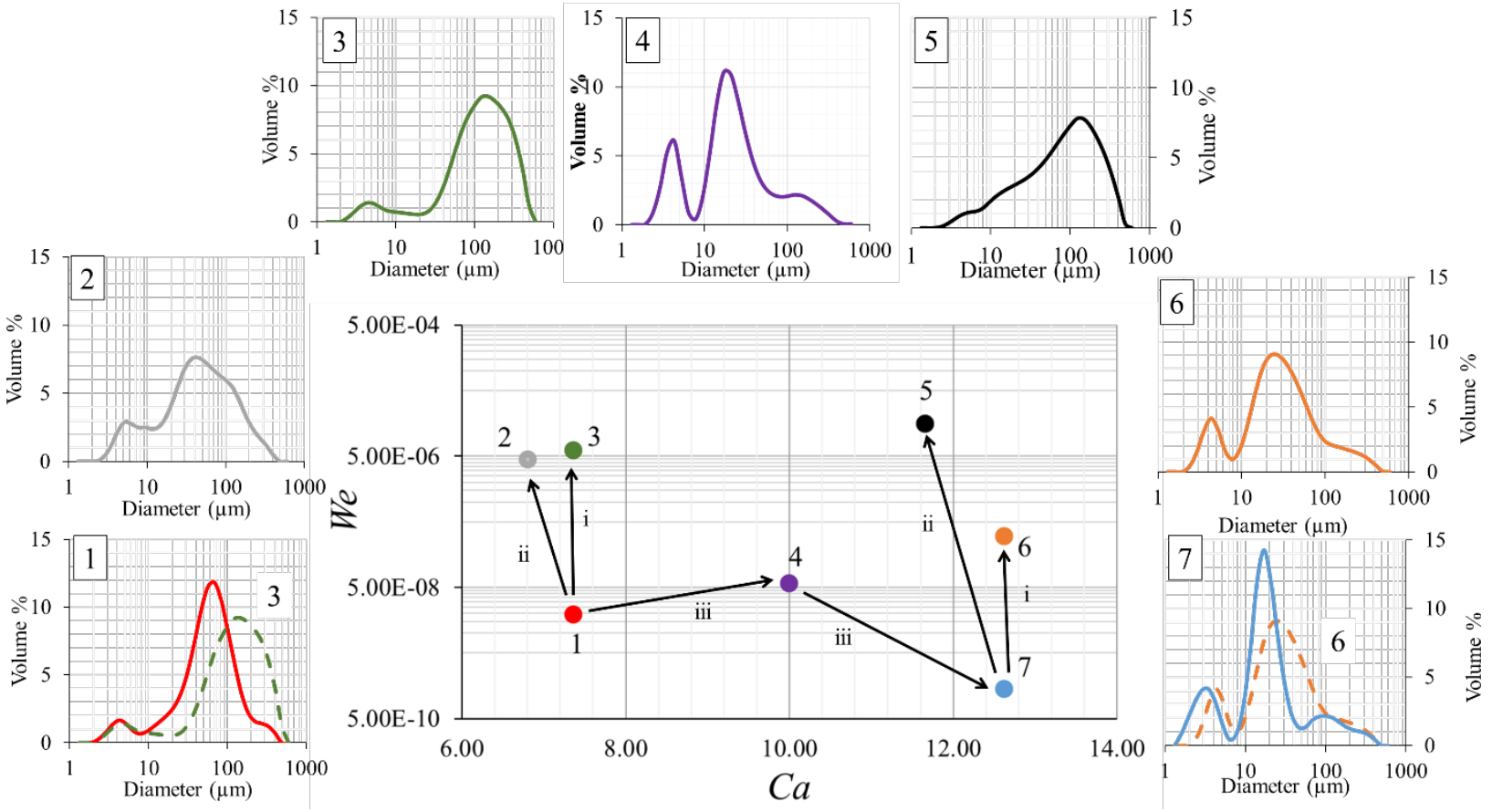

Figure 70: Particle size distributions for a range of cellulose microbead dispersions as a function of the Ca and We values used to produce their corresponding emulsions (Table 11). For sample 1 and 7, the higher P_{tm} jetting counterparts (samples 3 and 6 respectively) are also shown by dashed lines. The central chart depicts the changing values of Ca and We for all sets of conditions and arrows represent **i:** increase of transmembrane pressure (P_{tm}) and therefore the disperse phase velocity (v_d); **ii:** reduction of the concentration of cellulose in the disperse phase (from 8 to 4 wt%); and **iii:** increase of the continuous phase flow rate (Q_{cp}) and therefore the continuous phase velocity (v_{cp}) from 1.4 to 1.9 to 2.4 Lmin^{-1} for samples 1, 4 and 7 respectively.[142]

Table 11: Disperse phase composition, process parameters, calculated values for We and Ca and parameters describing microbead size and distribution for the range of samples represented in Figure 70. The continuous phase in all cases consisted of Sunflower oil with 2 wt% Span 80.

Sample	Cellulose wt%	Q_{cp} ($Lmin^{-1}$)	P_{tm} (bar)	v_d (ms^{-1})	Q_{dp} ($Lmin^{-1}$)	We	Ca	$D_{peak\ max}$[a] (μm)	$fwhm$[b] (μm)
1	8	1.4	0.02[c]	5.19×10^{-5}	6.1×10^{-3}	2.0×10^{-8}	7.4	65	86(3)
2	4	1.4	0.03[d]	8.22×10^{-4}	9.6×10^{-2}	4.5×10^{-6}	6.8	42	144(10)
3	8	1.4	0.25	9.22×10^{-4}	1.1×10^{-1}	6.1×10^{-6}	7.4	135	318(19)
4	8	1.9	0.03	8.98×10^{-5}	1.1×10^{-2}	5.8×10^{-8}	10.0	19	21(1)
5	4	2.4	0.05	1.53×10^{-3}	1.8×10^{-1}	1.5×10^{-5}	11.7	135	281(16)
6	8	2.4	0.06	2.03×10^{-4}	2.4×10^{-2}	3.0×10^{-7}	12.6	25	51(1)
7	8	2.4	0.01	1.41×10^{-5}	1.6×10^{-3}	1.4×10^{-9}	12.6	17	14(1)

[a] Mode at peak maximum for dominant peak, [b] $fwhm$, full width half maximum,

[c] $P_c = 0.004$ bar; applicable to all 8 wt% cellulose samples,

[d] $P_c = 0.005$ bar; applicable to all 4 wt% cellulose samples.

cellulose in the OES) (Section 4.4 Figure 36) therefore Ca was solely influenced by the value of the velocity of the continuous phase (v_{cp}). Similarly, the We was mainly influenced by the velocity of the disperse phase (v_d) as there was found to be little variation in the density of the disperse phase (ρ_{dp}) within the range of composition studied (Chapter 4, Figure 42).

Applying a $P_{tm} \leq 7.5 \times P_c$ to an 8 wt% cellulose disperse phase led to the formation of dispersions of cellulose microbeads with a narrower size distribution (for the main population of beads). As mentioned previously, the calculated P_c (Equation 13) does not account for two major effects that influence the pressure required to drive the disperse phase through the membrane pore, that being the inherent tortuosity of SPG membrane pores[141] and the high viscosity of the cellulose disperse phase., hence the fairly high P_{tm} required. However, optimal distributions, with this system, were achieved for continuous phase flow rates of 1.4, 1.9 and 2.4 $Lmin^{-1}$ (Figure 70, samples 1, 4 and 7), representing the three lowest values of disperse phase velocity (v_d), and therefore We values (Table 11). On increasing v_d (indicated by arrow i, Figure 70), a transition occurred from a dripping to a jetting regime in emulsion droplet production, reflected in a broadening of the main particle size distribution (Figure 70 – dashed lines in

sample 1 and 7 graphs). A similar increase in polydispersity was also observed upon reduction of the concentration of cellulose in the disperse phase (Figure 70, arrow ii). This arose from the inverse relationship between the total flow rate of the disperse phase (Q_{dp}) and the viscosity of the disperse phase (μ_{dp}) defined in Equation 31 (derived in section 5.2.2). The less viscous 4 wt% solution was therefore extruded from the membrane pores at a much higher rate (lower We) than its 8 wt% counterpart, due to its lower viscosity: 0.13 versus 1.18 Pa.s (Figure 33).

The force balance between the wall shear force (τ_w), generated by the mobility of the continuous phase, and the interfacial tension is responsible for cleavage of the growing emulsion droplets from the surface of the membrane.[146] Here, as the interfacial tension remains constant, the continuous phase flow rate (Q_{cp}) determined the growth period of a droplet. The Q_{cp} of 1.4, 1.9 and 2.4 Lmin^{-1} imparted a wall shear on a growing emulsion droplet of 9, 13 and 16 Pa respectively (determined from Re using Equations 16 and 17). This increase in shear force reduced the droplet growth period before cleavage from the membrane surface, giving progressively smaller droplets (arrow iii, Figure 70). This was reflected in the particle size data (Figure 70) for samples 1, 4 and 7, where an increased flow rate led to a significant reduction in the average bead diameter, $D_{peakmax}$, from 65 μm to 19 μm and 17 μm respectively (with concomitant narrowing of distribution from 86 to 21 and 14 μm), in agreement with previously published data on membrane emulsification.[109,153] In the ranges investigated, Ca did not have a significant impact in promoting jetting behaviour in the emulsion formation process.

Comparison of samples 1 and 4 (Figure 70) revealed an increase in the volume % of small particles ($<\sim 5$ μm) in sample 4, although the peak reflecting the largest population of particles remained narrow. We hypothesise that sample 4 represented a situation in which a small proportion of larger membrane pores were producing droplets in a jetting manner brought about by a higher P_{tm} compared with sample 1 and 7 (Table 11), whilst the majority of pores produced droplets in a dripping regime. While pore size ranges in SPG membranes are narrow, these are not without some larger outlet pores arising from the tortuous paths resulting from the spinodal decomposition mechanism used to produce the

membranes (Figure 64).[141] Some smaller pores, which would have a higher P_c, may have become active with the increased P_{tm} of sample 4 compared with 1 and 7, generating a greater number of smaller droplets/beads.

Careful consideration of the effect of controllable factors on We and Ca, allows one to discern appropriate conditions for the generation of microbeads with defined size and narrow polydispersity. Here parameters must be selected to yield a low We (i.e. interfacial tension forces dominating over inertia), which can be achieved by the combined effect of a higher viscosity disperse phase and a lower applied transmembrane pressure (P_{tm}) resulting in a low v_d. In this system, use of a disperse phase with higher viscosity provided a clear benefit for production of microbeads with narrow polydispersity, though it also resulted in a reduction of Q_{dp} which, in turn, reduced the quantity of product generated per unit time and membrane area. From the calculated Q_{dp} (Table 11), the productivity of cellulose microbead generation using an optimised hypothetical system in which the emulsion could be removed without having to recirculate the continuous phase, was determined to be 11 and 3 $kgh^{-1}m^{-2}$ for samples 1 and 7, assuming no membrane fouling, or product loss. Clearly an increase in productivity could be achieved with a higher P_{tm}, such as that used to generate sample 3, with a productivity of 197 $kgh^{-1}m^{-2}$, whilst operating in a jetting regime producing a more polydisperse product. These production rates could be improved by numbering up of membranes, or increasing the membrane area by use of longer tubular membranes to form more concentrated emulsions with a single pass through the membrane. These calculations do not however account for post processing required to extract the final cellulose bead product which included filtration of the product mix, and removal of residual OES from the cellulose matrix.

Membrane Pore Size

The results documented in this section so far have relied on the production of cellulose microbeads from a single membrane average pore size of 10 μm. A leading factor in controlling the average size of the droplet produced is the size of the pore at which the droplet grows, research in the literature

highlighting the linear relationship between average pore diameter (d_p) and average droplet diameter (d_d)(Equation 15).[146] To test if this translated to this system, two disperse phase compositions consisting of 8 and 4 wt% MCC in OES were emulsified using a 1 μm pore membrane, which was treated to the same functionalisation as described in the previous section, into a continuous phase consisting of 2 wt% Span 80 in SFO. These dispersions were compared with the earlier obtained samples produced using a 10 μm pore size.

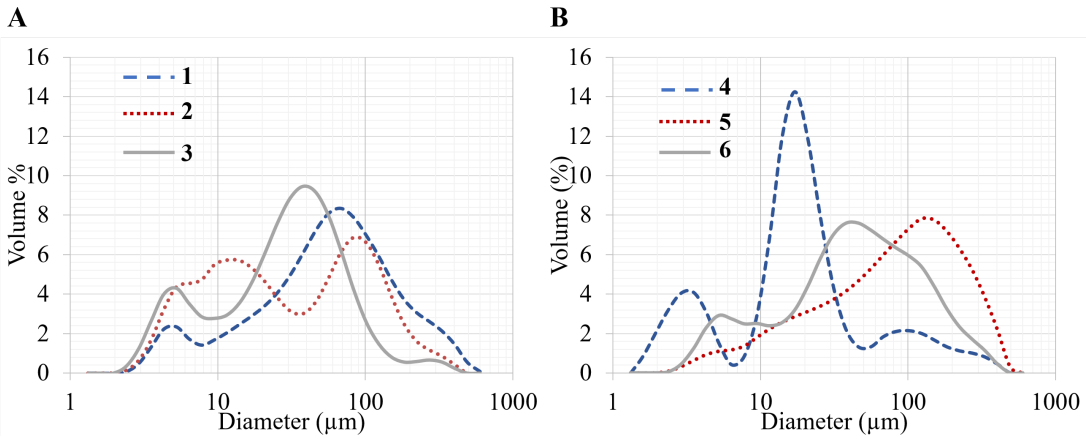

Figure 71: Particle size distributions of microbeads produced using A: 1 μm and B: 10 μm pore SPG membranes. Experimental conditions are documented in Table 12.

Table 12: Experimental conditions used to produce cellulose microbeads from two membrane pore sizes (d_p) quoting the continuous phase flow rate (Q_{cp}) and transmembrane pressures (P_{tm}) used to generate the beads. Cellulose was dissolved in 70:30 (w/w) DMSO:[EMIm][OAc]. The accompanying particle size distributions are presented in Figure 71.

Chart	d_p (μm)	Distribution	Cellulose (wt %)	Q_{cp} (Lmin^{-1})	P_{tm} (bar)	P_c (bar)	$D_{peak\ max}$ (μm)	$fwhm$ (μm)	Ca	We
Figure 71 **A**	1	1	8	2.4	0.40	0.043	67	137	12.6	1.2×10^{-10}
		2	4	2.4	0.25	0.049	92	114	11.7	2.7×10^{-9}
		3	4	1.4	0.10	0.049	38	61	6.8	8.5×10^{-11}
Figure 71 **B**	10	4	8	2.4	0.01	0.004	17	14	12.6	1.4×10^{-9}
		5	4	2.4	0.05	0.005	135	281	11.7	1.5×10^{-5}
		6	4	1.4	0.03	0.005	42	144	6.8	4.5×10^{-6}

Interestingly, in most cases decreasing the average pore size by a factor of 10 (10 - 1 μm) did not scale the average bead size accordingly. When using a 4 wt%

MCC disperse phase, reducing the membrane pore size did lead to a reduction in $D_{peakmax}$ which was not seen when using a 8 wt% solutions. Moving to a 0.1 μm pore size resulted in no permeation whatsoever with either disperse phase composition in the pressure range explored (<3 bar).

Decreasing the pore size increased the calculated P_c by an order of magnitude (Table 12). Using an 8 wt% disperse phase, permeation through a 1 μm membrane with a P_{tm} <10 $\times$ P_c could not be achieved outside of a jetting regime (Figure 71 A). Comparing distributions between a 1 and 10 μm pore using an 8 wt% disperse phase (Figure 71 A dis 1, B dis 4) highlighted the increase in the $fwhm$ of the main peak (Table 12 A dis 1, B dis 4) when using a narrower pore. Reducing the cellulose concentration from 8 to 4 wt% enabled permeation at a lower pressure through the narrower pore membrane (Figure 71 A dis 2) due to a significant reduction in the viscosity of the solution (Chapter 4, Figure 33). As found earlier, using a 4 wt% cellulose solution with a 10 μm pore membrane resulted in high v_d which led to jetting of the disperse phase, increasing the final polydispersity of the dispersion. Reducing the pore size to 1 μm allowed formation of beads with populations (reflected in the main peak) of a narrower size distribution (Table 12 A dis 2) but a greater bimodal nature overall. This was most likely due to the high P_{tm} applied to the disperse phase for this sample. Reducing the flow rate and P_{tm} again gave particle size distributions with a narrower $fwhm$ for the 1 compared to 10 μm samples (Table 12 A dis 3, B dis 6).

As with samples produced from a 10 μm pore, each sample prepared using a 1 μm pore size membrane yielded a size distribution which included a <10 μm population. This provided evidence that this "shoulder" was indeed a product of irregularities in the membrane, which could occur at any membrane pore size, when using an SPG membrane. Vladisavljevic *et al.* have shown that the geometry and structure of an SPG pore does not change significantly with average pore size.[141]

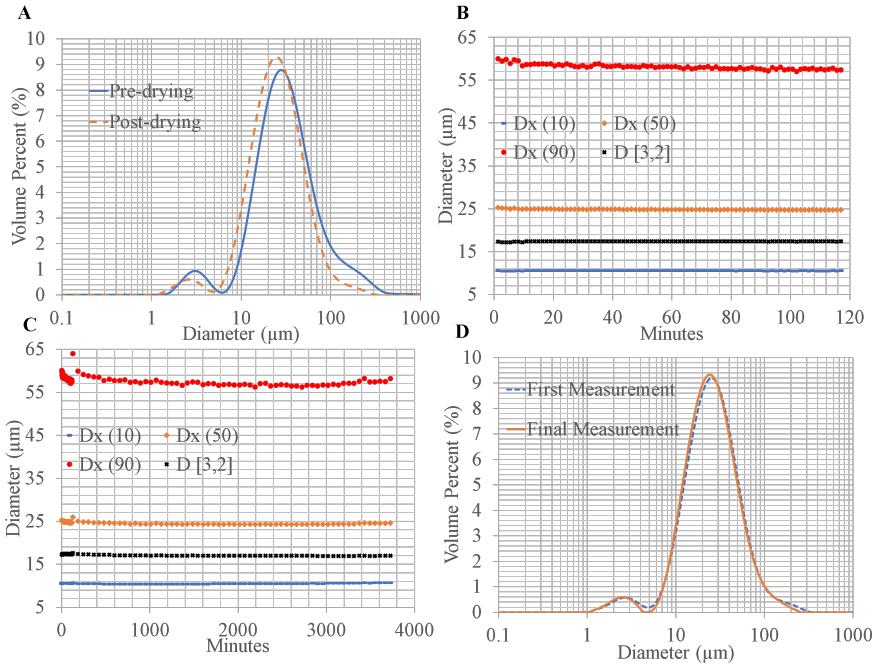

Figure 72: A: Particle size distributions of cellulose microbeads before and after drying from ethanol, B: the change in $Dv(10)$, (50) and (90) as well as the Sauter Mean Diameter ($D[3,2]$) for dried cellulose microbeads with measurements taken every minute from initial addition of the dried beads to water and C: taken every hour following on from this (62 hours total). D: Particle size distributions of the dried cellulose microbeads before and after agitation in water for 62 hours.

5.3.3 Drying and Swelling of Cellulose Microbeads

Looking towards possible wider application, the microbeads produced would most likely be used as a powder which is redispersed in a relevant solvent, such as water, to formulate the product required. It was therefore important to determine the extent of size reduction on drying, and subsequent swelling on redispersion of the cellulose microbeads. All samples in this section were produced using an 8 wt% cellulose-OES dispersed in 2 wt% Span 80-SFO under the same production parameters: P_{tm} 0.02 bar, Q_{cp}: 2.4 Lmin^{-1}, 10 μm pore. Once formed, by phase inversion and extracted via Soxhlet extraction (ethanol), the microbeads were dried under reduced pressure with agitation (rotary evaporator, 50 °C) from ethanol.

The microbeads reduced in size slightly from a $Dv(50)$ of 26.8 ±0.2 to 24.7

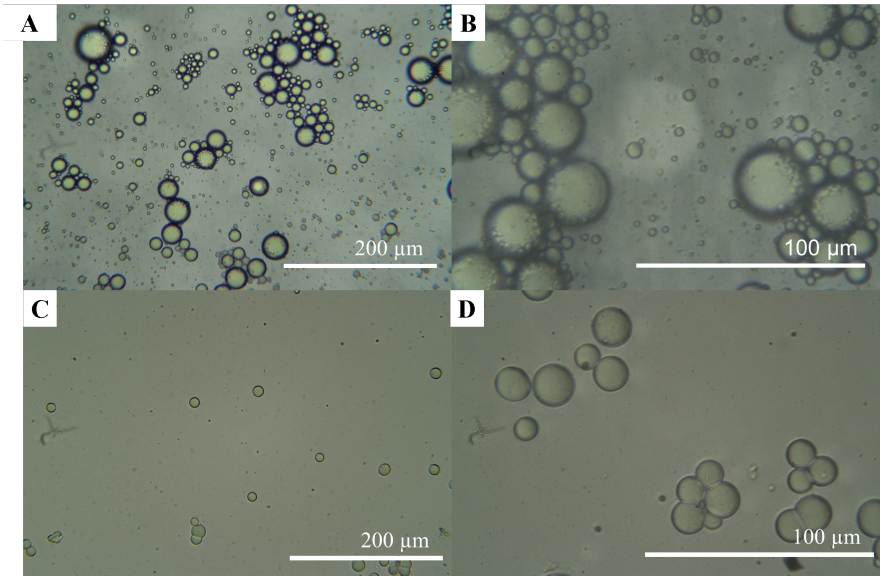

Figure 73: Optical micrographs showing A, B:"never dried" and C, D: dried cellulose micro-beads in water.

± 0.3 μm (Sauter mean 18.1 ± 0.5 to 17.2 ± 0.2) (Figure 72 A) when dried and remained at this size even when redispersed in water and soaked over a 62 h period (Figure 72 B, C). Values for $Dv(10)$ and $D[3,2]$ also showed no variation. The particle size distributions of the beads initially dispersed in water and those soaked in water for 62 hours were within experimental error of each other (Figure 72 D) with no observable difference. It appeared that the densification of the bead on drying was not reversible and the beads did not swell in water to any extent over the period tested.

Comparing optical micrographs between microbeads prior to and post drying showed a slight reduction in bead diameter (Figure 73 A, C) with some aggregation between beads (Figure 73 B, D). These aggregates were shown to breakup with agitation (during particle size analysis) seen by a slight reduction in $Dv(90)$ whilst the sample was being dispersed in water (Figure 72 B, C).

5.4 Dropping Process

Cross-flow membrane emulsification has been shown to be a suitable route for formation of cellulose microbeads with far reaching potential. It was however, only applicable for production of beads of smaller diameter (<500 μm) due to the inherent difficulty in stabilising emulsion droplets of greater size. Other non-emulsion based processes exist which can accommodate production of larger diameter beads (0.5 - 3 mm).[22] A dropping procedure involves extruding a solution of cellulose from a suitably sized opening from which droplets can be produced, directly into an anti-solvent bath. Factors that control the size and shape of the final solid bead have been discussed in the literature review (Chapter 2, section 2.3).

5.4.1 Single Tip Process

There is a range of dropping heights in which spherical beads can be achieved, with many of the dropping processes described in the literature utilising a shallow dropping height (e.g. 1-2 cm) due to the low viscosity cellulose solutions.[36] In the case of the viscous 8 wt% cellulose-OES solutions used in this work, the dropping phase required a greater time, or distance, before reaching the anti-solvent bath to form a spherical droplet once extruded from the needle tip (Figure 74 A). The optimal dropping height range was found to be 7-12 cm from the needle to the surface of the solvent bath. Dropping the cellulose solution from a lower height resulted in tailing of the final material (Figure 74 B). Using this method, cellulose beads with a average wet diameter of 2.7 $\pm$0.09 mm and dry diameter of 1.51 $\pm$0.03 mm (44 % shrinkage) (Figure 74 C) with an average weight per bead of 2.2 $\pm$0.1 mg could be produced from a 21 G (OD 0.82 mm, ID 0.51 mm) (at ambient temperature) needle when dropped into a bath of ethanol. To completely remove residual IL and DMSO, the beads were subject to Soxhlet extraction using ethanol. Once dried, these extracted beads had a slightly smaller diameter of 1.3 $\pm$0.03 mm (52 % shrinkage).

Figure 74: A: Picture of a syringe based dropping apparatus for the generation of cellulose beads, B: image of "failed" beads formed from a dropping height <7 cm from a solution of 8 wt% MCC dissolved in DMSO:[EMIm][OAc] (70:30, w/w) and C: spherical beads produced from a height of 7 cm (dropping height greater than this formed discs.

5.4.2 Multihead Process - Scale Up

The use of a single needle to extrude the solution into the anti-solvent bath was clearly a limiting factor in the productivity of the overall process, producing 4 droplets/beads min^{-1}. This could be improved by "numbering up" of extrusion tips. This was achieved by numbering up an 8 tipped multi pipette head producing a total of 72 tips (9 heads) (Figure 75 C). A peristaltic pump (Figure 75 B) was used to drive the dropping phase through these tips from a 2.5 L tank (Figure 75 A).

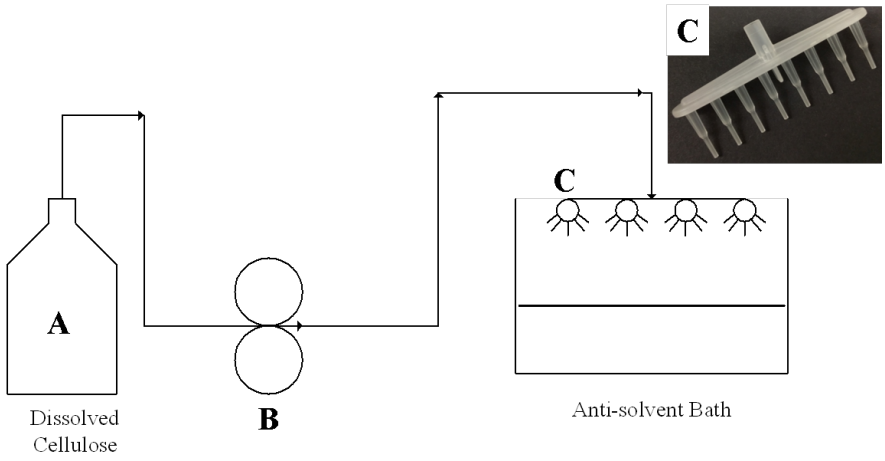

Figure 75: Schematic of the dropping rig developed for the generation of cellulose beads highlighting the A: dropping phase reservoir, B: peristaltic pump and C: multi-tipped pipette head.

1.8 L of cellulose-OES phase could be processed into solid beads every hour. Clearly this was a huge increase in the productivity of this process and could be increased even further with the use of more heads. As more volume was dropped into the anti-solvent, the volume of the bath increased and the distance between the tip and solvent surface reduced. This change in the dropping height over time was acceptable due to the range of distances (7-12 cm) which produced spherical beads, enabling longer operation of the apparatus and processing of more material. The tips used had a slightly larger diameter (OD 1.5 mm, ID 0.6 mm) compared with the previous process (21 G needle) and therefore produced slightly larger beads in the wet state. The final beads were of uniform size and shape with an average wet diameter of 3.0 ±0.2 mm shrinking to 1.5 ±0.1 mm (2.0 ±0.3 mg average weight per bead) when Soxhlet extracted (ethanol) and dried, comparable in dry size and weight to the previous samples.

5.4.3 Techno-Economic Analysis

Scaling up of any processes comes with inherent challenges. In the case of this work, the major hurdle was not the production of the material, but devising an efficient recycling stream for the various components used, especially the IL - [EMIm][OAc], due to its high economic cost.

One of the benefits of using an IL based dissolution process was the potential for efficient recycling routes due to the ILs negligible vapour pressure. In the case of the multihead dropping process, after removal of the cellulose bead products via filtration, the filtrate, consisting of DMSO, [EMIm][OAc] and ethanol was separated via distillation under reduced pressure. It was found that a two stage distillation was required to achieve purities of ethanol and DMSO:[EMIm][OAc] suitable for reuse in the process (Figure 76).

The first vacuum distillation took place at 70 mbar at a temperature of 50 °C (rotary evaporator). The resulting distillate of ethanol was of a high purity (99.7 wt% purity, confirmed by NMR, Figure S4) and could be again used for cellulose coagulation in an anti-solvent bath (Figure 76 A) and/or [EMIm][OAc]:DMSO extraction from the cellulose matrix (Soxhlet) (Figure 76 B). The solvent used

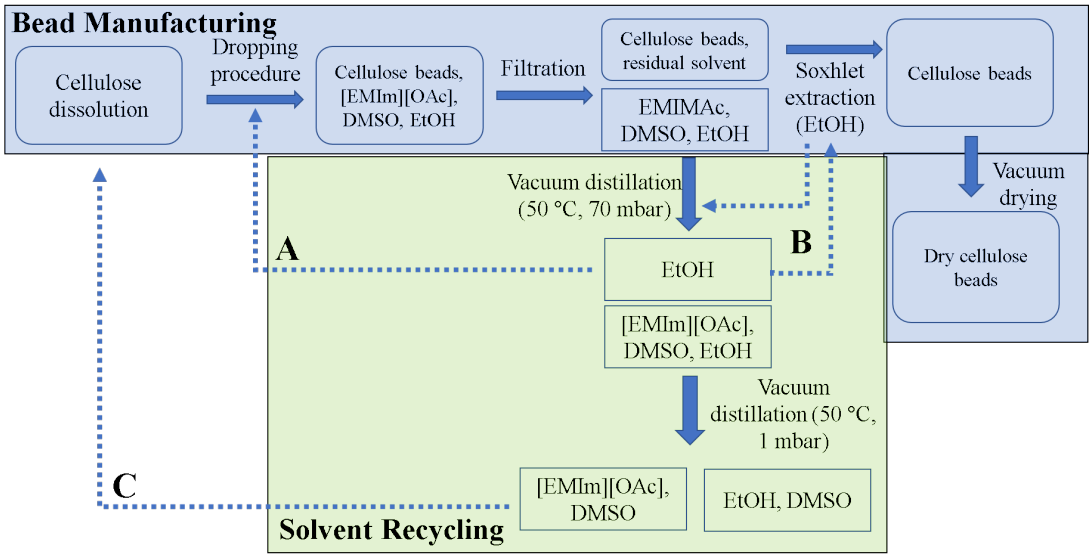

Figure 76: Schematic of the production and recycling process used to generate cellulose beads from a scaled up dropping process. Dotted arrows denote recycling pathways. The anti-solvent bath was located on a rocker which kept the bath agitated to aid in OES leeching.

during Soxhlet extraction was also fed back into the vacuum distillation recycling stream. After the first distillation, the remaining solvent consisted of 28.6 : 50.2 : 21.1 ethanol:DMSO:[EMIm][OAc] (weight ratio)(Figure S5). A second vacuum distillation was used to remove the remaining ethanol (50 °C, 1 mbar, rotary evaporator). Excess conditions were used to ensure the removal of ethanol which would impede the dissolution of cellulose. Due to this, some DMSO was also removed during this second step resulting in a final DMSO:[EMIm][OAc] ratio of 66:34 (w/w) (Figure S6). Lab trials have shown that this solvent system can again be used to dissolve cellulose (Figure 76 C) with the addition of more DMSO to account for the volume that was lost through the second vacuum distillation.

The material cost to produce a gram of cellulose beads without utilising the recycling streams was calculated to be £3.34 (Figure 77) based on the prices listed in the experimental chapter (Chapter 3, section 3.9). Ethanol contributed the highest initial capital investment (£2.03 per gram of beads produced, 61 % of the cost per gram), due to the high volume used (15.63 mL anti-solvent bath, 12.5 mL Soxhlet extraction per gram of beads), followed by [EMIm][OAc] (£1.02, 31 % per gram of product). The recycling process described in Figure 76 resulted in

80% recovery of materials used (excluding cellulose product, 99 % [EMIm][OAc], 82 % DMSO, 79 % ethanol). Implementation of this recycling stream reduced the cost of a gram of cellulose beads to £0.58 with the cost of supplying new materials dropping significantly (Figure 77, [EMIm][OAc] - £0.01, DMSO - £0.03, ethanol - £0.44 per gram of cellulose beads).

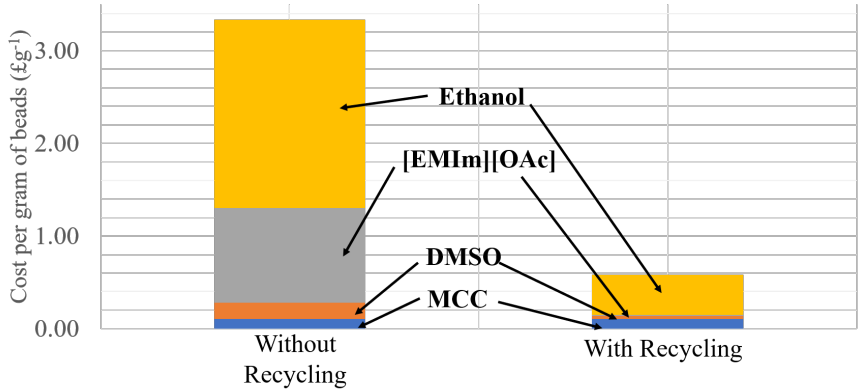

Figure 77: Chart showing the raw material cost per gram of cellulose bead produced, with and without recycling of components, used to form cellulose beads from a multihead dropping process.

This techno-economic analysis was used to investigate the cost of materials and did not take into account the initial capital required for equipment or running costs (labour, lab running costs etc.) or the potential reduction in cost of raw materials when purchased in bulk from other suppliers. The economic viability of this process could be improved further with the introduction of another separation stream to purify the ethanol:DMSO distillate from the second distillation, which was discarded in these calculations, and by increasing the volume fraction of cellulose-OES solution:ethanol in the anti-solvent bath maximising the mass of product produced per gram of ethanol. Other cellulose dissolution, shaping and reforming process, for fibres and films, utilising ILs have highlighted the applicability of recycling in producing "zero-waste" manufacturing streams, although co-solvents were not used which complicates the process.[76]

5.5 Chapter 5 Conclusions

The first example of a continuous process for the production of cellulose microbeads utilising membrane emulsification technology has been presented here. A wide range of average bead sizes ($Dv(50)$ 15 - 150 μm) were obtained by adjusting production parameters as well as the compositions of both the disperse and continuous phases. An [EMIm][OAc]-DMSO OES was shown to be a suitable processing solvent for cellulose. The developed apparatus was highly functional and capable of forming cellulose microbeads under continuous operation. The flow rate of the continuous phase (0.4-2.4 $Lmin^{-1}$), transmembrane pressure, disperse phase velocity and surfactant concentration (0.25-2.00 wt%) were all shown to impact the size and size distribution of the microbeads formed. These factors influenced the size via the wall shear force, viscosity of the disperse phase and the interfacial tension. Generally, at a set surfactant concentration and pore size, a set of conditions which gave a low Weber number produced the narrowest particle size distribution, which is in agreement with simulated data.[147]

The SPG membranes selected for this process were shown to be effective for production of microbeads of reproducible size, but the monodisperse emulsions often described in the literature when using these membranes remained out of reach for these cellulose-OES disperse phases. Closer inspection of the internal surface of the tubular membranes highlighted the undulating topography and tortuous nature of the membrane pores and surface. This was hypothesised to generate a variation in the wall shear force and transmembrane pressure imparted on the growing emulsion droplets due to the variation in pore size and membrane surface height. This had the effect of producing consistent polydispersed particle size distributions.

Published data, which documents the linear relationship between membrane pore size and average droplet diameter, appear not to apply to this system. Viscosity of the disperse phase is often overlooked in these cases and is most likely the cause of these apparent discrepancies with the published literature. However, we have shown that these solutions can be processed using membrane emulsification technology, with suitable adjustments, forming reproducible cellulose microbeads.

This was taken a step further by implementing these solution in the scale up of a dropping process able to produce high volumes of larger wet diameter (2-3 mm) cellulose beads, in a consistent manner.

Chapter 6

Cellulose Bead Post-Processing and Composite Formation

6.1 Introduction

A desirable attribute of cellulose is the ability to alter its chemistry, topography and mechanical stability via chemical reactions, either to modify the surface or bulk material. Etching can also be used to tailor the material towards a particular application, for example as a support where an increased surface roughness is a sought after attribute to shield the active coating, such as a biofilm, from excessive shear forces.[154] The effect of glyoxal cross-linking was investigated as a means to modulate hardness and mechanical strength of the material. Along with this, a range of acidic, enzymatic and hydrophobic surface treatments were also explored. This was extended further with the formation of chitosan coated cellulose beads and an investigation into the formation of cellulose composites, specifically cellulose-ammonium polyphosphate (APP) beads. This organic filler was chosen as it imparts fire-retardancy to similar cellulose materials (shown in the literature and via unpublished research in the group).[155]

Results and Discussion

6.2 Glyoxal Cross-Linking

We turned our attention to the tribological properties that might be required to make cellulose beads applicable to a range of products. For example, production of hard cellulose microbeads for abrasive applications and beads with high mechanical strength could serve as blasting media for paint stripping.[156] To modulate bead hardness, cross-linking was employed to cellulose beads formed from an 8 wt % cellulose-OES using the small scale dropping-phase inversion process described in Chapter 5 section 5.4 (Figure 74). The commercially available, REACH registered dialdehyde, glyoxal, was used to form acetal/hemi-acetal linkages between the cellulose chains within the formed bead (Figure 78).[105]

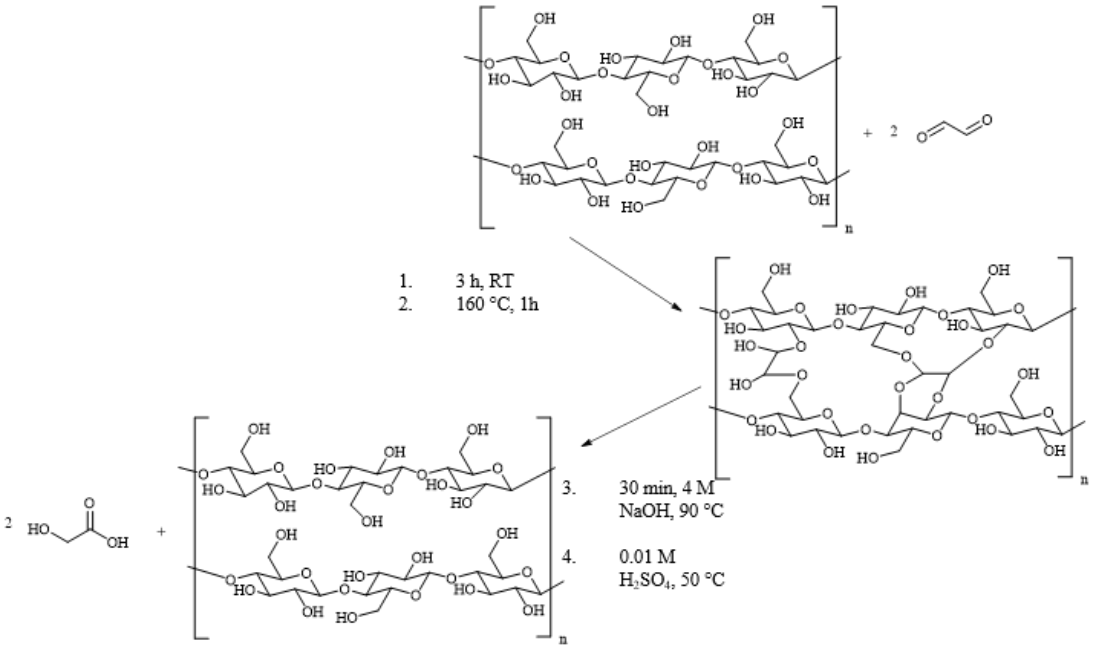

Figure 78: The cross-linking reaction between glyoxal and cellulose leading to the formation of acetal or hemi acetal linkages. Subsequent removal of the cross-linker, for quantification, forming glycolic acid after protonation in the mobile phase (0.01 M H_2SO_4, 50 °C) during HPLC analysis is also shown.[105,142]

The cross-linking reaction produced a colour change in the cellulose beads

from a colourless to a light yellow translucent material in the samples cross-linked with a 6 wt% glyoxal solution, and dark orange for 12 wt% glyoxal (Figure 79), which has been noted in other research.[157]

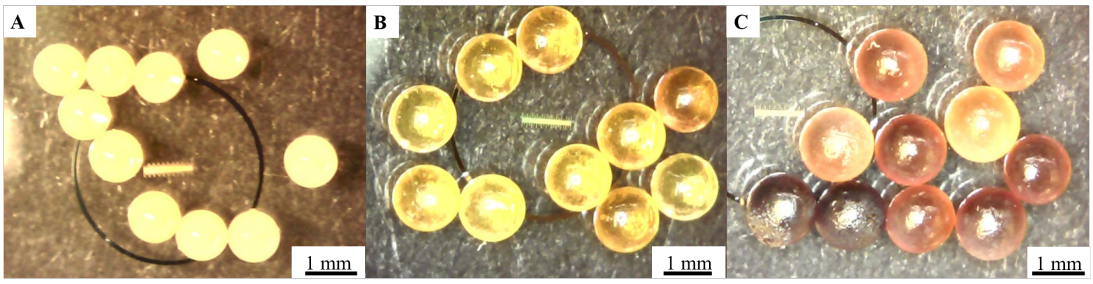

Figure 79: Image of A: dried cellulose beads and dried cross-linked cellulose beads, cross-linked with a solution of B: 6 wt% or C: 12 wt% glyoxal (160 °C, 1 h).

There was a variation in the colour of the 12 wt% samples (Figure 79 C) which suggested a difference in the extent of reaction, a point that will returned to in due course. Compared with non-cross-linked beads, cross-linked samples did not shrink to the same degree with drying. Dried cellulose beads, also produced from a 8 wt% MCC-OES, had an average diameter of 1.3 ±0.03 mm whereas samples cross-linked with a 6 and 12 wt% glyoxal solution had an average size of 1.40 ±0.05 mm and 1.60 ±0.06 mm respectively. This was due to increased chain rigidity because of the primary bonding between chains which lowered mobility. Glyoxal cross-linked cellulose samples have also been shown to have a lower relative water absorption capacity compared with non-cross-linked variants due to this more rigid, less mobile structure.[105]

Exposing a cross-linked bead to excess OES (>99 wt%) over a 3 day period (50 °C) did not lead to dissolution of the polymer bead (non-cross-linked samples dissolved after 16 hours), which has also been shown in the literature.[105] The formation of acetal and/or hemiacetal linkages between cellulose chains prevented the chains from separating, hindering the dissolution of cellulose. This resistance to dissolution could be reversed via the addition of base which resulted in cleavage of the acetal/hemiacetal linkages producing glycolic acid, which could be quantified using HPLC analysis to gain a value of the extent of cross-linking (Figure 78). The recovered polymer was shown to be soluble in the OES after removal of cross-linker.

6.2.1 Quantification of the Degree of Cross-linking

The method of Schramm *et al.*[104] was used to quantify the degree of cross-linking in cellulose bead samples by removal of the cross-linker by heating in NaOH and quantifying the expelled glycolic acid.

Analysis of the HPLC chromatograms (Figure S8) indicated a cross-linker:anhydroglucose unit (AGU) molar ratio of 1.4 ±0.1 or 2.1 ±0.0 (for samples exposed to 6 and 12 wt% glyoxal solutions respectively), which is comparable to other work utilising similar materials and conditions.[158] There was a low level of variation between repeats of the two samples which suggested that the difference in colour observed in the 12 wt% samples (Figure 79) did not reflect a significant variation in the extent of cross-linking between samples. The colour change could have potentially been caused by residual OES solution in the cellulose matrix which degraded during the cross-linking reaction.

6.2.2 Compression Tests

Cross-linking increased the bead's mechanical resistance to compression. Attempts to compress the beads by 30 % resulted in fracture at loads of 98 or 186 N (1.4, 2.1 glyoxal:AGU respectively, mol/mol) before significant compression was achieved (12 and 9 % respectively) (Figure 80). Compared with non-crosslinked samples, which did not fracture and required 59 N of force to compress by 30 %, cross-linking imparted significant embrittlement to the materials which has also been shown by others.[105] This is due to the small length of the cross-linker which reduces the flexibility of cellulose chains meaning when a load is applied chains are less mobile, forming a less compressible material.[105,159]

All samples were Soxhlet extracted using ethanol prior to analysis. Removing this extraction step led to retention of residual OES in the cellulose beads which was shown to impart a plasticising effect on the material, increasing the compressibility and lowering the rigidity of the beads (3 N at 30 % compression) (Figure 80 B). These samples also had a lower shrinkage % on drying (Table 13), due to being swollen with [EMIm][OAc] and potentially DMSO

which was not removed using vacuum drying. This highlighted how the presence of residual OES could impact the mechanical performance of the beads and conveyed the need for extensive extraction of the beads via Soxhlet (ethanol) post formation.

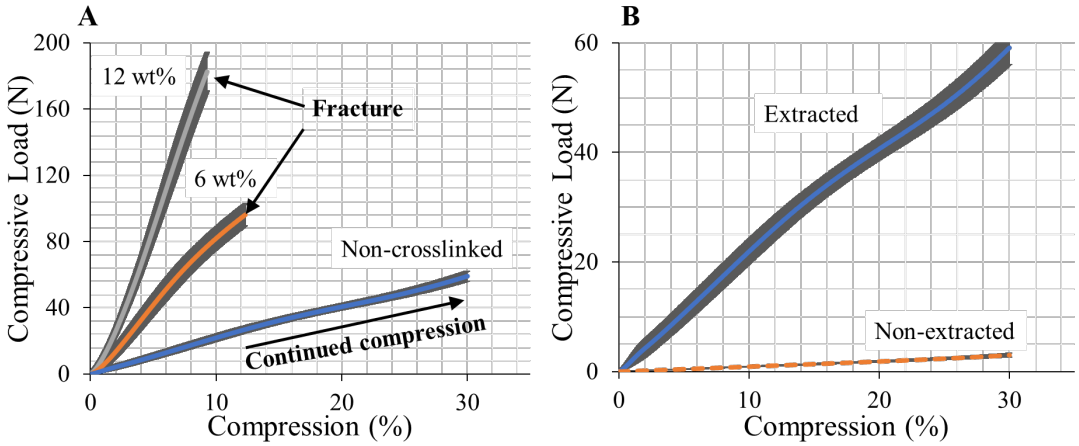

Figure 80: Graphs showing the mechanical compressibility of cellulose beads. A: exposed to differing concentrations of cross-linker solution and B: the effect of residual OES (non-extracted) in the bead. Non-cross-linked (A) and Extracted (B) are the same sample.[142]

Table 13: Effects of cross-linking on bead size, hardness and brittleness.

Cross-linking degree (glyoxal:AGU)	Reduction in diameter with drying	Force required for compression up to 30 % (N)	Compression at fracture
Non-extracted	45%	3	No Fracture
0 (extracted)	56 %	59	No Fracture
1.4	49 %	98	12 %
2.1	43 %	186	9 %

6.2.3 Microscopy

SEM analysis highlighted that non-cross-linked samples developed a rough surface topography and a dense inner structure when dried under vacuum (Figure 81 A). This roughening of the surface, suggested to arise from the shrinkage of the amorphous beads with a dense "skin" layer developed during phase inversion (the anti-solvent ethanol, used here, produces highly amorphous materials),[62] was reduced in bead samples reacted with 6 wt% glyoxal solutions (Figure 81

B). In this case, after cross-linking, the surface appeared generally smooth with some locations showing signs of pitting, presumably arising due to loss of water during heating and drying (Figure 81 C). At the same time, the internal structure appeared less dense than that of its non-cross-linked counterparts (Figure 81 D) as expected from the reduced shrinkage. Increasing the concentration of glyoxal in the cross-linking solution to 12 wt% created a consistently dimpled surface topography (Figure 81 E) and the presences of some craters was also noted (Figure 81 F). The internal structure appeared very similar to samples with lower degrees of cross-linking, showing some granularity (Figure S10).

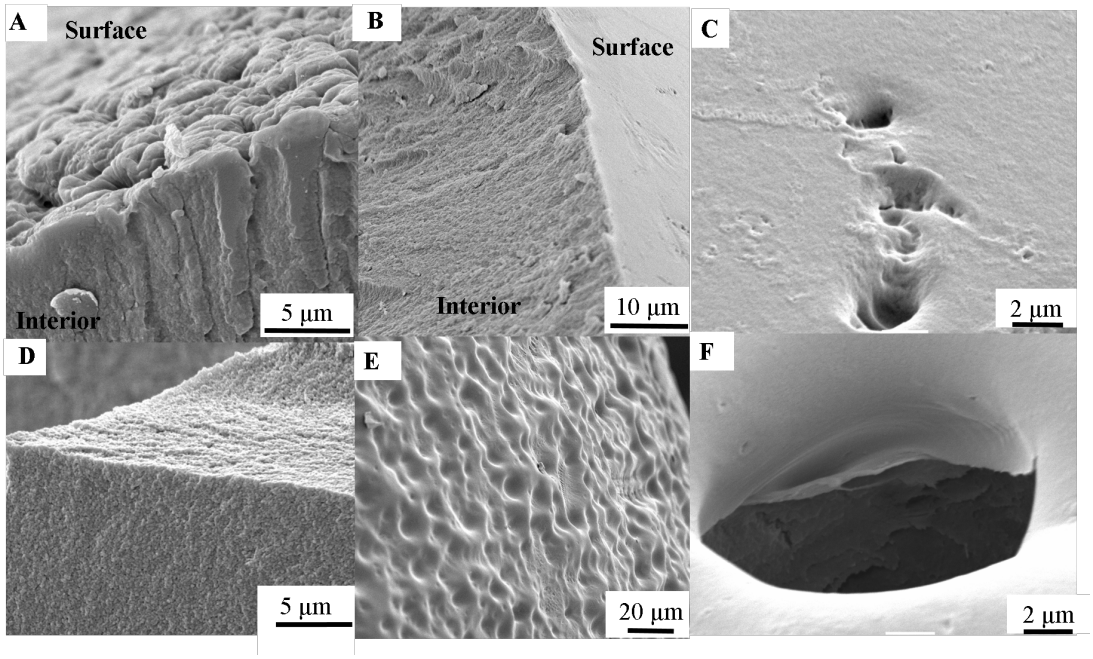

Figure 81: SEM micrographs of cellulose beads, A: cross section of a non-cross-linked bead; B: the cross section, C: surface and D: internal structure of beads cross-linked with a 6 wt% glyoxal solution and E, F: surface of a bead cross-linked with 12 wt% glyoxal. C, F show the pitting seen on 6 and 12 wt% cross-linked samples respectively.[142] More SEM images can be found in the Appendix (Figure S10.)

It appeared that the expulsion of excess water, from the solvent and produced during the reaction, led to the creation of pits and holes in the surface of the bead under both cross-linker concentrations used, with the size and quantity of both increasing in the higher concentration sample (12 wt% glyoxal). Theoretically, 4 moles of water can be generated per mole of glyoxal, meaning the

high concentration cross-linking solution (12 wt%) would produce significantly more water, the removal of which under increased temperature generated this undulating surface. The formation of the undulating surface could be favourable for specific applications, such as a support material, in which shielding of an active surface from excessive shear force is a sought after attribute.[154]

6.2.4 Thermogravimetric Analysis (TGA)

Cross-linking of cellulose with glyoxal has been shown to reduce the material's thermal stability.[105,157] The extent of this thermal instability was investigated in this section. Initially however, it was appropriate to determine the effect of cellulose bead size (μm vs mm) and cellulose concentration (in the forming solution) on thermal stability of the materials. Three cellulose bead samples formed from an 8 wt% MCC-OES using a dropping and a membrane emulsification process, and a 4 wt% MCC-OES sample, produced using the same membrane emulsification process, were thermally degraded to determine if the concentration of cellulose in the cellulose-OES solution and/or size of the bead had an effect on thermal degradation rate/temperature. The thermal degradation of cellulose is a two stage process the first step: occurring between 220-300 °C, for the breakdown of cellulose, and the second between 300-475 °C, the oxidation of the remaining materials.[160] Both of these regions can be clearly seen in Figure 82. It has been noted from the literature that the produced thermograms show little variation between inert and oxidising environments due to the high oxygen content within cellulose.[161]

Each of the three cellulose samples began degrading at the same temperature (around 200 °C) with the two microbead samples losing more mass above 250 °C, due to the increased surface:volume ratio. Microbeads generated from an 8 wt% cellulose-OES solution lost slightly less weight compared with the 4 wt% sample, most likely due to an increased density, but this difference was minimal. All samples were completely degraded with <0.2 wt% of the original mass tested remaining.

In agreement with the literature, cross-linked beads were found to have a

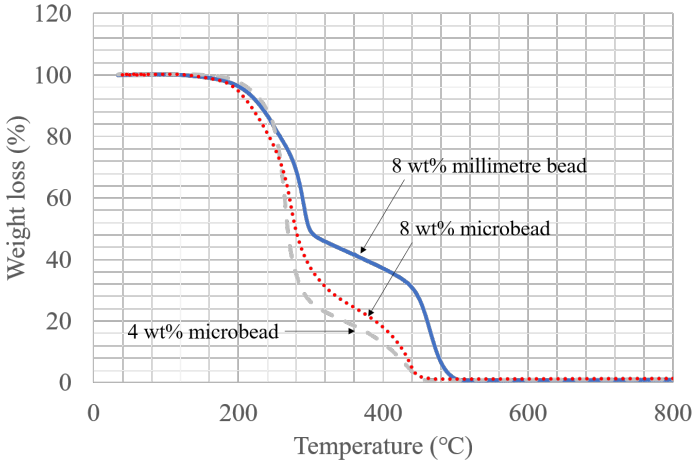

Figure 82: TGA in air of dried cellulose beads formed from either a dropping process (millimetre beads) or membrane emulsification process (microbeads) using an 8 (5 °C/min) or 4 wt% cellulose-OES (10 °C/min, held at 800 °C for 1 h, air).

lower onset temperature than non-cross-linked variants, the extent of which scaled with the concentration of glyoxal in the cellulose bead, due to the degradation of the cross-linker at lower temperatures (Figure 83).[105,157] At the end point (400 °C), the samples cross-linked with a 6 w% glyoxal solution had a higher remaining mass than the non-cross-linked samples. Potentially, a secondary cross-linking reaction took place after the initial decomposition producing a more thermally stable material. However, beads reacted with a 12 wt% glyoxal solution had the smallest mass, post heating, then either of the other samples. This could be attributed to potential loss of samples from the crucible, which was shown to occur later in the chapter.

Pyrolysis of Cross-linked Cellulose Beads

Pyrolysis of cross-link cellulose beads was conducted and analysed for topographical changes. Beads were swollen in a 12 wt% glyoxal solution and subjected to a lower cross-linking temperature (100 °C down from 160 °C) before heating in an inert atmosphere (900 °C, 10 °C/min and held for 1 h, Ar), with a faster temperature ramp rate compared with Figure 83, in the TGA instrument. At roughly 200 °C, a significant drop in the mass of the sample was witnessed (Figure 84) attributed to the loss of beads from the crucible.

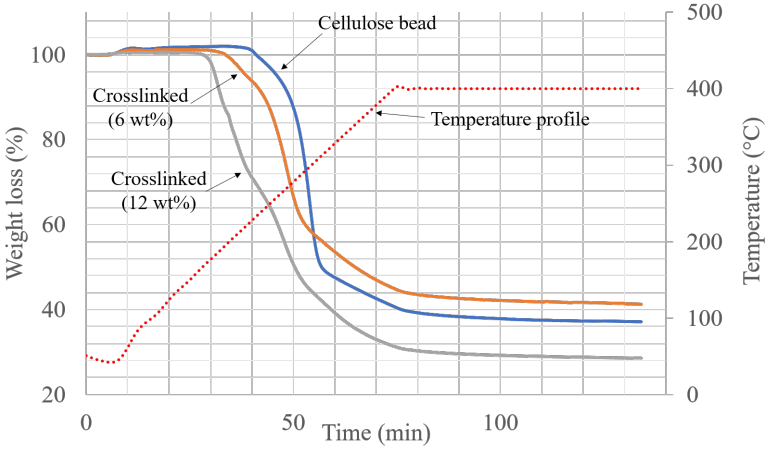

Figure 83: TGA of dried cellulose beads without cross-linking, and cross-linked with a 6 or 12 wt% glyoxal solution (5 °C/min, held at 400 °C, for 1 h under argon).

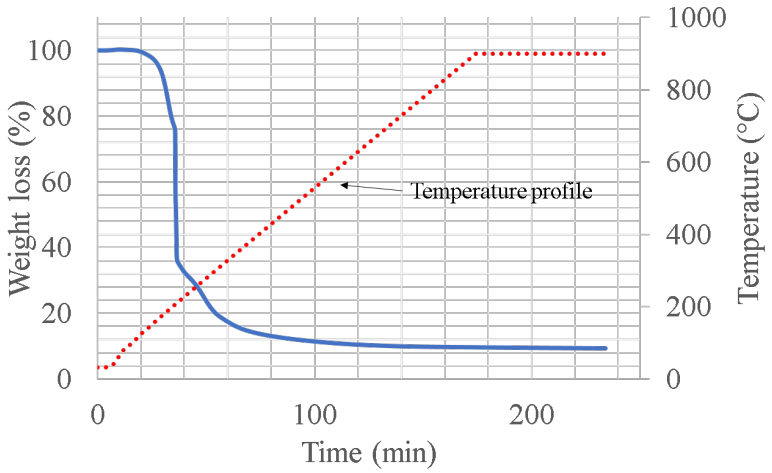

Figure 84: TGA of cellulose beads cross-linked with 12 wt% glyoxal at 100 °C (1 h) before heating to 900 °C (10 °C/min, held at max temp for 1 h under argon). Some beads were expelled from the crucible around 200 °C. SEM images of these samples post analysis are documented in Figure 85

SEM investigations of the pyrolysed cross-linked beads showed significant rupturing of the beads presenting a fine, porous mesh like internal framework (Figure 85 A, B, D), a stark contrast to the initial cross-linked materials (Figure 81 E). The surface appeared to consist of small holes (Figure 85 **C**) located in a dense cellulose matrix which continued into the core of the bead until reaching the porous mesh (Figure 85 **B**). The mechanism for this interesting structural formation is reminiscent of that of popcorn formation, the critical temperature

of which is remarkably similar to the temperature found here (180-200 °C).[162] We hypothesise that the increased temperature ramp rate (10 °C/min) prevented water, formed from the degradation of the cellulose/cross-linker, from escaping at lower temperatures. Increasing the temperature led to a build up of pressure, until around 200 °C at which point the pressure was great enough to break the outer shell. The "popping" in this case was fierce enough to expel some beads from the crucible during analysis, creating the sudden drop in weight during analysis. Other gases are known to form during pyrolysis of cellulose but at much higher temperatures (>400 °C) leading to the hypothesis that this "popping" was caused by water.[163] This effect was only found for cross-linked samples as heating non-cross-linked cellulose beads in the same manner, although under air, resulted in no "popping" or loss of sample from the crucible (Figure 82).

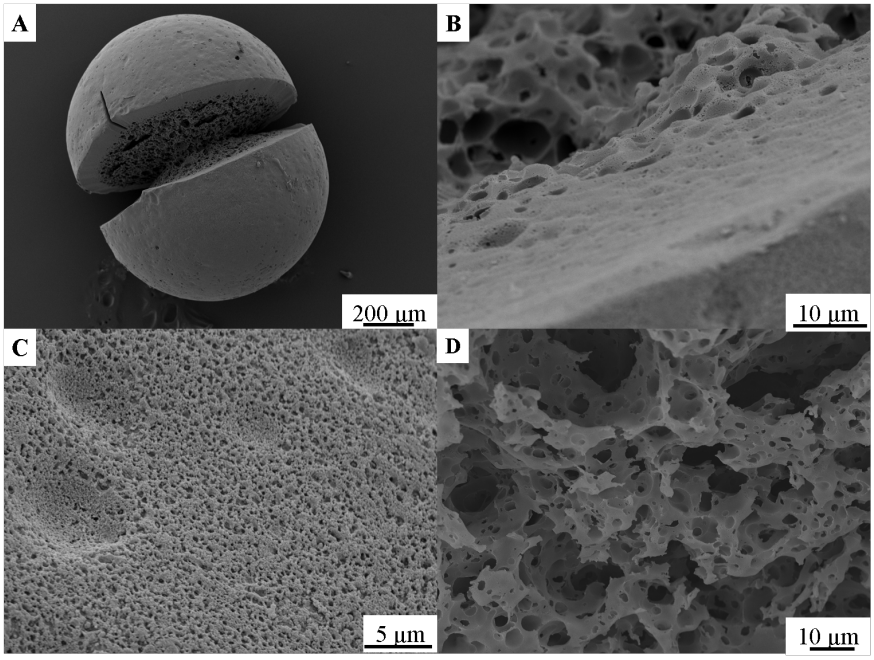

Figure 85: SEM images of a cellulose beads cross-linked with 12 wt% glyoxal followed by heating to 900 °C (10 °C/min, for 1 h under argon - corresponding temperature profile can be see in Figure 84). A: Full beads, B: the change in texture between the outer and inner structure, C: the surface structure and D: the internal structure.

Using a different heating profile (10 °C/min, 100 °C (1 h), 160 °C (1 h), cooling to 30 °C, heating to 900 °C) (Figure 86) designed to remove a greater amount of water prior to pyrolysis, led to a similar expulsion of sample from the

crucible around 200 °C, but formed a different bead structure (Figure 87 A). In this case, the internal network appeared denser than the previous sample (Figure 87 D) although still an interconnecting network. The outer skin layer, although still present (Figure 87 B), contained much larger pores/holes (Figure 87 C).

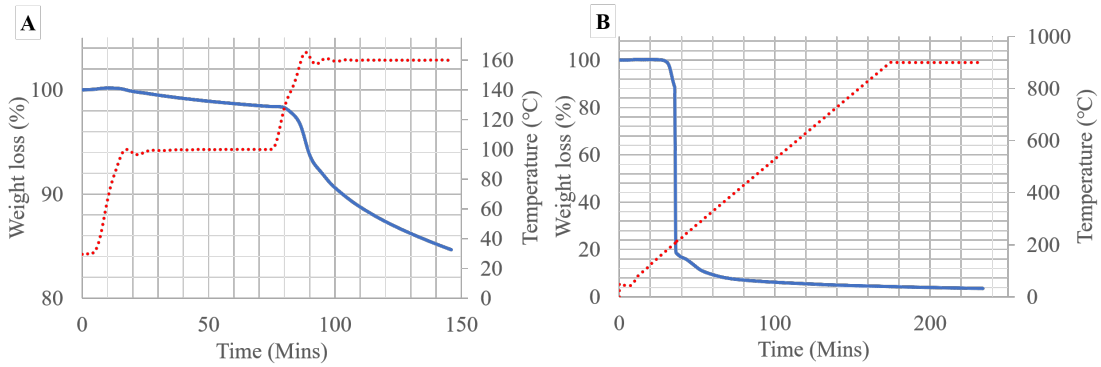

Figure 86: TGA of cellulose beads cross-linked with 12 wt% glyoxal A: with an added cross-linking/drying step (10 °C/min, 100 °C (1 h), 160 °C (1 h)) and B: held at 900 °C (10 °C/min) for 1 h under argon. Cellulose beads were observed to have expelled from the crucible at 200 °C. SEM images of the samples post analysis can be seen in Figure 87

The inclusion of a drying step removed some residual moisture prior to pyrolysis, however, Figure 86 A showed that not all of it was removed. This residual water and that created during heating still led to formation of gaseous water and a build up of pressure in the bead responsible for rupturing the material. In this case, the high reaction temperature (160 ° compared with 100 °C Figure 84) produced a dimpled surface (Figure 87 A, C) similar to that presented previously for beads reacted with 12 wt% solutions of glyoxal (Figure 81 E). This did not occur when the reaction took place at 100 ° (Figure 85) presumably due to a lower pressure imparted by gaseous water at lower temperatures.

6.2.5 Kilogram Scale Cross-linking

In an attempt to scale up the cross-linking reaction, to meet production levels achieved with the mutilhead dropping process described in Chapter 5 section 5.4, >1 kg of wet beads where exposed to high concentration glyoxal cross-linking solution, up to 32 wt%. The cellulose beads, swollen with water,

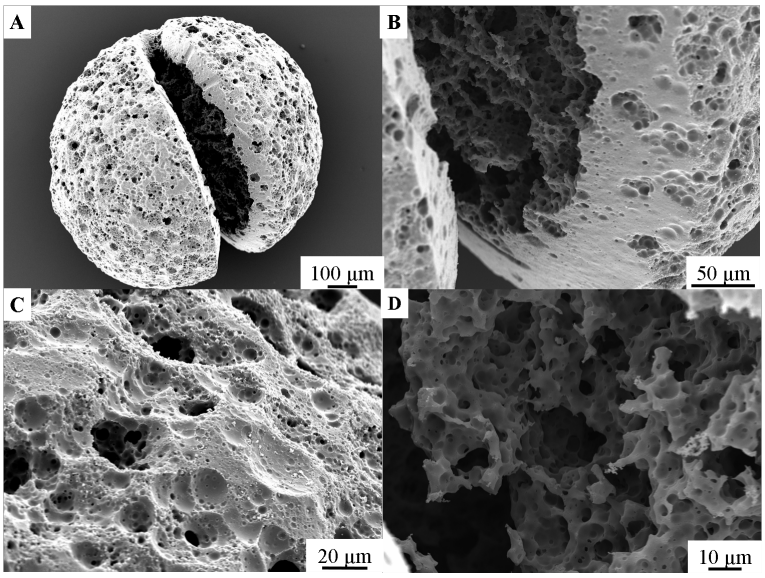

Figure 87: SEM images of a cellulose beads cross-linked with 12 wt% glyoxal followed by a drying temperature profile and heating to 900 °C (10 °C/min, held a max temp 1 h under argon). A: Full beads, B: the change in texture between the outer and inner structure, C: the surface structure and D: the internal structure. The corresponding TGA trace can be seen in Figure 86

floated on the surface of the 32 wt% glyoxal solution sinking to the base of the vessel over a 15 min period as they became swollen with cross-linking solution (a 40 wt% glyoxal solution has a density of 1.27 g/cm^3).

Once cross-linked, under heating (160 °C), the beads produced were slightly larger than those produced in the previous section due to the use of wider dropping tips in the multi-head scaled up process. The average diameter also scaled with the concentration of the cross-linking solution used (Figure 88 A), not the molar ratio between glyoxal:AGU in solution (Figure 88 B).

HPLC analysis of the resulting glycolic acid, formed after exposing the sample reacted with a 32 wt% glyoxal cross-linking solution to NaOH, highlighted a glyoxal:AGU mole ratio of 12.1 (reaction solution = 23.5 glyoxal:AGU ratio). This suggested significant dimerisation of the glyoxal moieties within the cellulose matrix as a single AGU contains three OH groups able to react with one molecule of glyoxal each. Halving the mass of the glyoxal solution (12.4 glyoxal:AGU ratio) whilst keeping the same concentration of glyoxal (32 wt%) reduced the amount

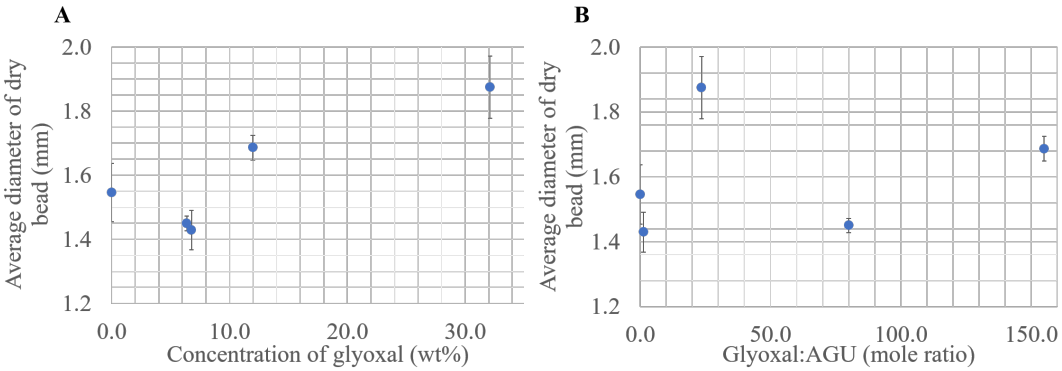

Figure 88: The effect of A: glyoxal concentration and B: mole ratio (glyoxal:AGU) in the reaction solution on the average diameter of dried cross-linked cellulose beads formed from a scaled up multi-head process.

Table 14: Effects of cross-linker concentration and mole ratio (glyoxal:AGU) in the reaction solution on the average diameter of dried cellulose beads (taken from 18 beads, 3 measurements per bead).

Cross-linking solution concentration (wt%)	Molar ratio of cross-linker in solution (glyoxal:AGU, AGU=1)	Dry diameter (mm)
0	0	1.55 ±0.09
6.4	80	1.40 ±0.04
6.8	1.3	1.43 ±0.06
12.0	155.0	1.69 ±0.04
32.1	23.5	1.87 ±0.10

of cross-linker in the final sample to 7.3 (glyoxal:AGU). Dimerisation has been shown to cease after the formation of a dioxolone ring trimer within solution, therefore one would expect a maximum of 9:1 glyoxal:AGU (Figure 89).[164] The cross-linking between cellulose chains and the high temperature of this reaction, potentially enabled the formation of longer oligomers within the material.

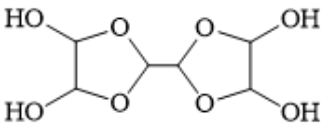

Figure 89: A trimer formed from the ring closure of three moles of glyoxal. Typically found in solution.[164]

SEM images of the beads cross-linked with a 32 wt% solution of glyoxal

(Figure 90 A) showed a mostly smooth external surface bearing a few voids (Figure 90 B, C). The internal structure appeared the same as that of other cross-linked samples presented earlier (Figure 90 **D**). The high level of cross-linking in the 32 wt% sample produced a tough bead, preventing it from collapsing upon drying, therefore obtaining a larger dry diameter and smooth tough outer skin which was not undulating, as seen with samples containing a 2.1 glyoxal:AGU ratio (mol/mol, reacted with 12 wt% cross-linking solution)(Figure 81 E).

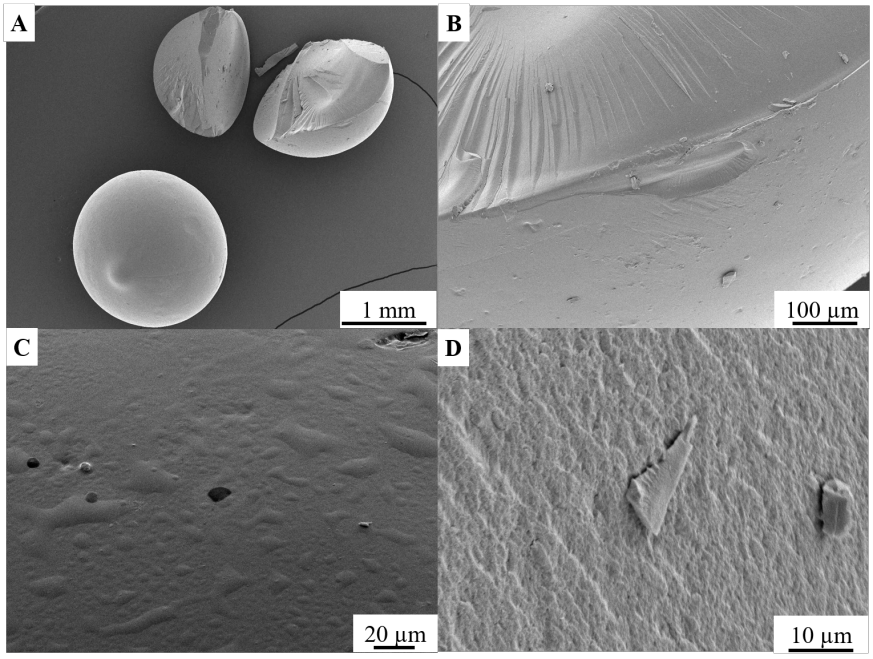

Figure 90: A, B: Cross-linked cellulose beads from a 32 wt% glyoxal solution with the C: surface and D: internal structure magnified.

Potentially, the larger glyoxal based dimers could have been acting as spacers between the cellulose chains enabling a higher diffusion of water from the materials preventing the formation of pits and surface roughness, resulting in the smooth topography seen in Figure 90.

Cross-linking of cellulose microbeads was attempted, however significant cross-linking between beads was witnessed leading to the formation of large aggregates that could not be fully dispersed (Figure 91). This was an issue with the microbeads, and not the larger millimetre beads, as the area of contact

between residual cross-linker located on the surface of the bead was less, relative to the size of the beads, on the larger beads. This potentially could be overcome by agitating the beads during heating, reducing contact between them and therefore the chance of bead binding. Another solution could be used to emulsify the suspension of the polar beads, swollen with cross-linking solution, in a non polar solvent, which is also immiscible with the cross-linking solution, reducing contact between the beads. Another route could be to wash residual cross-linking solution from the surface of the beads.

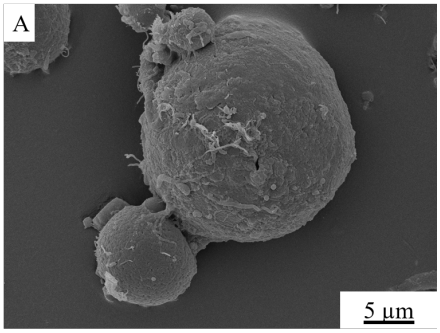

Figure 91: SEM image of a cross-linked cellulose microbeads from a 12.4 wt% glyoxal solution (glyoxal:AGU in solution = 126).

Although not readily transferable to microbeads, glyoxal cross-linking of cellulose has been shown to be an interesting and applicable route to the formation of mechanically rigid beads which could be manipulate by incorporating different concentration of cross-linker and using different heating profiles to produce significantly varied surface topography.

6.3 Functionalisation with Trichloro(octadecyl)silane

The surface of cellulose is inherently polar, which is beneficial when utilising the polymer in a polar media, but is problematic when attempting to formulate cellulose in non-polar materials, such as polyolefins or oil based formulations.[165] Functionalisation of the cellulose by imparting a non-polar group to the materials surface, can make it more compatible with non-polar materials.[166] To achieve this,

dried non-cross-linked beads (1.5 ±0.03 mm), formed from the small scale needle dropping process described in Chapter 5 section 5.4 (Figure 74), were reacted with trichloro(octadecyl)silane (TOS, TOS:AGU 2.4, mol/mol, 20 mL dry toluene, 1 h RT, N_2)(Figure 92).

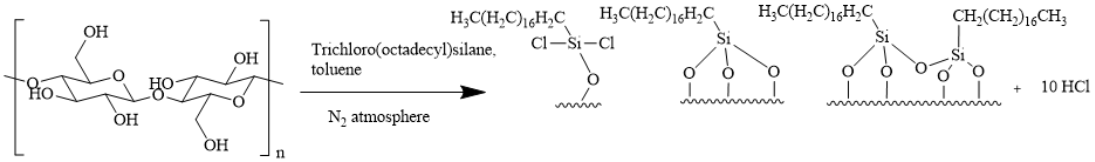

Figure 92: Trichloro(octadecyl)silane (TOS) reaction with cellulose in dry toluene showing the potential binding of TOS to the surface of cellulose.

The beads aggregated when initially placed in toluene but dispersed when TOS was added suggesting a change in the surface polarity to a non-polar regime. The beads were washed with excess ethanol and dried under vacuum (80 °C) during which they turned black. SEM images of the beads showed a smooth surface bearing large cracks (Figure 92 A). This could have been generated via the HCl produced as the reaction progressed remaining in the cellulose matrix which upon heating could have led to blackening and degradation of the bead surface.

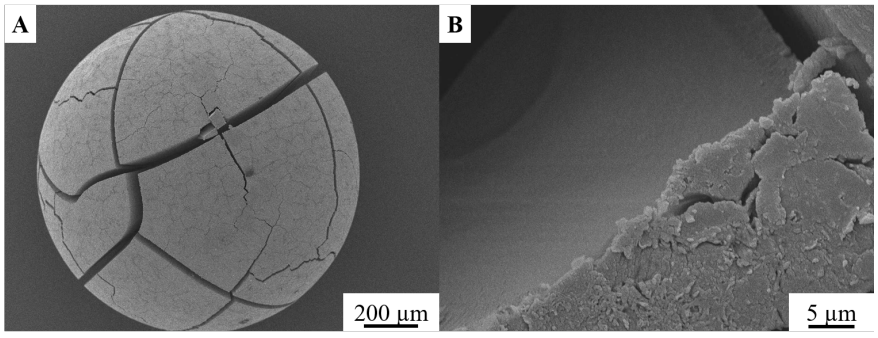

Figure 93: SEM images of cellulose beads treated with TOS A: the bulk bead and B: the edge of a crack.

The TOS reacted beads were smoother than pure cellulose samples which suggested a dampening of the surface topography via the hydrophobic coating or potentially removal of the surface roughness via acid etching. The samples were ruptured after freezing with liquid N_2 and analysed using energy dispersive X-ray spectroscopy (EDX) (Figure 94). Particular attention was paid to the cross

section of the samples in which a penetration depth of the surface reaction was determined (Figure 94 A, B). The surface of the samples was shown to contain a degree of silicon, from the silyl group on the surface of the bead and an increase in oxygen content, potential from the formation of Si-OH bonds (Figure 94 C, D). Based on the presence of silicon, the reactant was found to penetrate to a depth of *ca.* 4 μm into the surface of the bead (Figure 94 B). Mapping a cross section showing the surface and interior of the bead showed that silicon was concentrated on the surface of the sample, with slight penetration into the internal structure (Figure 94 C, D).

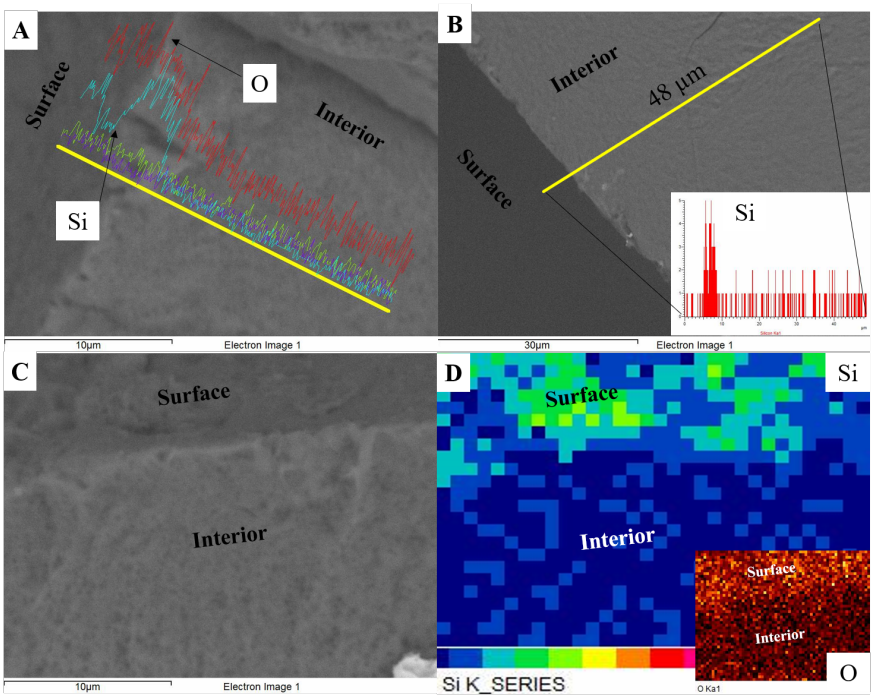

Figure 94: EDX analysis showing the change in silicon composition between the interior and surface of TOS treated cellulose beads. Sample were frozen and rupture before analysis to expose the interior. A: the element composition from the surface to the interior of the bead (yellow line), B: changes in silicon content from the surface to interior of the bead C, D: image and accompanying map for silicon and oxygen content.

6.3.1 Thermogravimetric Analysis

Thermal degradation of the cellulose-TOS material was used to quantify the silicon content and therefore the extent of functionalisation. There was little difference in the onset temperature between cellulose and TOS functionalised cellulose beads (Figure 95). The functionalised sample did however have a less defined weight loss with increasing temperature compared with the cellulose sample, which had two clearly defined regions of degradation. After full degradation of the samples (900 °C, 1 h), there was residue SiO_2 found in the crucible accounting for 0.62 wt% of the total sample weight (0.1 mg).

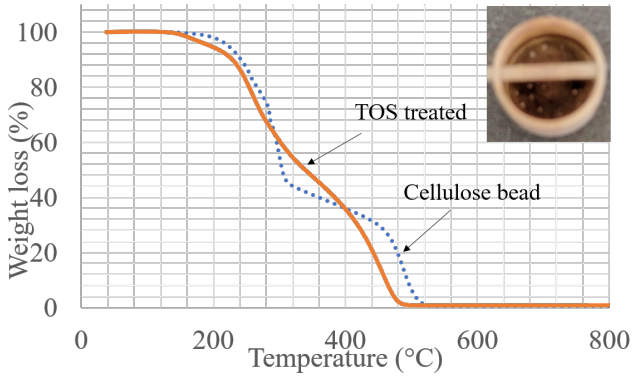

Figure 95: A comparison between the thermal decomposition in air of a cellulose bead and a cellulose bead surface treated with TOS (air, 5 °C min^{-1}). The residual sample after degradation are also shown.

Using the following equation, the silicon content of the sample could be determined from the final weight:[167]

$$Si(wt\%) = \left(\frac{0.467 \times W_{SiO_2}}{W_1} \times 100\right) \tag{33}$$

Where W_{SiO_2} is the weight of SiO_2 left after thermal degradation, W_1 is the original weight of the sample and 0.467 the mass fraction of silicon in silicon dioxide.[167] The total Si content was found to be 0.07 mg giving the TOS content as 3.6 wt% (assuming an RMM of 252.58 $gmol^{-1}$ from replacement of unreacted Cl with OH) or a mole ratio of 0.02 (TOS:AGU) reacted with the bead.

The successful reaction of a hydrophobic group to the surface of the produced cellulose beads has shown a potential path to increasing the applicability of cellulose beads as composite fillers or in oil based formulations in which a non-polar material is required.

6.4 Chitosan Coated Cellulose Beads

The anti-bacterial and enhanced cell adhesion properties of chitosan are a sought after attribute, but the bulk material suffers from poor tensile strength which can be overcome by blending with cellulose.[119,168–171] The formation of cellulose-chitosan cross-linked beads has been noted before,[172] as well as chitosan coated cellulose materials,[173] but there are no examples in the literature of chitosan coating of cellulose beads. A process described by a previous member of the group documented a novel procedure for the formation of chitosan coated cellulose films.[119] In the case of this work, replacement of the ethanol anti-solvent bath, used in the large scale multi-head dropping process described in Chapter 5 section 5.4.2 (Figure 75), with a solution of chitosan dissolved in aqueous acetic acid (0.24 M, 1.2 wt% low MW chitosan) enabled the formation of a chitosan coating on the exterior of the formed cellulose beads (Figure 96). The aqueous nature of the solution allowed for its successful use as an anti-solvent for droplets of cellulose-OES in placed of ethanol.

When using a 2 wt% chitosan solution as an anti-solvent bath, the droplets of 8 wt% MCC-OES solution remained on the surface and sank with agitation. This build up of un-coagulated droplets on the surface of the bath led to significant contact and coalescence between the droplets. The density of the chitosan solution was deemed too high to enable large scale synthesis of chitosan coated cellulose beads. Dilution of the chitosan anti-solvent bath to a final solution composition of 1.2 wt% chitosan (low MW) dissolved in 1.4 wt% acetic $\text{acid}_{(\text{aq})}$ (0.24 M) enabled the cellulose-OES droplets to sink through the solvent bath at a fast enough rate to prevent coalescence of droplets on the surface.

Using the multihead dropping apparatus developed in Chapter 5 section 5.4.2, chitosan coated cellulose beads were successfully formed at scale. A total

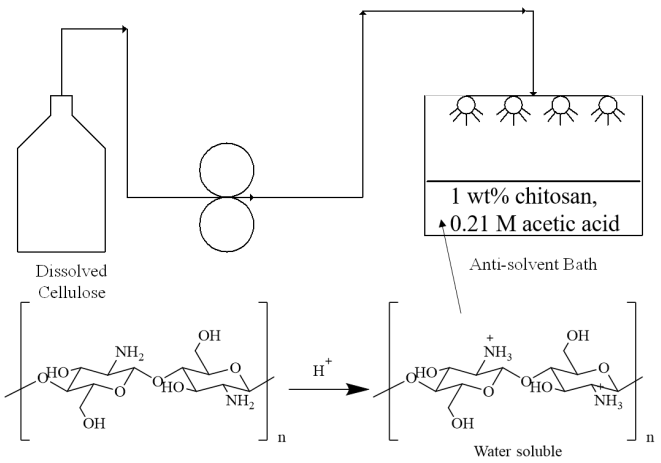

Figure 96: Schematic of the dissolution of chitosan in aqueous acid and the set up for the dropping rig used to produce chitosan coated cellulose beads.

of 2.4 L of 8 wt% cellulose-OES solution was dropped into a 2.5 L of 1 wt% chitosan solution taking 130 mins to process. The formed wet droplets had an average diameter of 2.9 ±0.1 mm (Figure 97 A), comparable in size with the cellulose beads formed previously (3.0 ±0.2 mm) using the same dropping procedure (Chapter 5 section 5.4.2).

SEM images of the chitosan coated cellulose beads presented a mostly smooth surface with some large protrusions from the surface (Figure 97 B, C, D), which were potentially chitosan deposits. This was in contrast to cellulose beads which underwent significant surface roughening during drying, brought about by shrinkage and wrinkling of the structure. In the case of the chitosan coated cellulose beads, coagulation took place in a chitosan aqueous acid solution opposed to ethanol in the other examples in this thesis. Water has been shown to produce more crystalline, and therefore rigid, materials when used as an anti-solvent for cellulose compared with ethanol (Chapter 2).[62] These materials would therefore be more resistant to deformation upon drying resulting in smoother surfaces.

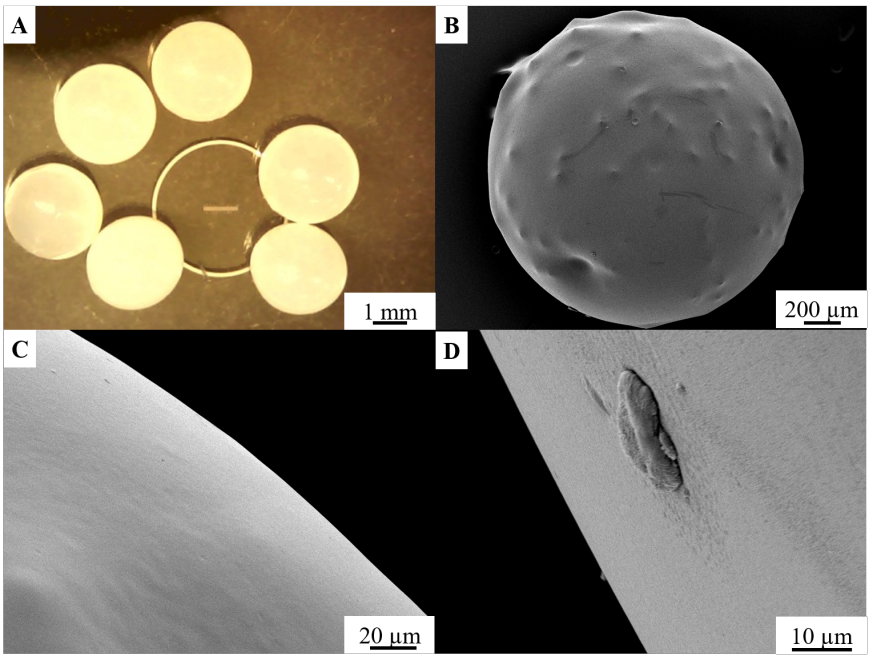

Figure 97: Images of chitosan coated cellulose beads including A: an optical micrograph and B, C: SEM images of the surface of the beads, D: the surface of the bead highlighting a potential chitosan deposit.

6.4.1 Cross-linking Chitosan Beads

Again, to improve the mechanical properties of the polymer, high concentration cross-linking of chitosan coated cellulose beads was conducted via a similar process described previously (section 6.2.5). In this case, a 40 wt% glyoxal solution was used (11.1 glyoxal:AGU in solution) to enable rapid uptake of the cross-linker by the beads. Initiating the cross-linking reaction with heating produced deep yellow coloured beads (Figure 98) with an average diameter of 2.2 ±0.2 mm (Figure 99 A), larger than any other dried beads produced so far, and a dry average mass per bead of 8.8 ±1.8 mg. It was unclear at this stage if this size was a result of the chitosan coating, or high levels of cross-linker.

Using SEM analysis, the beads were observed to have a smooth surface with some sub-micron roughness to them (Figure 99 B, C, D). Some shallow pits were also found on the surface of the material (Figure 99 C).

Removal of the cross-linker with base and quantification of the expelled

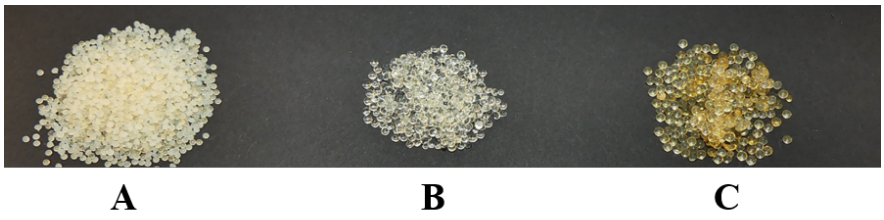

Figure 98: Images of A: cellulose beads, B: cross-linked cellulose beads and C: chitosan coated cross-linked cellulose beads.

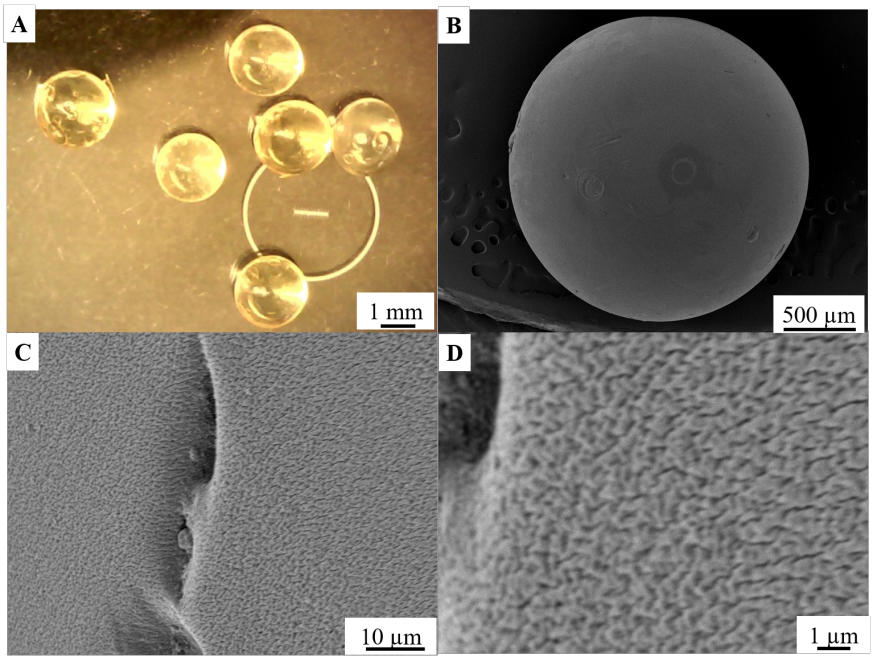

Figure 99: Images of chitosan coated cross-linked cellulose beads including A: an optical micrograph of cross-linked chitosan coated beads along with SEM images of B, C, D: the surface of the beads at increasing magnification.

glycolic acid suggested a high cross-linker uptake of 10.9 glyoxal moles per AGU. This being smaller than that of the 32 wt% reacted cellulose beads documented earlier (12.4 glyoxal:AGU in the bead, section 6.2.5) suggested that the increased size of the cross-linked chitosan coated cellulose beads was due to the surface coating of chitosan, not the amount of cross-linking which was lower than previously found (section 6.2.5). This coating also appeared to be responsible for the lower than expected extent of cross-linking compared with cross-linked cellulose beads. This could have been due to residual acetic acid being present in the chitosan layer, which would react with the cross-linker, although

this is unlikely as the beads were thoroughly extracted via Soxhlet (ethanol). Glyoxal cross-linking has been hypothesised to occur more favourably in the more accessible amorphous area of cellulose materials over crystalline region.[105] This potentially explains the lower degree of cross-linking in these samples compared with previous ethanol coagulated samples due to the expected higher degree of crystallinity, a result of coagulating in an aqueous media.

6.5 Surface Etching

As mentioned previously, in some applications, e.g. as supports, smooth beads are not as desirable as those with a rougher exterior.[154] Etching could potentially be used as a post production step to selectively hydrolyse the surface of the bead to increase its roughness. Acidic and enzymatic hydrolysis of cellulose has been widely applied to generate fermentable sugars for biofuel formation,[174] but in this research, we wish to only adjust the relative surface roughness of cellulose. Enzymatic etching has been shown to develop micropatterns on other biopolymer materials[175,176] and can also be used to selectively remove starch from starch-cellulose blends producing rough materials.[177] This section presents data of the effect of enzymatic and acid etching of cross-linked cellulose beads formed from a dropping process.

6.5.1 Enzymatic Treatment[1]

Here we propose the bulk treatment of cross-linked (with a 6.7 wt% glyoxal solution) and non-cross-linked cellulose beads with a cellulase enzyme solution (from *Trichoderma reesei*) to alter the topography of the bead. Exposing non-cross-linked cellulose beads to a 5% (v/v) enzyme solution (citrate buffer, pH 4.8, 50 °C, 1h) resulted in a rougher bead surface (Figure 100).

Under the same enzyme treatment, cross-linked samples (with a 6.7 wt% glyoxal solution) formed a consistent undulating surface from which the outer

[1]Some experimental data in this section was collected in conjunction with Davide Califano, a full list of which can be found in the Appendix.

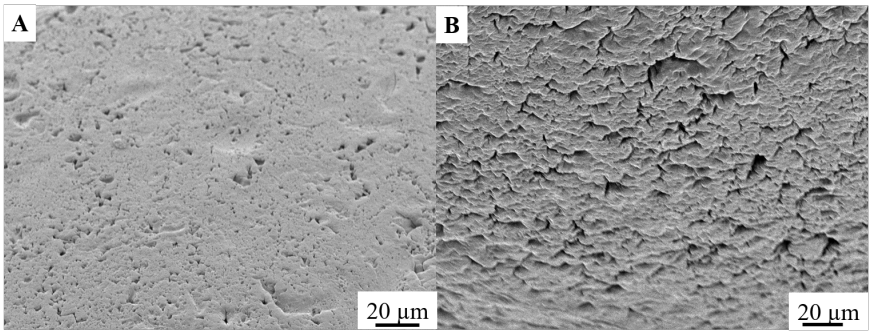

Figure 100: SEM images of a A: cellulose beads and B: one treated with 5 % enzyme (v/v) in a citrate buffer (pH 4.8, 50 °C, 1h) both were vacuum dried before imaging.

layer of the bead appeared to be peeling off (Figure 101). This differed to the topography gained when exposing non-cross-linked samples to the same enzymatic etching conditions and potentially could have occurred because of a greater degree of penetration by the enzyme-buffer solution into the cross-linked sample due to a more open accessible structure.

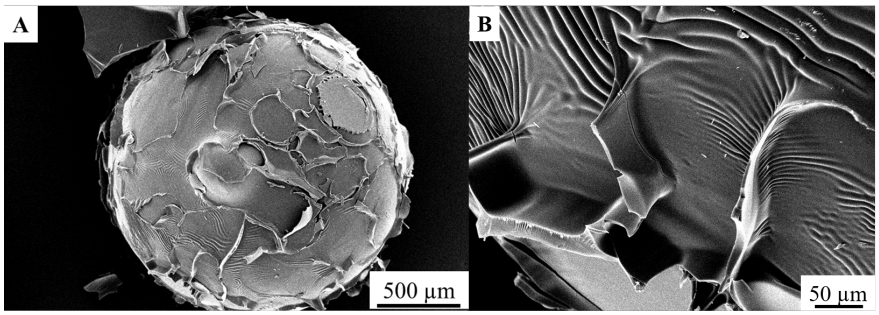

Figure 101: SEM images of a A, B: glyoxal cross-linked cellulose beads (with a 6.7 wt% glyoxal solution) treated with 5 % enzyme (v/v) in a citrate buffer (pH 4.8, 50 °C, 1h). Samples were vacuum dried before imaging.

Interestingly, when cross-linked samples were exposed to the enzyme solution (citrate buffer, pH 4.8, 50 °C, 1h) the beads were seen to swell significantly, absorbing the majority of the solution (Figure 102 B, C). The same was seen when exposed to the buffer solution with no enzyme.

The surface of the cross-linked bead exposed to buffer developed a wrinkled surface (Figure 103), this suggested the partial overlap of the outer layer on the surface of the beads or some extent of contraction of the internal structure causing the outer layer to wrinkle and overlapped upon drying. It appeared that

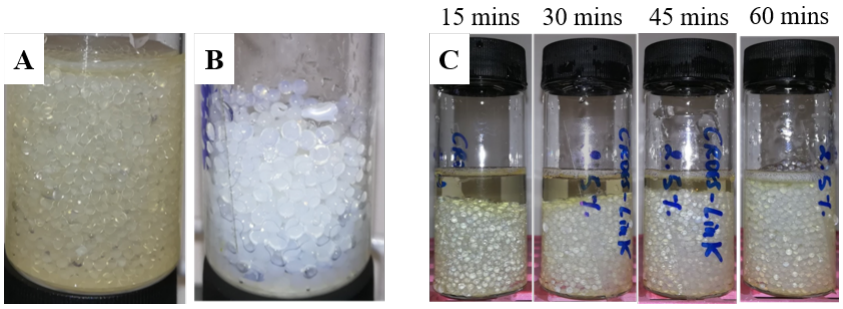

Figure 102: Images of cross-linked bead left in 15 mL of A: deionised water, B: buffer solution (citrate buffer, pH 4.8) and C: enzyme solution (5%, (v/v) citrate buffer, pH 4.8) for 1 h at 50 °C.

the swelling of the bead in the buffer and enzyme solution caused the outer layer to stretch out which upon drying lead to the wrinkled surface.

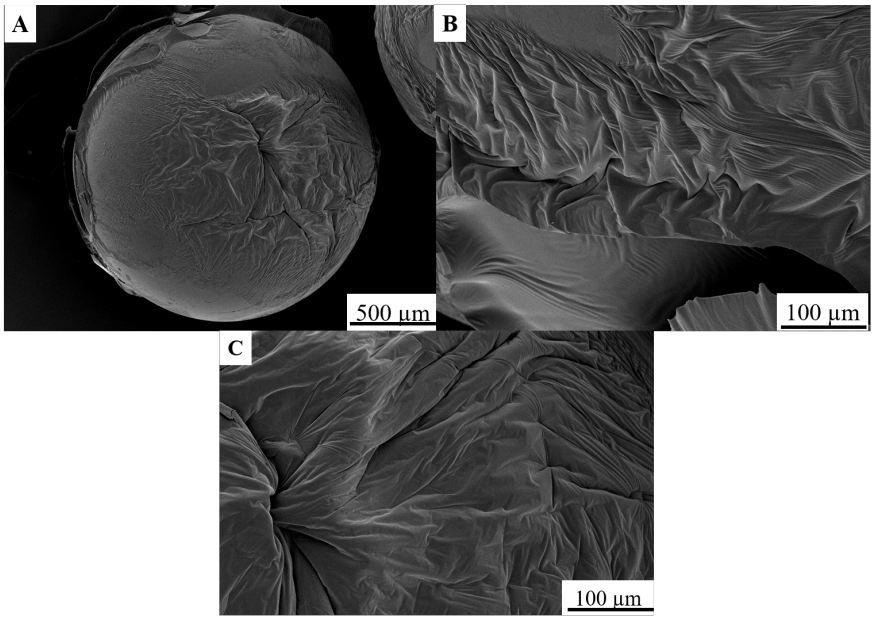

Figure 103: SEM images of a A, B, C: glyoxal cross-linked cellulose beads (with a 6.7 wt% glyoxal solution) treated with citrate buffer (pH 4.8, 50 °C, 1h). Samples were vacuum dried before imaging.

The exposure of cross-linked cellulose beads to enzyme solutions and citrate buffer was also found to greatly influence the mechanical properties of the beads. In both cases, cross-linked samples exposed to an enzyme-citrate solution (Figure 104 A) and a solely citrate based solution (Figure 104 B) become unable to resist delicate mechanical compression (spatula) and broke down into particles.

A non-cross-linked cellulose bead exposed to the same enzymatic solution was found to resist the compression and remain intact (Figure 104 **C**).

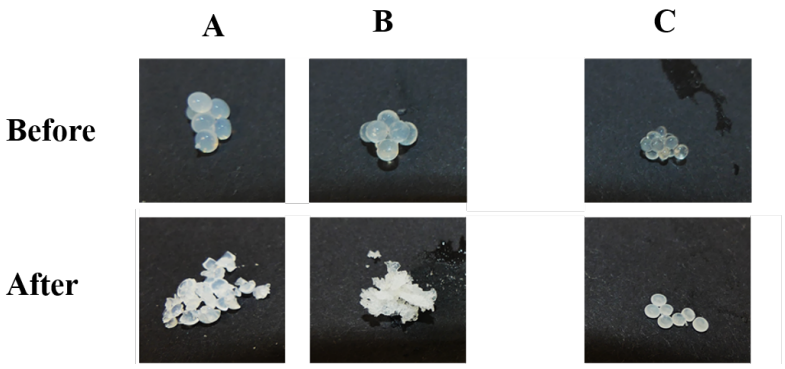

Figure 104: Images of wet bead samples exposed to brief manual compression. Specifically A: cross-linked cellulose beads - no enzyme (citrate buffer, pH 4.8), B: cross-linked cellulose beads - 5% enzyme (citrate buffer, pH 4.8) and C: cellulose beads (no cross-linking) - 5% enzyme (citrate buffer, pH 4.8).

The buffer solution had a profound effect on the cross-linked beads, more so than the non-cross-linked samples. It appeared that the cross-linked samples were more accessible to the buffer solution, swelling significantly when exposed to it. Potentially the open voids and holes in the materials surface could have acted as pathways for the buffer to diffuse into the material more readily than the dense collapsed structure of non-cross-linked dried cellulose beads. The acidic pH of the buffer solution (pH 4.8) could have also led to this as acids have been shown to swell cellulose, specifically in the amorphous regions of which these samples had many.[174] The addition of a cross-linker could potentially have led to an increased separation between some chains, because of the length of the oligomerised cross-linker, generating more "voids" for the uptake of acid and therefore becoming more accessible to the enzyme compared with non-cross-linked samples. These results suggested that cross-linked samples, somewhat counter intuitively, were more readily degraded using a cellulase enzyme than non-crosslinked samples, hypothesised to be due to the more open structure of the cross-linked beads compared with the dense non-cross-linked variants.

6.5.2 Acid Treatment

To investigate the effect of acid etching on the topography of cross-linked beads, aliquots of cross-linked cellulose beads (glyoxal:AGU = 12.1 in the final material) were exposed to varying concentrations of HCl or H_2SO_4 (1, 2.5 or 4 M) for 10, 35 or 60 mins at 65 °C. These factors and ranges were investigated in a DoE style (Table 15).

Table 15: The set of experiments used to determine the effect of acid concentration, acid type and exposure time on the surface topography of cross-linked cellulose beads.

Acid concentration (M)	Acid	Time (min)
1	H_2SO_4	10
1	HCl	60
2.5	H_2SO_4	35
2.5	HCl	35
4	H_2SO_4	60
4	H_2SO_4	10

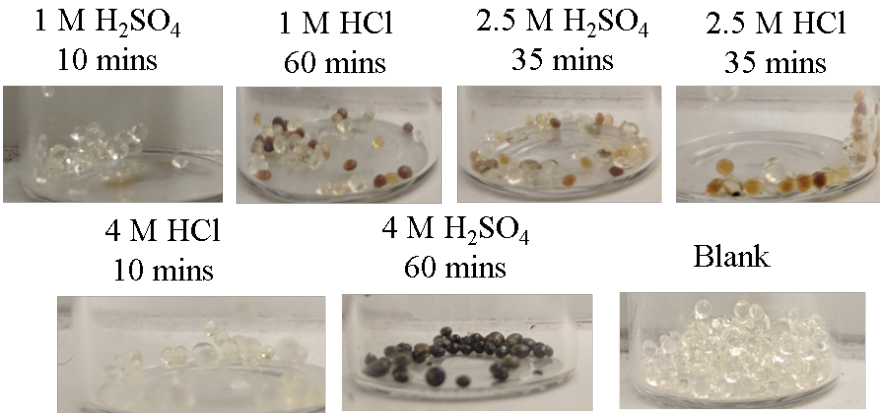

Figure 105: Images of cellulose beads etched with acid at 65 °C showing the concentration of acid, acid used and period of etching.

The samples were washed with excess water and vacuum dried prior to analysis. Figure 105 shows the difference in bead colour seen across the range of acid etched samples. Each cross-linked bead exposed to acid for 10 mins, no matter the concentration, did not change colour (see Figure 105). The sample exposed to 4 M H_2SO_4 for 60 mins underwent significant blackening of the surface,

comparable to cellulose beads reacted with TOS, hypothesised in that case to be due to excess heating in the presence of residual HCl. It was not possible to see a variation between the other samples without analysis via SEM, but discolouration was observed in each.

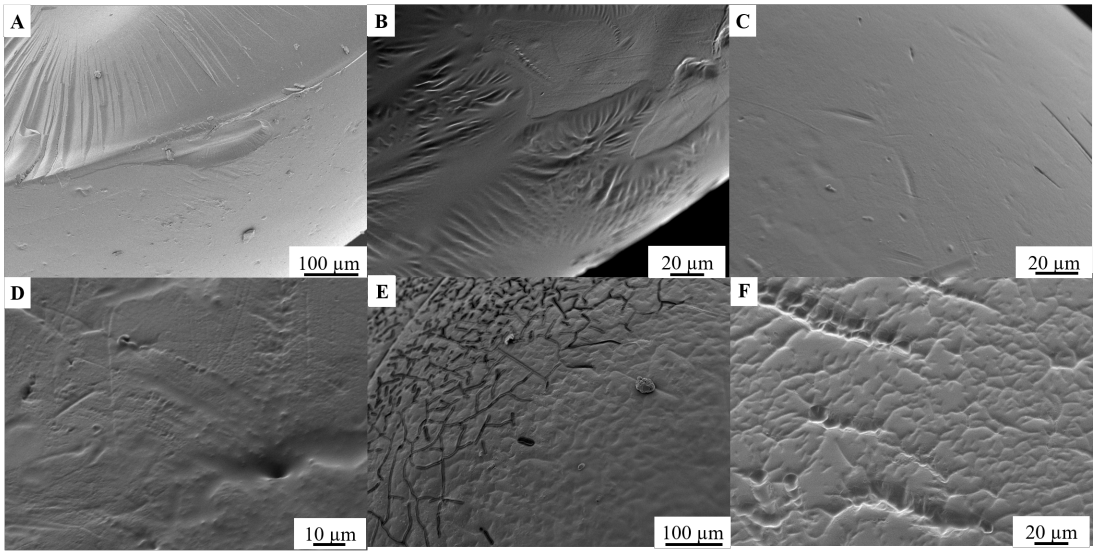

Figure 106: SEM images of A: glyoxal cross-linked cellulose beads (glyoxal:AGU = 12.1) treated at 65 °C with B: 2.5 M HCl (35 mins), C: 2.5 M H_2SO_4 (35 mins) D: 1 M HCl (60 mins) E: 4 M H_2SO_4 (60 mins) and F: 4 M HCl (10 mins). Samples were vacuum dried before imaging.

Comparing the two mid point samples (H_2SO_4/HCl, 2.5 M, 35 mins), the HCl exposed cross-linked cellulose bead showed signs of pitting on the surface as well as wrinkling (Figure 106 B), akin to samples exposed to citrate buffer (Figure 103). The H_2SO_4 sample on the other hand remained generally smooth (Figure 106 C) with slight roughening on the surface when compared with non-acid etched cross-linked cellulose beads (Figure 106 A). Samples exposed to 1 M H_2SO_4 for 10 mins received a complete lack of change in bead topography. 1 M HCl did lead to slight roughening of the bead surface after 60 mins of exposure (Figure 106 D) but not as much as the higher concentration. Both 4 M acid exposed samples showed significant roughening of the surface, but of differing forms. 4 M H_2SO_4 exposure for 60 mins generated cracking of the surface which appeared to permeate into the bead surface (Figure 106 E) and led to significant bead discolouration (Figure 105). 4 M HCl exposure for 10 mins on the other hand generated a consistent roughening of the surface with shallow ridges (Figure 106

F) and did not lead to any sample discolouration (Figure 105).

This result suggested that the concentration and type of the acid used to treat the bead surface played an important role in determining the type and extent of surface roughening observed. The discolouration of beads after acid etching did not appear to be related to the roughness of the surface but the length of time the sample was exposed to acid. It is possible that hydrolysis of the surface of the bead led to the generation of caramelisable sugars which under went the caramelisation process when heated discolouring the beads. To prevent this, and impart significant surface roughening, beads should be exposed to a high concentration acid solution (4 M) for a brief amount of time.

6.6 Cellulose - Ammonium Polyphosphate Composites[2]

Cellulose is widely documented as an applicable material for the formation of composites with superior benefits over the base material.[178,179] For example, improving the fire retardancy of cellulose, which in its pure form is highly flammable limiting its use in any application where ignition is a possibility, for examples in lithium-ion batteries and general storage of the dried material.[180] Therefore we turn our attention to the generation of cellulose-fire retardant composites.

Ammonium polyphosphate (APP), often used as a non-halogenated fire retardant in paper,[155] is seen as one of the most efficient flame retardant fillers due to its significant effect when used in smaller concentrations, especially when compared with inorganic flame retardant fillers.[181,182] APP retards fire spread via the generation of a inert charred layer on the surface of the material acting as a physical barrier against further combustion.[183] Particle size analysis of the provided APP powder (Chemox pound) showed a volume average particle size of 18.2 μm which could be reduced to 13.8 μm by dispersion using a sonic horn (30%

[2]Some experimental data in this section was collected in conjunction with James Close during an MEng project, a full list of which can be found in the Appendix.

intensity, 2 mins, water) which dispersed any aggregates (Figure 107). The MW of this APP (97) led to the material being insoluble in water and the OES, however the cellulose-OES-APP dispersion was not stable and would settle overtime. The particles themselves appeared rectangular and irregular in shape (Figure 107 B).

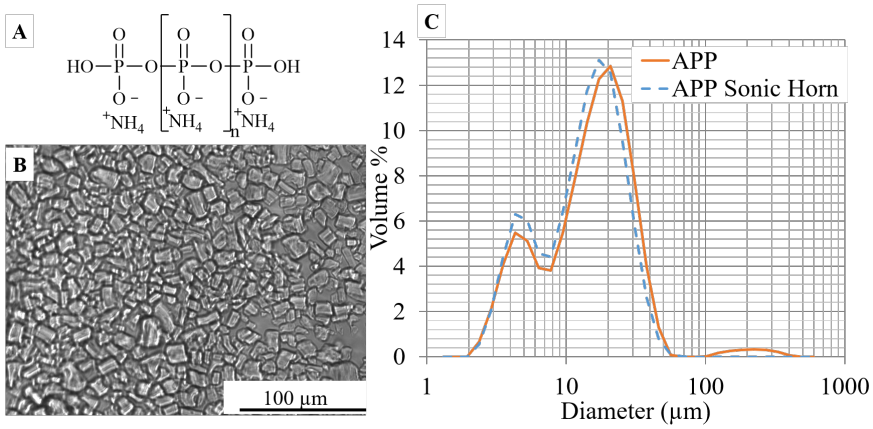

Figure 107: A: The structure of APP, B: an optical micrograph of APP (15 wt%) in water and C: particle size distributions of APP used as received (solid distribution) and dispersed using a sonic horn (dashed distribution, 30 %, 5 mins, 15 wt% in water).

APP was dispersed in 8 wt% cellulose-OES (DMSO:[EMIm][OAc], 70:30, w/w) and dropped into an ethanol bath via a small scale needle dropping procedure as described in Chapter 5 section 5.4, generating cellulose-APP composite beads. Three 8 wt% cellulose-OES-APP dispersion were made with the relevant concentrations to generate a final solid composition of 5, 10 or 15 wt% APP filler (labelled low, medium and high) in the final cellulose bead as well as a sample generated from a disperse phase which had been subject to centrifugation (3000 RPM, 3 mins) to remove large APP particles from a high APP concentration dispersion. A size distribution could not be obtained for the centrifuged sample as the cellulose-OES-APP dispersion could not be dispersed in water, due to its anti-solvent effect with regards to cellulose. Repeating the centrifugation with APP dispersed in water, in place of the OES, would have given different results due to the vast difference in polarity, density and viscosity between water and the cellulose-OES.

6.6.1 SEM-EDX

SEM analysis of the low and high concentration APP samples showed that the APP particles had been incorporated into the cellulose matrix (Figure 108 A, C) and were visible on the surface of the beads (Figure 108 D, F). Scratches were also see on the surface of these material (Figure 108 D), presumably resulting from shear generated between APP particles jutting out of the beads surface and the cellulose matrix on an adjacent bead. The mid-APP concentration sample however showed little to no presence of APP in the cellulose matrix (Figure 108 B), on the exterior at least (Figure 108 E). The unstable dispersion between cellulose-OES and APP could have led to a smaller than expected concentration of APP in the final bead.

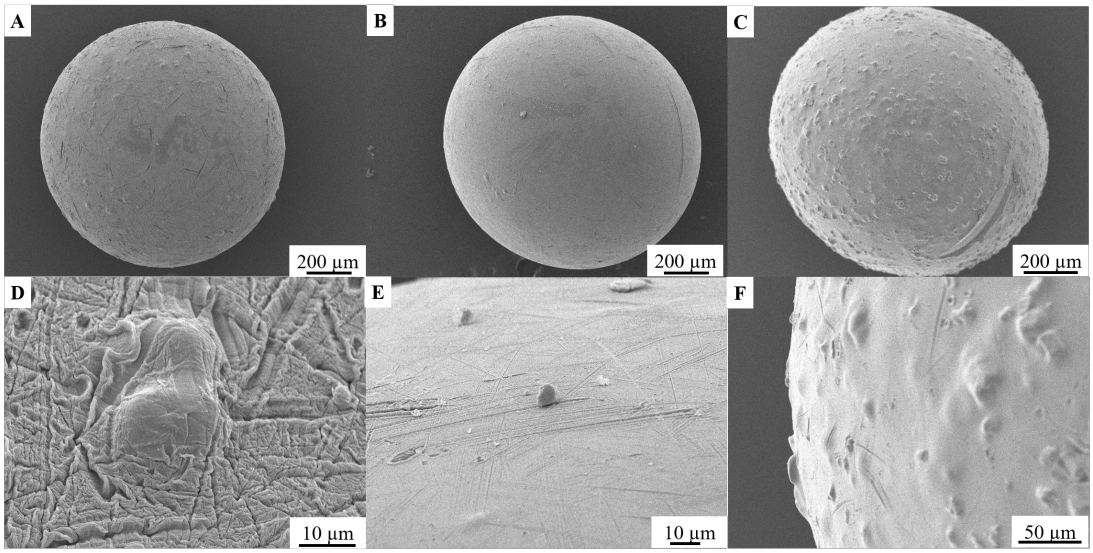

Figure 108: SEM images of cellulose-APP composite beads with following concentrations of APP in the bead; A, D: 5 wt% (low), B, E: 10 wt% (mid) and C, D: 15 wt% (high).

In the sample generated from a centrifuged dropping phase, APP was again clearly visible on the surface of the material (Figure 109 A, B), highlighting it incorporation into the bead.

EDX analysis showed that the particles present in the cellulose matrix were clearly phosphorous containing, both internally (Figure 110 A, B) and externally (Figure 110 C, D), and therefore could be concluded to be APP, which also

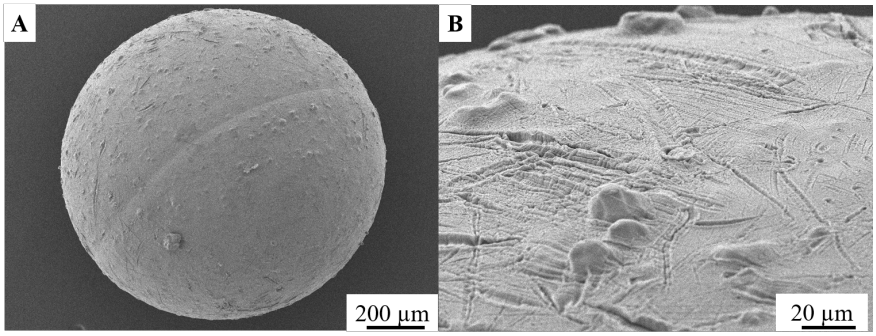

Figure 109: SEM images of cellulose-APP composite beads A, B: formed from a centrifuged 15 wt% APP dropping solutions.

appeared to be well distributed in the bead.

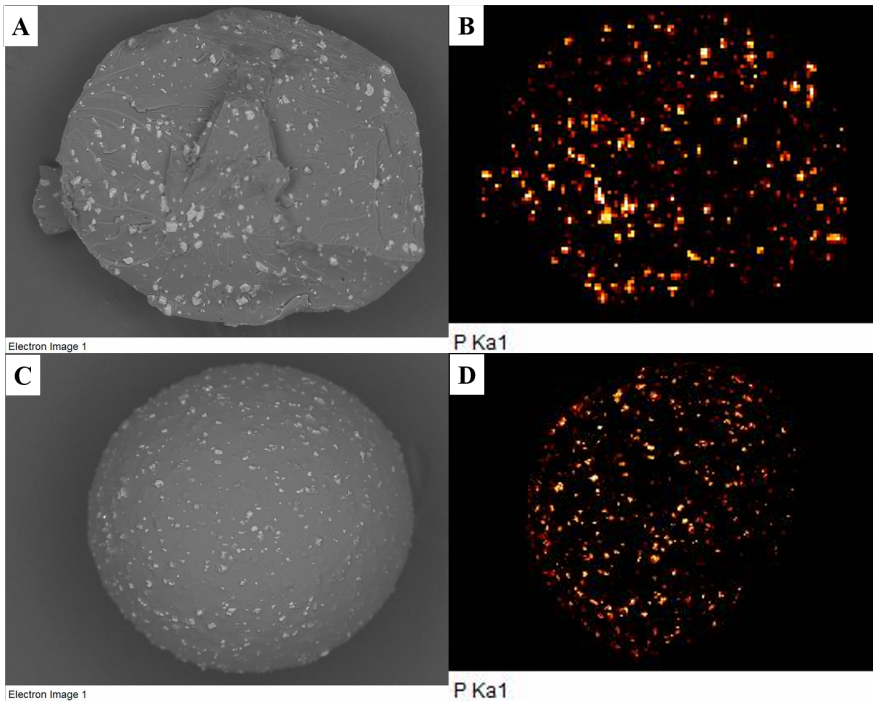

Figure 110: SEM images of a A: cross section, C: outer surface of cellulose-APP composite beads (15 wt% APP) and B,D: the accompanying phosphorous maps.

6.6.2 Compression Analysis

Compression analysis (up to 30% compression) of the four composite bead samples revealed a reduction in the mechanical stability of the APP composite

beads compared with pure cellulose beads (Figure 111). Samples containing mid and high APP concentration as well as the sample generated from a centrifuged dispersion, were all within error of each other, which suggested that the centrifuged samples contained a similar amount of APP to the other two samples. The samples containing a low concentration of APP were weaker and much more compressible under a lower force than any other sample.

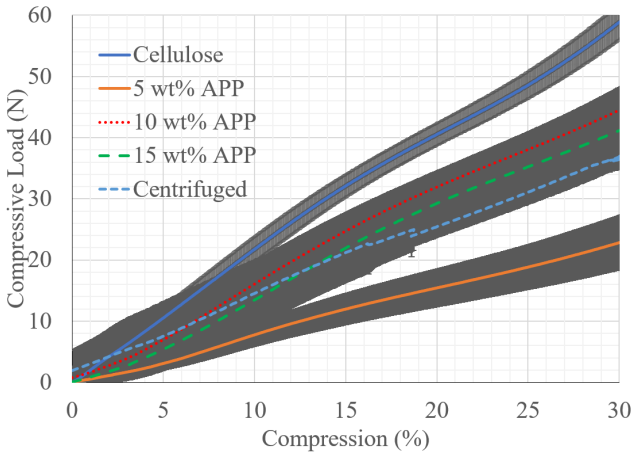

Figure 111: Graphs showing the compressability of cellulose-APP composite beads containing 5 (low), 10 (mid), 15 (high) wt% APP and a sample generated from a dropping phase (15 wt% APP) which was centrifuged before forming beads.

The addition of filler created areas of mechanical weakness, between the cellulose and APP, reducing the overall mechanical stability of the material. This suggested a poor stress transfer from cellulose to the APP filler due to weak adhesion between the two phases.[184]

The low and mid concentration APP samples showed no fracture when compressed further than 30 % (Figure 112 A, B) but upon increasing the APP loading in the bead fracturing began to occur at higher compression, with high concentration APP samples fracturing at around 50 N force with 38% compression (Figure 112 C), which may have been caused by the formation of a greater number microvoids when a higher concentration of APP was used, creating zones in which cracks could propagate.[185]

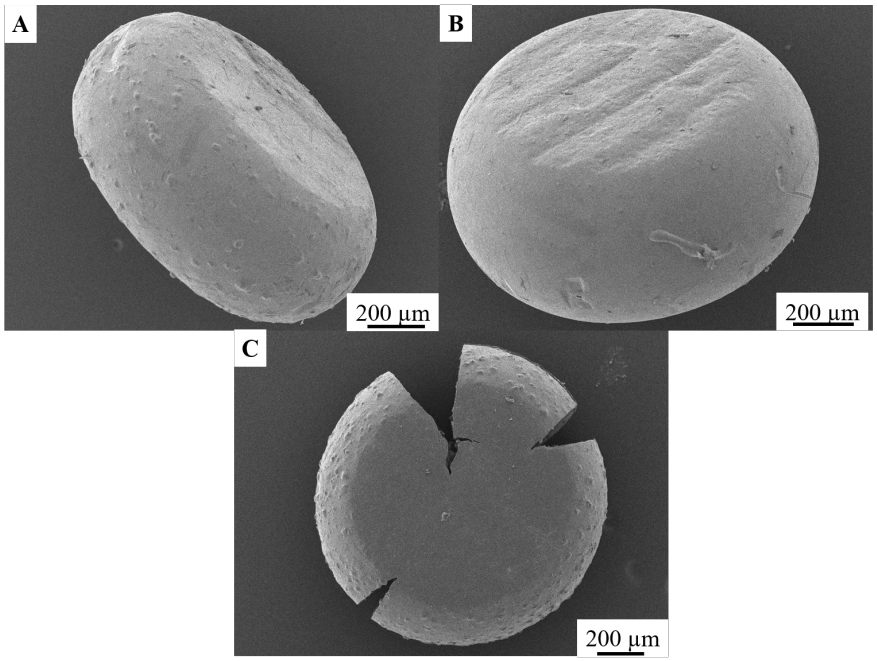

Figure 112: SEM images showing cellulose -APP composite beads after compression analysis. The beads contained A: 5, B: 10 and C: 15 wt% APP.

6.6.3 Thermogravimetric Analysis

The two stage degradation of APP is well documented in the literature. The first step consists of the elimination of NH_3 and H_2O around 300 °C, the release of which can dilute any potential gaseous fuel, retarding fire spreading, and creating a cross-linked polyphosphoric acid residue.[183] The second step occurs at 550 °C and involves the evaporation of polyphosphoric acid and/or its dehydration to P_4O_{10}.[186] The literature temperatures are comparable to the data collected here for the APP powder (Figure 113). In the case of the cellulose-APP composite beads, the temperature at which these two degradation steps begin was found to be much lower (200 and then 450 °C). This suggested partial degradation of cellulose by APP residue formed during thermal decomposition. A similar observation has been see in polyurethane-APP composites.[186]

The 10 wt% system appeared to be an outlier showing a higher onset degradation temperature comparable to that of cellulose, which matched with previous SEM and compression data which suggested a lower than expected

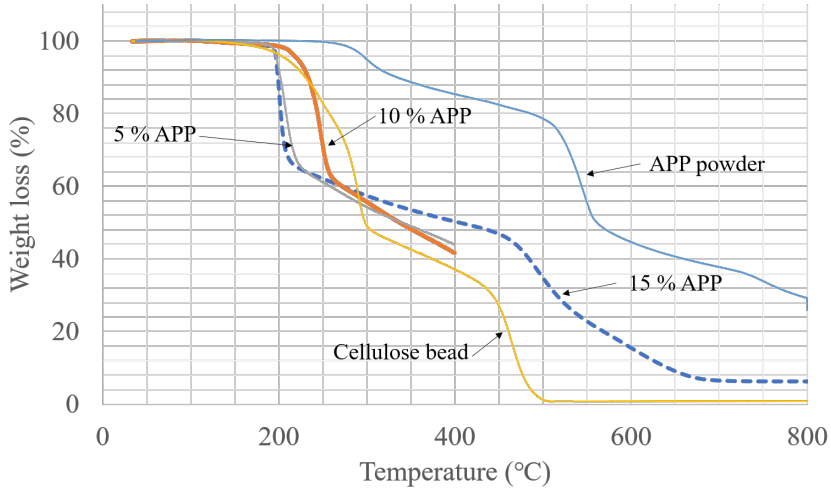

Figure 113: The thermal degradation in air of cellulose, APP powder and cellulose-APP composite beads containing 5 (low), 10 (mid) or 15 (high) wt% APP.

uptake of the APP filler in the final composite bead samples.

6.6.4 Cellulose-APP Microbeads

Forming cellulose-APP composites from a dropping procedure has been shown to be a viable process for the formation of cellulose-APP composite beads. Forming composite micro-beads could also potentially be achieved using the membrane process described earlier (Chapter 5, section 5.3). Particle size distributions for the APP filler (Figure 107 C) showed an average volume distribution of 13.8 μm. Passing this dispersion through a 10μm membrane would potentially lead to blockages of the pores. However, as a number distribution, many of the particles have a diameter less than 10 μm so some particle permeation was expected. The three concentrations of APP (forming 5, 10 and 15 wt% APP in the final material), again dispersed in an 8 wt% -cellulose-OES solution, were tested for the physical values related to membrane emulsification (Table 16) (as in Chapter 4).

There was little difference between each cellulose-OES-APP dispersions made with regards to the physical values measured. Compared to the cellulose-OES solution, the APP solutions were more viscous and had a higher

Table 16: Physical properties measured for cellulose-OES-APP solutions. Where applicable (interfacial tension, contact angle) a 2 wt% Span 80 SFO continuous phase was used.

APP concentration in bead (wt %)	Viscosity of cellulose-OES-APP dispersion (Pa.s)	Density g/ml	Interfacial Tension (mN/m)	Contact Angle (°)
0	1.18 ±0.01	1.133	1.57 ±0.02	133 ±3
5	1.51 ±0.03	1.134	1.77 ±0.06	134 ±6
10	1.57 ±0.03	1.138	1.76 ±0.03	135 ±4
15	1.58 ±0.05	1.139	1.78 ±0.06	136 ±5

interfacial tension whilst suspended in a 2 wt% Span 80-SFO continuous phase. The presence of particles in solution have been shown to increase the viscosity of said solution and it appears that particles at the surface of the droplets had a slight destabilising effect potentially due to partial interference with the surfactant coating.[124] There was no significant change in the contact angle or density of the solutions measured. To prevent blockages within the membrane the disperse phase, containing a high concentration of APP, used was subject to centrifugation (3000 RPM, 3 mins) prior to use to remove larger APP particles from the dispersion. This meant that the concentration of APP in the disperse phase was unknown, however through SEM, TGA and mechanical compression data it has already been shown that the centrifuged samples contained APP and the formed composite beads behaved similarly to the other dispersion of know APP concentration. Using a continuous phase flow rate (Q_{cp}) of 1.4 Lmin^{-1} and a transmembrane pressure (P_{tm}) of 0.03 bar cellulose beads were successfully produced (Ca of 6.51 and We of 4.70 $\times 10^{-10}$).

The measured particle size data (Figure 114) was comparable to those achieved previously (Chapter 5, section 5.3, Figure 70) and had a volume average of 17.7 μm. SEM analysis of the microbeads showed the clear presence of consistently shaped cellulose microbeads but could not highlight any clear presence of APP in the final sample (Figure 115).

Similarly, EDX analysis of the microbeads could not located any obvious phosphorous content in the sample (Figure 116 A-C). It appeared that the tortoise nature of the SPG pores and irregular size and shape of the APP particles prevented any noticeable diffusion of APP particles through the membrane. Further evidence for this theory was gained from the TGA analysis of these beads

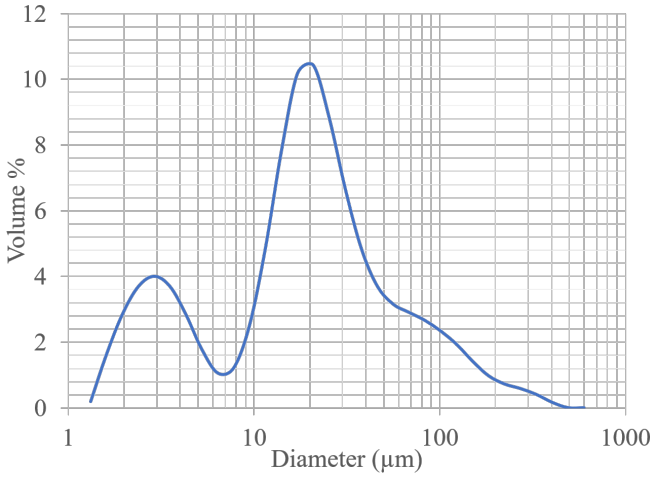

Figure 114: Size distribution of cellulose beads produced from membrane emulsification of centrifuged cellulose-OES-APP solution under the following conditions, continuous phase flow rate = 1.4 $Lmin^{-1}$, transmembrane pressure = 0.03 bar, continuous phase composition = 2 wt% Span 80 in SFO.

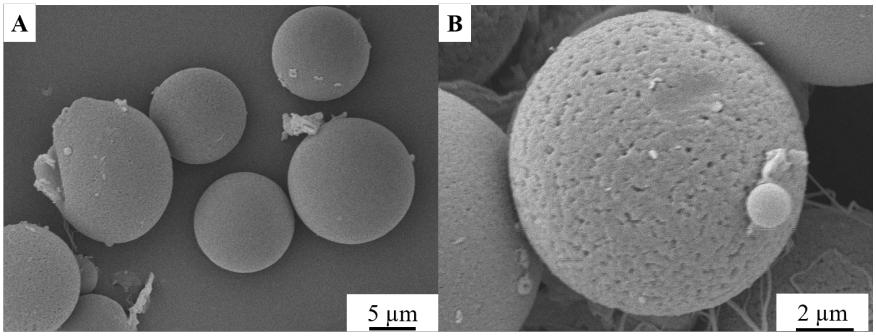

Figure 115: SEM images of a cellulose microbeads beads A,B: formed from a centrifuged high concentration APP disperse phase.

which showed no significant change between microbeads formed from a disperse phase containing APP, and from one without filler (Figure 117), the presence of which was shown in Figure 113 to reduce the onset temperature of the composite.

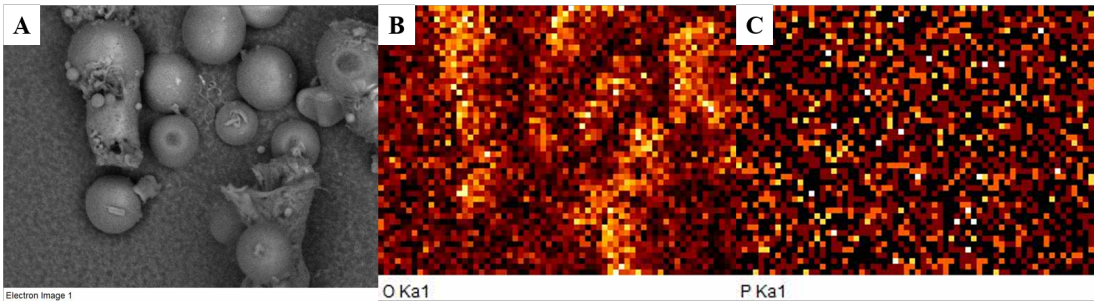

Figure 116: EDX analysis of A: cellulose microbeads formed from a centrifuged 15 wt% APP disperse phase B: highlighting the oxygen and C: phosphorous concentration).

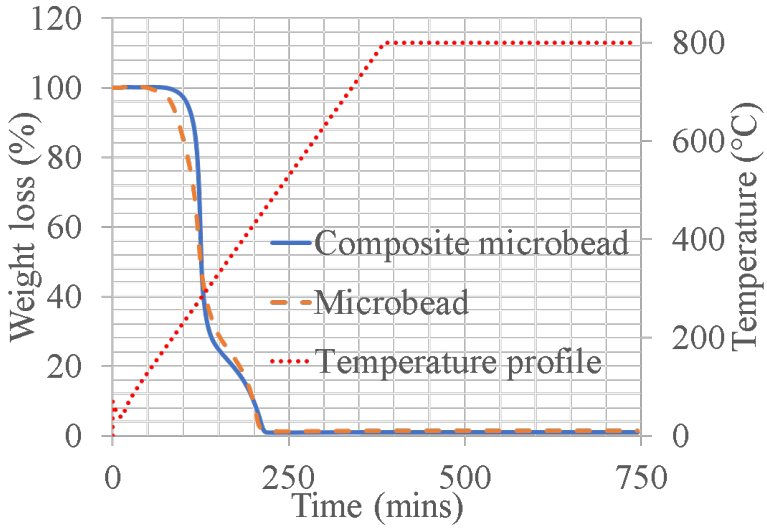

Figure 117: The thermal degradation in air of composite cellulose microbeads formed from a centrifuged 15 wt% APP disperse phase and cellulose microbeads generated without filler (5 °Cmin^{-1}, max temp 800 °C.

The generation of micro cellulose-APP beads would require a smaller filler particle size or larger membrane pore size to allow permeation through the membrane. It has been shown however, that cellulose is a desirable material for the generation of composites, which can be achieved with simply mixing the required filler in the cellulose-OES solution.

6.7 Chapter 6 Conclusions

It has been shown in this chapter that cellulose beads can be altered and adapted to implement physical and chemical attributes, from increased mechanical strength to surface coating with another biopolymer. Cellulose beads can be cross-linked by changing the final washing and drying steps to soaking in aqueous glyoxal solutions, heating, and drying, which are operations that can easily be incorporated into the process. Bead hardness scales with the degree of cross-linking, providing access to a range of materials that could replace plastic microbeads in applications from personal care products to abrasives. Examples achieving 1.4 - 12.4 glyoxal:AGU mole ratios have been shown to have varying topography and resistance to shrinking on drying. An expanded bead structure could also be achieved by adjusting cross-linking reaction temperatures producing a material with interesting exposed internal and surface structures.

The successful reaction of TOS on the surface of cellulose beads, confirmed by TGA and EDX analysis, was shown to significantly alter the surface of the material and impart a different surface functionality to the materials, similarly with the formation of chitosan coated cross-linked cellulose beads. Acidic and enzymatic etching was shown as a potential route to impart surface roughness on these beads, an attribute that is often required for support applications.

Finally, it was shown that cellulose-APP composite beads could be form by simply dispersing the filler in the cellulose-OES solution, which shows the simplicity of generating cellulose composites.

Chapter 7

Conclusions

The main aim of the research described in this thesis was *"To investigate the processability of cellulose, solubilised in an ionic liquid solvent system, towards the production of sustainable cellulose bead-based materials utilising membrane emulsification and dropping processes."* This was achieved by the completion of the objectives contributing to this overall aim.

Chapter 4 introduced DoE as a valuable tool for experimentation via the development of three designs to investigate the rheology, interfacial tension and contact angle of cellulose-OES. These solutions were shown to be Newtonian (when subject to shear rates of > 1 s^{-1}), when using a MCC source, and the viscosity could be altered via the concentration of co-solvent used, the concentration of cellulose dissolved and the temperature of the solution (in descending order of significance). Thus it was concluded that a cellulose solvent system of 70:30 (w/w) DMSO:[EMIm][OAc] was optimal for cellulose processing - low concentration of IL, desirable viscosity, ease of dissolution. Specifically looking towards membrane emulsification, the interfacial tension, between the cellulose-OES and a SFO-Span 80 continuous phase, and contact angle, between the cellulose-OES and membrane surface, where also shown to be influenced by surfactant and cellulose concentration to varying degrees. These three DoEs enabled the completion of the first objective.

Building on the results of the previous chapter, in Chapter 5 the

applicability of these solutions to the formation of cellulose microbeads using membrane emulsification was highlighted presenting a unique and previously undocumented approach for the formation of these sought after and versatile materials. The first rig design was tested, using DoE, and improved upon, resulting in the development of a process able to operate continuously and form reproducible materials. This was taken a step further by mapping the production space via the capillary (Ca) and Weber (We) numbers. We were able to conclude that, at a set membrane pore size and disperse phase composition, the optimal emulsion, and therefore, following further processing, beads, were formed when utilising parameters resulting in a low We. In the case of this system, average bead size did not scale linearly with changes in membrane pore size, as is often concluded in the literature. It is hypothesised that this was due to the significantly higher viscosity of the disperse phase compared with those described in the literature. The average bead size could, however, be controlled by adjusting the continuous phase flow rate and the surfactant concentration.

This was complemented with the formation of larger cellulose beads, of diameters inaccessible using emulsification processes, via a scaled up multihead dropping process. The economic feasibility of this process was assessed in terms of material cost, which highlighted the need for an efficient recycling stream to reuse the significant quantities of ethanol and expensive [EMIm][OAc] to make this process viable.

The materials produced, as described in Chapter 5, were chemically functionalised to impart specific chemical and physical functionality geared towards final applications, detailed in Chapter 6. The mechanical stability of the beads could be adjusted via quantifiable cross-linking with glyoxal, which was shown to significantly increase the compressive strength and brittleness of the beads (as well as to alter the surface topography) making the materials more applicable for applications which required either greater mechanical stability, such as supports, or hardness, e.g. blasting media. Cross-linking was investigated for its effect on the thermal degradation and pyrolysis of the materials during which beads were shown to form interesting "popcorn" like structures. The beads were also successfully surface functionalised with TOS, imparting a hydrophobic surface to the materials, as well as coating in chitosan, again extending the

functionality of these materials. Post-production etching treatment, using enzymes or acids, was shown to greatly increase the surface roughness of the beads forming varying topography depending on the concentration, the time of etching, and the acid used. The final section detailed the formation of cellulose-APP composite beads via dispersion of the fire-retardant in the cellulose-OES prior to shaping and coagulation. This chapter highlighted the versatility in imparting functionality, be it fire-retardancy, mechanical strength, surface roughness or hydrophobicity, to these formed materials, thereby achieving the final objective.

7.1 Future Considerations

7.1.1 Microbeads

The recent ban on microbeads in the UK reflects a shift in attitude towards single use plastics. In terms of this ban, microbeads are defined as "any water-insoluble solid plastic particle of less than or equal to 5 mm in any dimension" and importantly, a plastic as "a synthetic polymeric substance".[17,187] These definitions, as they stand, potentially leave space for non-synthetic, i.e. natural, polymers to be used in place of the current materials. However, a clear indication on whether biodegradable alternatives will be exempt from this ban has not been provided. It is clear that if cellulose microbeads are to be used as an alternative to persistent plastic beads, the degradation of the biopolymer in waste water treatment plants and/or marine environments must be systematically tested. Considering that the produced beads (non-cross-linked) consist solely of cellulose, breakdown would occur rapidly via natural decomposition routes, however this has not yet been shown or rigorously tested for all variants of these cellulose microbeads. A colleague, Davide Califano, has developed an enzyme based protocol that provides a good indication of the efficacy of a typical cellulase enzyme "cocktail", produced for the biofuels industry, for saccharification of the beads. Initial findings have shown that both cross-linked and non-cross-linked variants are readily digestible enzymatically.

7.1.2 Cellulose Processing

The [EMIm][OAc] and DMSO OES system is clearly an efficient solvent for cellulose processing. However, there are a range of other ILs and co-solvents that could potentially be used, which may have less of an environmental impact,[78] or cost less.[60] To investigate the wide range of potential combinations of anions, cations and co-solvents was out of the scope of this project where we chose to rely on a widely tested OES combination, however this author is confident that improved solvent systems will be found in the future, as the research community looks towards scale up of these processes (see KH-NILCELL^{TM} process).[76] There remains questions about the environmental and, indeed, human toxicity of [EMIm][OAc]. As already discussed in the literature review (Chapter 2), initial findings suggested little environmental impact, however there is a lack of an extensive toxicological study on the effect of this IL, which will need to be addressed.

Solvent Recycling

Having an effective extraction and recycling process for the OES and ethanol anti-solvent, will limit the environmental impact and reduce costs. There are many examples described in the literature boasting $> 99\%$ recovery of the IL.[42,76] The use of distillation to separate components is, however, an energy intensive process that may negate any cost savings gained through material recycling. It would be beneficial to investigate other recycling methods, including organic solvent nanofiltration, or pervaporation, which may be able to alleviate the energy cost associated with the recycling currently used.[42] Therefore a full techno-economic (TEA) analysis, building on that presented in Chapter 5, encompassing material, operational, equipment and labour costs, is required. Along with this, a related TEA and recycling stream would need to be investigated for the membrane emulsification process, looking towards larger scale manufacturing, which has the added complexity of residual sunflower oil (SFO) removal from the OES phase.

Long term stability testing of the OES is also another avenue that would

need to be explored to determine the number of cycles that the solvent system can be used for whilst remaining an efficient solvent for cellulose. Others have noted the potential for side reactions between the IL and cellulose, which may indicate a need for an in depth analysis.[29,68–71]

Material Drying

Throughout processing, an increase in water content would be expected due to the hygroscopic nature of the components used (cellulose, [EMIm][OAc], DMSO), therefore one would expect that drying of each component would have to take place during long term manufacturing. Acceptable levels of water content would have to be determined based on the affect on the dissolution capability of the OES, and indeed, the effect water has on the final cellulose bead, as there are known differences in crystallinity that results when using water or an alcohol as an anti-solvent (noted in the literature review, Chapter 2). Drying of components could also increase energy costs of production. A potential alternative to vacuum drying, utilised here, would be the use of fluidised bed drying in which the beads are suspended in an up-ward flowing heated gas. Drying can be aided with microwave heating.[84] This could also be potentially used as a method for initiating the glyoxal cross-linking reaction on a large scale.

Membrane Emulsification

In this research, the widely publicised use of Shirasu porous glass (SPG) membranes to produce monodisperse products,[153,188] remained elusive. After much investigation, it was concluded that the membranes used were, in part, responsible for the polydisperse nature of the microbeads. Looking towards future development, it is vital to test this hypothesis with the use of other membranes with more monodisperse pore size, including metal membranes,[115] which would be expected to produce monodisperse emulsions and therefore beads. This could also overcome another issue with SPG membranes: high price and often lengthy delivery times.

There are few examples described in the literature of the scale up of

membrane emulsification processes, and none detail the formation of particles.[112] It is widely agreed that the technology has begun to be transferred to industry, with some more recent publications dealing with scale up in more detail.[111,116] A common issue raised with scale up of membrane emulsification processes is the low flux of disperse phase through the membrane. Methods for dealing with this include increasing the length/size of the membrane and/or numbering up of membranes.[116] Utilising pre-mixed emulsions, in which an emulsion is used as the disperse phase and passed through a membrane, could also be an option, as such systems can be subjected to higher transmembrane pressures and therefore increased flux through the membrane, but this involves the inclusion of another (pre) emulsification step.[116]

References

[1] R. Geyer, J. R. Jambeck and K. L. Law, *Science Advances*, 2017, **3**, 25–29.

[2] J. L. Scott and J. Lee, *Green Chemistry*, 2016, **18**, 6157–6159.

[3] M. Burke, *EU leaders announce plans to tackle plastic waste*, 2018, https://www.chemistryworld.com/news/eu-leaders-announce-plans-to-tackle-plastic-waste/3008557.article, Accessed: 10/04/2018.

[4] L. S. Fendall and M. A. Sewell, *Marine Pollution Bulletin*, 2009, **58**, 1225–1228.

[5] I. E. Napper, A. Bakir, S. J. Rowland and R. C. Thompson, *Marine Pollution Bulletin*, 2015, **99**, 178–185.

[6] F. Murphy, C. Ewins, F. Carbonnier and B. Quinn, *Environmental Science and Technology*, 2016, **50**, 5800–5808.

[7] S. Greenberg, *Microbeads*, http://www.greenberg-art.com/.Toons/.Toons, Environ/Microbeads.html, Accessed: 12/04/2018.

[8] C. A. King, J. L. Shamshina, O. Zavgorodnya, T. Cutfield, L. E. Block and R. D. Rogers, *ACS Sustainable Chemistry & Engineering*, 2017, **5**, 11660–11667.

[9] BBC and D. Shukman, *Companies sign up to pledge to cut plastic pollution*, 2018, http://www.bbc.co.uk/news/business-43901328, Accessed: 26/04/2018.

[10] M. R. Gregory, *Marine Pollution Bulletin*, 1996, **32**, 867–871.

[11] S. A. Mason, V. Welch and J. Neratko, *Synthetic Polymer Contamination in Bottled Water*, State university of new york technical report, 2018.

[12] A. Karami, A. Golieskardi, C. Keong Choo, V. Larat, T. S. Galloway and B. Salamatinia, *Scientific Reports*, 2017, **7**, 46173.

[13] L. Van Cauwenberghe and C. R. Janssen, *Environmental Pollution*, 2014, **193**, 65–70.

[14] *Beat the Micro-Bead*, http://www.beatthemicrobead.org/, Accessed: 05/12/2017.

[15] D. Hirst and O. Bennet, *House of Commons Library*, 2017, 1–16.

[16] US Congress, *Microbead-Free Waters Act of 2015*, 2015.

[17] UK Government, *The Environmental Protection (Microbeads) (England) Regulations 2017*, http://www.legislation.gov.uk/ukdsi/2017/9780111162118/pdfs/ukdsi{_}9780111162118{_}en.pdf, Accessed: 16/01/2018.

[18] UK Government Office for Science, *Foresight Foresight Future of the Sea*, Government office for science technical report, 2018.

[19] D. Mazurais, B. Ernande, P. Quazuguel, A. Severe, C. Huelvan, L. Madec, O. Mouchel, P. Soudant, J. Robbens, A. Huvet and J. Zambonino-Infante, *Marine Environmental Research*, 2015, **112**, 78–85.

[20] C. M. Rochman, S. M. Kross, J. B. Armstrong, M. T. Bogan, E. S. Darling, S. J. Green, A. R. Smyth and D. Veríssimo, *Environmental Science and Technology*, 2015, **49**, 10759–10761.

[21] D. Klemm, B. Heublein, H. P. Fink and A. Bohn, *Angewandte Chemie (International ed. in English)*, 2005, **44**, 3358–3393.

[22] M. Gericke, J. Trygg and P. Fardim, *Chemical Reviews*, 2013, **113**, 4812–4836.

[23] X. Luo and L. Zhang, *Journal of Chromatography. A*, 2010, **1217**, 5922–5929.

[24] G. Crini, *Progress in Polymer Science*, 2005, **30**, 38–70.

[25] X. Guo and F. Chen, *Environmental Science & Technology*, 2005, **39**, 6808–18.

[26] A. Knowles, *Environmentalist*, 2008, **28**, 35–44.

[27] F. Hermanutz, F. Gähr, E. Uerdingen, F. Meister and B. Kosan, *Macromolecular Symposia*, 2008, **262**, 23–27.

[28] E. Kontturi, T. Tammelin and M. Osterberg, *Chemical Society Reviews*, 2006, **35**, 1287–1304.

[29] A. Brandt, J. Gräsvik, J. P. Hallett and T. Welton, *Green Chemistry*, 2013, **15**, 550–583.

[30] R. Atalla and D. Vanderhart, *Science*, 1984, **223**, 283–285.

[31] Y. Nishiyama, P. Langan and H. Chanzy, *Journal of the American Chemical Society*, 2002, **124**, 9074–9082.

[32] Y. Nishiyama, J. Sugiyama, H. Chanzy and P. Langan, *Journal of the American Chemical Society*, 2003, **125**, 14300–14306.

[33] R. J. Moon, A. Martini, J. Nairn, J. Simonsen and J. Youngblood, *Chemical Society Reviews*, 2011, **40**, 3941–3994.

[34] M. Wada, Y. Nishiyama, P. Langan and H. Chanzy, *Macromolecules*, 2004, **37**, 8548–8555.

[35] A. J. Ragauskas, C. K. Williams, B. H. Davison, G. Britovsek, J. Cairney, C. A. Eckert, W. J. Frederick, J. P. Hallett, D. J. Leak, C. L. Liotta, J. R. Mielenz, R. Murphy, R. Templer and T. Tschaplinski, *Science (New York, N.Y.)*, 2006, **311**, 484–489.

[36] J. Trygg, P. Fardim, M. Gericke, E. Mäkilä and J. Salonen, *Carbohydrate Polymers*, 2013, **93**, 291–299.

[37] H. Mahmood, M. Moniruzzaman, S. Yusup and T. Welton, *Green Chemisty*, 2017, 2051–2075.

[38] H. Wang, G. Gurau and R. D. Rogers, *Chemical Society Reviews*, 2012, **41**, 1519–1537.

[39] A. Potthast, T. Rosenau, R. Buchner, T. Röder, G. Ebner, H. Bruglachner, H. Sixta and P. Kosma, *Cellulose*, 2002, **9**, 41–53.

[40] Y. H. Percival Zhang, S. Y. Ding, J. R. Mielenz, J.-B. Cui, R. T. Elander, M. Laser, M. E. Himmel, J. R. McMillan and L. R. Lynd, *Biotechnology and Bioengineering*, 2007, **97**, 214–223.

[41] N. V. Plechkova and K. R. Seddon, *Chemical Society Reviews*, 2008, **37**, 123–150.

[42] Y. Cao, J. Wu, J. Zhang, H. Li, Y. Zhang and J. He, *Chemical Engineering Journal*, 2009, **147**, 13–21.

[43] M. J. Earle, J. M. S. S. Esperança, M. A. Gilea, J. N. C. Lopes, L. P. N. Rebelo, J. W. Magee, K. R. Seddon and J. A. Widegren, *Nature*, 2006, **439**, 831–834.

[44] M. Armand, F. Endres, D. R. MacFarlane, H. Ohno and B. Scrosati, *Nature Materials*, 2009, **8**, 621–629.

[45] D. Mecerreyes, *Progress in Polymer Science*, 2011, **36**, 1629–1648.

[46] V. Pino, M. Germán-Hernández, A. Martín-Pérez and J. L. Anderson, *Separation Science and Technology*, 2012, **47**, 264–276.

[47] M. Abai, M. P. Atkins, A. Hassan, J. D. Holbrey, Y. Kuah, P. Nockemann, A. A. Oliferenko, N. V. Plechkova, S. Rafeen, A. A. Rahman, R. Ramli, S. M. Shariff, K. R. Seddon, G. Srinivasan and Y. Zou, *Dalton Transactions*, 2015, 8617–8624.

[48] A. M. Socha, R. Parthasarathi, J. Shi, S. Pattathil, D. Whyte, M. Bergeron, A. George, K. Tran, V. Stavila, S. Venkatachalam, M. G. Hahn, B. A. Simmons and S. Singh, *Proceedings of the National Academy of Sciences of the United States of America*, 2014, **111**, E3587–E3595.

[49] R. P. Swatloski, S. K. Spear, J. D. Holbrey and R. D. Rogers, *Journal of the American Chemical Society*, 2002, **124**, 4974–4975.

[50] Y. Qin, X. Lu, N. Sun and R. D. Rogers, *Green Chemistry*, 2010, **12**, 968–971.

[51] M. Abe, T. Yamada and H. Ohno, *RSC Advances*, 2014, **4**, 17136–17140.

[52] D. A. Fort, R. C. Remsing, R. P. Swatloski, P. Moyna, G. Moyna and R. D. Rogers, *Green Chemistry*, 2007, **9**, 63–69.

[53] R. A.A. Muzzarelli, *Carbohydrate Polymers*, 2009, **76**, 167–182.

[54] C. Pillai, W. Paul and C. P. Sharma, *Progress in Polymer Science*, 2009, **34**, 641–678.

[55] C. Graenacher, *US 1943176 A*, 1934.

[56] R. Rinaldi, *Chemical Communications*, 2011, **47**, 511–513.

[57] S. Wang, A. Lu and L. Zhang, *Progress in Polymer Science*, 2015, **53**, 169–206.

[58] B. Peric, J. Sierra, E. Martí, R. Cruañas, M. A. Garau, J. Arning, U. Bottin-Weber and S. Stolte, *Journal of Hazardous Materials*, 2013, **261**, 99–105.

[59] M. Petkovic, K. R. Seddon, L. P. N. Rebelo and C. Silva Pereira, *Chemical Society Reviews*, 2011, **40**, 1383–1403.

[60] A. George, A. Brandt, K. Tran, S. M. S. N. S. Zahari, D. Klein-Marcuschamer, N. Sun, N. Sathitsuksanoh, J. Shi, V. Stavila, R. Parthasarathi, S. Singh, B. M. Holmes, T. Welton, B. A. Simmons and J. P. Hallett, *Green Chem.*, 2015, **17**, 1728–1734.

[61] S. Ostadjoo, P. Berton, J. L. Shamshina and R. D. Rogers, *Toxicological Sciences*, 2018, **161**, 249–265.

[62] X. Geng and W. A. Henderson, *RSC Advances*, 2014, **4**, 31226–31229.

[63] D. Klein-Marcuschamer, B. A. Simmons and H. W. Blanch, *Biofuels, Bioproducts and Biorefining*, 2011, **5**, 562–569.

[64] C. Olsson, A. Idström, L. Nordstierna and G. Westman, *Carbohydrate Polymers*, 2014, **99**, 438–446.

[65] K. A. Le, R. Sescousse and T. Budtova, *Cellulose*, 2012, **19**, 45–54.

[66] M. Abe, Y. Fukaya and H. Ohno, *Chemical Communications*, 2012, **48**, 1808.

[67] Y. Fukaya and H. Ohno, *Physical Chemistry Chemical Physics : PCCP*, 2013, **15**, 4066–72.

[68] L. K. J. Hauru, M. Hummel, A. W. T. King, I. Kilpeläinen and H. Sixta, *Biomacromolecules*, 2012, **13**, 2896–2905.

[69] S. Chowdhury, R. S. Mohan and J. L. Scott, *Tetrahedron*, 2007, **63**, 2363–2389.

[70] M. T. Clough, K. Geyer, P. A. Hunt, S. Son, U. Vagt and T. Welton, *Green Chemistry*, 2015, **17**, 231–243.

[71] G. Ebner, S. Schiehser, A. Potthast and T. Rosenau, *Tetrahedron Letters*, 2008, **49**, 7322–7324.

[72] J.-M. Andanson, A. A.H. Padua and M. C. Gomes, *Chem. Commun.*, 2015, **51**, 4485–4487.

[73] M. Amde, J. F. Liu and L. Pang, *Environmental Science and Technology*, 2015, **49**, 12611–12627.

[74] REACH, *REACH database*, https://echa.europa.eu/information-on-chemicals/cl-inventory-database/-/discli/details/91677, Accessed: 21/04/2018.

[75] A. Jordan and N. Gathergood, *Chemical Society Reviews*, 2015, **44**, 8200–8237.

[76] J. Zhang, J. Wu, J. Yu, X. Zhang, J. He and J. Zhang, *Mater. Chem. Front.*, 2017, **1**, 1273–1290.

[77] M. Gericke, T. Liebert, O. A. E. Seoud and T. Heinze, *Macromolecular Materials and Engineering*, 2011, **296**, 483–493.

[78] E. Gale, R. H. Wirawan, R. L. Silveira, C. S. Pereira, M. A. Johns, M. S. Skaf and J. L. Scott, *ACS Sustainable Chemistry & Engineering*, 2016, **4**, 6200–6207.

[79] A. Takegawa, M.-A. Murakami, Y. Kaneko and J.-i. Kadokawa, *Carbohydrate Polymers*, 2010, **79**, 85–90.

[80] J. Sundberg, G. Toriz and P. Gatenholm, *Polymer*, 2013, **54**, 6555–6560.

[81] A. Takegawa, M. A. Murakami, Y. Kaneko and J.-i. Kadokawa, *Polymer Composites*, 2009, **30**, 1837–1841.

[82] K. Schweikert, M. Egorova, R. D. Juch, F. Lefevre and H. Westenfelder, *EP2907498*, 2015, https://www.google.com/patents/EP2907498A1?cl=en.

[83] K. F. Du, M. Yan, Q. Y. Wang and H. Song, *Journal of Chromatography A*, 2010, **1217**, 1298–1304.

[84] A. Nussinovitch, *Polymer Macro- and Micro-GEl beads: Fundamentals and Applications*, Springer, 2010, vol. 53.

[85] D. L. Minnick, R. A. Flores, M. R. Destefano and A. M. Scurto, *Journal of Physical Chemistry B*, 2016, **120**, 7906–7919.

[86] P. Coussot, *Rheophysics Matter in all States*, Springer, Les Ulis, eBook edn., 2014.

[87] H. F. Xia, D. Q. Lin and S. J. Yao, *Journal of Chromatography. A*, 2007, **1175**, 55–62.

[88] J. J. O' Neill Jr and P. R. Emerald, *US 2543928 A*, 1951.

[89] K. Imagawa, T. Omura, Y. Ihara, K. Kono, T. Suzuki and H. Minami, *Cellulose*, 2017, **24**, 3111–3118.

[90] L. K. Voon, S. C. Pang and S. F. Chin, *Materials Letters*, 2015, **164**, 264–266.

[91] F. Naseeruteen, N. S. A. Hamid, F. B. M. Suah, W. S. W. Ngah and F. S. Mehamod, *International Journal of Biological Macromolecules*, 2018, **107**, 1270–1277.

[92] L. S. Blachechen, P. Fardim, D. F. S. Petri, A. Prof, L. Prestes and S. P. Brazil, *Biomacromolecules*, 2014, 3440–3448.

[93] C. Chang and L. Zhang, *Carbohydrate Polymers*, 2011, **84**, 40–53.

[94] X. Shen, J. L. Shamshina, P. Berton, G. Gurau and R. D. Rogers, *Green Chem.*, 2016, **18**, 53–75.

[95] Q. L. Zhang, F. Shi, P. Wang, D. Q. Lin and S. J. Yao, *Journal of Applied Polymer Science*, 2014, **131**, 40060.

[96] G. T. Vladisavljevic, I. Kobayashi and M. Nakajima, *Microfluidics and Nanofluidics*, 2012, **13**, 151–178.

[97] T. Suzuki, K. Kono, K. Shimomura and H. Minami, *Journal of Colloid and Interface Science*, 2014, **418**, 126–131.

[98] M. Hirano, Y. Suzuki, K. Kanaya, A. Kanda, T. Suzuki, Y. Kawai and K.-i. Morio, *US 2013/0172538 A1*, 2013.

[99] T. Omura, K. Imagawa, K. Kono, T. Suzuki and H. Minami, *ACS Applied Materials & Interfaces*, 2016, **9**, 944–949.

[100] C. X. Lin, H. Y. Zhan, M. H. Liu, S. Y. Fu and L. A. Lucia, *Langmuir*, 2009, **25**, 10116–10120.

[101] G. T. Vladisavljevic and R. A. Williams, *Advances in Colloid and Interface Science*, 2005, **113**, 1–20.

[102] S. M. Joscelyne and G. Trägårdh, *Journal of Membrane Science*, 2000, **169**, 107–117.

[103] H. Qi, Y. Huang, B. Ji, G. Sun, F. L. Qing, C. Hu and K. Yan, *Carbohydrate Polymers*, 2016, **135**, 86–93.

[104] C. Schramm and B. Rinderer, *Analytical Chemistry*, 2000, **72**, 5829–5833.

[105] F. Quero, M. Nogi, K. Y. Lee, G. V. Poel, A. Bismarck, A. Mantalaris, H. Yano and S. J. Eichhorn, *ACS Applied Materials & Interfaces*, 2011, **3**, 490–499.

[106] A. Stoyanov and S. Naieni, *US20050019563A1*, 2005.

[107] M. Braun, R. Dyllick-Brenzinger, M. Maase, F. Stein, M. Turner and E. Uerdingen, *WO 2009037146 A1*, 2007.

[108] C. Charcosset, I. Limayem and H. Fessi, *Journal of Chemical Technology & Biotechnology*, 2004, **79**, 209–218.

[109] S. M. Joscelyne and G. Trägårdh, *Journal of Membrane Science*, 2000, **169**, 107–117.

[110] F. Spyropoulos, D. M. Lloyd, R. D. Hancocks and A. K. Pawlik, *Journal of the Science of Food and Agriculture*, 2014, **94**, 613–627.

[111] E. Piacentini, E. Drioli and L. Giorno, *Journal of Membrane Science*, 2014, **468**, 410–422.

[112] F. Spyropoulosa, R. D. Hancocks and I. T. Norton, *Procedia Food Science*, 2011, **1**, 920–926.

[113] T. Nakashima, M. Shimizu and M. Kukizaki, *Membrane Emulsification Operation Manual*, Department of chemistry industrial research institute of miyazaki prefecture technical report, 1991.

[114] G. T. Vladisavljevic, *Advances in Colloid and Interface Science*, 2015, **225**, 53–87.

[115] S. Morelli, R. G. Holdich and M. M. Dragosavac, *Chemical Engineering Journal*, 2016, **288**, 451–460.

[116] F. Spyropoulos, D. M. Lloyd, R. D. Hancocks and A. K. Pawlik, *Journal of the Science of Food and Agriculture*, 2014, **94**, 628–638.

[117] M. Alroaithi and S. Sajjadi, *RSC Advances*, 2016, **6**, 79745–79754.

[118] X. Q. Li, Q. Li, F. L. Gong, J. D. Lei, X. Zhao, G. H. Ma and Z. G. Su, *Journal of Membrane Science*, 2015, **476**, 30–39.

[119] M. Johns, *PhD Thesis*, The University of Bath, 2016.

[120] L. Härdelin, E. Perzon, B. Hagström, P. Walkenström and P. Gatenholm, *Journal of Applied Polymer Science*, 2013, **130**, 2303–2310.

[121] M. J. Anderson and P. J. Whitcomb, in *Kirk-Othmer Encyclopedia of Chemical Technology, 1*, John Wiley & Sons, 2010, pp. 1–22.

[122] L. Eriksson, *Design of Experiments - Principles and Applications*, 2000, vol. 46, p. 350.

[123] J. D. Berry, M. J. Neeson, R. R. Dagastine, D. Y. Chan and R. F. Tabor, *Journal of Colloid and Interface Science*, 2015, **454**, 226–237.

[124] P. Bartlett, W. Briscoe, T. Cosgrove, S. Davis, J. Eastman, J. Eastoe, D. Fermin, R. Hughes, N. O. A. Kwamena, J. P. Reid, P. Reynold, R. Richardson, J. Riley, J. van Duijneveldt and B. Vincent, *Colloid Science: Principles, Methods and Applications*, Wiley, 2011.

[125] M. J. Neeson, D. Y. C. Chan and R. F. Tabor, *Langmuir*, 2014, **30**, 15388–15391.

[126] J. Goodwin and R. Hughes, *Rheology for Chemists*, The Royal Society of Chemistry, 2008, pp. P001–264.

[127] M. Gericke, K. Schlufter, T. Liebert, T. Heinze and T. Budtova, *Biomacromolecules*, 2009, **10**, 1188–1194.

[128] B. Nazari, N. W. Utomo and R. H. Colby, *Biomacromolecules*, 2017, **18**, 2849–2857.

[129] J. R. Rumble, *CRC Handbook of Chemistry and Physics*, CRC Press Taylor & Francis, 98th edn., 2018.

[130] Z. Wang, S. M. Richter, J. R. Bellettini, Y. M. Pu and D. R. Hill, *Organic Process Research and Development*, 2014, **18**, 1836–1842.

[131] M. T. Clough, K. Geyer, P. A. Hunt, J. Mertes and T. Welton, *Physical Chemistry Chemical Physics : PCCP*, 2013, **15**, 20480–95.

[132] R. Sescousse, K. A. Le, M. E. Ries and T. Budtova, *The Journal of Physical Chemistry. B*, 2010, **114**, 7222–7228.

[133] H. Zhang, J. Wu, J. Zhang and J. He, *Macromolecules*, 2005, **38**, 8272–8277.

[134] R. L. De Oliveira, H. Da Silva Barud, R. M. De Assunção, C. Da Silva Meireles, G. O. Carvalho, G. R. Filho, Y. Messaddeq and S. J. L. Ribeiro, *Journal of Thermal Analysis and Calorimetry*, 2011, **106**, 703–709.

[135] A. Michud, M. Hummel, S. Haward and H. Sixta, *Carbohydrate Polymers*, 2015, **117**, 355–363.

[136] R. De Silva, K. Vongsanga, X. Wang and N. Byrne, *Cellulose*, 2015, **22**, 2845–2849.

[137] R. Sescousse, K. A. Le, M. E. Ries and T. Budtova, *The Journal of Physical Chemistry B*, 2010, **114**, 7222–7228.

[138] V. Schröder, O. Behrend and H. Schubert, *Journal of Colloid and Interface Science*, 1998, **202**, 334–340.

[139] T. Schmidts, P. Schlupp, A. Gross, D. Dobler and F. Runkel, *Journal of Dispersion Science and Technology*, 2012, **33**, 816–820.

[140] J. Schuermann, T. Huber, D. LeCorre, G. Mortha, M. Sellier, B. Duchemin and M. P. Staiger, *Cellulose*, 2016, **23**, 1043–1050.

[141] G. Vladisavljevic, M. Shimizu and T. Nakashima, *Journal of Membrane Science*, 2005, **250**, 69–77.

[142] J. Coombs OBrien, L. Torrente-Murciano, D. Mattia and J. L. Scott, *ACS Sustainable Chemistry & Engineering*, 2017, 5931–5939.

[143] D. H. Everett, *Basic Principles of Colloid Science*, The Royal Society of Chemistry, 1988, pp. P001–243.

[144] M. J. Lawrence and G. D. Rees, *Advanced Drug Delivery Reviews*, 2000, **45**, 89–121.

[145] J. Bibette, F. Leal-Calderon, V. Schmitt and P. Poulin, *Emulsion Science: Basic Principles An Overview*, 2002.

[146] S. J. Peng and R. A. Williams, *Institution of Chemical Engineers*, 1998, **76**, 894–901.

[147] M. Pathak, *Journal of Membrane Science*, 2011, **382**, 166–176.

[148] Malvern Instruments Limited, 2012.

[149] Horiba, *Horiba Instruments, Inc*, 2013.

[150] R. D. Hancocks, F. Spyropoulos and I. T. Norton, *Journal of Food Engineering*, 2013, **116**, 382–389.

[151] A. K. Pawlik and I. T. Norton, *Journal of Membrane Science*, 2012, **415-416**, 459–468.

[152] F. Spyropoulos, D. M. Lloyd, R. D. Hancocks and A. K. Pawlik, *Journal of the Science of Food and Agriculture*, 2014, **94**, 628–638.

[153] G. T. Vladisavljević and H. Schubert, *Journal of Membrane Science*, 2003, **225**, 15–23.

[154] M. Piculell, P. Welander, K. Jönsson and T. Welander, *Environmental Technology (United Kingdom)*, 2016, **37**, 732–743.

[155] H. Zhao and L. Sha, *Journal of Bioresources and Bioproducts*, 2017, **2**, 30–35.

[156] U. N. A. F. Army, *Plastic Media Blasting (PMB) Paint Stripping, US Joint Service Pollution Prevention Handbook,*, 2011.

[157] E. S. Lee and S. I. Kim, *Fibers and Polymers*, 2004, **5**, 230–233.

[158] J. C. Courtenay, C. Deneke, E. M. Lanzoni, C. A. Costa, Y. Bae, J. L. Scott and R. I. Sharma, *Cellulose*, 2018, **25**, 925–940.

[159] J. Rojas and E. Azevedo, *International Journal of Pharmaceutical Sciences Review and Research*, 2011, **8**, 28–36.

[160] L. Szczesniak, A. Rachocki and J. Tritt-Goc, *Cellulose*, 2008, **15**, 445–451.

[161] S. V. Vassilev, D. Baxter and C. G. Vassileva, *Fuel*, 2013, **112**, 391–449.

[162] E. Virot and A. Ponomarenko, *Journal of The Royal Society Interface*, 2015, **12**, 20141247–20141247.

[163] D. K. Shen and S. Gu, *Bioresource Technology*, 2009, **100**, 6496–6504.

[164] J. Kua, S. W. Hanley and D. O. De Haan, *Journal of Physical Chemistry A*, 2008, **112**, 66–72.

[165] C. Gousse, H. Chanzy, M. L. Cerrada and E. Fleury, *Polymer*, 2004, **45**, 1569–1575.

[166] Z. Hu, R. M. Berry, R. Pelton and E. D. Cranston, *ACS Sustainable Chemistry & Engineering*, 2017, **5**, 5018–5026.

[167] X. Xiong, L. Zhang and Y. Wang, *Journal of Chromatography A*, 2005, **1063**, 71–77.

[168] Y. B. Wu, S. H. Yu, F. L. Mi, C. W. Wu, S. S. Shyu, C. K. Peng and A. C. Chao, *Carbohydrate Polymers*, 2004, **57**, 435–440.

[169] N. Li and R. Bai, *Separation and Purification Technology*, 2005, **42**, 237–247.

[170] C. Stefanescu, W. H. Daly and I. I. Negulescu, *Carbohydrate Polymers*, 2012, **87**, 435–443.

[171] W. Xiao, Q. Chen, Y. Wu, T. Wu and L. Dai, *Carbohydrate Polymers*, 2011, **83**, 233–238.

[172] U.-J. Kim, H. J. Kim, J. W. Choi, S. Kimura and M. Wada, *Cellulose*, 2017, **24**, 5517–5528.

[173] T. Kamal, S. B. Khan, S. Haider, Y. G. Alghamdi and A. M. Asiri, *International Journal of Biological Macromolecules*, 2017, **104**, 56–62.

[174] H. Amiri and K. Karimi, *Industrial and Engineering Chemistry Research*, 2013, **52**, 11494–11501.

[175] H. Liu, R. Chen, H. Yang, W. Qin, T. K. Borg, D. Dean, M. Xu and B. Z. Gao, *Biotechnology Letters*, 2014, **36**, 1245–1252.

[176] M. Ganesh, J. Nachman, Z. Mao, A. Lyons, M. Rafailovich and R. Gross, *Biomacromolecules*, 2013, **14**, 2470–2476.

[177] H. Miyamoto, C. Yamane, M. Seguchi and K. Okajima, *Food Science and Technology Research*, 2009, **15**, 403–412.

[178] T. Huber, J. Müssig, O. Curnow, S. Pang, S. Bickerton and M. P. Staiger, *Journal of Materials Science*, 2012, **47**, 1171–1186.

[179] B. Wicklein, A. Kocjan, G. Salazar-Alvarez, F. Carosio, G. Camino, M. Antonietti and L. Bergström, *Nature Nanotechnology*, 2014, 1–7.

[180] J. Zhang, L. Yue, Q. Kong, Z. Liu, X. Zhou, C. Zhang, Q. Xu, B. Zhang, G. Ding, B. Qin, Y. Duan, Q. Wang, J. Yao, G. Cui and L. Chen, *Scientific Reports*, 2014, **4**, 1–8.

[181] L. Z. Sha and K. F. Chen, *Journal of Thermal Analysis and Calorimetry*, 2016, **123**, 339–347.

[182] B. Dittrich, K. A. Wartig, R. Mülhaupt and B. Schartel, *Polymers*, 2014, **6**, 2875–2895.

[183] L. Lowden and T. Hull, *Fire Science Reviews*, 2013, **2**, 4.

[184] M. I. Ofem and M. Umar, *ARPN Journal of Engineering and Applied Sciences*, 2012, **7**, 213–215.

[185] I. C. Chukwujike, C. M. Ewulonu, S. C. Nwanonenyi and I. C. Uche, *American Journal of Materials Science and Engineering,*, 2015, **3**, 29–36.

[186] S. Duquesne, M. L. Bras, S. Bourbigot, R. Delobel, G. Camino, B. Eling, C. Lindsay, T. Roels and H. Vezin, *Journal of Applied Polymer Science*, 2001, **82**, 3262–3274.

[187] *Explanatory Memorandum to the Environmental Protection (Microbeads) (England) Regulations 2017*, http://www.legislation.gov.uk/ukdsi/2017/9780111162118/pdfs/ukdsiem{_}9780111162118{_}en.pdf, Accessed: 6/01/2018.

[188] C.-J. Cheng, L.-Y. Chu and R. Xie, *Journal of Colloid and Interface Science*, 2006, **300**, 375–82.

Appendix

Chapter 5 Appendix

Experimental Design - Cellulose Bead Particle Size Analysis

Table S1: Reproduction of Table 9 showing the experimental design conducted to determine the effect of cellulose concentration, continuous phase flow rate, continuous phase temperature and Span 80 concentration on the size of cellulose beads.

Experiment Number	Cellulose Concentration in Disperse phase (wt%)	Continuous Phase Flow Rate (Q_{cp}) (L/min)	Continuous Phase Temperature (°C)	Span 80 Concentration in Continuous phase (wt%)
1	4	0.4	30	0.25
2	8	2.4	30	0.25
3	4	2.4	60	0.25
4	8	0.4	60	0.25
5	4	2.4	30	2.00
6	8	0.4	30	2.00
7	4	0.4	60	2.00
8	8	2.4	60	2.00
9, 10 ,11	6	1.4	45	1.13

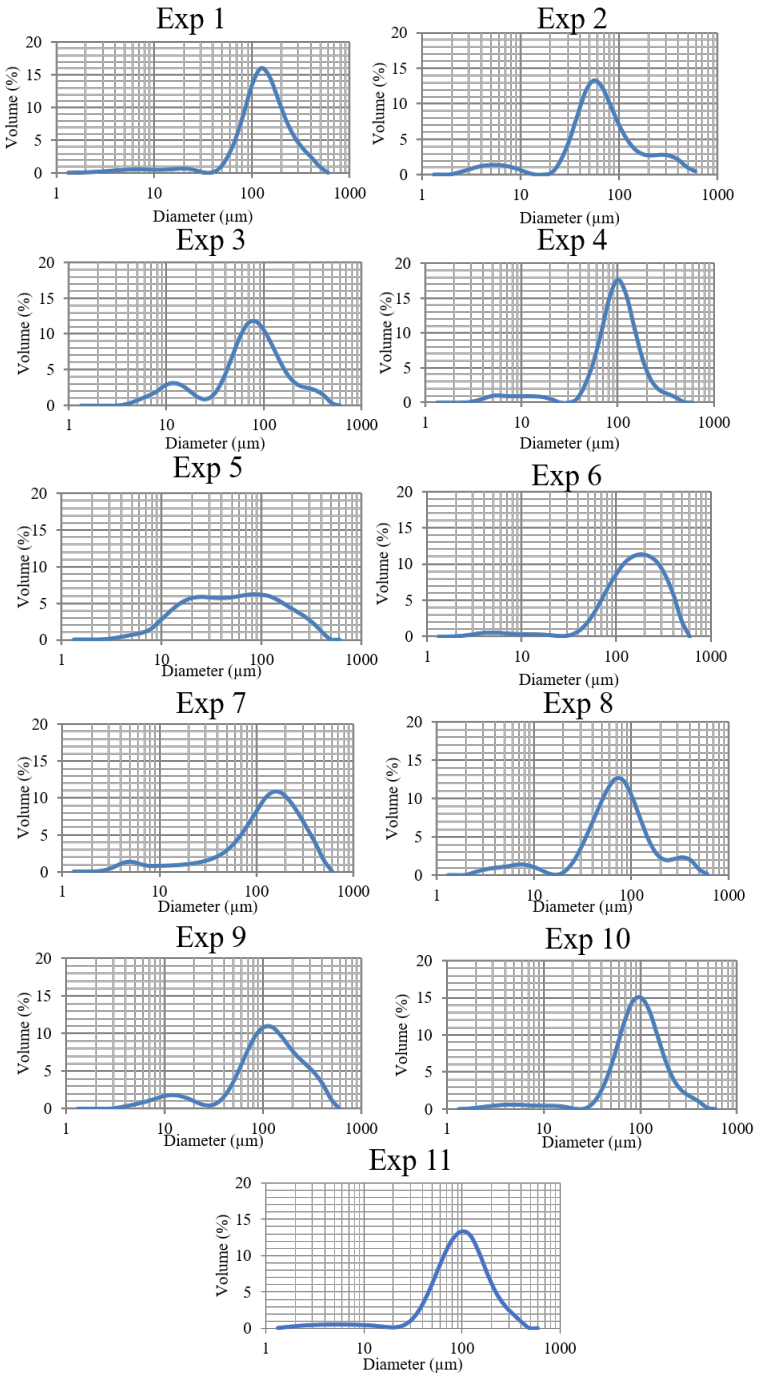

Figure S1: Particle size distributions for the experimental design assessing the impact of factors on cellulose bead average size. Experimental conditions are listed in Table 9 reproduced below for convenience.

Rose Bengal Staining of Cellulose-OES

A low concentration (<0.03 wt%) of rose bengal successfully stained and was fully soluble in a solution of cellulose (8 wt% MCC in DMSO:[EMIm][OAc] (70:30 w/w)) and pure [EMIm][OAc] with no particles detected visually in either solution (Figure S2). It was also partially soluble in Span 80 with insoluble fractions being observed at the bottom of the vial after 28 days. In the continuous phase (SFO), rose bengal showed very low (if any) solubility and after 28 days significant insoluble fractions had settled to the bottom of the vial (Figure S2). Significant colour change was witnessed in the [EMIm][OAc]-rose bengal sample over the 28 days period with a deep purple solution resulting. This suggested possible degradation of the dye and highlighted the need to avoid long term storage of the dyed cellulose-OES solutions. Cellulose-OES solutions were therefore dyed with rose bengal just before being subject to emulsification to overcome this potential side reaction.

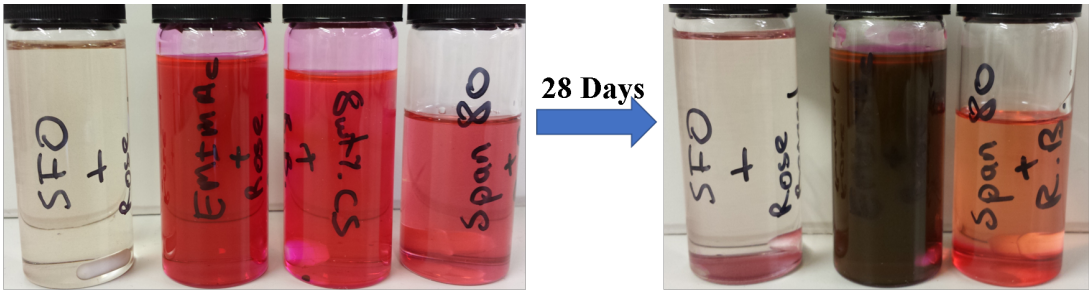

Figure S2: Pictures of sunflower oil, [EMIm][OAc], * CS - an 8 wt% microcrystalline cellulose solution dissolved in DMSO:[EMIm][OAc] (70:30, w/w) and Span 80 exposed to the labelled concentration of rose bengal. Samples were sealed, left for 28 days and photographed again.

Extruding the dyed cellulose-OES solutions from a needle into an ethanol anti-solvent bath resulted in dyed cellulose beads from which the dye could be leeched (Figure S3). The formation and leeching of rose bengal from the cellulose samples highlighted two important factors, that the dye had an affinity for the cellulose polymer and that it could be removed, if required, with repeat immersion in ethanol or other appropriate solvent. A similar process would occur utilising

membrane emulsification for cellulose microbead formation.

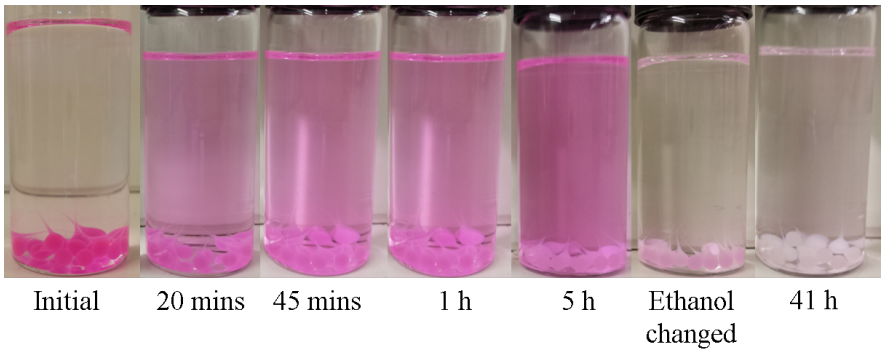

Figure S3: Picture of cellulose beads formed from an 8 wt% microcrystalline cellulose solution dissolved in DMSO:[EMIm][OAc] (70:30, w/w) mixed with rose bengal (0.019 wt%) dropped into an ethanol anti-solvent bath. The beads were left in ethanol for 5 hours after which the leeching solution was exchange with fresh ethanol. Pictures showed the leeching of rose bengal from the cellulose beads.

Data Collected in Conjunction with James Close

- Pendant drop measurements and determination of interfacial tension of an 8 wt% solution in a 1.13 wt% Span 80 dissolved in sunflower oil continuous phase.
- All cellulose samples produced by membrane emulsification and the subsequent particle size measurements.

All other data, and subsequent calculations, were collected by the author of this thesis.

Table S2: Values for the flow rate and velocity of the continuous phase used through a tubular membrane with a cross section diameter of 0.01 m and a cross sectional area of = 7.85×10^{-5} m^2

Continuous phase flow rate ($Lmin^{-1}$)	Continuous phase velocity (ms^{-1})
0.4	0.08
1.4	0.30
1.9	0.40
2.4	0.51

Purity of Recycled solvents

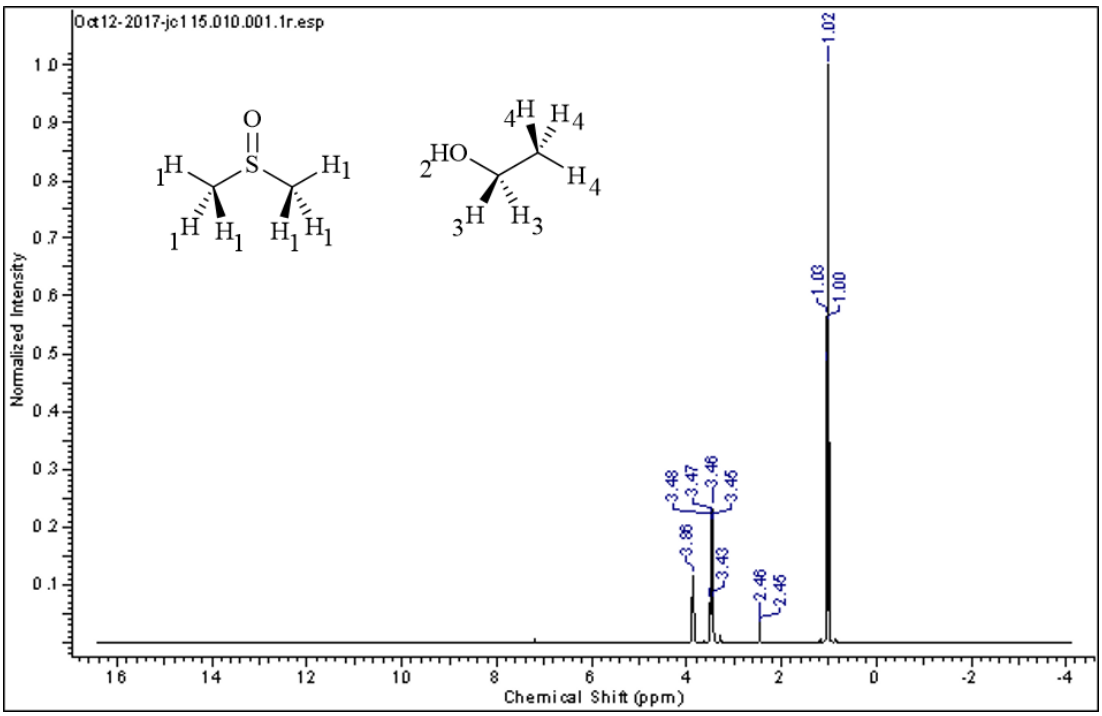

Figure S4: ^{1}H NMR spectrum ($CDCl_3$, 400 MHz) of the distillate after the first distillation (50 °C, 70 mbar).

The chemical shift (ppm), assigned hydrogen, splitting, and integration for Figure S4 were as follows: $\delta = 3.86$ H_2 (s, 1H, 0.16), 3.46 H_3 (q, 2H, 0.32), 2.46 H_1 (s, 6H, 0.01), 1.02 H_4 (t, 3H, 0.48).The following concentration were calculated from the integration of CH_3 peaks assign to each of the two components (Figure S4), DMSO: 0.3 wt% and ethanol: 99.7 wt %. This gave a [EMIm][OAc]:DMSO w/w of 29.6:70.4.

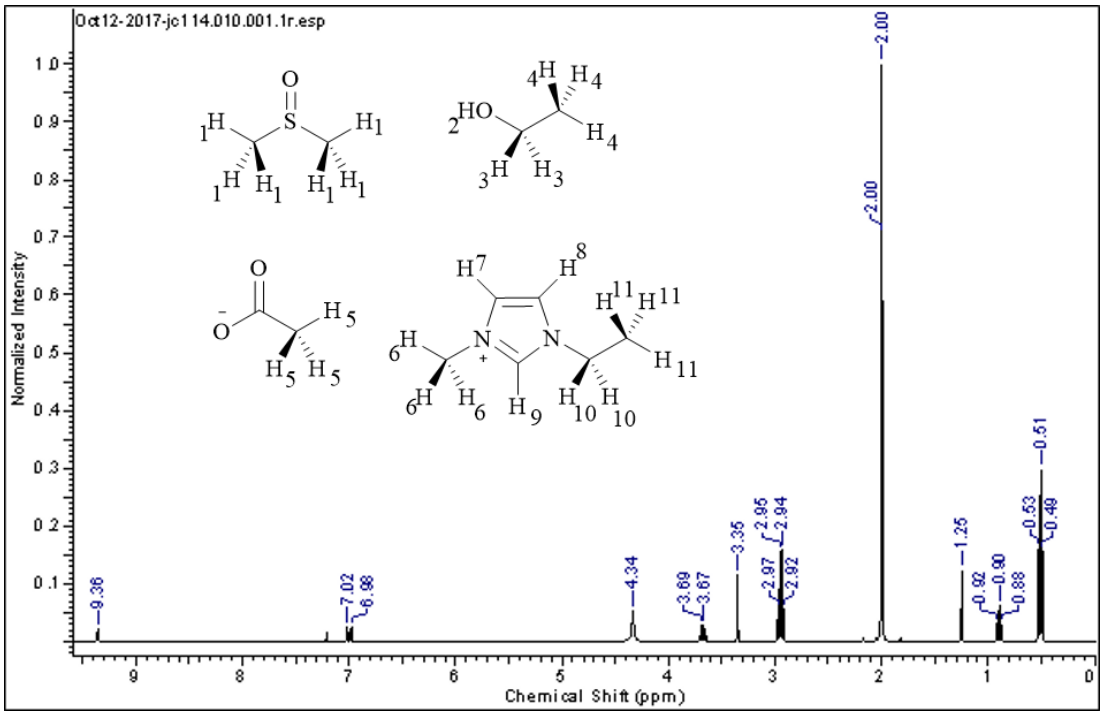

Figure S5: ^{1}H NMR spectrum ($CDCl_3$, 400 MHz) of the remaining solvent after the first distillation (50 °C, 70 mbar).

The chemical shift (ppm), assigned hydrogen, splitting, and integration for Figure S5 were as follows: δ = 9.36 H_9 (s, 1H, 0.01), 7.00 H_7 (d, 1H, 0.01), 7.00 H_8 (d, 1H, 0.01), 4.34 H_2 (s, 1H, 0.08), 3.68 H_{10} (q, 2H, 0.03), 3.35 H_5 (s, 3H, 0.04), 2.94 H_3 (q, 2H, 0.13), 2.00 H_1 (s, 6H, 0.39), 1.25 H_6 (s, 3H, 0.04), 0.90 H_{11} (t, 3H, 0.04), 0.51 H_4 (t, 3H, 0.19). The following concentration were calculated from the integration of CH_3 peaks assign to each of the three components (Figure S5), [EMIm][OAc]: 21.1 wt%, DMSO: 50.2 wt% and ethanol: 28.6 wt %.

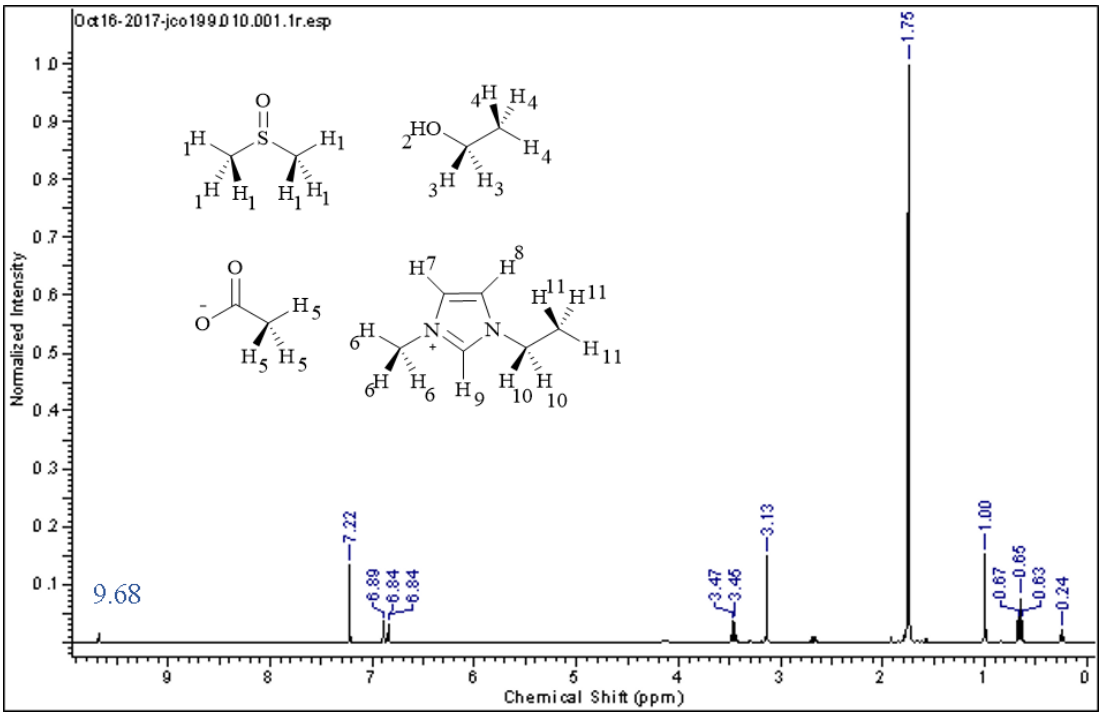

Figure S6: ^{1}H NMR spectrum ($CDCl_3$, 400 MHz) of the remaining solvent after the second distillation (50 °C, 1 mbar).

The chemical shift (ppm), assigned hydrogen, splitting, and integration for Figure S6 were as follows: δ = 9.68 H_9 (s, 1H, 0.01), 6.86 H_7 (d, 1H, 0.01), 6.86 H_8 (d, 1H, 0.01), 3.46 H_{10} (q, 2H, 0.05), 3.13 H_5 (s, 3H, 0.07), 1.75 H_1 (s, 6H, 0.6), 1.00 H_6 (s, 3H, 0.07), 0.65 H_{11} (t, 3H, 0.07), 0.24 H_4 (t, 3H, 0.02). The following concentration were calculated from the integration of CH_3 peaks assign to each of the three components (Figure S6), [EMIm][OAc]: 33.3 wt%, DMSO: 65.4 wt% and ethanol: 1.3 wt %. This gave a [EMIm][OAc]:DMSO w/w of 33.7:66.3.

Chapter 6 Appendix

Exposing a cross-linked sample to base resulted in the extraction solution turning yellow, whilst remaining colourless for non-cross-linked samples (Figure S7).

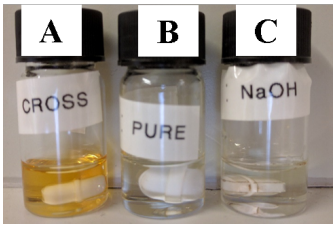

Figure S7: Image of the solutions resulting from exposure of A: cross-linked and B: non-cross-linked cellulose beads to 4 M NaOH (90 °C, 30 mins). A solution of C: 4 M NaOH treated under the same conditions shown for reference.

HPLC for Crosslinker Quantification

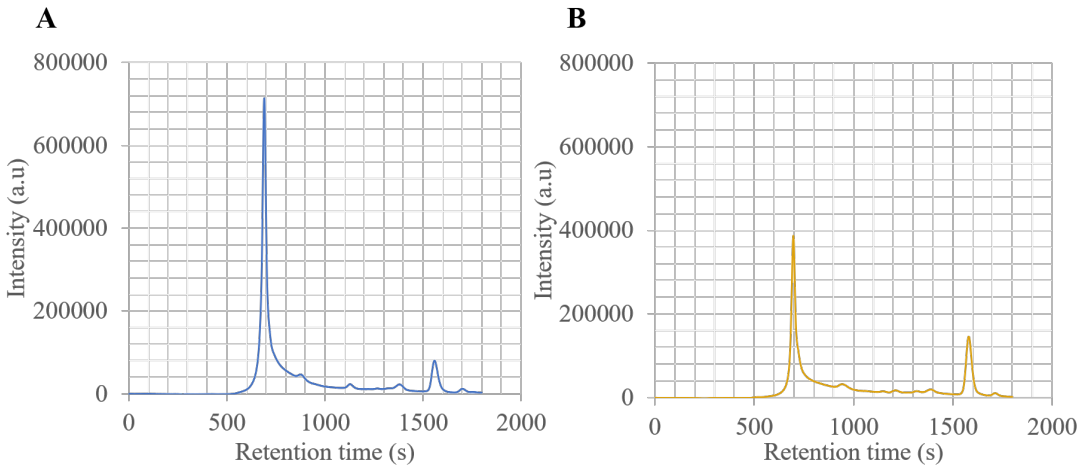

Figure S8: HPLC chromatograms of the glycolic acid produced from cellulose beads cross-linked with a solution of A: 6 and B: 12 wt% glyoxal and exposed to NaOH to remove the cross-linker as glycolic acid (Aminex Organic Acid Analysis Column (HPX-87H, 300 mm x 7.8 mm, 50 °C), mobile phase 0.01 M H2SO4 (0.6 $mLmin^{-1}$) and UV detector $\lambda = 210$ nm).

Glycolic acid Calibration Curve

Table S3: Concentration and integration values for the calibration curve (Figure S9) for glycolic acid

Glycolic acid peak integration	Concentration of glycolic acid (mg/L)
4.43×10^4	20
5.30×10^4	50
1.39×10^5	120
5.07×10^5	480
1.07×10^6	990
5.58×10^6	5020
1.15×10^7	10085
3.17×10^7	30100

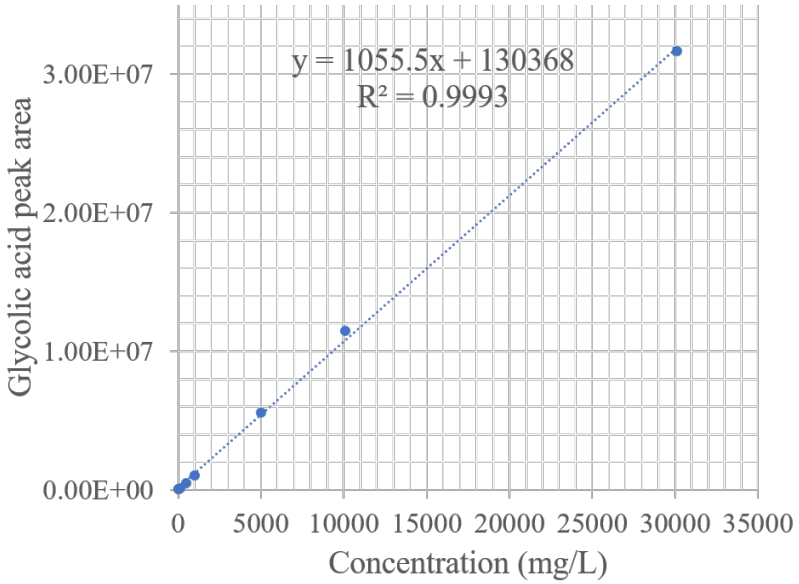

Figure S9: HPLC calibration curve of glycolic acid (aminex organic acid analysis column - HPX-87H, 300 × 7.8 mm, 50 °C,mobile phase - 0.01 M H_2SO_4, 0.6 $mLmin^{-1}$, and UV detector $\lambda = 210$ nm. Concentration and integration values are listed in Table S3.

SEM Images

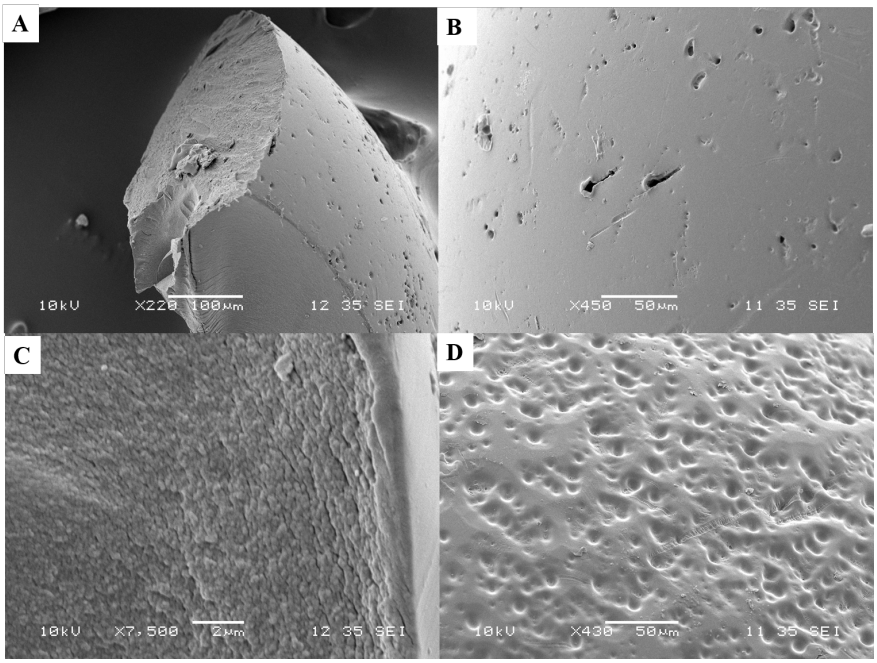

Figure S10: SEM images of crosslinked cellulose beads. A: Cross section and B: surface of a bead crosslinked with a 6wt% glyoxal solution. C: Cross section and D: surface of a bead crosslinked with a 12 wt% solution of glyoxal.

Data Collected in Conjunction with Davide Califano

- Generation of enzyme and buffer solutions
- Enzyme etching experiments
- Enzyme etched cellulose bead mechanical analysis.

The samples bead samples were generated and SEM images collect by the author of this thesis.

Data Collected in Conjunction with James Close

- Dispersion and particle size data for APP particle
- Synthesised all cellulose-APP beads
- Mechanical compression analysis of cellulose-APP composite beads

- Operated membrane emulsification rig for the attempted generation of cellulose-APP microbeads with particle size data.
- Density, viscosity, interfacial tension and contact angle determination for cellulose-OES-APP solutions
- Calculations of We, Ca numbers

All TGA, SEM and EDX data were collected by the author of this thesis.